Dissertation

submitted to the

Combined Faculty of Mathematics, Engineering and Natural Sciences

of Heidelberg University, Germany

for the degree of

Doctor of Natural Sciences

Put forward by

Bastián Alejandro Reinoso Reinoso

born in: Calama, Región de Antofagasta, Chile

Oral examination: 15-04-2024

FORMATION OF MASSIVE BLACK HOLE SEEDS THROUGH RUNAWAY STELLAR COLLISIONS AND GAS ACCRETION IN DENSE STELLAR SYSTEMS

Referees: Prof. Dr. Ralf Klessen

Prof. Dr. Michela Mapelli

Abstract

The goal of this work is to gain a better understanding of the processes that lead to the formation of massive black hole seeds in the early Universe, in order to provide insights into the rapid emergence of the highest redshift quasars. Two different seeding mechanisms were studied via numerical simulations. The first mechanism explores the onset of runaway stellar collisions in dense clusters of Population III stars, focusing on understanding the role of an external potential for modelling the gas during the embedded phase. Stellar collision rates were also explored in a similar environment with the goal of confronting analytic estimates with numerical simulations. The study of this seeding mechanism demonstrates the plausibility of forming black hole seeds with $> 1000\,\mathrm{M}_\odot$ through runaway stellar collisions that produce very massive stars. Furthermore, an analytic model for estimating the number of collisions in dense star clusters is presented, and the identification of a new collision channel involving perturbations on binary stars is reported.

The second seeding mechanism explored in this work deals with the emergence of supermassive stars through the interplay of gas accretion and stellar collisions in environments resembling collapsed gas clouds in atomic cooling halos. The numerical implementation developed in this work allowed for a self-consistent treatment of stellar and gas dynamics for the exploration of this mechanism. The results show that the emergence of supermassive stars with $10^4\,\mathrm{M}_\odot$ is inevitable and a binary system of supermassive stars is the outcome in one third of the cases.

This thesis concludes by summarizing and discussing the results found in these studies and commenting on the future work needed to improve the models presented here.

Zusammenfassung

Das Ziel dieser Dissertation ist es, ein besseres Verständnis der Prozesse zu erlangen, die zur Entstehung massiver Schwarzlochkeime im frühen Universum führen, um Einblicke in die schnelle Entstehung des Quasars mit der höchsten Rotverschiebung zu geben. Mittels numerischer Simulationen wurden zwei verschiedene Seeding-Mechanismen untersucht. Der erste Mechanismus untersucht den Beginn sehr effizienter Sterkollisionen in dichten Clustern von Sternen der Population III und konzentriert sich dabei auf das Verständnis der Rolle eines externen Potenzials für die Modellierung des Gases. In einer ähnlichen Umgebung wurden auch die Kollisionsraten von Sternen untersucht, mit dem Ziel, analytische Schätzungen mit numerischen Simulationen zu vergleichen. Die Untersuchung dieses Seeding-Mechanismus zeigt die Plausibilität der Bildung von Schwarzer Löcher mit > 1000 M$_\odot$ durch Sternkollisionen. Darüber hinaus wird ein analytisches Modell zur Schätzung der Anzahl von Kollisionen in dichten Sternhaufen vorgestellt und über die Identifizierung eines neuen Kollisionskanals berichtet, der Störungen an Doppelsternen beinhaltet.

Der zweite untersuchte Seeding-Mechanismus befasst sich mit der Entstehung supermassereicher Sterne durch das Zusammenspiel von Gasakkretion und Sternkollisionen in Umgebungen, die kollabierten Gaswolken in Halos mit metallfreier atomarer Kühlung. Die entwickelte numerische Implementierung ermöglichte eine selbstkonsistente Behandlung der Stern- und Gasdynamik zur Erforschung dieses Mechanismus. Die Ergebnisse zeigen, dass die Entstehung supermassereicher Sterne mit 10^4 M$_\odot$ unvermeidlich ist und in einem Drittel der Fälle ein Doppelsystem supermassereicher Sterne entsteht.

Die Dissertation schließt mit einer Zusammenfassung und Diskussion der Ergebnisse dieser Studien und einem Ausblick auf zukünftige Arbeiten, die zur Verbesserung der hier entwickelten Modelle erforderlich sind.

Dedicado a mis hermanos, a mi madre, y a mis abuelos

Contents

List of Figures

Chapter 1

Introduction

The existence of quasars at very high redshifts ($z > 6$) poses a challenge to our understanding of black hole formation and growth. More specifically, when we observe objects at redshifts of $z = 6$ we are observing an epoch when the Universe was only 918.000 years old[1], which is less than 10% its current age (assuming a Λ-CDM cosmology with Planck Collaboration et al. (2020) parameters $H_0 = 67.4$ km s^{-1} Mpc^{-1}, $\Omega_m = 0.321$ and $\Omega_\Lambda = 0.679$). The fact that the light emitted by those objects can make it all the way to the Earth and be bright enough as to be detected by our instruments is remarkable, and implies that quasars are incredibly luminous. This brightness can be explained if the light emitted by these objects originates in the accretion disk around a supermassive black hole (SMBH). With this picture in mind comes one of the big questions that has so far eluded a definitive answer:

How did the supermasive black holes powering the highest redshift quasars formed within such a short time-span?

This works presents a research carried-on to help elucidate this interrogative by studying the formation of massive black holes in the early Universe through numerical simulations.

The first chapter of this thesis is an introduction to black holes, their supermassive counterparts and quasars, followed by a short story of their discovery and characterization. Chapter 2 presents a brief description of high redshift quasar properties and the methods used to measure their masses. The subject of Chapter 3 is oriented towards presenting the hypotheses proposed to explain the rapid emergence of supermassive black holes in the early Universe, focusing on the seeding mechanisms and followed by a condensed description of their growth for completeness. Chapter 4 describes the methods used to produce the numerical simulations used to investigate the black hole formation channels explored in this thesis. Chapters 5, 6, and 7 contain the scientific publications produced during this research. Fi-

---

[1]https://www.astro.ucla.edu/ wright/CosmoCalc.html

nally, Chapter 8 presents a summary and the conclusions, including comments about future studies in the field of massive black hole seed formation in the early Universe.

1.1   Black holes, supermassive black holes, and quasars

A black hole is an object with an escape velocity v_{esc} higher than the speed of light

$$v_{\text{esc}} = \sqrt{\frac{2GM}{r}}, \tag{1.1}$$

where G is the gravitational constant, M the mass of the object, and r the size of the object.

Black holes are a consequence of extreme space-time curvature in Einstein's field equations. One of the earliest suggestions of the existence of black holes came from the mind of Karl Schwarzschild in 1916 during his time in the army (Elizalde, 2020). He published a solution to Einstein's field equations for the gravitational field of a spherical non-rotating body of mass M (Schwarzschild, 1916). He showed that the escape velocity is equal to the speed of light for an object with a size

$$r_{\text{s}} = \frac{2GM}{c^2}, \tag{1.2}$$

where c is the speed of light, and r_{s} is known as the Schwarzschild radius. This radius marks the position of the event-horizon for a non-rotating black hole, a boundary beyond which events cannot affect an observer.

The idea of an object with this characteristics remained as a mathematical curiosity until the discovery of the X-ray source Cygnus-X1, which provided the necessary evidence to conclude that black holes indeed exist. X-ray detection from outside the Earth's atmosphere became possible in 1959 (Lewin and Goldstein, 2011). Among the X-ray sources discovered and presented in Bowyer et al. (1965), the Cygnus-X1 source revealed a rapid variability, implying that the X-ray emission originated in a region smaller than the Sun. Subsequent radio observations allowed an accurate determination of the source location, discovering that it was part of a binary system with a supergiant star as a companion (Bolton, 1972), which in turn opened up the possibility of calculating the mass of the X-ray source from orbital parameters. This ultimately led to the characterization of the source as non-detectable in the visible part of the electromagnetic spectrum, compact, and massive ($> 2\ \text{M}_\odot$), suggesting that the source was indeed a black hole (Webster and Murdin, 1972). The accepted paradigm is that the X-ray emission of Cygnus-X1 originates in the accretion disk around a $\sim 14\ \text{M}_\odot$ black hole (Orosz et al., 2011; Rothschild et al., 1974).

Black holes can be formed when an object exceeds the Tolman–Oppenheimer–Volkoff limit (Oppenheimer and Volkoff, 1939), a mass above which a neutron star inevitably collapses into a black hole. The current value of this limit is in the range of $2.01 - 2.16\ \text{M}_\odot$

(Rezzolla et al., 2018). This limit can be surpassed in processes involving stellar evolution and mass transfer in binary systems. Our current understanding of stellar evolution for isolated stars predicts maximum black hole masses in the range of $20 - 30$ M$_\odot$ (Belczynski et al., 2010), however we know of the existence of black holes with 10^6 M$_\odot$, like Saggitarius A* at the center of the Milky Way, and even 10^9 M$_\odot$ like M77* in the M77 galaxy. Because of their immense masses these black holes receive the prefix "supermassive".

Supermassive black holes are believed to play an important role during the formation and evolution of their host galaxy. The discovery of correlations between black hole mass and velocity dispersion of stars in the bulge of spiral galaxies could be an indication of feedback effects that quench or trigger star formation in their vicinity, this would be of utmost importance during some galactic processes.

In the recent past the study of black holes has seen the emergence of opportunities to investigate these enigmatic objects with new techniques, as demonstrated by the detection of the signal GW150914 in 2015 by the Laser Interferometer Gravitational-Wave Observatory (LIGO). The signal originated from the merger of a pair of black holes with masses around 29 and 36 M$_\odot$ (Abbott et al., 2016). We are just seeing the beginning of gravitational-wave astronomy. Future interferometers like LISA[2] will extend the detection range up to the elusive intermediate mass black holes ($1000 \lesssim M \lesssim 10^5$ M$_\odot$), whose existence has not been unequivocally confirmed yet although several candidates exist (Chilingarian et al., 2018).

It is also imperative to mention the important achievement of the Event Horizon Telescope collaboration that produced the very first image of the shadow of a black hole (Event Horizon Telescope Collaboration et al., 2019a) presented in Fig. 1.1. The target was the supermassive black hole at the center of the closest elliptical galaxy, M87, which lies at a distance of 16 Mpc (Tonry et al., 2001). This was followed by the release of an image of the supermassive black hole Saggitarius A* in 2022, which inhabits the center of the Milky Way.

An interesting phenomena associated to supermassive black holes is the existence of quasars. According to our current understanding quasars are supermassive black holes surrounded by an accretion disk that emits copious amounts of light due to the friction produced as the gas in the disk orbits the SMBH at immense velocities. Quasars are observed at extremely large distances and early in the history of the Universe, and their existence challenge our models for their formation and growth.

The next sections present part of the history of the discovery of some of the most distant quasars known to date, describing the observations that led to their identification and the techniques used to measure their masses.

---

[2]Laser Interferometer Space Antenna (Amaro-Seoane et al., 2023)
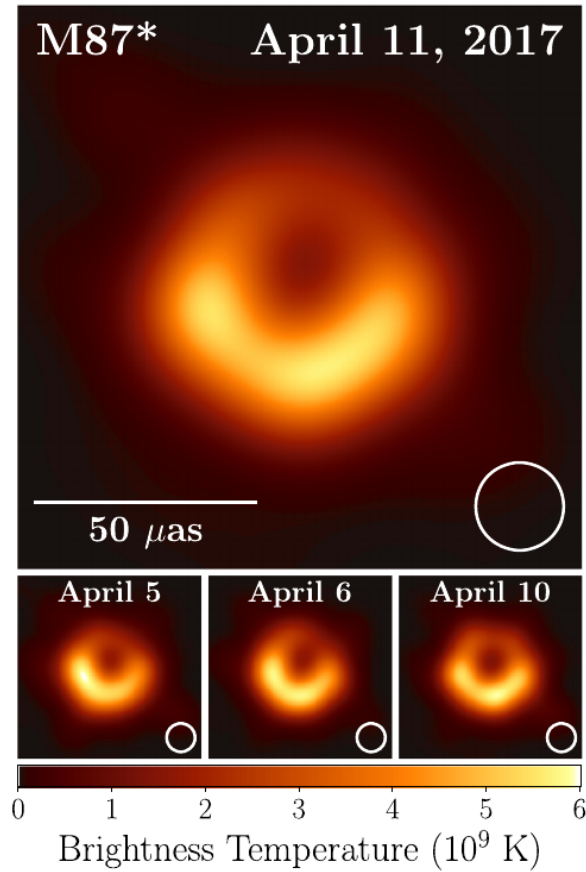
Figure 1.1. Image of the shadow of the supermassive black hole M87* published in April 2019 by the Event Horizon Telescope Colaboration (Event Horizon Telescope Collaboration et al., 2019b). The top image is the average of the three images presented at the bottom. The white circles show the size of the Gaussian kernel used to convolve the images. The color of the image is presented in units of the brightness tempertaure defined as $T_b = S\lambda^2/2\kappa_b\Omega$, where S is the flux density, λ is the observing wavelength, κ_b is Boltzmann's constant, and Ω is the solid angle of the resolution element. Credits: Event Horizon Telescope Collaboration et al. (2019b).

1.2   Brief history of quasars

Quasars are the most luminous individual, non-transient objects known in the Universe, with measured luminosities as high as 4×10^{13} L$_\odot$ (e.g. Bañados et al., 2018), capable of outshining their host galaxy and allowing us to detect them at incredibly large distances. A brief history of the discovery and characterization of these objects is presented here. A more complete narrative is presented in Shields (1999).

The history of quasars began with the first observations that showed - what we now know are - the first hints of accretion-powered light emission from galactic nuclei. A study of the

spectra of M77 (also known as NGC 1068 and shown in Fig. 1.2) revealed the presence of prominent lines both in absorption and emission (Fath, 1909). These lines were then also detected in in the spectra of other galaxies (Hubble, 1926; Slipher, 1917). The question at that time was: If the light emitted by a Galaxy is the combined light of all its stars, why do we see prominent emission and absorption lines?

Figure 1.2. M77 as seen by the Hubble Space Telescope. Image created by a combination of 8 HST images taken by different instruments and in different wavelengths. A supermassive black hole resides at the center. This image obtained the second place in the Hubble's Hidden Treasures initiative (https://esahubble.org/news/heic1305/#1). Credits: Andre van der Hoeven (https://www.flickr.com/photos/avdhoeven/).

In 1943 Carl Seyfert published a work describing the study of six galaxies that showed forbidden emission lines. Some of them corresponded to Oxygen ([OII], [OIII]), Nitrogen ([NI], [NII]) and Iron ([FeVIII]), as well as emission lines of Hydrogen ($H\alpha$, $H\beta$) and Helium (HeI). He reported wide profiles for some of these lines, in particular for the hydrogen lines these values were as high as $7000 - 8000$ km s^{-1} (Seyfert, 1943). The mechanism responsible of producing the lines was not identified, but this provided important clues towards solving the puzzle. Nowadays galaxies showing bright high-ionization emission lines in their nuclei are named Seyfert Galaxies and sublcassified into Type I or Type II depending on the presence of both wide and narrow (Type I) or only narrow (Type II) emission lines in their spectra. Seyfert galaxies are a type of active galactic nuclei (AGN), a type of galaxy in which the nuclei has a high surface brightness and presents high-ionization emission lines.

The serendipitous discovery of a strong radio signal originating in the Milky Way by Karl Jansky in 1932 paved the way for the birth of Radioastronomy and provided a cru-

cial tool for investigating AGNs. The work of Grote Reber produced the first sky survey in radio wavelengths (Reber, 1944), and after World War II, Radioastronomy became an increasingly popular field, with many groups gathering data and trying to understand the physical process that give origin to the radio emission from these galaxies. During this task variable radio sources were identified, for example in the Cygnus constellation (Hey et al., 1946). Subsequent observations started to reveal the strange morphology of some of these sources (Hanbury Brown et al., 1952) and the identification of forbidden emission lines like [OIII] and [NII], and a total energy emitted in radio even higher than the energy emitted in the optical (Baade and Minkowski, 1954). Eventually Kiepenheuer (1950) denomstrated that the radiation came indeed from electrons being accelerated in galactic magnetic fields, i.e., synchrotron radiation.

New catalogs in radio wavelengths were produced afterwards (Bennett, 1962; Edge et al., 1959). The improved position determinations allowed the optical identification of the source 3C 295 with a member of a cluster of galaxies, and the spectroscopic data revealed its enormous redshift $z = 0.4614$ tagging it as the most distant object discovered at that time (Minkowski, 1960). Continuing with the attempts to determine precise positions of additional radio sources, Hazard et al. (1963) took advantage of the lunar occultation of the source 3C 273 and observed it with the Parkes telescope in Australia. The precise measurements delivered by this technique resulted in the characterization of this source as a two component emitter separated by 19.5 arcsec and the identification of one of these components with a 13 mag star as the optical counterpart. Spectroscopic observations showed unusual emission lines that could be satisfactorily explained as redshifted Balmer lines, [OIII], and MgII (Schmidt, 1963), with a redshift of $z = 0.158$. This interpretation would be supported by the identification of the Hα line at infrared wavelengths (Oke, 1963). Additionally, spectrscopic observations of 3C 48 by Greenstein (1963) also detected the presence of MgII and [OIII] with an associated redshift of $z = 0.16$. This new class of radio sources were similar to AGNs, but with star-like appearances and highly redshifted spectral lines. These objects were later named quasars (Chiu, 1964).

1.3   Towards a physical understanding of quasars

Having identified this new class of objects the next natural step was to propose models that could explain all the features observed. In this line of reasoning the excellent work of Greenstein and Schmidt (1964) discussed the problems of the hypothesis that 3C 48 and 3C 273 were massive, distant stars, whose observed redshift was of gravitational origin, and that were surrounded by a gas cloud in which the emission lines were produced. They also considered the hypothesis that the redshift was of cosmological origin, concluding that

"The simplest model of the quasi-stellar sources is one in which a small mass of 10^9 M$_\odot$ is surrounded by shells of increasing radius in which the optical continuum, the emission lines, and the radio continuum, respectively, originate.".

The sample of quasars then began to increase as Schmidt and Matthews (1964) published redshifts of $z = 0.425$ for 3C 47, and $z = 0.545$ for 3C 147. Aided by accurate positions from Radio observations, optical positions, and photometry, 21 new quasi-stellar sources were identified and described in Sandage et al. (1965). Additionally, sources with redshifts as high as $z = 1.2410$ started to emerge (Sandage, 1965), and the possibility to detect absorption lines associated to high-redshift atomic Hydrogen in the intergalactic space (the Lyman-α forest), were recognized (Gunn and Peterson, 1965; Scheuer, 1965).

Nowadays the accepted paradigm is that quasars are a type of AGN that can be detected at high redshifts. Their high luminosities are a consequence of accretion-powered continuum emission from an accretion-disk orbiting a central supermassive black hole. This region is in turn surrounded by a thick dusty torus that can hide part of the light emitted from the very center and thus the differences between observed AGNs depend on how much of the central region is hindered from us by this torus and if we observe the jet that emerges from the central region. This is illustrated in Fig. 1.3
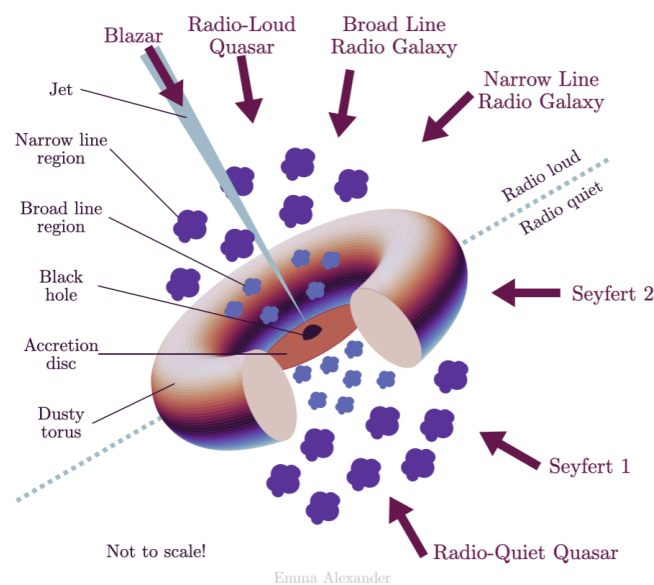
Figure 1.3. Illustration of the unified AGN theory showing the black hole at the very center surrounded by an accretion disk. The clouds closest to the BH orbit very fast and thus produce the broad emission lines. On the other hand, the clouds further away move much more slowly and the emission lines are not broadened. Black arrows represent different viewing angles and the classification given accordingly. Credits: Emma L. Alexander https://emmaalexander.github.io/resources.html .

Chapter 2

High redshift quasars and supermassive black holes

The existence of the $z = 7.54$ quasar J1342+0928 in 2018 by Bañados et al. (2018), among others, demonstrates that gigantic black holes were formed early on in the history of the Universe. In fact, the observation implies that the mass of this black hole was already 8×10^8 M$_\odot$ when the Universe was only 690 million years old. This is only one of the more than 200 quasars known at redshift $z > 5.7$ (Fan, 2006). Explaining the huge black hole masses measured for these objects at such early times is difficult.

This chapter presents, for completeness and rather briefly, some of the techniques employed for discovering high redshift quasars and the methods used to measure the masses of the black holes that power them. The combinations of these techniques ultimately led to the discovery and characterization of the most distant and most massive black holes that still challenge our understanding of their formation and growth.

2.1 The search and study of high redshift quasars

Along with an increase in the number of detected quasar candidates from catalogues in radio wavelengths (Sandage et al., 1965; Schmidt and Matthews, 1964), and understanding that their luminosity originates in the accretion disk around supermassive black holes (Shakura and Sunyaev, 1973), it was understood that the study of these objects would provide an indirect method for studying the early Universe and galaxy formation. Subsequent efforts were focused on finding the highest redshift quasars.

Thanks to the emergence of digital large sky surveys, the first techniques used to detect high redshift quasars were developed, and relied on detecting outliers in color-color diagrams. These sources would then be analyzed spectroscopically to confirm their nature. The plausibility of this method was demonstrated by the detection of a $z > 4.3$ quasar from a

survey recorded with the UK schmidt telescope (UKST) using five different filters U,J,V,R,I (Warren et al., 1987). The outliers in color-color diagrams can be clearly seen in Fig. 2.1.
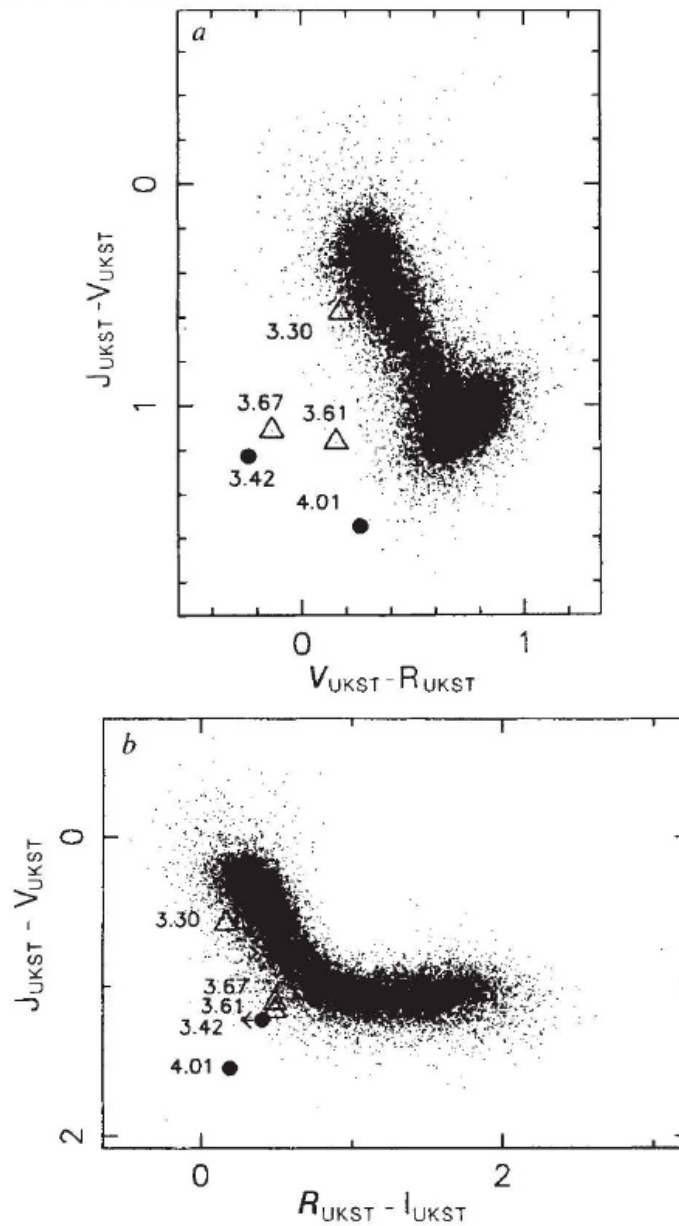
Figure 2.1. Color-color diagrams showing the sources detected in the UKST survey. Known quasars are represented by triangles and the two new confirmations of the study are represented by black circles. Credits: Warren et al. (1987).

Thanks to the advent of the Sloan Digital Sky Survey (SDSS), a survey dedicated to map the sky in five photometric filters in the range $3551 - 8932$ Å; as well as spectroscopic follow-up of selected candidates, a large number of quasars were progressively discovered and studied.

Fig. 2.2 presents another example of a color-color diagram constructed with SDSS data in which quasars are separated from stars.
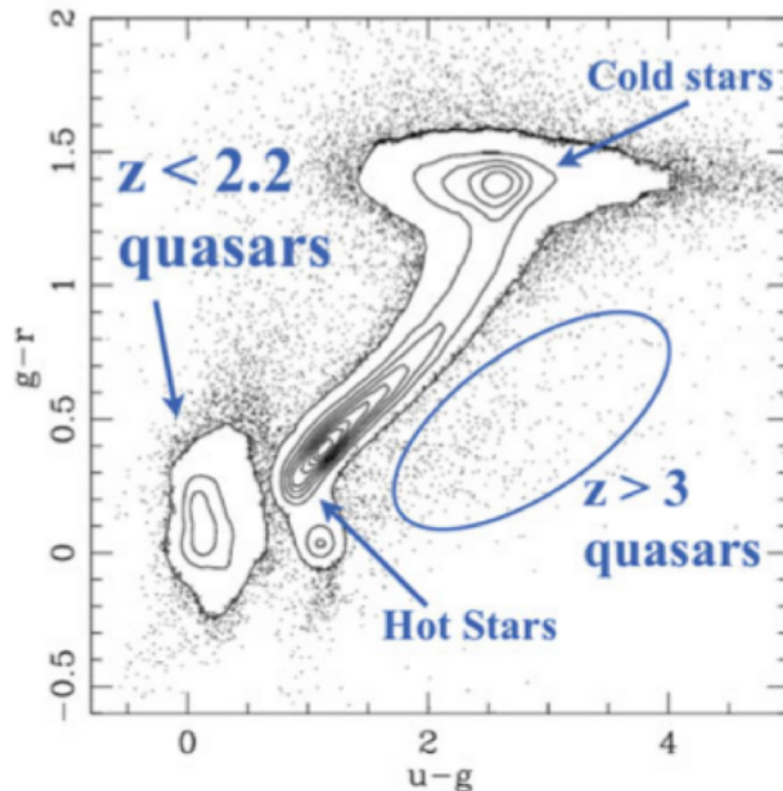
Figure 2.2. Quasar selection technique based on SDSS photometric colors. Nearby quasars ($z < 2.2$) have bluer $u - g$ colors than stars, whereas high redshift quasars ($z > 3$) have redder $u - g$ colors. Credits: Ivezić et al. (2014).

A clear demonstration of this technique is presented by Fan et al. (2001a) who searched for "i-dropout quasars", i.e., quasars in which the Lyman break falls entirely in the i band of the SDSS. This occurs for quasars at $z > 5.8$. They also included longer wavelength observations from the 2MASS catalog (Skrutskie et al., 1997) to help discriminate cool dwarf stars from their candidate sample, the main contaminant when using the i and z photometric filters from the SDSS data as shown in Fig. 2.3. In this work they describe the discovery of three new quasars, SDSS 0836+0054 ($z = 5.82$), 1306+0356 ($z = 5.99$), and 1030+0524 ($z = 6.28$). This last object is particularly interesting, and in the words of Xiaohui Fan "For the $z = 6.28$ quasar SDSS 1030+0524 the flux is consistent with zero in a region of 300 Å immediately blueward of Lyα emission. It suggests a tentative detection of a complete Gunn-Peterson trough, indicating that at $z \sim 6$ the universe is close to the reionization epoch".

Additionally the authors estimate the masses of the BHs powering those quasars. For this they first obtain their bolometric luminosity assuming no lensing effects and that the continuum spectrum of the quasars is the same as the mean obtained by Elvis et al. (1994). Furthermore, they assume that the quasar bolometric luminosity equals the Eddington lumi-

nosity. Under these assumptions they derive BH masses of 4.82×10^9 M$_\odot$, 2.0×10^9 M$_\odot$ and 1.9×10^9 M$_\odot$ for SDSS 0836+0054, 1306+0356, and 1030+0524, respectively.
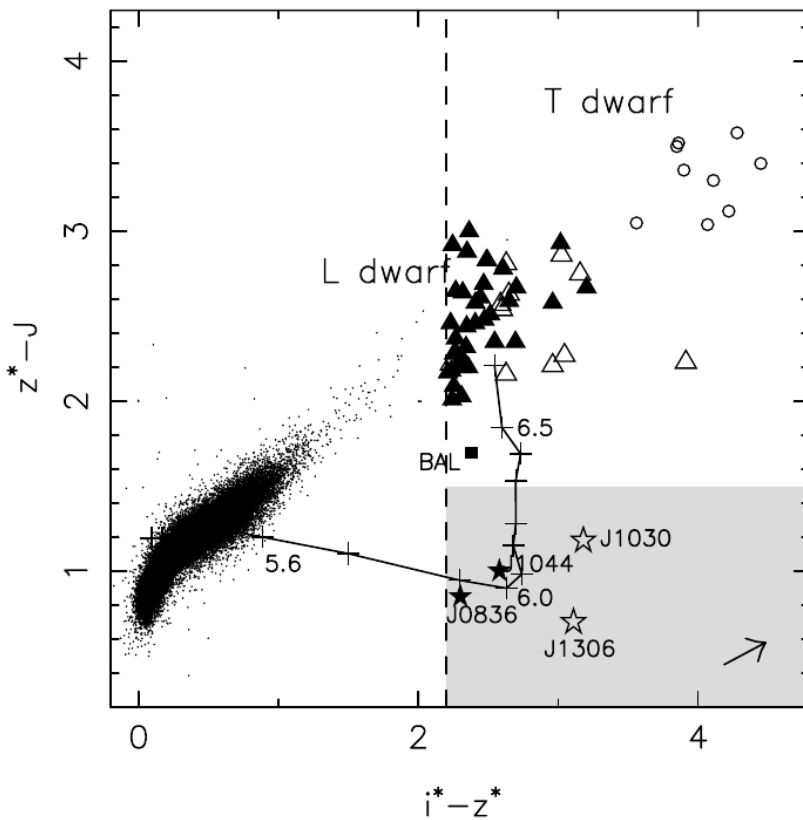
Figure 2.3. $z^* - J$ as function of $i^* - z^*$ colors for the i-dropout sample obtained by Fan et al. (2001a). The circles represent T dwarfs, triangles for L dwarfs, stars for $z > 5.8$ quasars, squares for BAL quasar. Filled symbols for S/N in the i band higher than 4, otherwise empty symbols were adopted.The i^* and z^* notation was used because the u, i, g, r, z photometric system was still being calibrated. The black line and crosses show the median track of simulated quasar colors. Credits: Fan et al. (2001a).

Thanks to subsequent efforts by Fan et al. (2004, 2001a, 2002, 2003, 2001b), by the year 2006 a total 19 quasars detected from the SDSS had been reported and some important characteristics were recognized. One of the most important was the strikingly similar Spectral Energy Distribution (SED) among the high- and low-redshift quasar population. It is evident from Fig. 2.4 that the SED of high redshift quasars is very much the same ignoring the effects of the Lyman-α forest at shorter wavelengths, which eventually turns into a Gunn-Peterson trough for $z \gtrsim 6$, marking the transition to a largely ionized IGM (Fan, 2006). The last imaging data release of the SDSS (DR9) in 2012 covers more than 35% of the sky, including new spectra for > 100.000 quasars with a median redshift of $z \sim 2.32$ (Ahn et al., 2012).

Following the success of quasar identification efforts, the limitations of the color-color
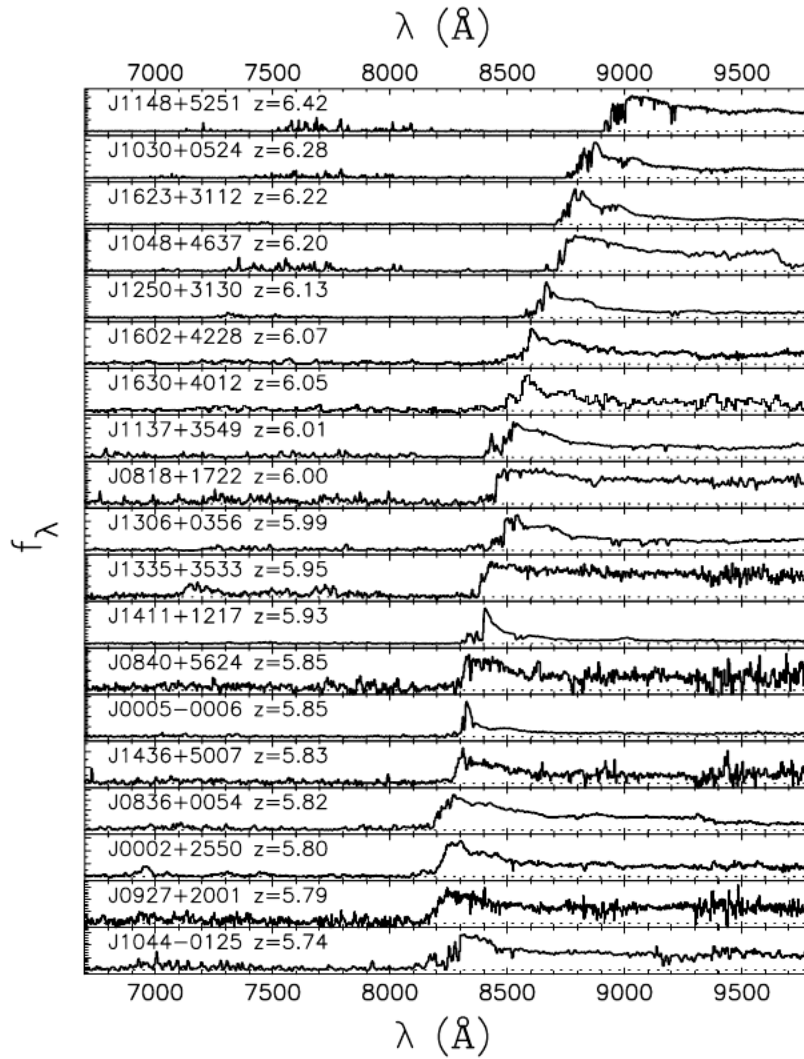
Figure 2.4. The spectra of 19 $z > 5.7$ quasars detected from the SDSS data. Strong Lyman-α absorption is seen blueward of the Lyman break. Credits: Fan (2006).

selection technique were rapidly identified, in particular, for the SDSS survey, which could only detect quasars up to $z \sim 6.5$ (Fan et al., 2000). This comes from the criteria used to detect the candidates and the redshift of distant objects. Because of the absorption of photons with wavelengths shorter than the Lyman limit and the Lyman-α forest, high redshift quasars show a close to zero emission bluewards of the Lyman-α line. At higher redshifts this break in luminosity moves to increasigly longer wavelengths as depicted in Fig 2.4. For the z filter of the SDSS centered at 8932 Å, the redshift at which the emitted Lyman-α line photons ($\lambda = 1215.67$ Å) fall into this filter is

$$z = \frac{\lambda_{obs} - \lambda_{emit}}{\lambda_{emit}} \sim 6.4,$$

imposing a limit to the redshift of the quasars that can be identified with the dropout method. It is then evident that surveys at longer wavelengths are required if the $z = 7$ limit is to be surpassed.

Precisely this was one of the objectives that impulsed the creation of the UKIRT Infrared Deep Sky Survey (UKIDDS). This survey is a seven-year observing campaign that made use of the Wide Field Camera of the United Kingdom Infrared Telescope (UKIRT) on Mauna-Kea in Hawaii (Lawrence et al., 2007) to observe 7500 deg^2 of the northern sky. The survey was conducted making use of five filters Z, Y, J, H, K with a wavelength range in between $0.836 - 2.380\ \mu$m, which is equivalent to $8360 - 23\,800$ Å, making it an infrared counterpart to the SDSS. It was the combination of UKIDSS data with SDSS that allowed the identification of a quasar candidate that would later be confirmed via spectroscopic observations with the Gemini North telescope to be a $z = 7.085$ quasar (Mortlock et al., 2011).

Seraching for quasars at even higher redshifts is a difficult task. On one side they appear less bright, so deeper surveys are needed and only the brightest ones can be detected. The final SDSS $z \sim 6$ quasar sample covers more than 11.000 deg^2, yet only 52 quasars have been detected (Fan et al., 2023). On the other side, Lyman break dropout techniques that use optical and NIR photometric data will encounter objects that display similar colors to high redshift quasars, with these objects being dwarf stars of type M, L, and T, and early-type galaxies, as illustrated in Fig.2.5.
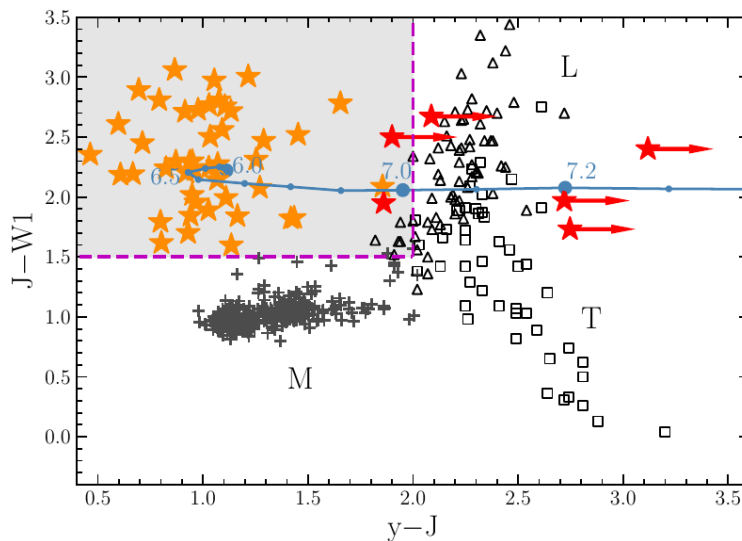
Figure 2.5. Color-color diagram used to identify high redshift quasars with the inclusion of MIR photometric data from the WISE survey (W1 band). Orange stars represent known quasars at $6.5 < z < 7$, red stars are known quasars at $z > 7.0$ and black symbols represent M, L, and T dwarfs. The cyan line represents the color-redshift relation based on simulated quasar spectra. Credits: Fan et al. (2023) and Wang et al. (2019).

A strategy to help overcome this last difficulty is the inclusion of MIR photometric data, in particular from the WISE survey (Wright et al., 2010), since it helps to separate quasars at $6 < z < 7$ from M,L, and T dwarfs in color-color plots. In fact, the highest redshift quasars

known to date have been detected thanks to a combination of NIR, optical, and MIR photometry, and are: J1342+0928 at $z = 7.54$ (Bañados et al., 2018) ; J1007+2115 at $z = 7.52$ (Yang et al., 2020); and J0313-1806 at $z = 7.64$ (Wang et al., 2021). In addition, probabilistic methods have been applied to help discriminate contaminants. One of such methods consist on a Bayesian model comparison, where given a photometric measurement, a posterior probability is computed taking into account the surface density distribution of quasars, brown dwarfs, and galaxies. This method was applied by Mortlock et al. (2011). Another strategy presented in Reed et al. (2017) consists in comparing the photometric data of a candidate to modelled SEDs of quasars, brown dwarfs, and early-type galaxies. By calculating reduced χ^2 values one can then narrow down the number of candidates to the ones that most likely are quasars. These are only two of many methods utilized to help with contaminant discrimination in quasar selection techniques. A good summary of more strategies can be found in the review by Fan et al. (2023).

In the future, deeper surveys at optical and NIR wavelengths will certainly increase the number of known high-redshift quasars. The sensitivity of the Vera Rubin observatory will allow the detection of $25 - 26$ mag sources thanks to The Legacy Survey of Space and Time, which will map the southern sky during 10 years in optical wavelengths. Complementary to this, the Euclid mission will obtain photometric data at NIR wavelengths (as well as optical) by mapping 15000 deg^2 of the sky, reaching magnitudes as faint as 24 in the Y, H, and J bands. The combination of data from these telescopes is expected to provide thousands of AGN detections at $z \sim 6.5 - 7$ and 25 quasars at $z > 7$, with up to 8 at $z > 8$ (Euclid Collaboration et al., 2019). The faint sources detected in this way will need to be further studied by more powerful spectrographs, like those on-board the JWST and in future 30-m telescopes.

2.2 Measuring black hole masses

Having presented the methods used to detect quasars at high redshift ($z > 4$) it is then important to understand the methods used to measure the masses of the BHs that power them, and that together with the tools previously presented, have ultimately led to the problem of rapid supermassive black hole formation and growth.

The methods used for determining the mass of a black hole can be broadly classified in two categories. The first one relies on measuring the dynamical effects of the black hole on surrounding stars. The second method consists in measuring the properties of the gas surrounding the black hole. This section aims to briefly introduce some of these techniques.

2.2.1   Stars orbiting the black hole

The most reliable method for measuring black holes masses consists in resolving the scales at which stars orbit around them, as done for Sgr A*, the BH in the center of the Milky Way. By measuring the position of the S-stars orbiting the BH, in particular, of the S2 star, at different epochs as illustrated in Fig. 2.6, in combination with Kepler's third law we know that Sgr A* has a mass of 4.148 ± 10^6 M$_\odot$(GRAVITY Collaboration et al., 2019). However this method cannot be used for high-redshift quasars since at these distances, these scales are impossible for us to resolve.
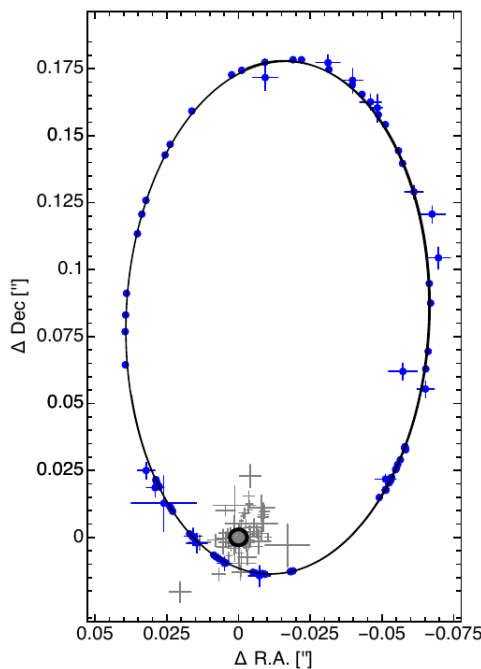
Figure 2.6. Orbit of the S2 star as seen on the sky by interferometric data from the Very Large Telescope and Keck observatories. The blue dots mark the position of the S2 star at different epochs, whereas the black circle marks the position of Sgr A*, which agrees with the position of flares seen by Adaptive Optics observations (grey crosses). Credits: GRAVITY Collaboration et al. (2019).

Another approach that relies on stellar kinematics consist in measuring the velocities of stars that are within the radius of influence r_{infl} of the black hole. This radius delimits the region inside which the gravity is dominated by the BH mass, and is approximately given by

$$r_{\mathrm{infl}} = \frac{GM_{\mathrm{BH}}}{\sigma^2} \approx 13 \left(\frac{M_{\mathrm{BH}}}{10^8 \, \mathrm{M}_\odot} \right)^{0.5} \mathrm{pc}, \tag{2.1}$$

where M_{BH} is the mass of the BH, and σ is the velocity dispersion of the stars. One example of the application of this method can be found in the work by Kormendy and Richstone (1992). They present a set of spectroscopic measurements at different positions along the

semi-major axis of the galaxy NGC 3115, including photometric measurements as well. Velocity dispersion were measured by the width of stellar absorption spectral lines, whereas rotation was measured from doppler shifts of the lines. By using the second moment of the collisionless Boltzmann equation to fit the kinematic data (as illlustrated in Fig. 2.7), combined with models for the brightness profile of the central parts of the galaxy they were able to demonstrate high mass-to-light ratios (> 50) consistent with the presence of a 2×10^9 $M_\odot$ SMBH at the center.
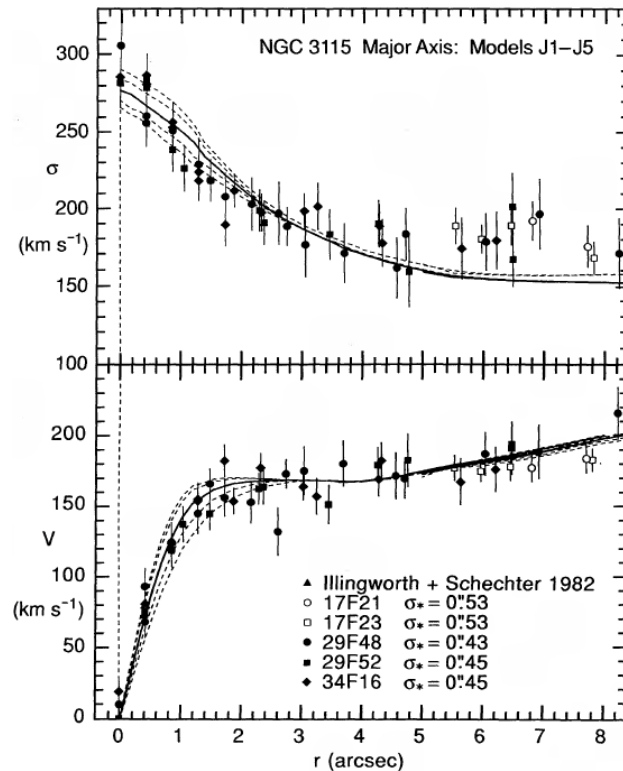
Figure 2.7. Stellar velocity dispersion and rotation along the semi-major axis of NGC 3115. Solid and dashed lines show the fits to the data for different models. Credits: Kormendy and Richstone (1992).

2.2.2 Reverberation mapping

Another approach consists in observing the properties of the gas orbiting the central BH in AGNs. Assuming that the motion of the gas around the BH is dominated by the BH's gravity one can use Newton's law of gravitation to derive another method for measuring the BH mass. Let us assume a circular motion of a test mass m orbiting a point mass $M_{\rm BH}$ at distance R with velocity v. Equating the gravitational force and the centrifugal force we

obtain

$$
\begin{aligned}
G\frac{m\,M_{\mathrm{BH}}}{R^2} &= m\frac{v^2}{R^2}R, \\
M_{\mathrm{BH}} &= \frac{v^2 R}{G},
\end{aligned}
$$

where G is the gravitational constant. It is then evident that one just needs a measure of the orbital velocity of the gas and its orbital distance in order to calculate the mass of the central BH. In practice the equation employed is given by

$$
M_{\mathrm{BH}} = f\frac{(\Delta V)^2 R_{\mathrm{BLR}}}{G}, \tag{2.2}
$$

where $(\Delta V)^2$ is the velocity dispersion squared of the gas in the Broad Line Region (BLR), R_{BLR} is its orbital distance, and f is a correction factor that accounts for the shape of the BLR.

The BLR is the place where the broad emission lines observed in AGNs are produced. By taking a spectra of the gas in this region one can obtain the orbital velocity of the gas given that the broadening is caused by Doppler shifts of the rapidly orbiting material. The technique for measuring R_{BLR} was reported by Blandford and McKee (1982) who named it Reverberation Mapping. The idea behind is that luminosity variations in the continuum (produced in the accretion disk that orbits the BH) will travel to the BLR and produce a change in the flux of the emission lines. Then the time-delay between the variations in the continuum and in the flux of the broad lines is equal to

$$
t_{\mathrm{delay}} = \frac{R_{\mathrm{BLR}}}{c}, \tag{2.3}
$$

where c is the speed of light.

Having obtained $(\Delta V)^2$ from spectroscopy and R_{BLR} with the reverberation mapping technique, the mass of the black hole M_{BH} can be computed with Eq.(2.2).

2.2.3   The R-L relation

The success of the Reverberation Mapping technique is elegantly presented in the work of Peterson and Wandel (1999). By gathering 8-year observational data of the Seyfert I Galaxy NGC 5548, the time-delay and width of several emission lines could be measured, yielding consistent estimates of a 7×10^7 M$_\odot$ BH at its center and confirming the expected $R_{\mathrm{BLR}} \propto V_{\mathrm{FWHM}}^{-2}$ relation expected for virialized motions of the BLR around a point-mass. This study also pointed at a possible correlation between the luminosity of the continuum emission of the AGN and the emission-line flux for broad emission lines.

By using a large sample consisting of a combination of 17 quasars plus several Seyfert I AGN from the literature, Kaspi et al. (2000) also demonstrated a correlation between the

time-delay and the width of different emission lines, consistent with previous similar studies. Moreover they expanded on the R_{BLR}-Luminosity relation, including a sample of AGNs that varies by over 2 orders of magnitude in luminosity. They found that the size of the BLR scales with the 5100 Å Luminosity as $R \propto L^{0.7}$.

One of the latest studies of this correlation was carried on by Bentz et al. (2009), who put additional efforts on modelling the host galaxy contribution to the Hβ line as well as to the 5100 Å luminosity. They found the relation

$$\log\left(R_{\mathrm{BLR}}\right) = -21.3 + 0.519 \log\left(\lambda L_{\lambda,5100}\right), \tag{2.4}$$

with R_{BLR} in light-days and $\lambda L_{\lambda,5100}$ being the luminosity at 5100 Å in units of erg s^{-1}.

It is then clear that the R-L relation provides a convenient way for determining R_{BLR} as an alternative to the expensive Reverberation Mapping technique, since it does not require long monitoring campaigns, and thus can be applied to quasars, for which direct measurements using stellar or gas kinematics is impossible. The method for weighing BHs with the R-L relation is also known as single-epoch method.

The determination of the size of the BLR obtained from the AGN luminosity can therefore be combined with the width of a broad line to yield a BH mass. Not only the Hβ line can be used but also CIV and the MgII line. In particular Vestergaard and Osmer (2009) derive a BH mass estimator using the MgII line of the form

$$M_{\mathrm{BH}} = 10^{zp(\lambda)} \left[\frac{\mathrm{FWHM(MgII)}}{1000 \text{ km s}^{-1}}\right]^2 \left[\frac{\lambda L_\lambda}{10^{44} \text{ erg s}^{-1}}\right]^{0.5}, \tag{2.5}$$

where the the value of the zero point $zp(\lambda)$ depends on the observed wavelength.

It was the use of this relation that delivered a BH mass of 2×10^9 M$_\odot$ by using the MgII line and the 3100 Å luminosity for the $z = 7.085$ quasar reported in Mortlock et al. (2011), and a mass of 7×10^8 M$_\odot$ for the BH powering the quasar ULAS J1342+0928 at $z = 7.54$ (Bañados et al., 2018).

The choice of the emission line to be used for the BH mass computation depends on whether the line is available in the observed spectral region, and whether the line is affected by absorption lines or blending with other lines such as FeII or HeII (Vestergaard, 2002). While the most used estimators are the Hα and Hβ lines that fall on the optical for low redshift quasars, one has to rely on the detection of lines that fall on the rest-frame UV when observing quasar spectra with optical telescopes for the high redshift quasar population. Two other lines are typically employed, the CIV λ1549 Å and MgII λ2798 Å, with the latter presenting less scatter when correlated with the luminosity at 5100 Å (Shen and Liu, 2012).

2.2.4   Mega-Masers

This is a method based on the dynamics of gas orbiting a black hole at sub-parsec scales. The word MASERS stands for Microwave LASERS, and just like LASERS they are produced when a population inversion is present, with the difference being in the wavelength of the amplified light. Masers are known to exist in young star-forming regions, in molecular envelopes of evolved stars and in the nuclei of galaxies (Reid, 2002; Reid and Moran, 1981). The most common type are the OH and H_2O masers that emit at $\lambda = 18$ cm and $\lambda = 1.35$ cm. The prefix "Mega" simply indicates that the luminosity derived for this type of masers is ~ 6 orders of magnitude higher than typical luminosities of masers found in star-forming regions.

The galaxy NGC 4258 displays the archetypal circumnuclear H_2O maser. Since masers are detected at radio wavelengths, Very Long Baseline Interferometry (VLBI) observations allowed high-resolution measurements for the positions and velocities of these sources. The data clearly showed a spatial velocity gradient, velocity variations with time, and high-velocity sources differing up to 1000 km s^{-1} from the systemic velocity (Greenhill et al., 1995; Miyoshi et al., 1995; Moran et al., 1995), all of them nicely explained by maser emission in a thin Keplerian disk around an SMBH. This is illustrated in Fig. 2.8. The mass can be then calculated by fitting a keplerian rotation curve to the maser data as shown in panel (c) of Fig. 2.8. With this method Miyoshi et al. (1995) estimated a mass of 3.6×10^7 M$_\odot$ for the central SMBH in NGC 4258.

2.2.5   The $M - \sigma$ relation

Armed with a set of measured BH masses with the methods mentioned previously, in particular with the stellar kinematic methods presented in Sec. 2.2.1 and the gas dynamical methods of Sec. 2.2.2 and 2.2.4, Ferrarese and Merritt (2000) showed that a correlation exists between the mass of the BH and the velocity dispersion of the stars in the bulge of their host galaxy. This relation was also independently found by Gebhardt et al. (2000). This is know as the $M - \sigma$ relation and can be seen in Fig. 2.9. The existence of this relation implies the presence of a mechanism responsible for maintaining the correlation (see e.g. King, 2003; Silk and Rees, 1998).

Irrespective of the ultimate cause behind this relationship, this tight correlation (with a scatter < 0.3 dex as estimated by Tremaine et al. (2002)) provides the opportunity to estimate the mass of a BH, provided one can obtain the velocity dispersion of the stellar component in the central region of a galaxy, for example, with integral field spectroscopy (McConnell et al., 2011).
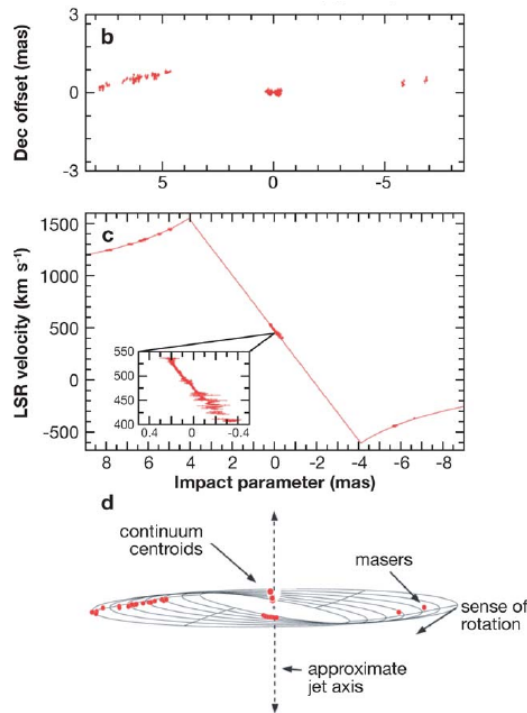
Figure 2.8. Illustration of mega-masers originating in the accretion disk around the SMBH in NGC 4258. Panel (b) shows the spatial distribution of the maser sources. Panel (c) shows the rotation curve of the maser emission. Panel (d) shows an illustration of a warped disk model fitted to the spatial distribution of the maser emission. Credits: Lo (2005).
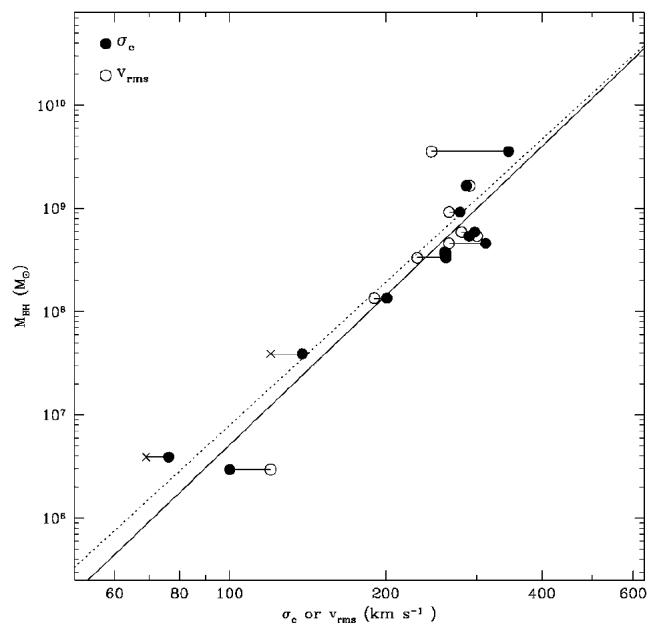
Figure 2.9. The $M - \sigma$ relation. This figure shows a correlation between the mass of the BH (y-axis) and the velocity dispersion of the stars (x-axis) that inhabit the centers of many galaxies. Credits: Ferrarese and Merritt (2000)

Chapter 3

Explaining the rapid emergence of supermassive black holes

After a description of high redshift quasars, the methods employed for their discovery and study, and the techniques used to measure their masses, it is now time to present some of the hypotheses developed to explain their rapid emergence.

The supermassive black holes that power the highest redshift quasars were formed during the dark ages of the Universe, and their rapid assembly can be explained by a combination of black hole seed formation and subsequent growth.

This chapter begins by presenting the cosmological model that sets the ground for characterizing the epoch of massive black hole seed formation. Then the seed formation mechanisms are presented, focusing on the three main hypotheses studied by the astronomical community in this context. These mechanisms are classified depending on their potential to form light seeds (< 1000 M$_\odot$) or heavy seeds (≥ 1000 M$_\odot$). Towards the end of the chapter a brief introduction to black hole growth is presented for completeness.

3.1   The cosmological model

Our universe and its evolution on large scales is described by a cosmological model. Such a model makes use of Einstein's field equations and the cosmological principle, which states that the Universe is homogeneous and isotropic on large enough scales. The combination of these ideas ultimately results in the Friedmann equations, one of which is frequently written as

$$H^2 = H_0^2 \left(\Omega_m \, a^{-3} + \Omega_r \, a^{-4} + \Omega_\Lambda + \Omega_k \, a^{-2} \right),$$ (3.1)

where a is the scale factor, a time-dependent dimensionless quantity that parameterizes the expansion of the Universe. By definition, the value of the scale factor at present time is $a_0 = 1$, with decreasing values for earlier times and increasing values for future times. H

is the Hubble parameter defined as

$$H \equiv \frac{\dot{a}}{a},$$ (3.2)

and H_0 is its value at present time, i.e., when $a = a_0 = 1$. H_0 is also known as the Hubble constant and quantifies the expansion rate of the Universe. The density parameter Ω is defined as

$$\Omega \equiv \frac{\rho}{\rho_c},$$ (3.3)

and is used to express the contribution of different types of matter and energy. These contributions come from matter ρ_m, radiation ρ_r, the geometry ρ_k, and a cosmological constant ρ_Λ. The critical density ρ_c is defined as

$$\rho_c \equiv \frac{3H^2}{8\pi G}.$$ (3.4)

Therefore Eq.(3.1) takes into consideration the effects of radiation, matter, the geometry of the Universe and a cosmological constant through the parameters Ω_r, Ω_m, Ω_k, and Ω_Λ respectively.

Several observational probes are used to constraint these parameters. In particular the observation of anisotropies in the Cosmic Microwave Background (CMB) presented in Fig. 3.1 reveals that the Universe has a flat geometry, so that $\Omega_k = 0$ (Bennett et al., 2013). On the other hand, the supernova cosmology project provided evidence that supports the need for a positive value of the cosmological constant (Riess et al., 1998). At present, many methods have been combined for measuring the parameters in Eq.(3.1), some of which are: CMB anisotropies, Supernovae, gravitational lensing, Big Bang Nucleosynthesis, and Baryon Acoustic Oscillations (BAO). The data of Planck Collaboration et al. (2020) is consistent with a flat Universe containing 67.9% of the matter-energy density in the form of dark energy ($\Omega_\Lambda = 0.679$), and 32.1% in the form of matter, ($\Omega_m = 0.321$, with 4.9% baryonic matter plus 27.2% cold dark matter). Additionally the density parameter for radiation has been found to be $\Omega_r \sim 10^{-5}$ (Tanabashi et al., 2018).

At the moment of writing this thesis there is an important discrepancy in the value of the Hubble constant H_0 obtained from the cosmological parameters constrained by the CMB and BAO data (early Universe), and the value of H_0 measured via Type Ia SNe, strong lensing time delays of quasar images, and VLBI observations of water masers (late Universe). The values delivered by these methods are $H_0 = 67.4^{+1.1}_{-1.2}$ (early Universe) and $H_0 = 73.3^{+0.8}_{-0.8}$ (late Universe), discrepant at a significance of $> 4\sigma$ (Verde et al., 2019), with a growing number of observations that rule out the possibility of systematic errors in the distance ladder (late Universe method) (Riess et al., 2023, 2019), while at the same time making very
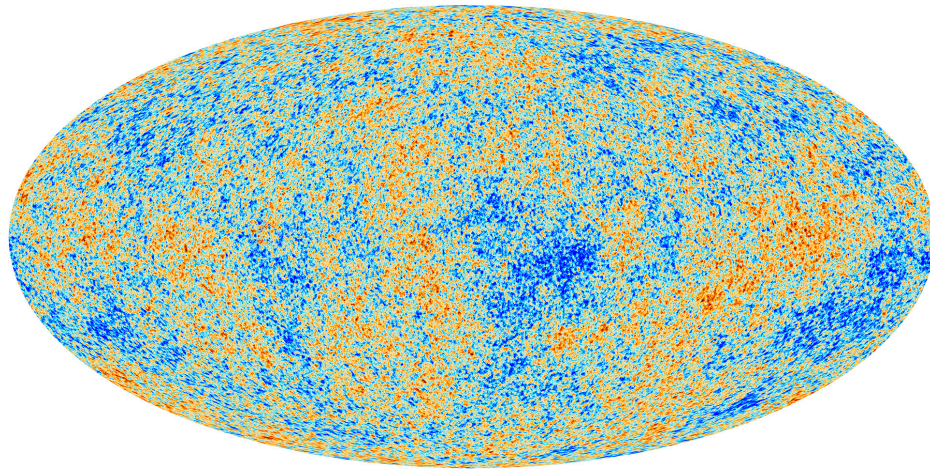
Figure 3.1.   The cosmic microwave background as observed by the Planck satellite.   Colors represent temperature, with orange being at higher temperature than blue. The maximum difference in temperature is in the order of 10^{-5} K, demonstrating the homogeneity of the Universe at recombination.   Credits: ESA Planck collaboration (https://sci.esa.int/s/WLGmGdw).

difficult to change the model without degrading the extremely well fitted CMB data. There are possible routes for solving the problem. Some of these rely on decreasing the sound horizon scale at recombination, for example by invoking self-interacting neutrinos (Kreisch et al., 2020) or energy injection by a scalar field (Agrawal et al., 2023), both acting before recombination.

Despite the current conflicts that this cosmological model faces and the possibility of revision in the near future, the Λ-CDM model is the current best cosmological model. It includes a cosmological constant Λ and cold dark matter, and is able to account very well for the existence of the CMB, the large scale structure of the Universe as mapped by galaxy surveys, the abundance of Hydrogen and Helium, and an accelerated expansion of the Universe.

As mentioned in the introduction of this chapter, the emergence of the SMBHs powering the highest redshift quasars occurred during the dark ages of the Universe, an epoch that began after recombination and that ended with the reionization of the Universe. The formation of the first stars and galaxies took place during that time as well. Understanding how the Universe transitioned from such a homogeneous state as indicated by the CMB (see Fig. 3.1), to a more heterogeneous disposition is the goal of structure formation studies. These studies show that the small inhomogeneities present in the CMB were amplified by gravity, creating dark matter halos that contained baryonic matter out of which the first stars and galaxies formed. Analytic studies are useful for gaining a better understanding of the physics of structure formation (Press and Schechter, 1974). However the best tool for studying the
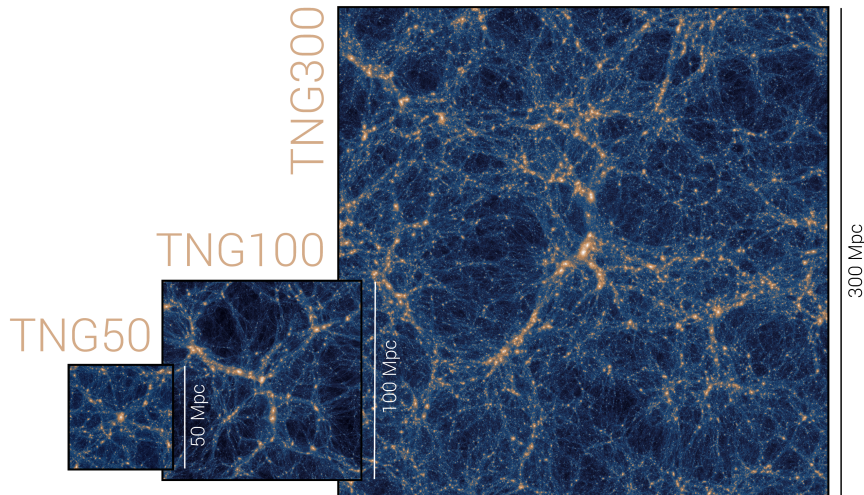
Figure 3.2. Large scale structure formation with numerical simulations. The figure presents three snapshots of the Illustris TNG simulations showing the distribution and density of dark matter. Credits: Vogelsberger et al. (2014).

conditions in which the first stars, galaxies, and black hole seeds were formed are provided by computer simulations, with one of the primal examples being the Millenium Simulation (Springel et al., 2005), and more recently, the Illustris project (Vogelsberger et al., 2014). The large scale structure produced by the Illustris TNG simulations is presented in Fig. 3.2.

3.2 Light Seeds: Stellar mass black holes from the first stars

The first stars in the Universe were formed during the dark ages at redshift $z \gtrsim 30$ from primordial gas, i.e., gas with abundances set by Big Bang Nucleosynthesis. Such gas contained 25% of Helium-4 by mass, trace amounts of deuterium (10^{-5}), Helium-3 (10^{-5}), Lithium-7 (10^{-10}), and the rest (almost 75%) in the form of Hydrogen (see Perlov and Vilenkin, 2017, Ch.13.2). Star formation occurred in this zero-metallicity gas and produced the very first generation of stars, the so-called Population III (Pop. III) stars (Partridge and Peebles, 1967).

As the first studies attempting to characterize these objects were conducted, a first picture emerged in which these stars were born in isolation and were much more massive than present day stars (Abel et al., 2000; Bromm et al., 1999). Subsequent studies were conducted but using more sophisticated numerical algorithms that were capable of studying gas fragmentation at small scales, providing a picture in which not only one but several stars with lower masses would be formed because of disk fragmentation (Latif and Schleicher, 2015), or due to turbulence in star forming clouds (Clark et al., 2011b; Prieto et al., 2011). The

most recent studies on the subject include numerical simulations that include more physical processes, exploring the effects of an improved thermodynamic treatment of the gas by following the evolution of different chemical species, including the effects of magnetic fields, and initial explorations of the effects of luminosity feedback (Latif et al., 2022; Riaz et al., 2018, 2023; Sharda et al., 2020, 2021; Wollenberg et al., 2020). It is now well established that primordial star formation is as complicated as present-day star formation. Sufficiently detailed numerical simulations can only probe the initial stages of this process. This limitation combined with a lack of observational constraints makes a proper characterization of the first stellar systems very complicated. Nevertheless, although the exact shape of the IMF is still under debate, the general consensus is that the shape is logarithmically flat in mass and peaking at higher stellar masses than the present-day IMF (see Klessen and Glover, 2023, for a comprehensive review).

The next section introduces the physics of the formation of Pop. III stars and the black hole masses expected at the end of their lives.

3.2.1 Primordial star formation

The very first studies attempting to understand the formation of the first stars pictured a very simple scenario. The initial conditions for this problem are easily set by knowing the density perturbations in the primordial material of the Universe at very early times. The phenomenon that gives rise to the first stars is the gravitational collapse of primordial gas clouds. On large scales the baryonic component of the Universe follows the evolution of the dark matter component, which can be approximated as a pressure-less and zero-temperature fluid. On smaller scales however, the effects of pressure become important on the baryonic component.

The thermodynamics of the gas in dark matter halos thus plays a major role during the collapse of the gas which gives origin to the first stars. The cooling processes in zero-metallicity gas are dominated by Hydrogen. The first halos in which the gas will undergo gravitational collapse are the ones in which the virial temperature reaches values higher than the temperature set by gas cooling. Because of the hierarchical nature of structure formation in the Universe, this occurs first for the smaller halos, the ones with masses in the order of 10^6 M$_\odot$. In these dark matter halos, the collapse is triggered by the presence of H$_2$. At the initial low densities of the primordial gas in these dark matter halos, the hydrogen molecule is formed through a process that involves H$^-$ which is in turn created by free electrons reacting with hydrogen atoms via

$$\mathrm{H} + \mathrm{e}^- \;\;\rightarrow\;\; \mathrm{H}^- + \gamma, \tag{3.5}$$

$$\mathrm{H}^- + \mathrm{H} \;\;\rightarrow\;\; \mathrm{H}_2 + \mathrm{e}^-, \tag{3.6}$$

and contribution from the interaction with H^+ is also possible via

$$H + H^+ \rightarrow H_2^+ + \gamma, \tag{3.7}$$

$$H_2^+ + H \rightarrow H_2 + H^+. \tag{3.8}$$

Simple estimates for the abundance of H_2 at this stage lie in the range of $f_{H_2} = 10^{-4} - 10^{-2}$ (Nishi and Susa, 1999).

The collapse of primordial gas due to H_2 cooling was investigated by Palla et al. (1983) by means of a one-zone model, in which a pressure-free collapse is modelled with the equation

$$\frac{d\rho}{dt} = \frac{\rho}{t_{\mathrm{ff}}}, \tag{3.9}$$

where ρ is the average gas pressure and t_{ff} is the free-fall timescale given by

$$t_{\mathrm{ff}} = \sqrt{\frac{3\pi}{32G\rho}}. \tag{3.10}$$

Eq.(3.9) is then combined with the heat equation

$$\frac{d\epsilon}{dt} = \frac{P}{\rho^2}\left(\frac{1}{t_{\mathrm{ff}}}\right) - \Lambda, \tag{3.11}$$

where P is the gas pressure, Λ is the cooling rate per unit mass, and ϵ is the specific energy. Three-body reactions for H_2 formation were also included. These reactions are

$$H + H + H \rightarrow H_2 + H, \tag{3.12}$$

$$H + H + H_2 \rightarrow H_2 + H_2, \tag{3.13}$$

which become important at $n \geq 10^8$ cm^{-3}. This study showed that at high densities the gas becomes fully molecular, lowering the temperature to the point at which the Jeans mass falls below 0.1 M$_\odot$.

Three-dimensional hydrodynamic calculations were later performed. Among these was the research by Bromm et al. (2002) who simulated the DM component and the gas by means of the SPH technique and including a primordial chemistry network that tracked the abundance of H_2. They found that the gravitational instability results in gas clumps with high densities ($n \sim 10^8$ cm^{-3}) and typical masses of 1000 M$_\odot$, suggesting a high mass reservoir from which protostars would accrete gas to become ~ 100 M$_\odot$ Pop. III stars. Subsequent studies improved upon the treatment of cooling at high densities by implementing optically thick line cooling and collision-induced continuum emission. The spherical collapse test performed by Yoshida et al. (2006) showed the characteristic features of cooling and heating of primordial gas during gravitational collapse. These are illustrated in Fig. 3.3. The first phase (point A in the top panel of Fig. 3.3) consist in a virialization of the gas cloud, which brings the temperature to ~ 1000 K while two-body reactions work to increase the

H_2 abundance via the processes described in Eq.(3.5)-(3.7). The increased abundance of H_2 brings the gas temperature down to 200 K, promoting the cloud collapse and eventually reaching the high density needed to boost the H_2 abundance through the three-body reactions presented in Eq.(3.12) and (3.13) (point D in top panel of Fig. 3.3).

The gas heats due to compressional heating, inefficient cooling, and increased opacity, until the steep decline of the H_2 line-cooling rate at 10^{16} cm^{-3} (point G in Fig. 3.3). An accretion rate of $\dot{M} \sim 10^{-3}$ M$_\odot$ yr^{-1} was reported within a 10 M$_\odot$ region around the formed protostar in agreement with previous research (Omukai and Yoshii, 2003).

More recent studies that incorporate detailed chemical and radiative processes (including chemical reactions that involve C and O), were able to follow the gas density up to $n = 10^{21}$ cm^{-3} when a hydrostatic core is formed (Omukai et al., 2010), confirming the findings of Yoshida et al. (2006) (see Fig.3.4). Also different values for the metallicity were explored. The results showed that at high densities the temperature increases adiabatically and a prestellar core of ~ 0.001 M$_\odot$ is formed. Interestingly accretion rates of $\dot{M} = 10^{-3}$ M$_\odot$ yr^{-1} were also reported in the low metallicity case.

The first three-dimensional studies of cloud collapse in the primordial gas typically assumed spherical symmetry and stopped once the gas density reached values of $n \sim 10^{16}$ cm^{-3} (see e.g. Yoshida et al., 2008) due to prohibitively small timesteps. The inclusion of the sink particle technique (Bate et al., 1995), along with the particle splitting technique for SPH (Kitsionas and Whitworth, 2002) allowed Clark et al. (2011b) to perform zoom-in simulations of primordial star formation focusing on the evolution of the accretion disk formed around the prestellar core, showing that the gaseous disk is prone to fragmentation because of the Toomre's instability that arises due to rapid mass load onto the disk (see Fig. 3.5). Fragmentation during the formation of the first stars has been reported by numerous studies (see e.g. Clark et al., 2011a,b; Greif et al., 2011; Hosokawa et al., 2016; Jaura et al., 2022; Machida et al., 2008; Riaz et al., 2018, 2023; Sharda et al., 2021; Smith et al., 2011; Turk et al., 2009; Wollenberg et al., 2020) and it is now understood that star formation in minihalos can be as chaotic as in the present day Universe. Apart from the small scale fragmentation process of the accretion disk around Pop. III protostars, large scale effects can also induce fragmentation. This is the case when including streaming velocity effects which arise because of the relative velocity of baryons and dark matter caused by baryonic acoustic oscillations prior to the moment of decoupling (Tseliakhovich and Hirata, 2010). This relative velocity increases the minimum mass of dark matter halos that contain cold gas (Schauer et al., 2019) and also increases the spin of the gaseous component (Chiou et al., 2018). Large streaming velocities cause more turbulence, and the resulting density perturbations are amplified during the gravitational collapse. The combination of turbulence and rotation can lead to the formation of a small cluster of a few tens Pop. III stars (see Fig 3.6),
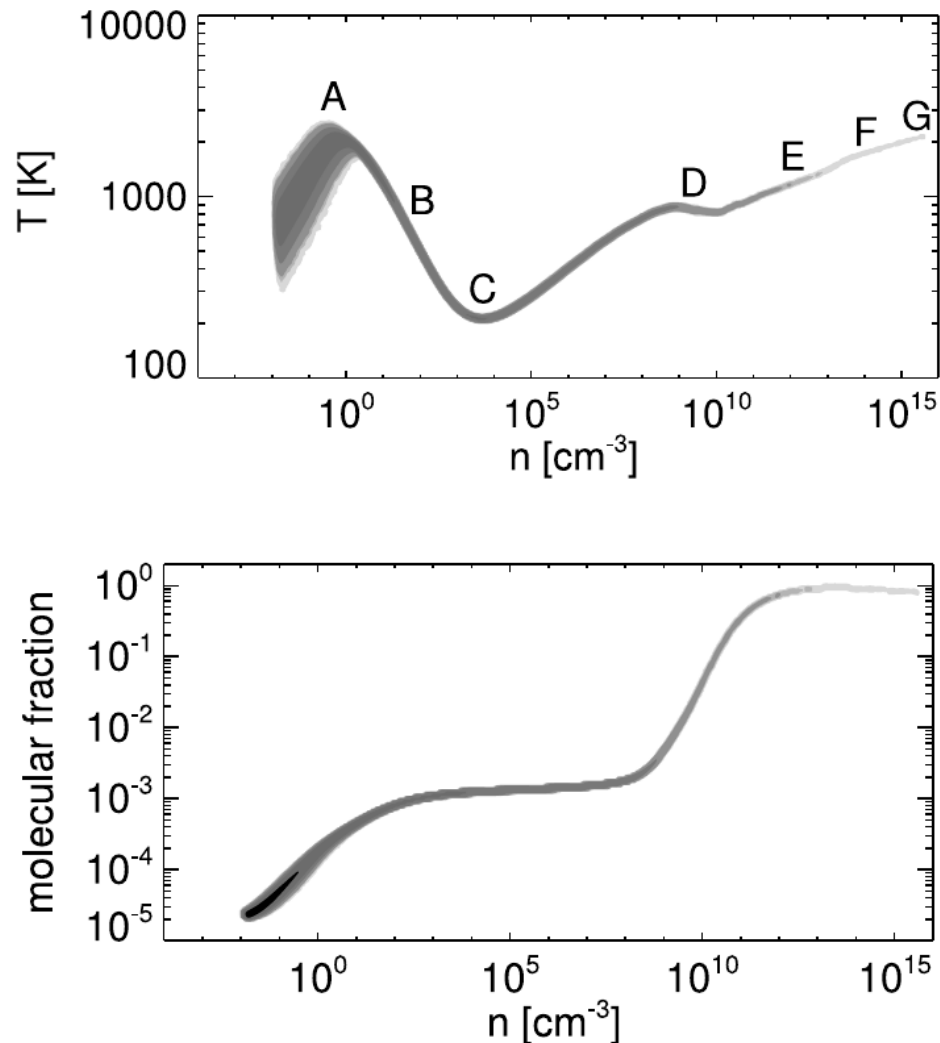
Figure 3.3. Top panel: Gas temperature plotted against density for a spherical collapse problem. Characteristic features are marked by capital letters and are explained as follows: (A) Gas temperature reaches 1000 K due to virialization while H_2 molecules form due to two-body reactions; (B) cooling due to molecular hydrogen brings the temperature down to 200 K; (C) H_2 cooling rates saturates as LTE is reached and cooling becomes ineffective; (D) H_2 is formed by three-body reactions and gas becomes fully molecular; (E) cloud opacity increases and cooling becomes less effective; (F) the dominant cooling process becomes collision-induced emission; and (G) H_2 dissociation begins at $T \sim 2000$ K. Bottom panel: Fraction of molecular hydrogen as function of the gas density. The increase at points A,D and plateau between C and D are clearly visible, along with the H_2 dissociation at G. Credits: Omukai et al. (2010).
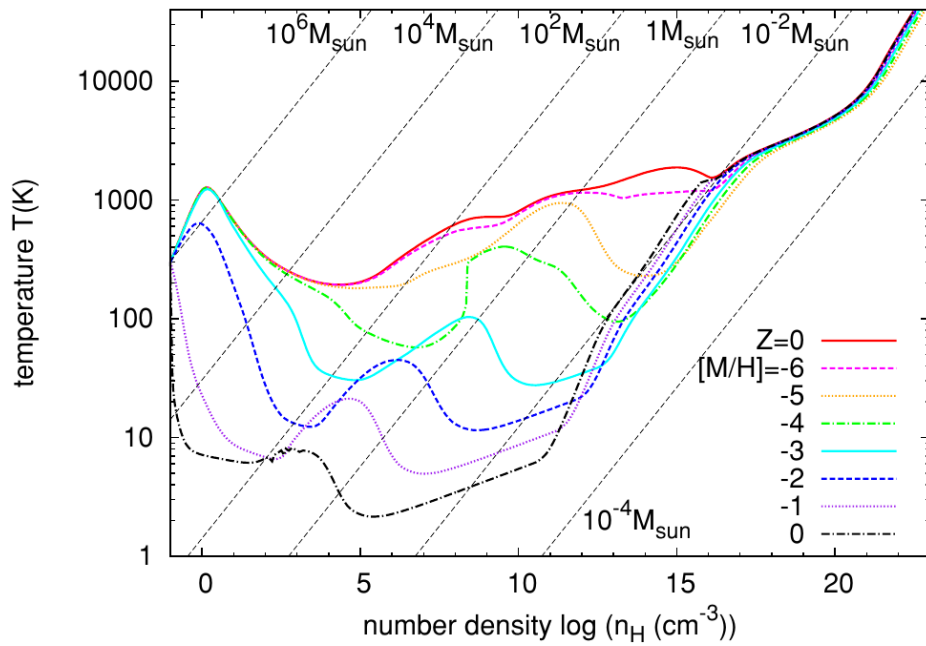
Figure 3.4. One-zone model calculations of the temperature evolution in prestellar cloud cores at different metallicities. The dashed black lines indicate the constant Jeans masses. Credits: Omukai et al. (2010).
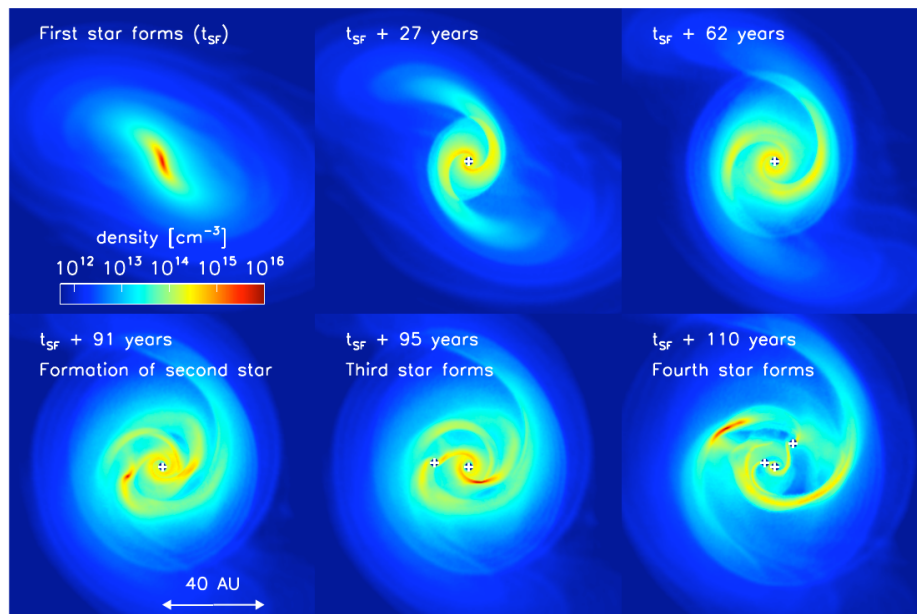
Figure 3.5. Fragmentation of the accretion disk around a Pop. III protostar. 110 years after the formation of the first protostar a total of 3 protostars have been formed, with the primary having a mass of 0.5 $M_\odot$ at this point. Credits: Clark et al. (2011b).

including binary systems as found by Riaz et al. (2018). Many of the studies addressing Pop. III star formation typically perform one simulation for a given combination of initial conditions. The recent work by Wollenberg et al. (2020) overcomes this issue by performing a total of 45 numerical simulations with the AREPO code, including detailed chemistry networks, sink particle formation, and accretion luminosity from the protostars. Their results indicate that significant scatter exist between different realizations of simulations with the same initial conditions, however the resulting Initial Mass Function (shown in Fig. 3.7) agrees well with previous studies in that the IMF is logarithmically flat and top-heavy compared to the present-day IMF (Clark et al., 2011a; Riaz et al., 2018; Sharda et al., 2020; Stacy et al., 2016; Susa et al., 2014).
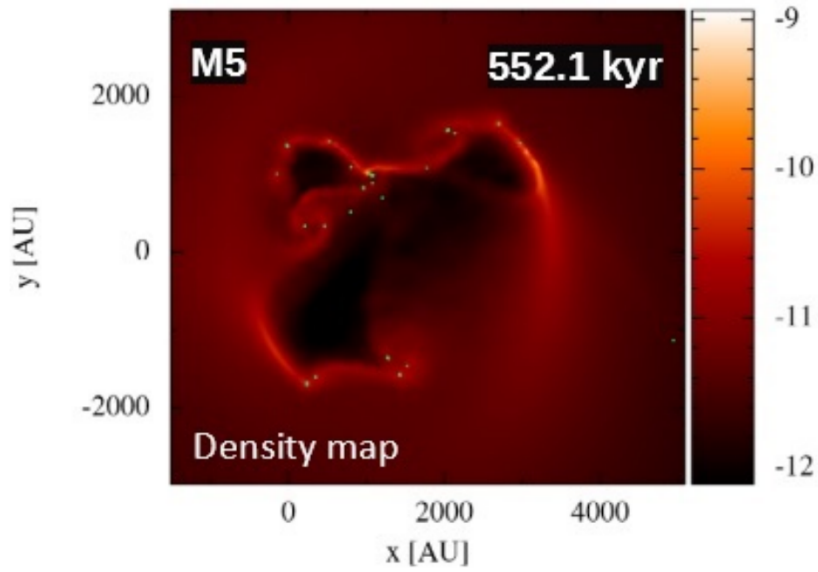
Figure 3.6. Formation of a small cluster of Pop. III stars following fragmentation of a collapsing primordial cloud including Mach equal 1 turbulence and a ratio of rotational to gravitational potential energy equal to 0.1. Credits: Riaz et al. (2018).
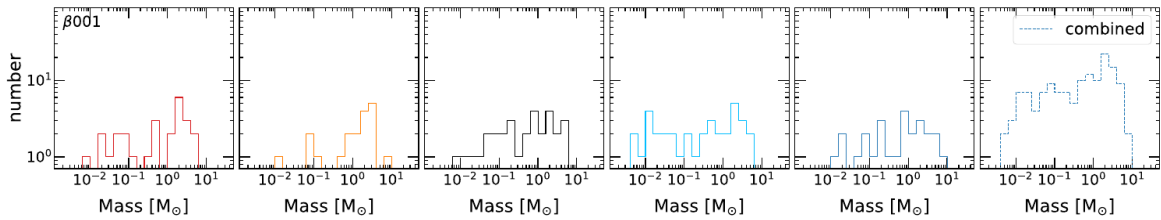
Figure 3.7. Mass distribution of Pop. III stars after 2000 yr of the formation of the first protostar. From left to right the first 5 panels present the mass distribution of individual simulations that include a rotation of 1%. The rightmost panel presents a combination of these 5 mass functions. Credits: Wollenberg et al. (2020).

Although a general consensus exists regarding the shape of the IMF, more work is

needed as to place stronger constraints on the mass limits. This is no easy task since one needs to consider additional effects that are difficult to model. One example of this is radiation feedback from the stars, which should impact the final masses and creation of new protostars. Three-dimensional radiation hydrodynamics simulations are expensive though, and it is usually prohibitive to follow the evolution of the system up to the point at which most of the mass has been accreted, or the gas has been evacuated due to radiation pressure. Recently Jaura et al. (2022) has identified a problem in previous treatments of radiation feedback in such simulations. The problem concerns the distance from the star at which ionizing photons are injected. When injected too far away, photons effectively bypass high-density regions in the accretion disk, thus artificially enhancing the effects of ionizing radiation feedback. When correctly modelled, the forming HII region could remain trapped at small scales, with no significant impact on fragmentation or mass accretion for longer times. A comparison of the IMF of Pop. III stars when including radiation feedback has been presented in Klessen and Glover (2023) (see Fig. 3.8). The low mass limit of the IMF obtained in numerical simulations is also influenced by the resolution, with higher resolution able to resolve the formation of smaller fragments.
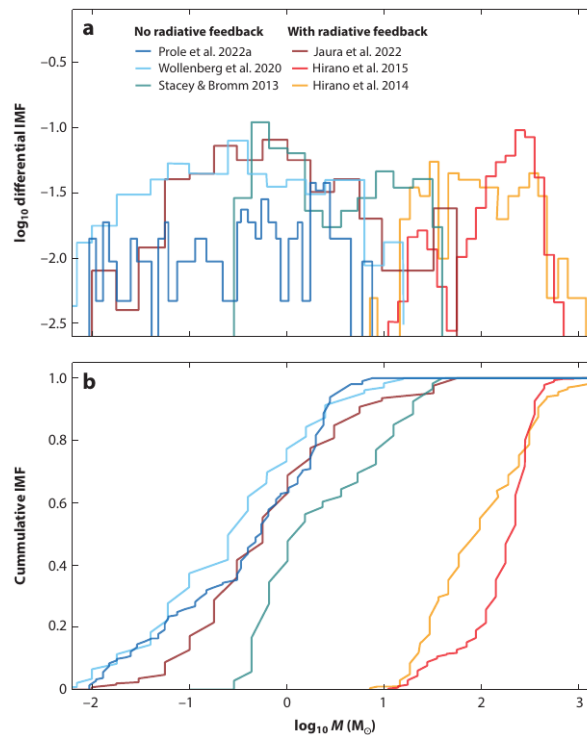
Figure 3.8. Impact of radiative feedback on the IMF of Pop. III stars produced in numerical simulations. Panel **a** shows different IMFs obtained in previous studies (Hirano et al., 2015, 2014; Jaura et al., 2022; Prole et al., 2022; Stacy and Bromm, 2013; Wollenberg et al., 2020), whereas the Panel **b** presents the cumulative IMF. Credits: Klessen and Glover (2023).

3.2.2   The evolution of Pop. III protostars

Following the formation of a prestellar core in an atomic cooling halo, its evolution and final mass will mainly depend on the accretion rates experienced by the object and the moment at which radiation feedback is able to prevent further growth.

A set of articles describing the early evolution of the protostars that gave origin to main sequence low metallicity stars were published in the last decade (see e.g. Hosokawa and Omukai, 2009; Hosokawa et al., 2012, 2013). It has been demonstrated through numerical simulations and analytic estimates that the accretion rates experienced by primordial protostars were much higher than in present day star formation. This can be understood by considering that the accretion rate onto prestellar cores is given (in the absence of turbulence) by

$$\dot{M}_* \sim \frac{c_s^3}{G} \approx 10^{-3} \; \mathrm{M_\odot \; yr^{-1}} \left(\frac{T}{500 \; \mathrm{K}} \right)^{3/2}, \qquad (3.14)$$

with c_s being the sound speed and T the temperature of the gas. The gas temperature during primordial star formation was in general much higher than in present-day molecular clouds because of the lack of efficient coolants, and thus the expected accretion rates were in general higher.

The evolution of a protostar can be understood by taking into account the mass accretion timescale and the Kelvin-Helmholtz (thermal) timescale, which are given by

$$t_{\mathrm{acc}} \;\; = \;\; \frac{M_*}{\dot{M}}, \qquad (3.15)$$

$$t_{\mathrm{KH}} \;\; = \;\; \frac{GM_*^2}{R_* L_{\mathrm{int}}}, \qquad (3.16)$$

where M_* and R_* are the protostellar mass and protostellar radius respectively, $\dot{M}$ is the accretion rate, and L_{int} is the internally generated luminosity. As long as $t_{\mathrm{KH}} > t_{\mathrm{acc}}$ the radiative energy loss is not important as to affect the evolution of the protostar, and so the evolution is mainly dictated by the effects of mass accretion. On the other hand when $t_{\mathrm{KH}} < t_{\mathrm{acc}}$ the evolution is mainly dictated by radiative energy loss.

The evolution of protostars under high accretion rates of up to $6 \times 10^{-3} \; \mathrm{M_\odot \; yr^{-1}}$ were studied by Hosokawa and Omukai (2009) by numerically solving the equations of stellar structure, as outlined in Stahler et al. (1986) and Palla and Stahler (1991). An illustration of the situation modelled in Hosokawa and Omukai (2009) is presented in Fig. 3.9.

The evolution of a protostar accreting at $10^{-3} \; \mathrm{M_\odot \; yr^{-1}}$ is better understood by dividing the process in four stages: (I) the adiabatic accretion phase, (II) the swelling phase, (III) the Kelvin-Helmholtz contraction phase, and (IV) the main sequence phase. The evolution of the structure of a protostar accreting at $10^{-3} \; \mathrm{M_\odot \; yr^{-1}}$ is presented in Fig. 3.10. A brief description of these phases is presented below.
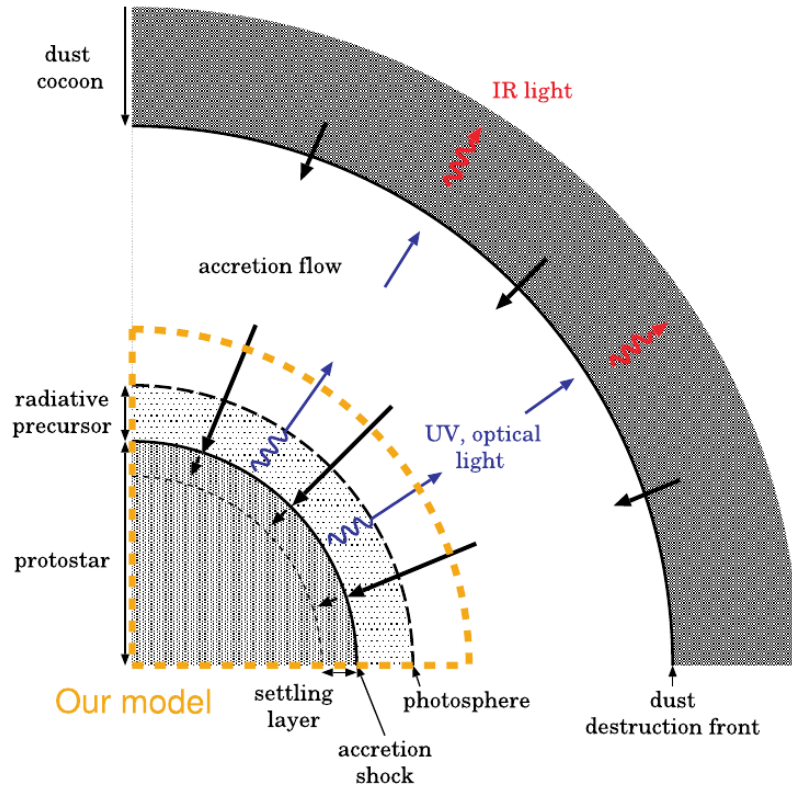
Figure 3.9. Illustration of the accreting protostar model investigated by Hosokawa and Omukai (2009). The situation considered assumes a surrounding accretion flow and dust cocoon in which the high energy radiation produced at the accretion shock is reprocessed into IR light. The model considered solves the detailed structure of the protostar and the accretion flow, enclosed by the dashed yellow line. This region contains the optically thick part of the accretion flow called the radiative precursor. The boundary between the protostar and the radiative precursor is the accretion shock which forms at the stellar surface. Credits: Hosokawa and Omukai (2009).

- (I) Adiabatic Accretion Phase: During this phase, the entropy generated at the accretion shock front is transported and embedded in the stellar interior with no entropy loss due to short cooling time-scales and long accretion time-scales. The entropy generated at the accretion shock slowly increases with mass and the radius gradually grows according to

$$R_* \sim 26\,\mathrm{R_\odot} \left(\frac{M_*}{\mathrm{M_\odot}} \right)^{0.27} \left(\frac{\dot{M}_*}{10^{-3}\mathrm{M_\odot\ yr^{-1}}} \right)^{0.41}, \tag{3.17}$$

which was derived in Stahler et al. (1986) for a radiative precursor with opacity dominated by H^- bound-free absorption. Unlike for protostars experiencing lower accretion rates, the temperatures reached in this phase are lower due to the increased radius of the protostar, and not high enough as to exceed to threshold for deuterium burning.
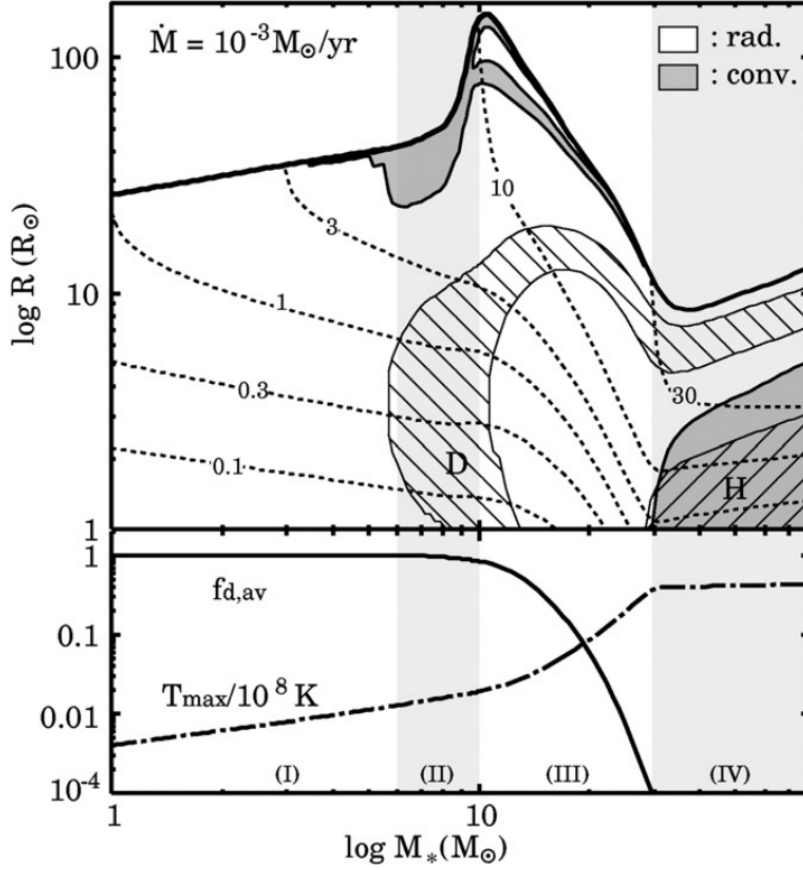
Figure 3.10. Stellar structure of a protostar accreting at $10^{-3} \, M_\odot \, \text{yr}^{-1}$. The upper panel shows the evolution of the radius as function of the mass. From left to right the four evolutionary phases are shown. The adiabatic accretion phase in white, the swelling in gray, the KH contraction in white and the MS phase in white. Gray areas inside the star indicate the convective regions, whereas white areas indicate the radiative regions. The hatched areas indicate regions of active nuclear burning for deuterium (D) and for hydrogen (H). The thin dotted curves represent loci of mass coordinates $M = 0.1, 0.3, 1, 3, 10$ and $30 \, M_\odot$. The lower panel shows the mass-averaged deuterium concentration $f_{d,av}$ (solid line) and the maximum temperature within the star T_{max} (dot-dahsed line). Credits: Hosokawa and Omukai (2009).

The temperature increases with stellar mass and affects the opacity which is given by Kramer's law $\kappa \propto T^{-3.5}$, so that the maximum luminosity within the star increases as

$$L_{max} \sim 0.2 \, L_\odot \left(\frac{M_*}{M_\odot} \right)^{11/2} \left(\frac{R_*}{R_\odot} \right)^{-1/2} . \tag{3.18}$$

Eventually the opacity decreases in such a way that radiative heat transport becomes important even in the deep interior of the protostar, and this leads to an altered entropy distribution and stellar structure, leading to the next phase.

- (II) Swelling Phase: As the outward heat flux begins to increase at the end of the previous phase, the entropy redistribution causes an expansion of the outer layers of the

protostar. While the entropy decreases in the deep interior (as the interior becomes less opaque), it increases in the outer layers. The boundary between the entropy-losing region and the outer absorbing layer is called the luminosity peak. This luminosity peak propagates outward and causes a swelling of the radius. This occurs at approximately 6 $M_\odot$ and the stellar radius exceeds 100 $R_\odot$. During the expansion only a tiny mass fraction of $\sim 0.03\%$ is contained at radii larger than 70 $R_\odot$.

- (III) Kelvin-Helmholtz Contraction: As the luminosity peak approaches the stellar surface, an increasing amount of energy flux escapes the protostar without being absorbed. Therfore the luminosity increases and causes a decrease in the Klevin-Helmholtz timescale. The protostar then begins to lose heat faster than it receives entropy from the accreted material, so it turns to contraction. The moment at which the star begins to contract is dictated by the accretion rate as

$$M_{*,\mathrm{rmax}} = 10.8 \ \mathrm{M_\odot} \left(\frac{\dot{M}_*}{10^{-3} \ \mathrm{M_\odot \ yr^{-1}}} \right)^{2/9}, \tag{3.19}$$

which is also the moment at which the stellar radius reaches its maximum.

- (IV) Main Sequence Phase: With the Kelvin-Helmholtz contraction, the temperature begins to rise, eventually reaching 10^7 K when the protostellar mass is 20 $M_\odot$, and igniting hydrogen at the center of the protostar. The mass radius relation that the star follows now corresponds to the one for main-sequence stars.

3.2.3 Remnants of the first stars

We are particularly interested here in the remnants of the first stars of the Universe, given their potential to produce massive black holes. So far this chapter has described the formation and evolution of protostars that eventually become the first stars of the Universe. However, characterizing the typical masses of these stars is still a challenging task.

Moreover, it is also challenging to predict the final fate of a star given the many variables involved. This process can be made easier by considering the evolution of isolated stars, i.e., those who do not form part of a binary or multiple system. Even then, many assumptions need to be made in order to get an idea of the end products.

Heger et al. (2003) made the attempt of predicting those end products by considering the evolution of isolated and non-rotating stars including the effects of mass loss. Mass loss was assumed to be mass dependent for Wolf Rayet stars, and wind-driven mass loss was assumed to depend on the metallicity of the star, also the κ and η pulsational mass loss were considered for very massive stars. They presumed that the explosion mechanism (when it occurs), and the remnant properties, are determined by the mass of the helium core when

the star dies. Their results are summarized in Fig. 3.11 which shows the fate of stars as function of their initial mass and metallicity. In the models it was assumed that stars with initial mass < 9 M$_\odot$ end their lives as white dwarfs as they do not form massive enough cores to collapse. In the narrow range between $9 - 10$ M$_\odot$ the final outcome was either a neutron star or a white dwarf. These limits are not affected by metallicity.

At higher initial masses a type II supernova occurs leaving a neutron star as remnant (up to ~ 25 M$_\odot$ for low metallicity stars). For initial masses in between $25 - 40$ M$_\odot$ the formation of a BH by fallback occurs, this is, the supernova explosion is not energetic enough for expelling the stellar atmosphere and this atmosphere eventually falls back onto the remnant neutron star, causing its collapse into a BH. At high metallicities, stellar winds remove enough mass so that no BH by fallback is formed. For higher masses ($40 - 140$ M$_\odot$ at low metallicity) no supernova explosion occurs and the helium core is massive enough to produce a BH, this is called a direct black hole. For even higher masses a pair-instability supernova (PISN) occurs and leaves no remnant. In this case, in a very massive helium core, the high temperatures reached produce energetic gamma ray photons, which in turn can produce electron positron pairs (Hubbell, 2006) effectively reducing the radiation pressure in the core of the star. Further compression causes a runaway thermonuclear explosion that completely disrupts the star (Fryer et al., 2001). At masses higher than ~ 260 M$_\odot$ the energy released by these thermonuclear reactions is not enough to counteract the gravitational force of the star and a direct black hole is formed instead.

Because of the low mass-loss rates expected for low metallicity stars, the separations between different final outcomes are nearly perfect vertical lines in Fig. 3.11. On the other hand, at higher metallicities mass loss becomes important, changing the final outcome.

For very low metallicities, adequate for the first generation of stars, line-driven winds are not efficient since metal-poor material presents only very few absorption lines, so that radiative pressure is weaker at the stellar envelope (Kudritzki, 2002). Therefore, under the assumption of no rotation, and for stars evolving in isolation, we can predict the masses of the black holes formed by the first stars of the Universe, provided that the high mass end of the IMF is also constrained. From previous studies it is reasonable to expect BHs with masses in the order of several 10 M$_\odot$(Heger and Woosley, 2010), and potentially $\gtrsim 100$ M$_\odot$(Ohkubo et al., 2009).

Note however that these assumptions might be too extreme. In fact, when considering stellar rotation, line-driven mass loss can still occur due to efficient mixing of nuclear fusion products, or due to a reduction of the Eddington limit, or because of the pulsational pair-instability, reducing the final masses of Pop. III stars (see e.g. Liu et al., 2021). In this regard Spera and Mapelli (2017) investigated the effects of pulsational pair-instability supernova (PPISN) for different metallicities ($Z \geq 2 \times 10^{-4}$ $Z_\odot$) with the SVEN code (Spera
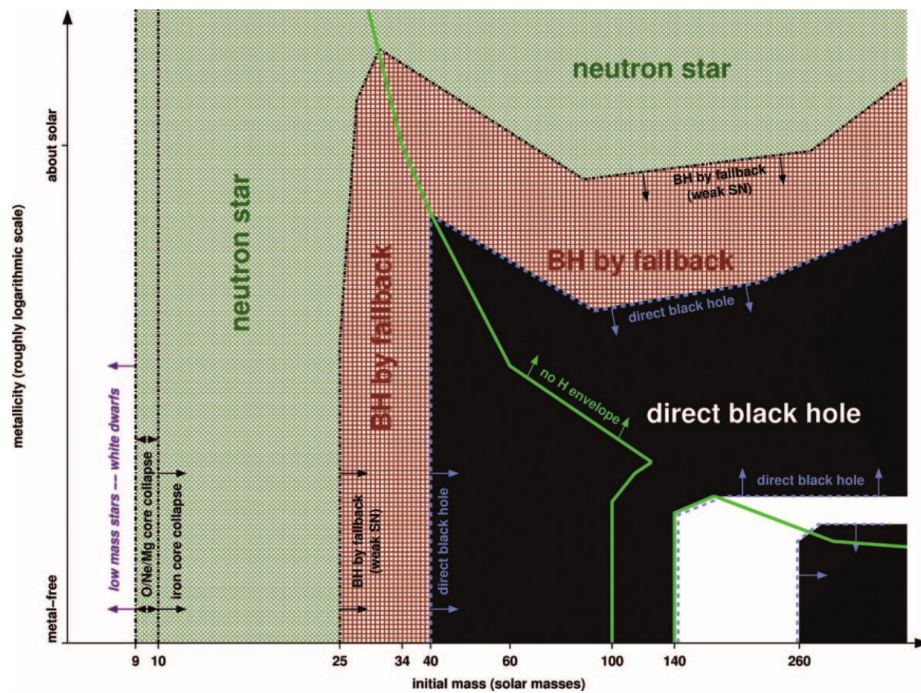
Figure 3.11. The fate of massive stars as a function of their initial mass and metallicity. The green solid lines separates the regimes in which the star keeps its hydrogen envelope or loses it. Green areas show the conditions under which a neutron star is the remnant, whereas red areas indicate the conditions under which a BH by fallback is formed. The black areas indicate regions in which a direct black hole is formed. The white zone between 140 and 260 $M_\odot$ indicates the conditions at which pair-instability supernovae occur, leaving no remnant. For masses < 9 $M_\odot$ white dwarfs are assumed to be the remnants. Credits: Heger et al. (2003).

et al., 2015) which interpolates on pre-calculated stellar evolution tracks to obtain physical properties of stars. An updated version of Fig. 3.11 is obtained form this study and shown in Fig. 3.12. The main effect of PPISNe and PISNe is to enahnce the formation of BHs with masses in the range $30 \leq M_{BH} \leq 50$ $M_\odot$, while preventing their formation in the range $60 \leq M_{BH} \leq 120$ $M_\odot$.

This picture is even more complicated when considering the effects that a binary companion has on the evolution of a star because of effects like mass transfer or stellar mergers (Sana et al., 2012; Schneider et al., 2015). In fact, some studies of Pop. III star formation predict that binary systems are a frequent outcome during the star formation in mini-halos (Riaz et al., 2018; Stacy and Bromm, 2013; Sugimura et al., 2020). In the context of gravitational wave detection, binary black hole merger rates have been calculated for black holes formed from the first stars by Santoliquido et al. (2023), using a semi-analytic method including stellar evolution in binary systems with an updated version of the SVEN code, predicting black hole masses of $30 - 40$ $M_\odot$.
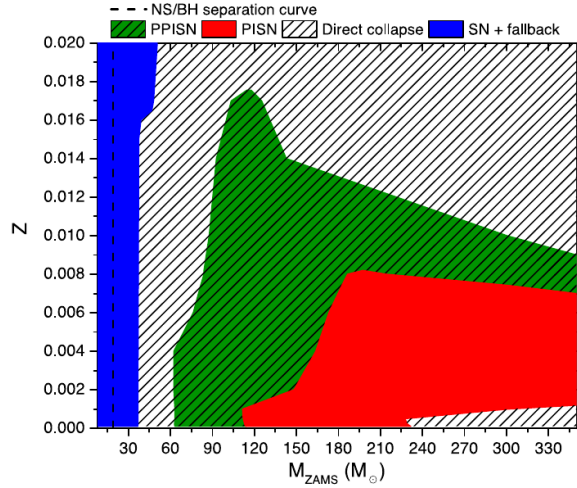
Figure 3.12. The fate of stars as function of their ZAMS mass and metallicity including the effects of PPISNe. Credits: Spera and Mapelli (2017).

Overall, when considering the black holes produced by the very first stars we might expect typical masses of $30 - 50 \ \mathrm{M_\odot}$, and maybe $\gtrsim 240 \ \mathrm{M_\odot}$. Multiple black holes with these masses would be probably born per minihalo, and a fraction of them in binary systems.

3.3   Heavy seeds: Runaway collisions in dense star clusters

Black Hole seeds with larger masses than the remnants of Pop. III stars can be produced when a very massive star is formed in a dense star cluster due to repeated collisions with other stars.

Stellar collisions in dense star cluster have been extensively studied through N-body (Portegies Zwart et al., 2004; Portegies Zwart and McMillan, 2002; Portegies Zwart and van den Heuvel, 2007), Monte Carlo (Freitag et al., 2006; Gürkan et al., 2004), or Fokker Planck modelling (Lee, 1994; Spurzem and Kamlah, 2023).

In order to understand how this mechanism is triggered, it is necessary to study the dynamical evolution of a star cluster. For this it is convenient to define the crossing time t_{cross}, which is the time taken for a star with the typical velocity to cross the cluster. For a star cluster in virial equilibrium, the crossing time is given by

$$t_{\mathrm{cross}} = \sqrt{\frac{R^3}{GM}}, \tag{3.20}$$

where R is the radius of the cluster and M its mass. The cluster evolution is driven by close stellar encounters between its constituent stars. The gravitational interactions resulting from these events cause a change in the velocity of the stars. The large number of stars in those systems results in a large number of close encounters, gradually changing their initial velocities.

An essential timescale associated to this process is the relaxation timescale, defined as the time needed for such encounters to produce a cumulative 90 degree deflection on the velocity. For a system containing equal mass particles, the half-mass relaxation time is defined as (Spitzer, 1987)

$$t_{\rm rh} = 0.138 \frac{N}{\ln(\gamma N)} t_{\rm cross}, \qquad (3.21)$$

where N is the number of stars and γ is an order-unity factor with value $\gamma = 0.11$ for a system of equal mass particles (Spitzer, 1987) (for a derivation see the book by Binney and Tremaine (1987)).

A natural consequence of star cluster evolution is the so-called core collapse. This is a process that consist in the contraction of the central portion of a stellar system while the outer parts expand. It is caused by a redistribution of the kinetic energy mediated by the stars comprising the system. Stellar encounters can result in the speed-up of one star while the other is decelerated and falls deeper in the potential well. As time passes, stars that are sped-up will be sent to the outskirts of the cluster whereas the decelerated population will be left with less kinetic energy at the cluster center, causing a contraction of the inner parts. This process has been investigated and confirmed with numerical simulations (see e.g. Aarseth et al., 1974; Lynden-Bell and Eggleton, 1980). The process of core collapse as computed by means of N-body simulations can be seen in the middle panel of Fig. 3.13 in which the 10%, 50% and 90% lagrangian radii are plotted as function of time in units of the crossing time (Reinoso et al., 2018). It is evident that the 10% lagrangian radius dramatically drops at ~ 40 crossing times, marking the moment of core collapse, while the 90% lagrangian radius is gradually increasing.

For a cluster of equal mass stars, the time of core collapse is $15 - 20$ times the half-mass relaxation time (Spitzer, 1987), but this is reduced when a stellar mass function is included, as reported in Portegies Zwart and McMillan (2002) and later confirmed with Monte Carlo and N-body models (Fujii and Portegies Zwart, 2014; Gürkan et al., 2004). This acceleration of the core collapse is understood as a consequence of mass segregation caused by dynamical friction, resulting in a central concentration of the most massive objects of the cluster at its center. This situation is then very favourable for stellar collisions since the most massive stars are concentrated at the cluster center.

This process opens up the possibility of forming very massive objects at the central parts of a star cluster due to repeated stellar collisions, the so-called runaway collision scenario, in which a single star experiences most of the collisions, thus growing rapidly in mass. This has been explored by means of N-body simulations of dense star clusters in which the stars are allowed to merge. These simulations show that it is possible to form an intermediate mass black hole (IMBH) through runaway collisions. This is proposed as an alternative to explain Ultra-Luminous X-ray (ULX) sources in young star clusters (Portegies Zwart
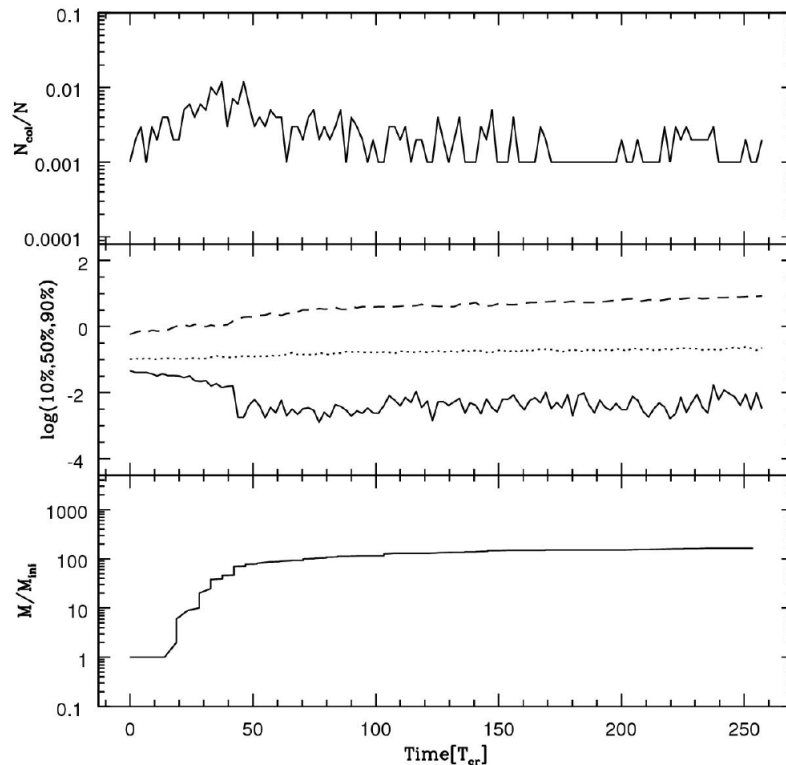
Figure 3.13. Dynamical evolution of a star cluster including stellar collisions. The top panel shows the number of collisions normalized by the initial number of stars. The middle panel shows the 10%, 50%, and 90% Lagrangian radii. The bottom panel shows the mass of the most massive object formed by runaway collisions, normalized by its initial mass. Credits: Reinoso et al. (2018).

and McMillan, 2002), showing that the formation of a 1000 $M_\odot$ BH is possible through this channel. Subsequent studies explored the conditions needed for the runaway growth to occur, recognizing that dynamical friction must be able to drive the most massive stars to the cluster center before they explode as supernova (Freitag et al., 2006; Portegies Zwart et al., 2004), suggesting that 3-4 Myr old, dense star clusters, could harbour IMBHs.

Having an understanding of the runaway collision growth of stars in dense star clusters, and supporting evidence from N-body simulations, it is then natural to explore this scenario in the context of massive black hole seed formation in the early Universe. One such attempt was followed by Katz et al. (2015), who put a big effort in obtaining the initial conditions from cosmological hydrodynamics zoom-in simulations. They identified a pair of mini-halos that remain at a close distance (~ 117 pc) such that one of them will first collapse and form Pop. III stars (see Fig. 3.14). These stars will then pollute the second minihalo to an assumed metallicity of 10^{-4} $Z_\odot$, a threshold metallicity above which a dense cluster of Pop. II stars should emerge (Omukai et al., 2008). The central dense region of the second collapsed minihalo was then mapped into a large set of initial conditions for the
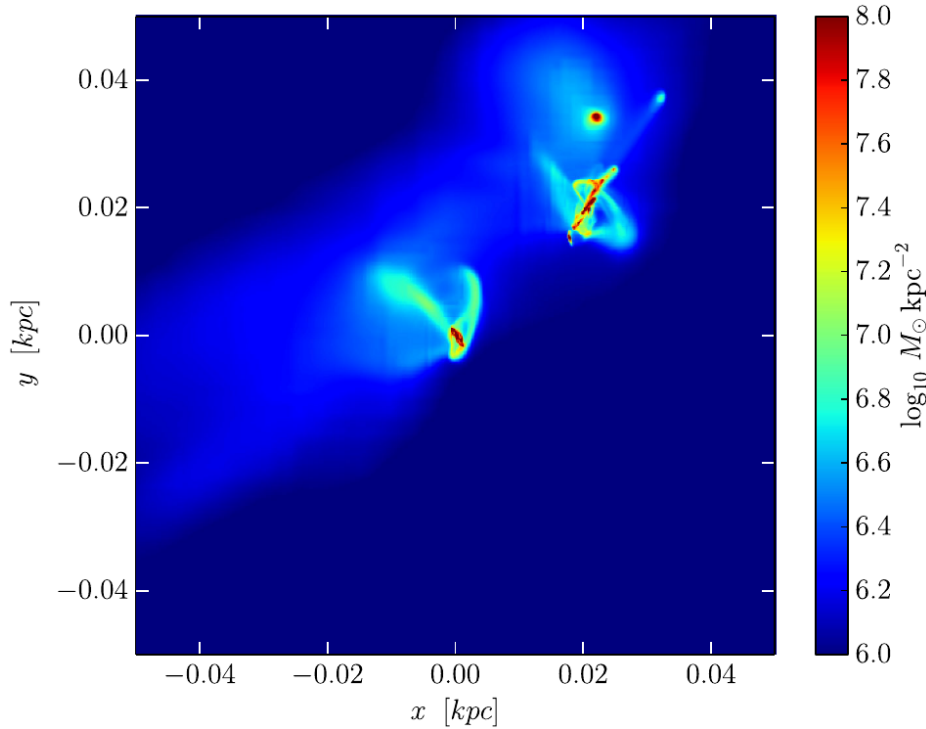
Figure 3.14. A pair of close minihalos from a cosmological hydrodinamical zoom-in simulation. The halo at the top right collapses first and triggers the formation of a Pop. III star cluster. The minihalo at the center collapses 12 Myr later and is assumed to produce a Pop. II star cluster following metal enrichment from the death of the Pop. III stars formed in the first collapsing minihalo. Credits: Katz et al. (2015).

GPU-accelerated version of the NBODY6 code (Nitadori and Aarseth, 2012). Their results show that the formation of a very massive star (VMS) with a mass $600 \leq M \leq 1000$ M$_\odot$ formed through runaway stellar collisions is a typical outcome in those environments and robust against changes in the IMF, the initial binary fraction, initial degree of mass segregation, and initial density profile.

A similar approach was followed by Sakurai et al. (2017) by identifying collapsing halos with masses $M \sim 10^7 - 10^8$ M$_\odot$ in a cosmological box and resimulating their collapse with higher resolution up to a number density of $n_{\rm H} = 10^7$ cm^{-3}. The resulting SPH distribution was then mapped into a stellar distribution (see Fig. 3.15) assuming virial equilibrium and adopting a power-law IMF. The evolution of the star clusters was then followed by means of N-body simulations including stellar collisions, and the process of core collapse was identified as the precursor to runaway stellar collisions that ultimately resulted in the formation of a very massive star with $400 - 1900$ M$_\odot$ in less than 3 Myr, as depicted in Fig. 3.16. The authors showed that the mass growth is the same as encountered in simulations of runaway
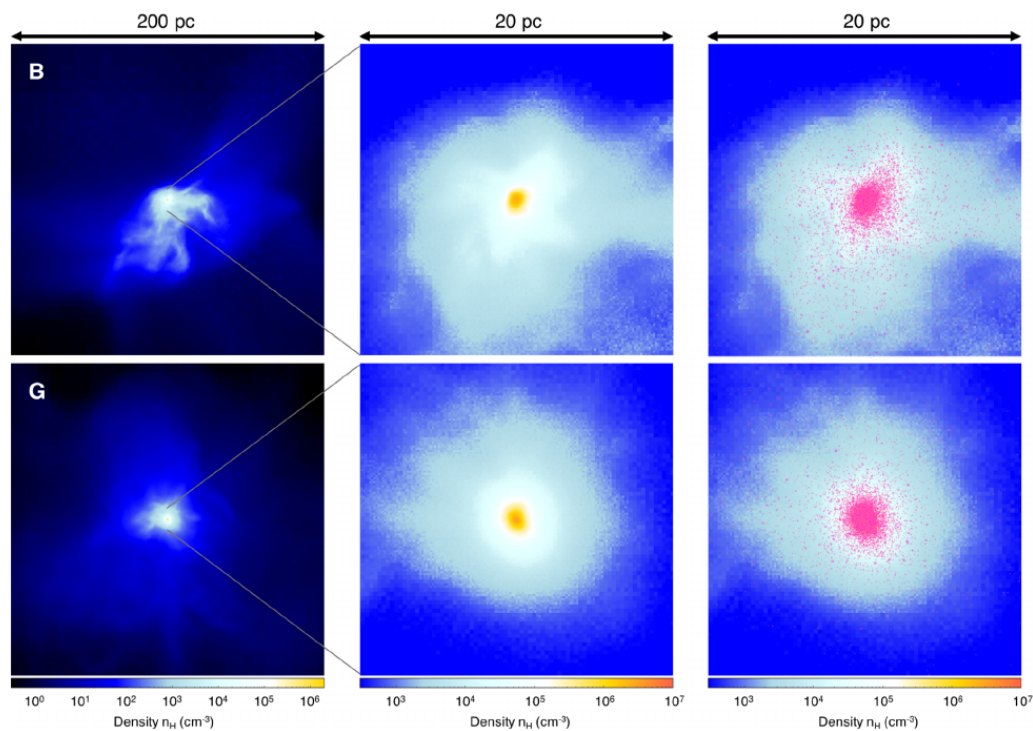
Figure 3.15. Initial conditions for N-body simulations of low-metallicity star clusters. The collapse of gas clouds is followed by means of cosmological hydrodynamical zoom-in simulations until reaching a central gas density of $n_{\mathrm{H}} = 10^7 \ \mathrm{cm}^{-3}$, at which point a fraction of the gas mass is transformed into stars. Credits: Sakurai et al. (2017).
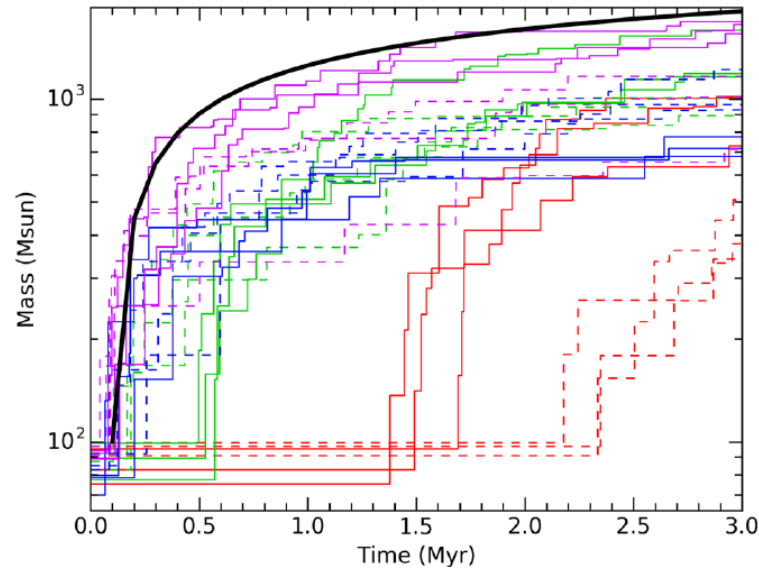
Figure 3.16. Mass growth of a very massive star through runaway stellar collisions in a dense star cluster. Each combination of line-colour and line-style represents a simulation with different initial conditions. A total of 3 realizations per set of initial conditions was performed. The rapid growth of the very massive star occurs when the clusters experience core-collapse. The solid black line shows the analytic expression of Eq.(3.22). Credits: Sakurai et al. (2017).

growth in young massive clusters, and is given by (Portegies Zwart and McMillan, 2002)

$$m = m_{\mathrm{seed}} + 4 \times 10^{-3} \, M_{\mathrm{cl}} \, f_{\mathrm{c}} \, \ln \Lambda \, \ln \left(\frac{t}{t_{\mathrm{cc}}} \right), \qquad (3.22)$$

where m_{seed} is the mass of the star that begins the runaway growth, f_{c} is the fraction of binaries that contribute to collisions, $\ln \Lambda$ is the Coulomb logarithm, and t_{cc} is the time of core collapse. The authors later expanded on this work to study the subsequent growth of the resulting BH through gas accretion following tidal disruption of the remaining stars in the cluster. Their findings show that a growth up to 2500 $\mathrm{M}_\odot$ is possible after 15 Myr (Sakurai et al., 2019).

These studies demonstrate that intermediate mass black holes can be formed in dense star clusters in the early Universe, provided the gas out of which these stars form is polluted to a metallicity of $Z \sim 10^{-4} \, Z_\odot$, which allows the gas to undergo dust-cooling and fragment at high densities (Omukai et al., 2008).

The runaway growth scenario has also been explored in a slightly different environment, considering the very first star clusters in the Universe formed out of gas that has not been previously polluted by exploding stars. From the mean-free path approximation one can see that the frequency of stellar collisions is given by

$$f_{\mathrm{coll}} = \sigma n v, \qquad (3.23)$$

where n is the number density of stars, v is the typical stellar velocity and σ is the cross-section for collisions. The cross-section is proportional to the square of the stellar radius $\sigma \propto R^2$, therefore when considering a cluster of stars that are inflated in radius, such as protostars accreting at high rates as expected during the formation of the first stars (see Sec. 3.2.2), it is possible that runaway stellar collisions become important. This has been explored by Reinoso et al. (2018) by considering a small stellar systems containing $N = 100 - 5000$ stars with radii varying between $R = 20\,\mathrm{R_\odot}$ and $R = 5000\,\mathrm{R_\odot}$ as expected for massive main sequence stars or accreting Pop. III stars. Their results show that a moderate enhancement of the mass of a star is possible, reaching values of $100\,\mathrm{M_\odot}$ in a low mass ($M \sim 1000\,\mathrm{M_\odot}$) Pop. III star cluster formed in a minihalo. In a more massive cluster of $10^4\,\mathrm{M_\odot}$ the mass enhancement is higher and a BH with a mass of $600\,\mathrm{M_\odot}$ might be formed. The authors however only considered equal mass and equal size stars in a gas-free star cluster. A similar study explored the effects of a different morphology of the stellar systems, considering inflated Pop. III stars as well. It was shown by Vergara et al. (2021) that rotation and flattening of a stellar system (as expected during the fragmentation of a gaseous disk) does not significantly impact the runaway growth of a star, which can still reach $> 1000\,\mathrm{M_\odot}$.

In the same context of collisions among inflated protostars, Boekholt et al. (2018) considered a system of Pop. III protostars embedded in gas, which was modelled as a background potential from which the particles accrete mass. Considering more massive clusters of $10^4 - 10^6\,\mathrm{M_\odot}$ their results show that the formation of massive BHs with up to $10^5\,\mathrm{M_\odot}$ is possible due to the combined action of stellar collisions and gas accretion.

Another variation of the runaway growth mechanism consist in considering the evolution of a Nuclear Star Cluster (NSC). Although too difficult to simulate at the moment with direct N-body simulations because of their huge masses ($\geq 10^6\,\mathrm{M_\odot}$) and therefore high number of stars ($N > 10^6$), there might be observational evidence showing that above a certain density such clusters are unstable against stellar collisions and their fate is to produce a massive BH (Escala, 2021). This scenario would be consistent with the coexistence of massive BHs and NSCs. A first attempt to numerically test this hypothesis was pursued by Vergara et al. (2023). Their findings suggest a clear mass threshold for NSCs above which the efficiency of BH formation greatly increases, as shown in Fig. 3.17. The stellar systems modelled are still far away from resembling NSCs and the results must be taken with caution but at the same time as promising. Runaway collisions in embedded NSCs of $10^5\,\mathrm{M_\odot}$ were also investigated by Das et al. (2021), although employing a more limited number of particles compared to the work of Vergara et al. (2023) due to differences in the software used. The results of this work however align with previous studies, finding final BH masses of $10^4 - 10^5\,\mathrm{M_\odot}$ due to a combination of stellar collisions and gas accretion.
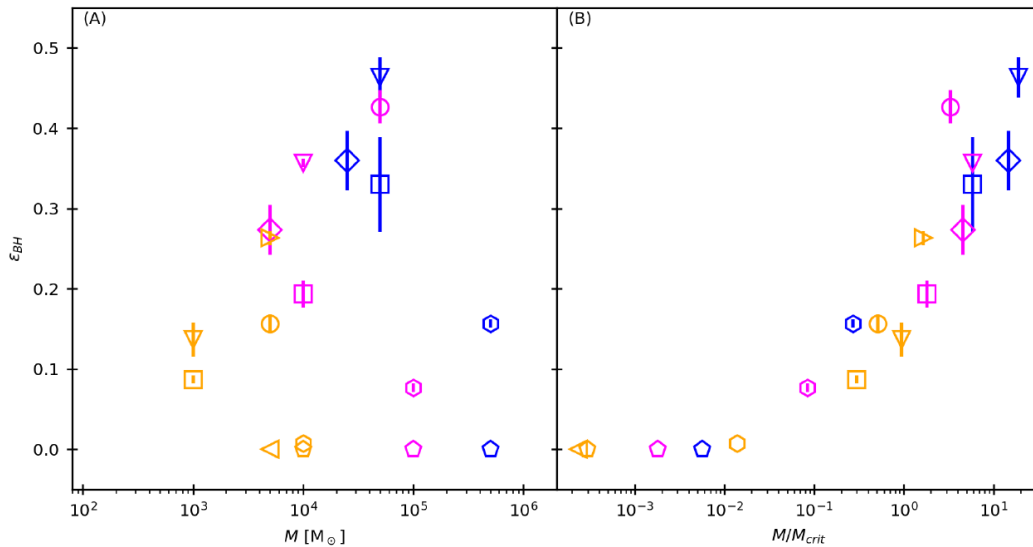
Figure 3.17. Black hole formation efficiency $\epsilon_{\mathrm{BH}} = M_{\mathrm{BH}}/M$ as function of the mass of a nuclear star cluster in the left panel. The right panel presents the same information but with the mass of the NSC normalized by the critical mass M_{crit}, a mass above which the cluster is unstable against stellar collisions. Different symbols represent different NSC models. Credits: Vergara et al. (2023).

Summarizing, so far it seems that the formation of 1000 M$_\odot$ BH through runaway stellar collisions is a natural outcome of very dense stellar systems, for either Pop. III or Pop. II star clusters, and it might even occur in dense nuclear star clusters. More elaborated models for Pop. II star clusters at high redshift have been explored (Katz et al., 2015; Sakurai et al., 2015, 2017), yielding consistent results among them and predicting the formation of a $600 - 2500$ M$_\odot$ BH as a consequence of repeated stellar collisions.

The conditions are different when considering Pop. III star clusters since less efficient fragmentation yields a lower number density of stars, but it might be compensated when considering the inflated radii of protostars accreting at high rates. Gas depleted models suggest the formation of ~ 1000 M$_\odot$ BHs in this case (Reinoso et al., 2018; Vergara et al., 2021). The final masses might be highly boosted when the effects of gas are included, potentially reaching 10^5 M$_\odot$ due to the interplay of gas accretion and stellar collisions (Alister Seguel et al., 2020; Boekholt et al., 2018). Further improvement of the numerical models is still needed. It is important to model the gas in the cluster with a hydrodynamics code instead of a spherically symmetric analytic potential. Furthermore, no IMF has been included in models of Pop. III star clusters so far, being thus unable to capture the effects of mass segregation.

Finally, the runaway collision scenario has also been explored in nuclear star cluster environments, also suggesting the formation of $10^4 - 10^5$ M$_\odot$ BHs as a result (Das et al.,

2021; Escala, 2021; Vergara et al., 2023). Those simulations however are still too far from reaching the high number of particles needed to realistically model these systems.

A caveat shared by all the previously mentioned models pertains to the treatment of stellar collisions, specifically the recipes for mass loss. While some analytic prescriptions have been employed in some of them, they depend only on the mass ratio of the colliding stars. This might yield acceptable results when considering Pop. II main sequence stars, but it has been shown that the stellar structure also plays a role in determining the mass loss of the collision product (Glebbeek et al., 2013), which might certainly be important for the very massive star formed or the inflated Pop. III protostars. Moreover, other factors such as the relative velocity between the colliding stars and the impact parameter have not been taken into account so far. The work by Freitag and Benz (2005) demonstrates the difficulty of finding analytic formulae that can predict the rate of mass loss based on those three parameters, but at the same time they identify cases in which a high fraction of mass ($> 10\%$) is lost. More work in this area is necessary to place strongest constraints on the final masses expected for BHs formed through runaway stellar collisions.

3.4   Heavy seeds: Direct collapse black holes

This section beings by clarifying what is referred to when writing Direct Collapse Black Hole (DCBH) since this term is usually adopted in the literature to specify objects of slightly different nature. As noted in Sec. 3.2.3, specifically in Fig. 3.11, a direct black hole (also sometimes referred to as direct collapse black hole in the literature) forms when the core of a massive star is so heavy that it inevitably collapses to a BH. This occurs for stars with initial masses of $40 \, \mathrm{M_\odot} \leq M \leq 140 \, \mathrm{M_\odot}$ or $M \geq 260 \, \mathrm{M_\odot}$. Under these considerations the massive stars produced in the runaway collapse scenario are technically also direct collapse black holes, however this term is usually reserved in the literature for BHs formed out of stars with $\gtrsim 10^4 \, \mathrm{M_\odot}$, and for BHs born due to the general relativistic instability that causes the collapse of a supermassive star (SMS) with $M \geq 10^5 \, \mathrm{M_\odot}$. This is further explained in Sec. 3.5. This section describes the conditions needed to produce supermassive stars with $> 10^4 \, \mathrm{M_\odot}$ that will later produce DCBHs.

3.4.1   Conditions for DCBH emergence

The conditions for the formation of a DCBH as explored here, are subject to the conditions that allow the formation of supermassive stars (SMS). While in Sec. 3.2.1 the formation of Pop. III stars in minihalos was discussed showing that they can become much more massive than present-day stars, they are still orders of magnitude lighter than SMSs. The typical

conditions for the formation of Pop. III stars do not suffice for SMS formation, and one needs to consider a slightly modified scenario.

The work by Loeb and Rasio (1994) considered the collapse of protogalactic gas clouds as a pathway for quasar formation. By means of SPH simulations they followed the collapse of rotating gas clouds that ultimately form a spherical configuration that resembles a galactic bulge, in which an SMBH could be formed. This study thus hinted at the possibility that gas collapse in protogalactic clouds could provide the conditions needed for the formation of very massive objects. Along this same line Bromm and Loeb (2003) studied gas collapse in the first galaxies, focusing on clouds in which gas cooling through H_2 is suppressed, thus maintaining temperatures of 10^4 K, increasing the Jeans mass and thus providing a massive self-gravitating cloud with enough mass to produce supermassive stars. A key ingredient in this recipe is therefore the suppression of H_2 cooling following its destruction. Molecular hydrogen can be destroyed by photons in the Lyman-Werner bands, whose energy range is $11.2 - 13.6$ eV, via the Solomon process

$$H_2 + \gamma \rightarrow H_2^* \rightarrow 2H, \tag{3.24}$$

in which the molecule in an excited electronic state H_2^* can decay to the vibrational continuum of the ground state, resulting in a dissociation (Stecher and Williams, 1967). The destruction of molecular hydrogen in protogalactic clouds can thus be achieved under the presence of a sufficiently intense Lyman-Werner radiation field. This intensity is denoted by J_{LW}. This radiation will not only destroy H_2, but will also suppress its formation through H^- photodissociation (which allows H_2 formation as shown in Eq.(3.5)).

In the absence of molecular hydrogen the next efficient coolant is atomic hydrogen. In this case, collisions between these atoms can transfer part of the collision energy by bringing them to an excited electronic state. The de-excitation occurs when the atom decays to the ground electronic state, emitting photons that take this energy away. This process therefore cools the gas and causes the collapse of clouds whose virial temperature is $T_{\mathrm{vir}} \sim 10^4$ K. The mass of those gas clouds is given by (Glover, 2013)

$$M_{\mathrm{atom}} = 5 \times 10^7 h^{-1} \left(\frac{\mu}{0.6} \right)^{-3/2} \Omega_m^{-1/2} \left(\frac{1+z}{10} \right)^{-3/2} M_\odot, \tag{3.25}$$

where h is the reduced hubble constant, μ is the mean molecular weight, Ω_m is the matter density parameter and z is the redshift. The dark matter halos in which this condition is fulfilled are usually called atomic-cooling halos, and they typically acquire enough mass by redshift $z \gtrsim 10$. Here the prevention of both H_2 cooling and metal pollution are crucial for this channel to operate, as otherwise the normal galaxy-formation scenario is expected (Greif et al., 2008).
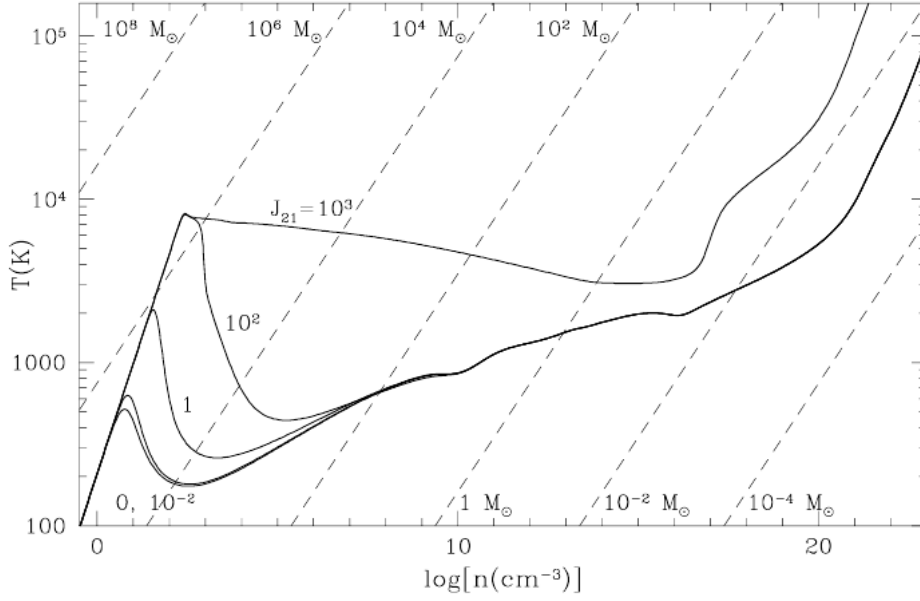
Figure 3.18. One-zone model calculations of the collapse of an atomic-cooling halo irradiated by a background radiation field. The field is modelled as thermal radiation at 10^4 K with zero intensity at frequencies higher than the Lyman-limit. The intensity is presented in units of $J_{21} = 10^{-21}$ erg cm^{-2} s^{-1} sr^{-1} Hz^{-1}. Credits: Omukai (2001).

By employing a similar method to the one described for the collapse of primordial gas clouds (see Sec.3.2.1), one-zone models provide an insight into the thermodynamical evolution during cloud collapse in metal free atomic-cooling halos, showing that the gas evolves isothermally over more than 13 orders of magnitude in density (Omukai, 2001), provided that the intensity of the background LW radiation field is high enough (see Fig. 3.18).

How intense the background radiation must be has been the focus of several studies. The radiation intensity above which H$_2$ formation remains suppressed is usually denoted by J_{LW}^{crit}. Typically this intensity is measured in units of J_{21} which is the specific intensity at the Lyman-limit and its value is

$$J_{21} = 10^{-21} \text{ erg s}^{-1} \text{ cm}^{-2} \text{ sr}^{-1} \text{ Hz}^{-1}. \tag{3.26}$$

Two different radiation spectra are usually considered, modelled as black bodies with different temperatures. Mimicking a Pop. III stellar population as a black body radiation source with effective temperature of 10^5 K yields $J_{LW}^{\text{crit}} \gtrsim 10^5$, whereas when mimicking a Pop. II stellar population as a black body with 10^4 K yields slightly lower values $J_{LW}^{\text{crit}} \lesssim 10^3$, with both values obtained from one-zone models (Omukai, 2001; Schleicher et al., 2010).

The studies that employed three-dimensional hydrodynamical simulations including chemical networks obtained a more accurate value for J_{LW}^{crit}. Along this line, AMR simulations with the ENZO and FLASH code were performed, finding somewhat lower but more variable values $30 < J_{LW}^{\text{crit}} \lesssim 1000$ (Latif et al., 2014a, 2011; Regan et al., 2014; Shang et al., 2010).

The situation is further complicated when considering the gas ionization which boosts H_2 formation when including the effects of X-ray radiation, raising the value of $J_{LW}^{\rm crit}$ by an order of magnitude (Glover, 2016; Inayoshi and Tanaka, 2015; Latif et al., 2015).

The evolution of atomic-cooling halos that remain metal free and are exposed to $J_{\rm LW} \geq J_{LW}^{\rm crit}$ has been followed by means of numerical simulations by several groups, employing hydrodynamical simulations with chemical networks that do not include H_2, assuming that it is efficiently destroyed by the background radiation field. The results of these studies demonstrate the plausibility of forming massive BHs that can grow to 10^9 $M_\odot$ by $z \sim 6$ (Latif et al., 2016a, 2014b, 2016c, 2014c, 2013; Regan and Haehnelt, 2009a,b).

Nevertheless, it is not only important to identify this channel as a possible route to SMBH formation in the early Universe, nor to characterize the radiation source needed to achieve the isothermal collapse. It is also important to asses whether the required conditions can actually be fulfilled during the evolution of the Universe, specially considering that the expected mean UV background radiation produced by the first stars is $\lesssim 0.1$ J_{21} (Johnson et al., 2008). In this regard the work by Dijkstra et al. (2008) shows that a small fraction $(10^{-8} - 10^{-6})$ of DM halos with $T_{\rm vir} \gtrsim 10^4$ K have a close luminous neighbour within 10 kpc, being exposed to a background LW radiation intensity of $J_{\rm LW} > 1000$ J_{21}. This situation has been called the "synchronized pair" scenario (Dijkstra et al., 2014; Visbal et al., 2014).

The occurrence of the right conditions for isothermal collapse of atomic-cooling halos has also been investigated via radiation hydrodynamical simulations of cosmological volumes. In this case, a nearby starburst galaxy is identified as crucial for providing the necessary $J_{\rm LW}^{\rm crit}$ (Chon et al., 2016; Regan et al., 2017). However this might still promote fragmentation due to tidal forces (Chon et al., 2016). A snapshot of one of these simulations is presented in Fig. 3.19. In this case the gas collapse has been followed with numerical simulations for up to 0.1 Myr (Chon et al., 2018), demonstrating that the formation of SMSs and subsequent DCBH is possible under these conditions.

At this point, the conditions required for the DCBH channel are very special and probably very rare. First, the gas that makes up the atomic-cooling halos must remain metal-free to prevent efficient cooling and fragmentation. Second, this gas must be exposed to an intense Lyman-Werner radiation field in order to dissociate and prevent the formation of H_2, otherwise a normal mode of Pop. III star formation is expected (see Sec. 3.2.1). This last requirement can be fulfilled in halos that are close to a star-forming galaxy, but not so close as to be metal-polluted or tidally deformed/disrupted. How rare these conditions are in the
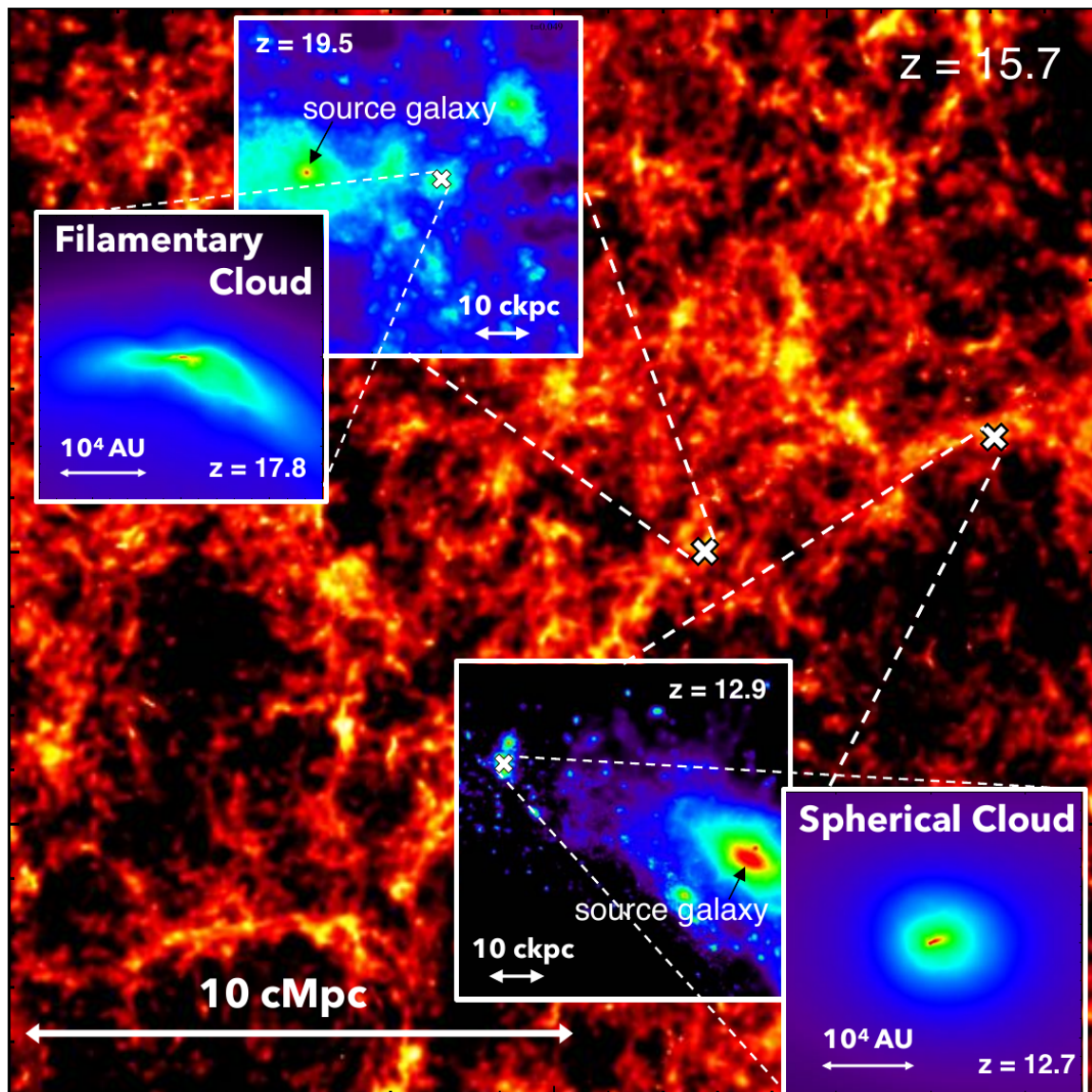
Figure 3.19. Identification of the sites for DCBH formation. In this snapshot of a cosmological simulation by Chon et al. (2016), two atomic-cooling halos are identified close to star-forming galaxies that provide the required radiation intensity that prevents H_2 formation. Credits: Chon et al. (2018).

early Universe has been investigated by Habouzit et al. (2016). Their study study compared results from analytical, semi-analytical, and hydrodynamical simulations, finding a wide range of predicted abundances of the sties in which DCBHs might emerge, with values for the number density in the range $\sim 10^{-9} - 10^{-1}$ per cMpc^3 (see Fig. 3.20) . The number density sensitively depends on the adopted critical intensity of the Lyman-Werner radiation, as well as on the supernova prescription adopted since it will impact metal pollution, star-formation, and hence LW background.

A new variation of the DCBH scenario was identified recently in cosmological radiation
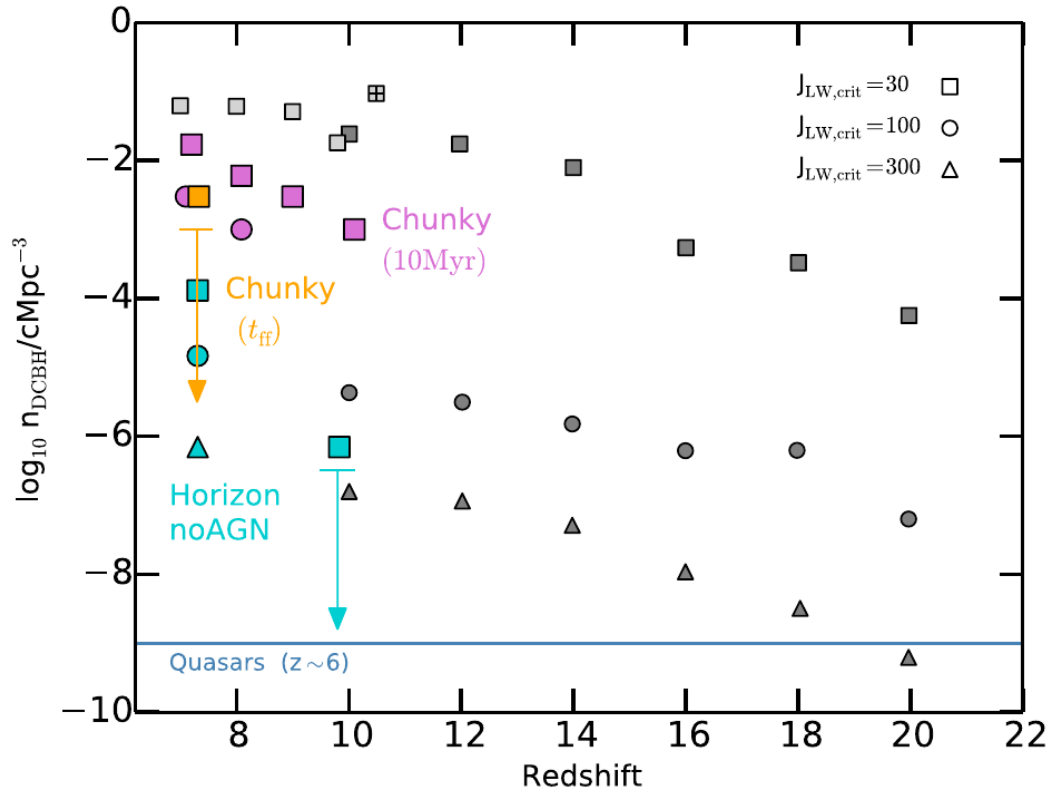
Figure 3.20. Number density of possible DCBH formation sites as function of redshift for different models. Different symbols represent different values of the critical LW intensity. Dark gray symbols were obtained from (Dijkstra et al., 2014). The light gray square with a cross inside at $z = 10.5$ is from Agarwal et al. (2014), whereas the light gray squares in the range $z = 10 - 7$ are from Agarwal et al. (2012). The coloured symbols are from Habouzit et al. (2016) and show the values obtained from cosmological simulations in which the halos are irradiated for 10 Myr (purple), for a cloud free-fall time (orange), and for a simulation with no AGN feedback. Credits: Habouzit et al. (2016).

hydrodynamical simulations reported by Wise et al. (2019). In this case, even when the Lyman-Werner intensity is far below J_{LW}^{crit}, a value of $J_{LW} = 3\ J_{21}$ is sufficient, provided the atomic-cooling is assembled through periods of major mergers, dynamically heating the gas as it virializes and preventing its early collapse (Regan et al., 2020). These conditions are expected in overdense regions of the Universe, and the authors provide an estimated abundance of $10^{-6} - 10^{-7}$ per cMpc^3.

3.4.2 The fate of gas clouds that are candidates for DCBH formation

Overall although the right conditions for DCBH formation can be rare, and expected to be found in overdense regions of the Universe (Lupi et al., 2021; Regan et al., 2020; Wise et al., 2019), it has been shown that once the conditions are met, high accretion rates of

$\dot{M} \gtrsim 0.1 \, \mathrm{M_\odot}$ onto massive gas clumps ($\sim 10^4 \, \mathrm{M_\odot}$) are always found in three-dimensional (radiation-) hydrodynamical simulations (Chon et al., 2018; Latif et al., 2015, 2014a, 2016a,b; Latif and Schleicher, 2015; Latif et al., 2014b, 2016c, 2014c, 2013, 2011; Latif and Volonteri, 2015; Latif et al., 2022; Regan et al., 2019; Regan and Haehnelt, 2009a,b; Regan et al., 2017; Wise et al., 2019). This however is not definitive evidence that a supermassive star that later collapses to a massive BH will be actually formed. In fact, these studies are unable to follow the gas cloud collapse to scales at which a protostar will form and subsequently grow to become an SMS (this is further explained in Sec. 3.5).

Still some hurdles at small scales could prevent the formation of an SMS, and certainly will impact the final masses expected for these objects, and probably also their multiplicity. Star formation in the early Universe has been shown to be affected by turbulence in the gas, and fragmentation at small scales is always present in high resolution simulations (Becerra et al., 2018; Greif et al., 2012; Jaura et al., 2022; Patrick et al., 2023; Suazo et al., 2019; Wollenberg et al., 2020), specially when an accretion disk is formed around growing protostars (Clark et al., 2011b). Fragmentation of an accretion disk around a forming SMS might reduce the accretion rate onto the central object. This could cause the emission of ionizing UV radiation from the SMS, thus halting gas accretion and further growth (Sakurai et al., 2015), or even their formation.

The assembly of SMSs from embryonic protostars following gas fragmentation during atomic-cooling halos must be further investigated. This was the aim of the research presented in Chap. 7 which reports the results of numerical simulations that self-consistently treat stellar and gas dynamics during the formation of SMSs from their birth as protostars until they become $10^4 \, \mathrm{M_\odot}$ supermassive stars.

3.5 Supermassive stars as embryos of supermassive black holes

Supermassive stars were originally conceived to explain strong radio emission in the center of Seyfert galaxies (Hoyle and Fowler, 1963a,b), as models of quasars with objects reaching masses of $10^5 \, \mathrm{M_\odot}$. In subsequent analytic studies that included General Relativity effects it was found that objects with these masses are unstable above $\sim 10^5 \, \mathrm{M_\odot}$(Chandrasekhar, 1964), and thus they became interesting objects for explaining the formation of supermassive black holes powering galactic nuclei as presented in the seminal paper by Rees (1984).

What is a supermassive star depends on the definition adopted. Typical definitions

are based on the mass of the star, frequently defining a supermassive star as a star with > 1000 M$_\odot$ (Gieles et al., 2018; Martins et al., 2020; Schleicher et al., 2013; Yungelson et al., 2008), or with a mass $M > 10^5$ M$_\odot$ (Fuller et al., 1986) . Alternatively, in the review by Woods et al. (2019a), they define a supermassive star as a star with a mass so large that it inevitably collapses to a black hole due to the Chandrasekhar (also Post-Newtonian, Chandrasekhar-Feynman, or GR) instability. This mass is given by

$$M_{\text{SMS}} \approx \left(0.32 \frac{Rc^2}{\mu G \text{M}_\odot} \right)^{2/3} \text{M}_\odot \sim 10^5 \text{M}_\odot, \qquad (3.27)$$

where R is the radius of the star, c is the speed of light, G is the gravitational constant and μ is the mean molecular weight of the gas comprising the star. This is valid for non-rotating stars modelled as an $n = 3$ polytrope. Detailed stellar evolution codes that include post-Newtonian approximations to general relativistic gravity, and hydrodynamics, confirm that such stellar models inevitably collapse to a black hole at masses $M > 10^5$ M$_\odot$ (Fuller et al., 1986). Some of the most recent calculations have explored the final fates of the so-called monolithic supermassive stars, objects with $10^4 - 10^8$ M$_\odot$ in the idealized case of wholly thermally relaxed objects, which are typically assumed to have been formed instantaneously (Hoyle and Fowler, 1963b), as opposed to supermassive stars formed from rapid gas accretion starting from ebryonic protostars (Regan et al., 2017) which have a very different internal structure (Hosokawa et al., 2013).

The fate of such monolithic supermassive stars depend on whether released nuclear burning energy is sufficient to halt the contraction before the Chandrasekhar instability causes runaway dynamical collapse. In a recent study, Woods et al. (2020) used the KEPLER stellar evolution code (Weaver et al., 1978; Woosley et al., 2002) that includes one-dimensional Lagrangian hydrodynamics, first order post-Newtonian corrections via a modified gravitational constant, and updated nuclear burning networks implicitly coupled to hydrodynamics (Woosley et al., 2004). They conclude that supermassive stars of primordial composition can survive past the core helium burning phase for masses $M \lesssim 6 \times 10^4$ M$_\odot$, otherwise they only survive until hydrogen in the core is exhausted after $\sim 10^6$ yr up to masses of $\sim 1.55 \times 10^5$ M$_\odot$, and for larger masses they collapse before reaching the core hydrogen burning phase. This is illustrated in Fig. 3.21.

Therefore, the fate of non-rotating supermassive stars of primordial composition with masses greater than 6×10^4 M$_\odot$ is the collapse to a black hole due to the Chandrasekhar instability. Survival until the core hydrogen burning phase is possible for masses $M < 1.55 \times 10^5$ M$_\odot$, and above that limit a dark-collapse occurs in which no hydrogen ignition at the core is possible before dynamical collapse.

It has been argued that monolithic supermassive stars are a good model for stars formed
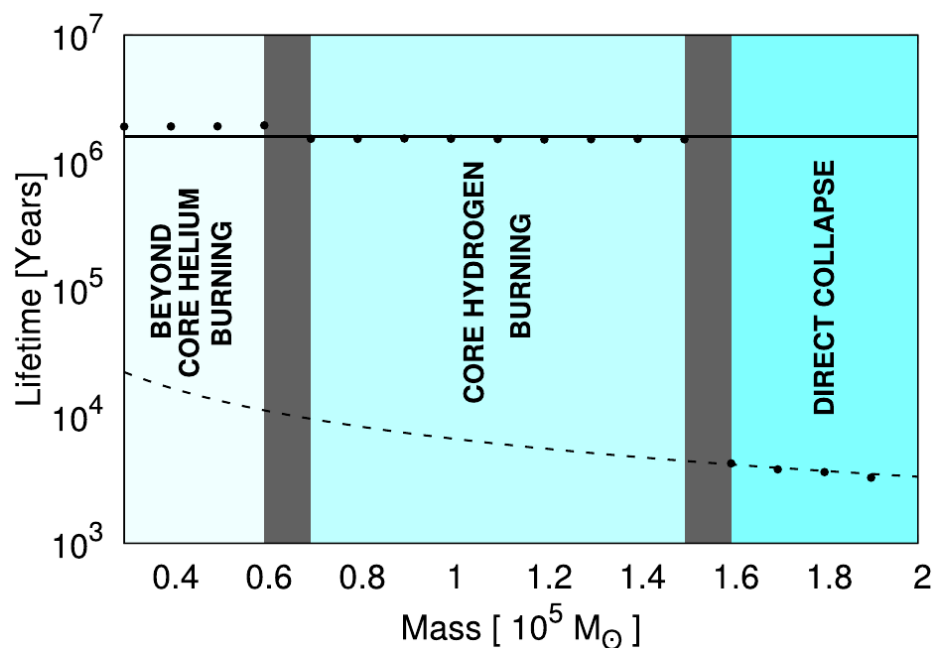
Figure 3.21. Lifetimes of non-rotating monolithic supermassive stars of primordial composition. Black dots mark the lifetime of the supermassive stars at different masses. The solid black line marks the hydrogen-burning lifetime. The dashed black line denotes the time-scale for thermal contraction. The vertical gray band at $\sim 0.6 \times 10^5$ M$_\odot$ marks the limit between supermassive stars that survive beyond core helium burning and supermassive stars that survive until core hydrogen burning exhaustion. The vertical gray line at $\sim 1.5 \times 10^5$ M$_\odot$ marks the limit between supermassive stars that survive until core hydrogen exhaustion and supermassive stars that collapse before core hydrogen ignition. Credits: Woods et al. (2020).

through runaway stellar collisions as presented in Gieles et al. (2018), in which a high number density of stars combined with high accretion rates $\gtrsim 10^5$ M$_\odot$ Myr^{-1} work together to induce a high stellar collision rate resulting in supermassive stars with $M > 1000$ M$_\odot$.

Even higher accretion rates have been explored in the context of (super) massive star formation. In sufficiently massive dark matter halos ($\gtrsim 10^7$ M$_\odot$) if molecular hydrogen is dissociated, the gas cools via electronic transitions in the hydrogen atom, the so-called atomic cooling halos, producing an isothermal collapse at $T \sim 8000$ K (Becerra et al., 2015; Omukai, 2001; Prieto et al., 2013; Regan et al., 2020; Safranek-Shrader et al., 2012; Volonteri et al., 2021a) as explained in Sec. 3.4.1. The accretion rates in those environments can easily exceed 10^{-1} M$_\odot$ yr^{-1}, and have the potential to produce supermassive stars with 10^5 M$_\odot$. Understanding the evolution of protostars that experience these high accretion rates has been important to understand the possible hurdles during their formation. In this context at least two different groups have studied the evolution of protostars under these conditions (Haemmerlé et al., 2018; Hosokawa et al., 2012). Here a summary of the main results obtained from these studies is presented, focusing on the work by Hosokawa et al. (2012).

In the work by Hosokawa et al. (2012) accretion rates up to 1 M$_\odot$ yr^{-1} are considered, and the equations for stellar structure solved as described in Hosokawa and Omukai (2009). The fiducial case of accretion at 0.1 M$_\odot$ yr^{-1} is considered here, and the evolution of a star under this condition is illustrated in Fig. 3.22. For such high accretion rates the KH timescale becomes shorter than the accretion timescale at $M_* \approx 40$ M$_\odot$, and the extent of the stellar radius is well described by

$$R_* \sim 26 \text{ R}_\odot \left(\frac{M_*}{\text{M}_\odot} \right)^{0.27} \left(\frac{\dot{M}_*}{10^{-3} \text{ M}_\odot \text{ yr}^{-1}} \right)^{0.41}. \tag{3.28}$$

Thus for a given stellar mass, the radius is larger the larger the accretion rate is, so that at the same stellar mass, a protostar accreting at a higher rate is more extended and has a lower interior temperature. This reduced temperature results in reduced opacity which prolongs the adiabatic accretion phase, even when $t_{\text{KH}} < t_{\text{acc}}$. At this point the stellar interior is contracting while the stellar radius is increasing, the bloated surface layer occupies only a small fraction of the total mass, and this layer absorbs the energy coming from the radiative interior, further expanding the outer layer as the interior contracts. Deuterium burning is ignited at ∼50 M$_\odot$ but its influence on subsequent evolution is negligible for accretion rates $\dot{M}_* > 10^{-4}$ M$_\odot$ yr^{-1} (Hosokawa and Omukai, 2009). Eventually the interior temperature reaches the threshold for hydrogen burning at $T \sim 10^8$ K when the protostar reaches 600 M$_\odot$. The protostar maintains a bloated envelope with a compact core and a

constant surface temperature of ~ 5000 K, unable to produce ionizing photons that could terminate accretion due to radiative feedback (see Fig. 3.22).

Important for the work presented in this thesis is the derivation of the mass radius relation that these accreting protostar follow during their evolution. The luminosity reaches the Eddington luminosity for $M_* \gtrsim 100$ M$_\odot$. This combined with the fact that the surface temperature remains at ~ 5000 K, and using the expression for the luminosity of a black body

$$L_* = 4\pi R_*^2 T_{\text{eff}}^4, \tag{3.29}$$

results in a mass radius relation of the form

$$R_* \approx 2.6 \times 10^3 \text{ R}_\odot \left(\frac{M_*}{100 \text{ M}_\odot}\right)^{1/2}. \tag{3.30}$$

The work by Hosokawa et al. (2012) confirmed that for sufficiently high accretion rates this relation holds at least until 1000 M$_\odot$, and then extended this range and confirmed the validity of Eq.(3.30) up to $M \gtrsim 10^4$ M$_\odot$ at which point the star reaches a size of ~ 100 AU, and the surface temperature never exceeds 10^4 K (Hosokawa et al., 2013). Although these studies did not include GR effects, subsequent studies that included post-Newtonian corrections confirm these results (Haemmerlé et al., 2018). The exact accretion rate above which a protostar evolves as an inflated supermassive star with a radius given by Eq.(3.30) seems to lie in between $0.01 - 0.06$ M$_\odot$ yr^{-1} (Herrington et al., 2023; Hosokawa et al., 2012).

The ultimate fate of accreting supermassive stars depends on the accretion rate. In the work by Schleicher et al. (2013) it is suggested that as long as a supermassive star keeps accreting at $\dot{M} >> 0.14$ M$_\odot$ yr^{-1} the core of the star will collapse due to the GR instability giving birth to a quasi-star, i.e., a star whose gravity pull is counteracted by radiation from an accreting BH rather than nuclear fusion (Begelman et al., 2008). The work by Umeda et al. (2016) confirms that SMSs can reach higher masses when accreting at higher rates, in particular for accretion rates of $0.3 - 1$ M$_\odot$ yr^{-1} the SMS encounters the GR instability during helium burning in the core at $2.3 - 5 \times 10^5$ M$_\odot$, and for even higher accretion rates of $\dot{M} = 10$ M$_\odot$ yr^{-1} the star collapses at 8×10^5 M$_\odot$ while hydrogen is being burned at the core. While different authors have found similar results for the final masses of supermassive stars at $\dot{M} \lesssim 1$ M$_\odot$ yr^{-1}, uncertainties remain for higher rates with values differing by a factor $2 - 4$ (see Fig. 3.23).

The studies mentioned before assumed constant accretion rates throughout the whole process of supermassive star formation. This is in reality most likely not the case. So what are the effects of a variable accretion rate during supermassive star assembly?. This question has been addressed by Sakurai et al. (2015) by solving the equations of stellar structure, similarly as done in Hosokawa et al. (2013) but including quiescent phases in which the accretion rate is set to zero. The results indicate that quiescent periods of ~ 1000 yr are
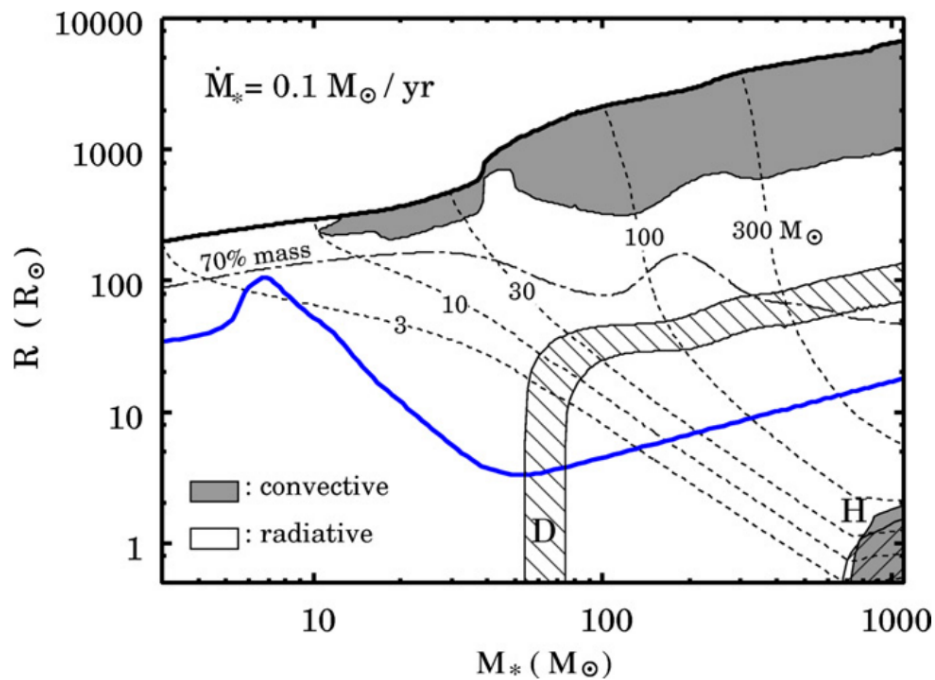
Figure 3.22. Structure of protostars evolving under very high accretion rates. The figure shows the stellar radius as a function of stellar mass for accretion rates of 0.1 $M_\odot$ yr^{-1} (solid black line) and 10^{-3} $M_\odot$ yr^{-1} (solid blue line) for comparison. Convective layers are indicated by shaded gray areas whereas white areas indicate radiative layers. The dot-dashed black line indicates the position at which 70% of the stellar mass is enclosed. Dashed lines indicate loci of constant mass of $M = 3, 10, 30, 100$, and 300 $M_\odot$. Hatched areas indicate layers of active nuclear burning of deuterium (D) and hydrogen (H). Credits: Hosokawa et al. (2012).

long enough as to allow a contraction of the supermassive star and trigger the production of ionizing photons that could be able to terminate further accretion. This indicates that it is not sufficient to just assume that accretion rates of $\dot{M} > 0.01$ $M_\odot$ yr^{-1} will inevitably lead to the formation of an SMS, but emphasizes the need to resolve the assembly of SMSs including the possibility of fragmentation of the accretion disk as found for studies about the formation of Pop. III stars (Clark et al., 2011b). A study along this line was pursued by Tagawa et al. (2020) which considered the possibility that frequent mergers of an SMS with surrounding fragments can keep the SMS inflated preventing ionizing radiation feedback. Complementing this semi-analytic method with detailed N-body plus Hydrodynamic simulations was one of the goals of the study presented in Chap. 7.
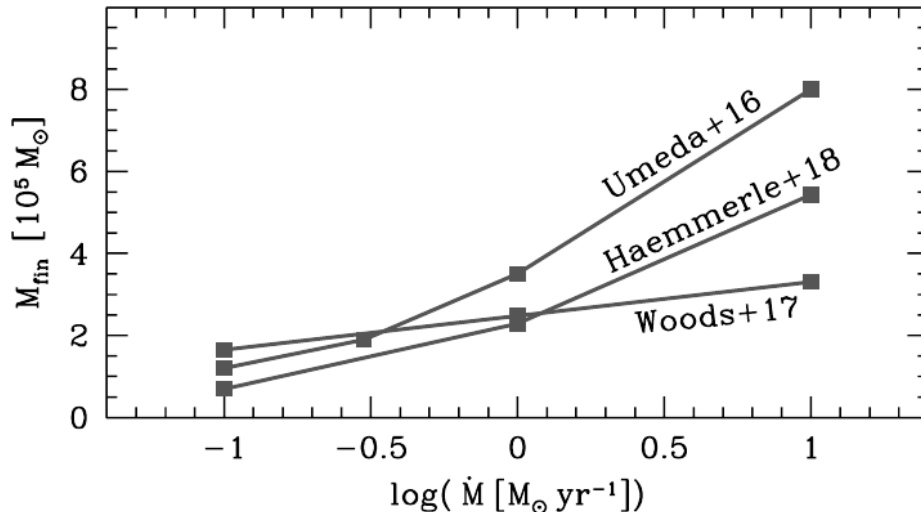
Figure 3.23. Final mass of accreting supermassive stars for different accretion rates. Credits: Woods et al. (2019b).

3.6 The growth of black hole seeds

Explaining the emergence of the massive, high redshift ($z \geq 6$) quasars observed to date inevitably requires a period of black hole growth. The growing BH will start as a seed formed through one of the channels mentioned before, and it must reach 10^9 M$_\odot$ before the Universe reaches an age of 1 billion years.

The classic argument for BH growth is that they typically acquire mass by accreting the surrounding gaseous matter. As a black hole accretes matter, an accretion disk is formed around it. The high density and velocities reached by the material orbiting the central BH implies frequent and energetic collisions between its constituent particles. This in turn heats up the accretion disk which then emits light, typically peaking in the X-ray range of the electromagnetic spectrum. Inside the gaseous accretion disk the material is transported inwards as angular momentum is transported outwards via viscous forces. The gas gradually moves closer to the BH and ultimately reaches the innermost stable circular orbit (ISCO). The amount of energy that can be released by accretion is given by the amount of energy that the orbiting material must lose in order to reach the ISCO. A fraction of the rest-mass energy of the accreting gas will be emitted as radiation, this is referred to as the radiative efficiency ϵ. In cosmological simulations a constant value of $\epsilon = 0.1$ is typically assumed (Booth and Schaye, 2009; Di Matteo et al., 2008). This value comes from a comparison between the quasar/AGN luminosity function and the local population of SMBHs (Shankar et al., 2004; Soltan, 1982; Yu and Tremaine, 2002). The mass lost by the disk is then related to the mass gained by the BH as

$$\dot{M}_{\mathrm{BH}} = (1 - \epsilon)\dot{M}_{\mathrm{disk}}. \tag{3.31}$$

The radiative luminosity L of a black hole accreting at $\dot{M}_{\mathrm{BH}}$ is therefore

$$L = \epsilon \dot{M}_{\mathrm{disk}} c^2, \tag{3.32}$$

$$L = \epsilon \frac{\dot{M}_{\mathrm{BH}} c^2}{(1-\epsilon)}, \tag{3.33}$$

where c is the speed of light. Therefore the black hole growth rate has an associated luminosity

$$\dot{M}_{\mathrm{BH}} = \frac{(1-\epsilon)}{\epsilon c^2} L. \tag{3.34}$$

This luminosity injects momentum into the surrounding gas, acting as a force opposite to the gravitational attraction of the BH. The Luminosity at which these two forces balance is called the Eddington Luminosity and is given by

$$L_{\mathrm{Edd}} = \frac{4\pi G M_{\mathrm{BH}} c}{\kappa}, \tag{3.35}$$

where κ is the opacity of the gas. For purely ionized hydrogen, opacity comes from Thompson scattering and in this case the Eddington Luminosity is

$$L_{\mathrm{Edd}} = \frac{4\pi G M_{\mathrm{BH}} m_p c}{\sigma_T}, \tag{3.36}$$

where m_p is the proton's mass and σ_T is the Thompson scattering cross-section.

The maximum accretion rate at which hydrostatic equilibrium can be maintained is obtained by setting $L = L_{\mathrm{Edd}}$ in Eq.(3.34) which leads to

$$\dot{M}_{\mathrm{BH}} = \frac{(1-\epsilon)}{\epsilon c^2} L_{\mathrm{Edd}}. \tag{3.37}$$

The accretion rate at which the radiative force produced as a consequence of gas accretion balances the gravitational force produced by the BH is called the Eddington accretion rate. When this accretion rate is surpassed, the radiative force stops further accretion onto the BH. This is however valid only under the assumption of spherically symmetric accretion, and in reality the radiative luminosity can surpass the Eddington luminosity without quenching accretion onto the BH when considering accretion through a gaseous disk. In general one can define the Eddington ratio f_{Edd} as the ratio of radiative luminosity to Eddington luminosity such that the accretion rate onto a BH can be described by

$$\dot{M}_{\mathrm{Edd}} = \frac{(1-\epsilon)}{\epsilon c^2} f_{\mathrm{Edd}} L_{\mathrm{Edd}}. \tag{3.38}$$

The final mass of a BH can then be found by integrating Eq.(3.38) as (Johnson et al., 2013)

$$M_{\mathrm{BH,final}} = M_{\mathrm{BH,ini}} \times \exp\left[\frac{f_{\mathrm{Edd}} f_{\mathrm{duty}} (1-\epsilon)}{\epsilon} \left(\frac{t_{\mathrm{fin}} - t_{\mathrm{ini}}}{t_{\mathrm{Edd}}} \right) \right], \tag{3.39}$$

where f_{duty} is the duty cycle defined as the fraction of time that the BH spends accreting mass. t_{ini} and t_{final} are the times at which the BH starts and stops growing by accretion. $t_{Edd} = 450$ Myr is the Eddington time which follows from Eq.(3.36)

$$
\begin{aligned}
L_{Edd} &= \frac{M_{BH}c^2}{t_{Edd}}, \\
\frac{M_{BH}c^2}{t_{Edd}} &= \frac{4\pi G M_{BH} m_p c}{\sigma_T}, \\
t_{Edd} &= \frac{\sigma_T c}{4\pi G m_p}.
\end{aligned}
\tag{3.40}
$$

One can then infer and put constraints on the masses of the BH seeds that are capable of growing into the quasar population observed at high redshift, under the assumption of different radiative efficiencies, Eddington ratios, and duty cycles. For the case of low mass BH seeds as expected for the remnants of Pop. III stars, uninterrupted accretion at the Eddington rate ($f_{duty}f_{Edd} = 1$) is required to grow these seeds into 10^9 M$_\odot$ BHs by $z = 7$ (Johnson et al., 2013; Smith et al., 2017; Wise, 2023), as depicted in Fig. 3.24.
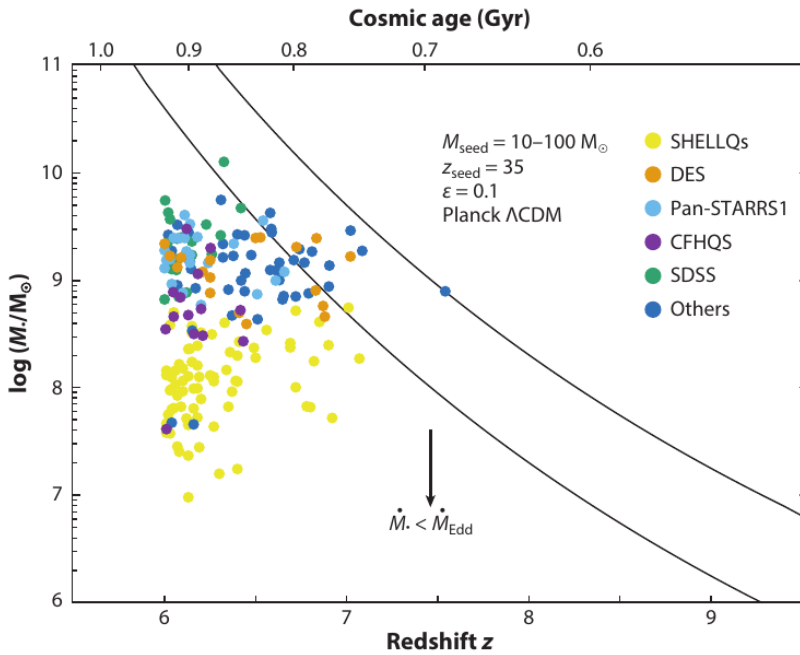
Figure 3.24. Masses and redshift of known quasars at $z \geq 6$ from different surveys marked with coloured dots. Solid black lines indicate the growth of BH seeds formed at $z = 35$ and considering a radiative efficiency of $\epsilon = 0.1$, assuming $f_{Edd}f_{duty} = 1$, and for seeds with 10 and 100 M$_\odot$ as initial mass. Credits: Inayoshi et al. (2020).

The situation is more complicated when considering the environments in which these seeds are expected to be born, i.e., a star cluster with high mass stars whose radiation and SN explosions are very effective in removing the gas from minihalos (Johnson and Bromm, 2007; Smith et al., 2018). In the model of Johnson et al. (2013) the growth of seeds from

Pop. III remnants is modelled with a delay of 100 Myr for the onset of accretion, the typical timescale for mergers of minihalos at $z \sim 30$, since mergers can deliver cold gas to the remnant BH, as found in cosmological simulations (Johnson and Bromm, 2007). A BH seed with ~ 10 $M_\odot$ is capable of growing to 10^9 $M_\odot$ by redshift 7 only if it accretes continually at the Eddington rate with a low radiative efficiency of $\epsilon = 0.07$ (see bottom panel in Fig. 3.25). It is important to note that such low radiative efficiencies are indeed possible in the slim disk solution for non-rotating BHs at $f_{\mathrm{Edd}} \leq 1$, or independent of BH spin at higher f_{Edd} (Madau et al., 2014), thus suggesting that super-Eddington accretion is needed in this case. Invoking super-Eddington rates does however not solve the problem because of the feedback effects associated, such as the launching of jets that can quench further accretion by evacuating the surrounding gas (Regan et al., 2019), although some authors argue that for sufficiently massive halos ($> 10^{10}$ $M_\odot$) the associated feedback would be inefficient (Mayer, 2019).

On the other hand, when considering more massive black hole seeds born as remnants of SMSs formed in atomic cooling halos, or formed through runaway stellar collisions in dense star clusters the parameter space of radiative efficiencies, Eddington ratios, and duty cycles is broader. In fact, for seeds as massive as 10^4 $M_\odot$, the combination $f_{\mathrm{Edd}}f_{\mathrm{duty}} = 0.5$ can still produce a 10^9 $M_\odot$ SMBH by $z = 7$ provided the radiative efficiency is low ($\epsilon = 0.07$), otherwise continuous accretion at the Eddington rate is required, but with radiative efficiencies that can be as high as $\epsilon = 0.15$ (see Fig. 3.25). Such a high ϵ is indeed expected for BHs with a spin of $a \sim 0.5$ (Madau et al., 2014).

While the formation of massive black hole seeds is important for providing a head-start during rapid SMBH assembly, the problem of subsequent growth through gas accretion must also be solved. In this regard the light seeds produced as remnants of Pop. III stars face two important hurdles: the evacuation of gas from the minihalos in which they are born, and the need to invoke super-Eddington rates or radiatively inneficient accretion. On the other hand, heavy seeds formed from the death of SMSs do not necessarily need to invoke super-Eddington rates as long as they accrete continuously. Continuous accretion ($f_{\mathrm{duty}} = 1$) was found to be possible for the most massive halos at high redshift, since they experience a high number of major mergers (~ 10) (Tanaka, 2014), with the assumption that the gas can be brought to the BH with no interruptions.

Finally, it is iportant to note that while the presence of quasars at the highest redshifts need to invoke the emergence of massive seeds and a combination of continuous gas accretion (or intermittent super-Eddington accretion), this is probably just the tip of the iceberg. The entire BH mass distribution at low redshift probably requires a combination of light and heavy seeds. Constraining the different seeding mechanisms requires the combination of diverse methods that compare model predictions with observations such as the BH luminosity function, BH abundance, and GW detections (Natarajan, 2014; Natarajan and Volonteri,
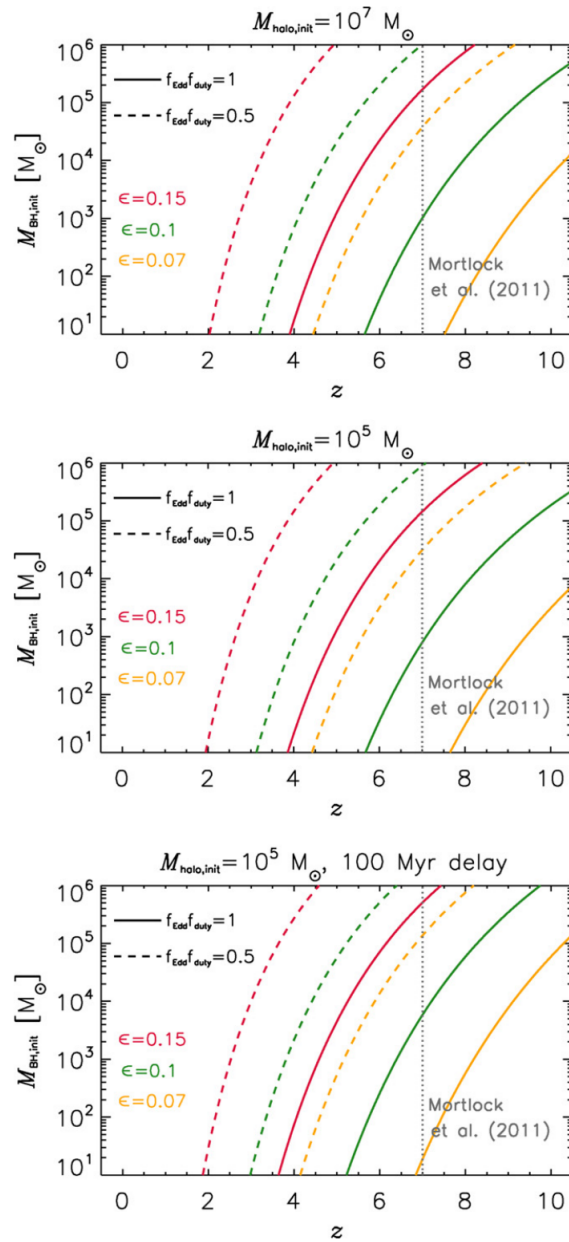
Figure 3.25. Initial BH seed mass as function of the redshift at which it grows to a 10^9 $M_\odot$ SMBH. The top panel considers BHs born in 10^7 $M_\odot$ halos, while the middle and lower panel consider BHs born in minihalos of 10^5 $M_\odot$. Additionally, the lower panel considers a 100 Myr delay between the BH formation and the onset of accretion, as could be expected for BH seeds from Pop. III stars. Credits: Johnson et al. (2013).

2012; Volonteri et al., 2021b; Volonteri and Rees, 2005).

Chapter 4

Methods

This thesis contains three scientific articles. In those articles the formation of massive black hole seeds in the early Universe was explored by means of numerical simulations. The article presented in Chap. 5 addresses the problem of runaway stellar collisions in dense star clusters embedded in gas. The article presented in Chap. 6 focuses on gas-free clusters and in comparing analytic collision rates with numerical simulations. In those works a suite of N-body simulations was presented and analyzed. All the simulations were performed with the NBODY6 code.

The article presented in Chap. 7 focuses on the formation of massive stars through the combined action of gas accretion and stellar collisions. The simulations treat the gas and stellar dynamics self-consistently and include sink particle formation, stellar collisions, and gas accretion, in an environment resembling a dense gas cloud formed in a metal free atomic-cooling halo. For the development of this work it was necessary to couple an N-body and an SPH code by utilizing the AMUSE interface.

The subject of this chapter focuses on complementing the articles included in this thesis by expanding on the description of the software utilized for running the simulations, as well as on additional algorithms included, and on the preparation of the initial conditions for the simulations presented in Chap. 7.

4.1 Nbody6

The research presented in Chap. 5 and Chap. 6 required the modelling of dense star clusters. The evolution of those systems was simulated with the code NBODY6[1] (Aarseth, 2000; Nitadori and Aarseth, 2012). This section presentes a brief description of the code, the algorithms included in these simulations, and the modifications required.

---

[1]NBODY6 can be obtained at: https://people.ast.cam.ac.uk/ sverre/web/pages/nbody.htm

4.1.1 The Hermite integrator

The NBODY6 code utilizes a fourth order Hermite integrator, which is a predictor-corrector method. In the Hermite integration method, the acceleration and the jerk are computed according to

$$\boldsymbol{a}_{0,i} = -\sum_{i \neq j} G m_j \frac{\boldsymbol{R}}{R^3}, \tag{4.1}$$

$$\dot{\boldsymbol{a}}_{0,i} = -\sum_{i \neq j} G m_j \left[\frac{\boldsymbol{V}}{R^3} + \frac{3\boldsymbol{R}(\boldsymbol{V} \cdot \boldsymbol{R})}{R^5} \right], \tag{4.2}$$

which are the acceleration $\boldsymbol{a}$ and jerk $\dot{\boldsymbol{a}}$ vectors for particle i at time t_0 due to the contributions of all other particles j with mass m_j, relative position $\boldsymbol{R}$, and relative velocity $\boldsymbol{V}$. With these quantities a predicted position $\boldsymbol{r_p}$ and velocity $\boldsymbol{v_p}$ for particle i are obtained from a Taylor expansion. The expressions for $\boldsymbol{r_p}$ and $\boldsymbol{v_p}$ are given by

$$\boldsymbol{r}_{p,i}(t) = \boldsymbol{r}_{0,i} + \boldsymbol{v}_{0,i}\Delta t + \boldsymbol{a}_{0,i}\frac{\Delta t^2}{2} + \dot{\boldsymbol{a}}_{0,i}\frac{\Delta t^2}{6}, \tag{4.3}$$

$$\boldsymbol{v}_{p,i}(t) = \boldsymbol{v}_{0,i}\Delta t + \boldsymbol{a}_{0,i}\Delta t + \dot{\boldsymbol{a}}_{0,i}\frac{\Delta t^2}{2}, \tag{4.4}$$

where $\boldsymbol{r}_{0,i}$ and $\boldsymbol{v}_{0,i}$, are the position and velocity at time t_0, and Δt is the timestep. Additionally, a Taylor expansion for the acceleration and the jerk yields

$$\boldsymbol{a}_i(t) = \boldsymbol{a}_{0,i} + \dot{\boldsymbol{a}}_{0,i}\Delta t + \frac{1}{2}\boldsymbol{a}_{0,i}^{(2)}\Delta t^2 + \frac{1}{6}\boldsymbol{a}_{0,i}^{(3)}\Delta t^3, \tag{4.5}$$

$$\dot{\boldsymbol{a}}_i(t) = \dot{\boldsymbol{a}}_{0,i} + \boldsymbol{a}_{0,i}^{(2)}\Delta t + \frac{1}{2}\boldsymbol{a}_{0,i}^{(3)}\Delta t^2. \tag{4.6}$$

So, at time t_0, the predicted position and velocity for particle i are computed from equations (4.3) and (4.4). With the new position and velocity, a predicted acceleration $\boldsymbol{a}_{p,i}$ and jerk $\dot{\boldsymbol{a}}_{p,i}$ are computed from Eq.(4.1) and (4.2). These quantities can then be inserted on the left-hand side of Eq.(4.5) and (4.6). Then by solving for $\boldsymbol{a}_{0,i}^{(2)}$ in Eq.(4.6) one obtains

$$\boldsymbol{a}_{0,i}^{(2)} = \frac{(\dot{\boldsymbol{a}}_{p,i} - \dot{\boldsymbol{a}}_{0,i})}{\Delta t} - \frac{\boldsymbol{a}_{0,i}^{(3)}}{2\Delta t}. \tag{4.7}$$

If one then inserts Eq.(4.7) into Eq.(4.5) and solves for $\boldsymbol{a}_{0,i}^{(3)}$ one obtains

$$\boldsymbol{a}_{0,i}^{(3)} = \frac{12(\boldsymbol{a}_{0,i} - \boldsymbol{a}_{p,i})}{\Delta t^3} + \frac{6(\dot{\boldsymbol{a}}_{0,i} + \dot{\boldsymbol{a}}_{p,i})}{\Delta t^2}. \tag{4.8}$$

Subsequently, the expression for $\boldsymbol{a}_{0,i}^{(3)}$ can be inserted into Eq.(4.7) to obtain

$$\boldsymbol{a}_{0,i}^{(2)} = -\frac{6(\boldsymbol{a}_{0,i} - \boldsymbol{a}_{p,i})}{\Delta t^2} - \frac{2(2\dot{\boldsymbol{a}}_{0,i} + \dot{\boldsymbol{a}}_{p,i})}{\Delta t}. \tag{4.9}$$

Furthermore, by expanding the Taylor series for position and velocity by two orders, one obtains new expressions for the corrected position $\boldsymbol{r}_c$ and velocity $\boldsymbol{v}_c$ of particle i after a time Δt. These expressions are given by

$$\boldsymbol{r}_{c,i} = \boldsymbol{r}_{p,i} + \boldsymbol{a}_{0,i}^{(2)}\frac{\Delta t^4}{24} + \boldsymbol{a}_{0,i}^{(3)}\frac{\Delta t^5}{120}, \tag{4.10}$$

$$\boldsymbol{v}_{c,i} = \boldsymbol{v}_{p,i} + \boldsymbol{a}_{0,i}^{(2)}\frac{\Delta t^3}{6} + \boldsymbol{a}_{0,i}^{(3)}\frac{\Delta t^4}{24}. \tag{4.11}$$

In this way, by employing the fourth order Hermite integrator, the local error in $\boldsymbol{r}$ and $\boldsymbol{v}$ after a timestep Δt is expected to be of the order $\mathcal{O}(\Delta t^5)$, and the global error for a fixed timestep of the order of $\mathcal{O}(\Delta t^4)$.

4.1.2   Block and individual timesteps

The main goal of NBODY6 is an adequate modelling of stellar systems containing a large number of particles. In N-body simulations the gravitational force calculation scales with the number of particles as $\propto N^2$ and the modelling of large N systems becomes expensive very quickly.

Reducing the frequency of the force computation is the goal of the individual timesteps. This is justified by noting that the stars in the outer parts of a star cluster feel a gravitational force that is slowly changing in time. On the other hand, the stars inhabiting the center of the cluster experience a force that is changing much more rapidly in time, compared to the most distant particles. The idea behind the block and individual timesteps scheme is to reduce the computational cost by recalculating the gravitational force only for the particles for which this is necessary. This is achieved by allowing each particle to have its own timestep, the individual timestep. This timestep must be a factor 2 commensurate with a global timestep, as this ensures that all the particles will eventually reach the same time. This is the block timestep.

An illustration of the individual and block timestep scheme is shown in Fig. 4.1. In this figure each particle m, l, k, i, has a different timestep, and the force on each of them is updated at the timesteps marked with an arrow. Therefore, up to a timestep of 8, only one force update has been applied to particle m, whereas two have been applied to particle l.

The value of the timestep must be adequately chosen and adjusted in order to avoid unphysical behaviour of the particles. The adjustment is done by taking into account the acceleration of the particles. In NBODY6 the higher order acceleration terms calculated as described in Sec.4.1.1 are used to obtain the timestep as

$$\Delta t_i = \sqrt{\eta \frac{|\mathbf{a_i}||\mathbf{a_i}^{(2)}| + |\mathbf{a_i}|^2}{|\mathbf{a_i}||\mathbf{a_i}^{(3)}| + |\mathbf{a_i^2}|^2}}, \tag{4.12}$$
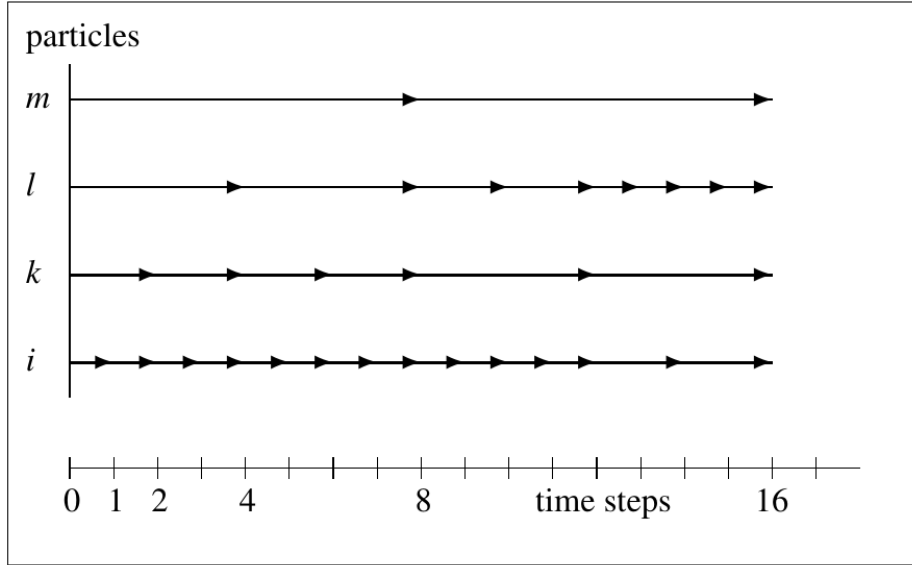
Figure 4.1.   Individual and block timestep scheme for four particles.   Credits: NBODY6++GPU user manual (https://github.com/nbodyx/Nbody6ppGPU).

with Δt_i being the timestep for particle i. This expression also depends on η, an accuracy parameter set typically to $\eta \approx 0.01$ to 0.02.

4.1.3   The Ahmad-Cohen scheme

Another way of reducing the amount of force computations per timestep is to consider only the closest neighbours to each particle. These neighbouring particles will change their relative positions more rapidly compared to the most distant ones. One can then consider, given a certain period of time, that the gravitational force exerted by the most distant stars remains constant, and only the gravitational force of the closest stars must be updated in each timestep. This is the idea behind the Ahmad-Cohen scheme (also referred to as neighbour scheme).

In order to achieve this, NBODY6 separates in two the net acceleration of a particle, i.e., $\mathbf{F} = \mathbf{F}_{\text{reg}} + \mathbf{F}_{\text{irr}}$, a regular force and an irregular force respectively. This means that the acceleration of a particle is divided in two: $\mathbf{a} = \mathbf{a}_{\text{reg}} + \mathbf{a}_{\text{irr}}$. The regular force is the force exerted by distant particles, and is updated after a time Δt_{reg}. The irregular force is the force exerted by the closest particles, and is updated after a time Δt_{irreg}.

In practice this means that at time t_0 an irregular acceleration and its first derivative are computed considering the closest neighbours of a particle using Eq.(4.1) and (4.2). Also a regular acceleration and its first derivative is computed considering the rest of the particles with Eq.(4.1) and (4.2). The full predictor correctror hermite scheme is applied using the
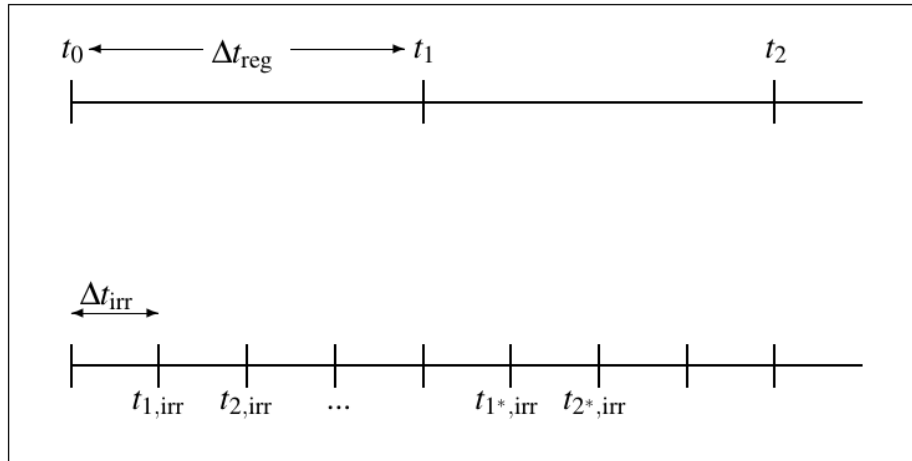
Figure 4.2. Regular and irregular time steps. Credits: NBODY6++GPU user manual (https://github.com/nbodyx/Nbody6ppGPU)

irregular and the regular acceleration. Then, at time $t_{1,irr}$, the irregular component of the acceleration and its first derivative are recalculated. The full predictor corrector Hermite scheme is applied only for the irregular acceleration, whereas no corrector is applied for the regular acceleration. This is illustrated in Fig. 4.2. To decide which particles are close enough as to be taken into account when calculating the irregular force, NBODY6 utilizes a sphere of variable radius. This radius is controlled by requiring that the number of particles is kept close to an optimal number of neighbours NNBOPT (an input parameter) with typical values in between 50 and 200 particles. The neighbour list is constructed at each regular timestep. The timestep for the regular and irregular force computation is given by Eq.(4.12), with independent and adjustable accuracy parameters $\eta_{irr} \approx 0.01$ and $\eta_{reg} \approx 0.02$. This scheme results in a significant gain in efficiency provided that the size of the neighbour list is $N_{nb} << N$.

4.1.4   KS regularization

The simulation of a star cluster involves a wide range in spatial scales. From the typical size of a globular cluster of ~ 2 pc all the way down to the separation of binary stars, in the order of AU. It also involves a wide range in temporal scales, from times comparable to the age of the Universe all the way down to the orbital period of binary stars, which can be in the order of days. The coexistence of such wildly different scales makes the simulation of these systems impractical and sometimes impossible for the standard N-body integrators.

The smallest temporal and spatial scales are found when close encounters between particles occur. Moreover, during close encounters one must deal with very small numbers which can lead to numerical artifacts. Additionally, the large accelerations reached during close encounters cause the particles to acquire timesteps that are too small. This makes im-

possible to follow the evolution of the entire system for scales of Gyr or sometimes even Myr.

It is inevitable to encounter such problems in the field of gravitational dynamics applied to dense stellar systems if one wishes to accurately follow their evolution. Fortunately, the development of a particular algorithm came into help, being capable of greatly increasing the performance of the NBODY6 code (and the NBODY code series presented in Aarseth (1999)). This algorithm is known as the Kustaanheimo-Stiefel (KS) regularization (Kustaanheimo and Stiefel, 1965).

Dealing with binary systems and close encounters is the main goal of the KS regularization. For this, when a close encounter is detected, the particles involved are replaced by a center of mass particle, and the internal motion of the regularized particles is calculated in a new coordinate system. The advantage is that in this new coordinate system an unperturbed binary system is mapped into an harmonic oscillator with double the frequency, greatly reducing the computational cost and numerical errors. For a pair of particles to be regularized they need to fulfill a series of criteria. First the impact parameter must be smaller than the impact parameter for a 90 degree deflection given by

$$p_{90} = 2G \frac{(m_1 + m_2)}{v_\infty^2},$$ (4.13)

where G is the gravitational constant, m_1 and m_2 are the masses of the particles, and v_∞ is their relative velocity at infinity. In NBODY6 the parameter RMIN is used to define the distance of a close encounter and is adjusted to the value of Eq.(4.13) if the option KZ(16)>0.

Second, their timestep must be sufficiently small, as estimated from

$$dt_{\min} = \kappa \left[\frac{\eta}{0.03} \right] \left(\frac{r_{\min}^3}{<m>} \right)^{1/2},$$ (4.14)

where κ is a free numerical factor, η is the general timestep factor, and $<m>$ is the average stellar mass. In practice this limiting timestep is defined for every simulation with the parameter DTMIN.

Once the particles fulfill these two conditions, i.e., that their relative distance is smaller than RMIN and their timestep smaller than DTMIN they are candidates for regularization. However, in order to be actually regularized they need to fulfill two additional criteria. They must be approaching each other and their mutual force be dominant. These additional criteria are defined as

$$\mathbf{R} \cdot \mathbf{V} > 0.1 \sqrt{G(m_1 + m_2)R},$$ (4.15)

$$\gamma \equiv \frac{|\mathbf{a}_{\text{pert}} \cdot R^2|}{G(m_1 + m_2)} < 0.25,$$ (4.16)

where $\mathbf{a}_{\text{pert}}$ is the differential acceleration due to other perturbing particles onto the two candidates, R, $\mathbf{R}$ and $\mathbf{V}$, are the relative distance and relative position and velocity vectors

between the two candidates respectively. A system of two bodies that fulfill these conditions is regularized, with an internal timestep that is independent of the orbital eccentricity, but dependent of the user defined parameter ETAU, resulting in a total of $50-100$ steps per orbit. Once the perturbation parameter defined in Eq.(4.16) falls below a minimum value GMIN (defined by the user, with a typical value equal to 10^{-6}), a KS-pair is considered unperturbed and the analytical solution corresponding to a keplerian orbit is adopted instead of doing a numerical integration. In practice the KS regularization occurs for short-lived hyperbolic encounters and for persistent binaries.

The KS-regularization was later expanded to the isolated 3- and 4-body problem, and finally to the N-body problem. The occurrence of stable triples and quadruples is rare in a simulation, but interactions between single and binaries or binary-binary are common. These interactions are treated with the chain regularization. A typical procedure when a regularized pair encounters a single particle is to consider the regularized pair as a single particle at the center of mass of the pair, and set the mass of these particles to zero. This will define a new KS-regularization with a single particle and a pseudo particle (the center of mass of the previously regularized pair). For encounters of two KS-pairs the procedure is analogous.

4.1.5 Modification of the code

The articles in Chap. 5 and Chap. 6 present an investigation of stellar collisions in dense star clusters. While in NBODY6 the collision between two stars is naturally included when the stellar evolution routines are activated, these were not well suited for the systems under investigation. For this reason a modification of the code was required. This section presents the procedure followed to adopt the necessary changes.

Deactivating the stellar evolution routines

The stellar evolution routines included in NBODY6 are based on a parametrization developed by Hurley et al. (2000) which are in turn based on stellar evolution calculations covering the range of metallicities $Z = 10^{-4}-0.3$ and stellar masses in the range $M = 0.5-50\,\mathrm{M_\odot}$. This is inadequate for the scenarios explored here, in the context of the first star clusters containing Pop. III stars, since their properties are different specially in the protostellar evolutionary phase (see Sec. 3.2.1). For this reason stellar evolution routines were deactivated.

The stellar evolution routines are in charge of initializing the radii of the particles. By deactivating these routines one needs to explicitly define the radius of each particle. For this one can reactivate an old NBODY6 routine contained in the file `intide.f`, which initializes

two stellar populations. To achieve this is necessary to erase a few comments in the routine
start.f. In this file the lines $60 - 62$ were initially commented, so one just needs to erase
the comments such that these lines now read:

```
        IF (KZ(27).GT.0) THEN
          CALL INTIDE
        END IF
```

Once the routine INTIDE is activated it needs to be modified as follows:

```
*              Assign individual radii for main-sequence and evolved stars.
        DO 30=1,N
*              Adopt a primitive scheme in case of no stellar evolution.
         IF (I.LE.IMS) THEN
           RADIUS(I) = RMS*RSTAR
           TEV(I)=10D+10
           SPIN(I)=0
           KSTAR(I)=1
         ELSE
           TEV(I)=10D+10
           SPIN(I)=0
           KSTAR(I)=1
           RADIUS(I) = REV*RSTAR
         END IF
        30 CONTINUE
```

The parameters TEV(I)=10D+10, SPIN(I)=0 and KSTAR(I)=1 for the two stellar popu-
lations are defined in this routine. These new parameters describe the evolutionary epoch
of the stars, the rotation, and the stellar type chosen to be 1 here (main-sequence stars) just
for initialization purposes.

For deactivating the stellar evolution routines one can simply include a return in each
of the associated files. These files are: star.f and hrdiag.f. This will prevent these
routines from modifying the properties of the particles such as mass and radius during the
evolution of the system.

Detecting stellar collisions

In NBODY6 stellar collisions are detected in the regularization routines, specifically in the file `ksint.f`. In this file, the collision criteria is defined based on the paper by Kochanek (1992) who studied the tidal capture process and tidal circularization of binary systems. The criteria for collisions is

$$R_{\text{coll}} = 1.7 \left(\frac{m_1 + m_2}{2m_1} \right)^{1/3} R_1, \tag{4.17}$$

where m_1 and m_2 are the masses of the regularized particles and R_1 is the radius of the particle with mass m_1. In this routine, if the distance between the particles at pericenter R_p is smaller than R_{coll}, the routine `cmbody.f` is called for treating the collision of the particles.

For the articles presented in Chap. 5 and Chap. 6 a different criteria for detecting stellar collisions was adopted. This new condition requires that the separation of the two particles be equal to, or smaller, than the sum of their radii, i.e.,

$$d \leq R_1 + R_2, \tag{4.18}$$

where d is the separation between the particles, and R_1, R_2, their radii. Therefore the criteria for R_{coll} was changed to

$$R_{\text{coll}} = R_1 + R_2. \tag{4.19}$$

For this it was necessary to modify the file `ksint.f` by commenting the line 470 and including a new line such that the file now reads

```
*           RCOLL = 1.7*FAC**0.3333*RADIUS(J1)
            RCOLL = RADIUS(J1) + RADIUS(J2)
```

Outcome of a stellar collision

When the distance between two particles becomes smaller than the distance for a stellar collision defined in Eq.(4.19), the routine to handle the collision `cmbody.f` is called. Here the new mass of the resulting particle is calculated (assuming no mass loss) as

$$M_{\text{new}} = m_1 + m_2. \tag{4.20}$$

The new particle is placed at the center of mass of the previous configuration and the velocity is calculated as

$$\mathbf{v}_{\text{new}} = \frac{m_1 \mathbf{v}_1 + m_2 \mathbf{v}_2}{m_1 + m_2}. \tag{4.21}$$

After switching off the stellar evolution routines the new radius of the star needs to be calculated in a different way. For doing that one can impose the condition that the density of

the stars remains constant, thus the radius of the new star is given by

$$R_{\text{new}} = R_1 \left(\frac{M_1 + M_2}{M_1} \right)^{1/3} . \tag{4.22}$$

These equations must be included in the file `cmbody.f`. The conditions are written in line 308 as:

```
*           Define global c.m. coordinates & velocities from body #I1 & I2
          ZM = BODY(I1) + BODY(I2)
          DO 12 K=1,3
            CM(K) = (BODY(I1)*X(K,I1) + BODY(I2)*X(K,I2))/ZM
            CM(K+3) = (BODY(I1)*XDOT(K,I1) + BODY(I2)*XDOT(K,I2))/ZM
       12 CONTINUE
```

The new radius for the particle must be calculated here. This is done by including in the line 365 of this file the next line:

```
          RADIUS(I1)=(ZM/BODY(I1))**0.3333*RADIUS(I1)
```

Effectively, this assumes that the collision product quickly settles into a new equilibrium configuration in which the density corresponds to that of an unperturbed star of the same mass. Different parameterizations are also possible to include by modifying this line.

Finally, the last step is to make sure that a collision can still be detected provided that the stellar evolution routines were deactivated. Stellar collisions are detected in the file `ksint.f`. The user must therefore ensure that the parameter regulating the minimum distance for regularization is set accordingly, i.e., RMIN$> R_1 + R_2$ for typical stellar radii in the simulation. The file `ksint.f` was modified at lines 439 and 568 as:

```
          "IF(KZ(19).GE.3...."——>"IF(KZ(19).GE.0...."
```

This last change results in the routine `cmbody.f` being called even if the stellar evolution package is not activated (`KZ(19) = 0`).

4.1.6 Input files

The research paper included in Chap. 5 presents the results of simulations of dense star clusters including stellar collisions and an external potential that follows a Plummer density profile. A template of the input file used to reproduce the results of these simulations is presented here:

```
    1 10000.0
    1000 1 10 2390 67 1
    0.02 0.01 0.28 1.0 1.0 3000.0 2.0E02 0.14 10.0
```

```
1 1 1 0 1 0 2 0 2 0
0 0 0 4 1 0 0 0 0 0
1 1 2 0 0 1 2 0 0 0
0 0 0 0 0 0 0 1 0 1
0 0 0 1 0 0 0 0 0 0
1.0E-03 0.001 0.1 1.0 1.0E-06 0.001
1.0 10.0 10.0 0 0 0.0001 0.0 0.0
0.5 0.0 0.0 0.0 0.125
1.0 0.59 10000 10000
1.0 1000 0 100.0 1.0
```

This input file was used to perform a simulation with 1000 particles, each of them with an initial mass of 10 $M_\odot$ and initial radius of 100 $R_\odot$. The last line in this input file contains the parameters required by `intide.f`, and includes the radius of a typical star in solar units RSTAR, the number of idealized main-sequence stars IMS, the number of idealized evolved stars IEV, the scale factor for main-sequence stars RMS and the scale factor for evolved stars REV. These scale factors are used to set the radius of these stellar populations as

$$R = \text{RMS} \times \text{RSTAR},$$
$$R = \text{REV} \times \text{RSTAR}.$$

The velocities of the stars are adjusted so that the system is in virial equilibrium. An external potential which follows a Plummer density distribution is included by setting the option KZ(14)=4. The properties of the external potential are defined in the line number 12, which specifies the mass of the external potential in N-body units, the scale length of the Plummer potential in N-body units, and two timescales related to gas expulsion also in N-body units. These timescales are set to a value much larger than the final time of the simulations so that no gas expulsion takes place. A rather high value for RMIN is set to make sure that particles are regularized before their mutual distance becomes smaller than the sum of their radii.

For the research paper presented in Chap. 6, the simulations did not include an external potential and the effects of tidal circularization were deactivated. The input file for one of the simulations with 5000 particles, each with a radius of 20 $R_\odot$ is:

```
1 10000.0
5000 1 10 9683 140 1
0.02 0.01 0.27 1.0 1.0 2000.0 2.0E02 0.14 2.0
```

```
1 1 1 0 1 0 2 0 2 0
-1 0 0 0 1 0 0 0 0 0
1 1 2 0 0 1 0 0 0 0
0 0 0 0 0 0 0 1 0 1
0 0 0 1 0 0 0 0 0 0
1.0E-03 0.001 0.05 1.0 1.0E-06 0.001
1.0 2.0 2.0 0 0 0.0001 0.0 0.0
0.5 0.0 0.0 0.0 0.125
1.0 5000 0 20.0 1.0
```

4.2   The AMUSE framework

For the third article included in this thesis, the cornerstone of the methodology was the use of the Astrophysical Multipurpose Software Environment (AMUSE[2]) (Portegies Zwart and McMillan, 2018), which is a PYTHON interface specially designed with the aim of allowing an easy coupling of existing astrophysical simulation codes.

The existing codes included in AMUSE are called community codes, and can be generally (but not always) classified into four main domains : Gravitational dynamics, Hydrodynamics, Stellar evolution, and Radiative transport (see Fig. 4.3). One can argue that some of the codes that exist in AMUSE cover more than one of these domains, as is the case of GADGET-2 (Springel, 2005a) which covers gravitational dynamics and hydrodynamics. Another example is the code NBODY6 (Aarseth, 1999; Nitadori and Aarseth, 2012), which covers gravitational dynamics and stellar evolution. However, one can recognize that while these codes are designed to tackle specific problems (Galaxy formation at cosmological scales in GADGET-2, or star cluster evolution in NBODY6), the numerical implementation that they offer can be combined with others in order to investigate new problems.

The AMUSE interface is written in PYTHON because of its flexibility and widespread use in the scientific community. This choice enables easy access to the community codes and relatively easy development of new software and simulation scripts. On the other hand, the community codes encompass a diverse set of programming languages that includes FORTRAN, C, CUDA and JAVA.

The structure of AMUSE can be divided into three main parts, as illustrated in Fig. 4.4. The first one is the top layer, where the user writes a PYTHON script. This script contains all that is needed to run a simulation and is usually specific to a single problem. In this script the user defines the initial conditions, manages unit conversion, and develops the coupling of

---

[2]AMUSE can be obtained from github: https://github.com/amusecode/amuse
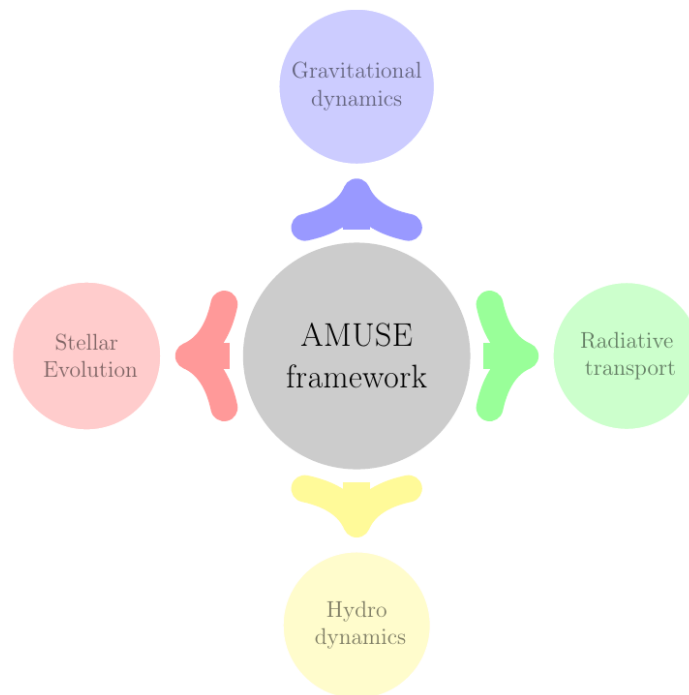
Figure 4.3. The main four domains into which most of the astrophysical codes contained in AMUSE can be classified. Credits: AMUSE user manual (Portegies Zwart and McMillan, 2018).

the different codes needed for the problem under investigation. In this layer, also a manager is present, which takes care of unit conversion between the user input data and the data passed to the community code. The manager also takes care of the data structure before passing it to the community code.

The second layer (middle blue layer in Fig. 4.4) is where the interface between the AMUSE framework and the community codes lies. The AMUSE interface for each code consists of two parts, one being a PYTHON file, called the proxy, that contains all the functions needed to use a given community code. The other file is called the partner and is written in the native language of the community code. These two interfaces communicate via the Messaging Passing Interface (MPI) whether or not they reside on the same node as the PYTHON script.

The third layer (bottom green layer in Fig. 4.4) is where the community code resides, in its native language. Here is where all the files specific to every code are contained. In an ideal AMUSE simulation, the user would never dig into the deepest layer of the framework, but it is strictly necessary sometimes, as it was for the work presented in Chap. 7. Note that the user is capable of easily utilizing any of the codes contained in the AMUSE framework with little to no knowledge of the code, which can be catastrophic. An adequate previous research of the codes needed is always advised.
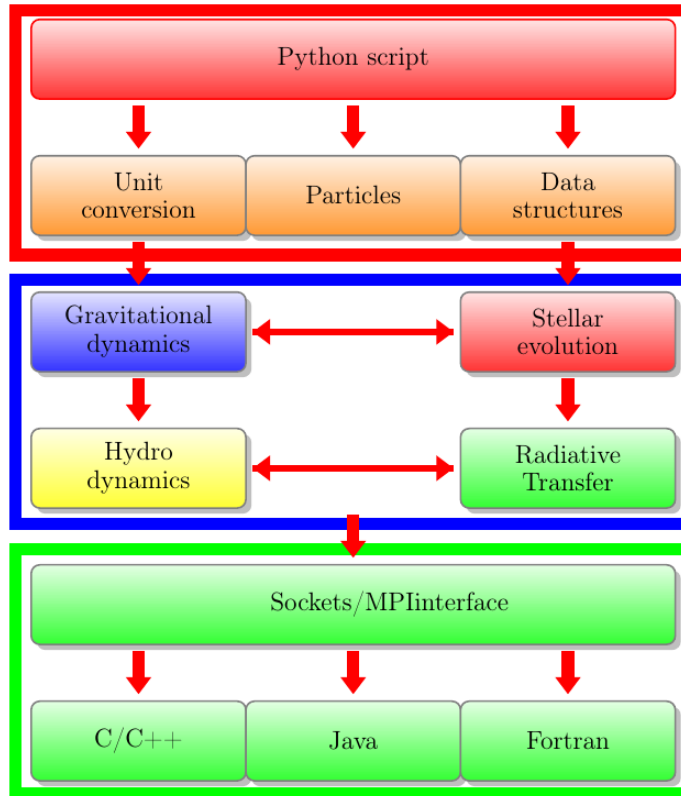
Figure 4.4. Illustration of the basic structure of AMUSE. The top red layer contains the PYTHON script written by the user. The middle blue layer represents the interface to the community codes. The bottom green layer is where the communication between the AMUSE framework and the community codes happen. The information flows as indicated by the red arrows from the user script down to the community codes, and also backwards to the Python script. Credits: AMUSE user manual (Portegies Zwart and McMillan, 2018).

With the help of the AMUSE interface the emergence of supermassive stars following the fragmentation of a gas cloud at sub-parsec scales was studied. Supermassive stars can reach extremely large sizes of up to 10^4 $R_\odot$ (Hosokawa et al., 2013). However, Before reaching that point a protostar is formed with only 0.1 $M_\odot$ initially (Becerra et al., 2018). Depending on their mass accretion rate they might or not reach the supermassive state, and, depending on the level of fragmentation of the cloud, not only one but many protostars might end up evolving as SMSs.

Therefore, the possibility of creating such big objects in a small space implies the possibility of frequent collisions, which in turn requires including an accurate dynamical treatment that is able to precisely capture the close encounters among these objects. For this reason, a pure N-body code is a good choice for dealing with this problem. Moreover, the gas must be also accurately modelled since the accretion rate of the protostars and their subsequent evolution will depend on the dynamics of this fluid as well. A straightforward

choice for this is a particle code for the hydrodynamics because it can be coupled to the N-body code more easily, therefore an SPH code was the natural choice for this problem.

The main idea of this section is to provide an insight into the codes utilized for running the simulations that produced the results presented in Chap. 7. For this end, the next sections introduce some of the most important characteristics of the numerical implementation developed for this work.

4.2.1   The N-body code PH4

The N-body code PH4 is a pure N-body code, which means that it calculates the gravitational force between the particles without approximations like the Neighbour scheme (or Ahmad-Cohen scheme) of the last versions of the NBODY code series (Aarseth, 1999), or the grouping of distant particles like Tree codes (Barnes and Hut, 1986).

Just like NBODY6, this N-body code makes use of the fourth order Hermite integrator described in Sec. 4.1.1. In the following the treatment of stellar collisions with PH4 is presented, followed by a description of the softening length adopted and the calculation of timesteps for the particles.

Stellar collisions

Each particle in PH4 has an attribute called `radius`. After every integration step, a function is called to detect particles whose radii overlap in space. In the AMUSE implementation of PH4, a stopping condition can be activated. This stopping condition interrupts the integration of PH4 once a radii overlap has been detected. Then, at the AMUSE level, one can decide the faith of the colliding particles. For this work the "sticking star" approximation was adopted, i.e., once the radii of two particles overlap, they are replaced by a single particle at the center of mass of the previous configuration. Therefore the position for the resulting particle is given by

$$\boldsymbol{r}_{\text{new}} = \frac{m_1\boldsymbol{r}_1 + m_2\boldsymbol{r}_2}{m_1 + m_2}, \tag{4.23}$$

and no mass loss during the collisions is assumed, so the new mass is

$$m_{\text{new}} = m_1 + m_2. \tag{4.24}$$

The new velocity of the resulting particle is calculated assuming linear momentum conservation as

$$\boldsymbol{v}_{\text{new}} = \frac{m_1\boldsymbol{v}_1 + m_2\boldsymbol{v}_2}{m_1 + m_2}. \tag{4.25}$$

Softening length and timestep

PH4 makes use of a softening length ϵ. The objective of introducing ϵ is to prevent extreme values of the gravitational force when the separation between two particles is very small. The magnitude of the gravitational force between two particles is calculated as

$$F = G\frac{m_1 m_2}{(\,|\mathbf{r}_{1,2}|^2 + \epsilon^2\,)^{3/2}}, \tag{4.26}$$

where m_1 and m_2 are the masses of the particles and $|\mathbf{r}_{1,2}|$ is their separation. In this study it was necessary to accurately resolve close encounters between the particles given the collisional nature of the system under investigation. For this reason the use of a small smoothing length of $\epsilon = 1\ \mathrm{R}_\odot$ was the choice.

Given that most of the close encounters involve a supermassive star with a radius of roughly $10^4\ \mathrm{R}_\odot$, no long-lived hard binaries are present in the simulations, and the problem of prohibitively small timesteps is not encountered, despite the choice of ϵ.

In PH4 the timestep calculation makes use of the higher-order derivatives of the acceleration used in the Hermite integrator scheme presented in Sec. 4.1.1. The equation used is

$$dt_{\mathrm{new}} = \eta\ dt\ \left(\frac{aa^{(2)} + \dot{a}}{[\,\dot{a}a^{(3)} + a^{(2)}\,]dt^2}\right)^{1/2}, \tag{4.27}$$

where dt is the old timestep, η is a parameter that controls the value of the new timestep and the acceleration terms are the ones descirbed in Sec. 4.1.1. The default value of $\eta = 0.14$ was adopted.

4.2.2   The SPH code FI

For the simulations presented in Chap. 7, the code FI (Gerritsen and Icke, 1997) was used. This code was designed for studies of the Interstellar Medium on galactic scales and was largely inspired by GADGET-2 code (Springel, 2005a). FI is a Smoothed Particle Hydrodynamics (SPH) code and is described in more detail in Pelupessy (2005).

Smoothed Particle Hydrodynamics (SPH) is a technique that was invented in 1977 (Gingold and Monaghan, 1977; Lucy, 1977). This method solves the equations of hydrodynamics in a Lagrangian approach by using a set of discrete points that move with the fluid velocity and map it during its evolution. A smoothing is applied to every SPH particle through a kernel function which can be thought of as if the particle was extended in space, and its properties determined by the contribution of all the particles that fall within its smoothing volume as illustrated in Fig. 4.5.

The SPH technique has found wide application across important areas of astrophysics, being employed in studies of turbulence (Kitsionas et al., 2009; Price et al., 2011), star (cluster) formation (Bate et al., 2003; Bonnell et al., 2003; Wurster et al., 2017), stellar collisions

$$W(|\boldsymbol{r}_i\text{-}\boldsymbol{r}_j|, h)$$
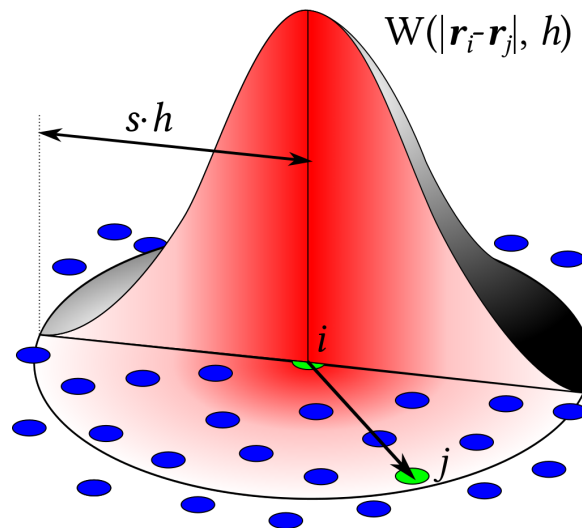
Figure 4.5. Illustration of the SPH smoothing kernel. Credits: https://commons.wikimedia.org/wiki/File:SPHInterpolationColorsVerbose.svg

(Freitag and Benz, 2005; Laycock and Sills, 2005), and for cosmological simulations of structure formation (Springel, 2005b), just to name a few.

Still the gravitational interactions must be calculated for the set of SPH particles when self-gravity cannot be neglected. The long range nature of this force poses an obstacle to the performance of an SPH code if every pair of particle-particle interaction is to be computed. Fortunately this problem is solved by employing a hierarchical multipole expansion, for example with the popular Tree algorithm (Barnes and Hut, 1986). The idea consist in grouping distant particles together into a single one for calculating the gravitational force, reducing the cost from N^2 to $N \log(N)$. Such a combination of Tree and SPH codes is also called a TREESPH code (Hernquist and Katz, 1989).

Self-gravity

FI includes self-gravity by employing a Barnes-Hut Tree algorithm (Barnes and Hut, 1986) for computing the gravitational forces. This method relies on a recursive division of the space, starting from a cubical root-node that encompasses the entire mass distribution and further dividing each node into eight daughter-nodes (an oct-tree) until every particle is enclosed by a single node. The gravitational force for each particle is then computed by walking the tree, starting from the root-node and making a decision on whether the multipole approximation provides a force that is sufficiently accurate. If accuracy is good enough, then the force is used and the walk along the current branch can be terminated, on the contrary if the accuracy is not sufficient, the node is opened and the process is repeated for each of its daughter-nodes. The required accuracy is controlled by an input parameter α, and depends on the calculated acceleration at the previous time-step $|\boldsymbol{a}|$, the mass of the node M, the

side-length of the node l, and the distance to the node r in the form

$$\frac{GM}{r^2}\left(\frac{l}{r}\right)^2 \leq \alpha |\boldsymbol{a}|. \tag{4.28}$$

If this condition is fulfilled, the node is used for the force calculation. The default value of $\alpha = 0.5$ was adopted here.

Hydrodynamics

An important aspect of every SPH code is the kernel function employed. FI makes use of the popular cubic spline kernel (Monaghan and Lattanzio, 1985a) just like many other SPH codes in astrophysics (GADGET-2, PHANTOM, SEREN). The cubic spline kernel is given by

$$W(r,h) = \frac{8}{\pi h^3} \begin{cases} 1 - 6\left(\frac{r}{h}\right)^2 + 6\left(\frac{r}{h}\right)^3, & 0 \leq \frac{r}{h} < \frac{1}{2}, \\ 2\left(1 - \frac{r}{h}\right)^3, & \frac{1}{2} \leq \frac{r}{h} \leq 1, \\ 0, & \frac{r}{h} > 1, \end{cases} \tag{4.29}$$

where h is the smooting length of the SPH particle and r a distance to another point in space.

Of fundamental importance in every SPH code is the computation of the density for every particle, which in FI is calculated as

$$\rho_i = \sum_{j=1}^{N} m_j W(|r_{ij}|, h_i), \tag{4.30}$$

where m_j is the mass of particle j, $W(|r_{ij}|, h_i)$ is the kernel function that depends on the distance between particle i and particle j, $|r_{ij}|$; and the smoothing length of particle i, h_i. The sum is over all the neighbours j of i. The dynamic range of conventional SPH is improved here by the use of adaptive smoothing lengths. The smoothing length for each particle is obtained by requiring a constant mass inside the smoothing volume. This is mathematically written as

$$\frac{4\pi}{3} h_i^3 (\rho_i + \tilde{\rho}) = N\overline{m}, \tag{4.31}$$

slightly different to the approach adopted in GADGET-2 since an additional term $\tilde{\rho}$ is included in order to put an upper limit to the smoothing length h_i.

The equation that determines the acceleration of particle i given the contribution to the pressure gradients and viscous forces from all its neighbours j is given by

$$\frac{dv_i}{dt} = -\sum_{j=1}^{N} m_j \left[f_i \frac{P_i}{\rho_i^2} \nabla_i W_{ij}(h_i) + f_j \frac{P_j}{\rho_j^2} \nabla_i W_{ij}(h_j) + \Pi_{ij} \nabla_i \overline{W}_{ij} \right], \tag{4.32}$$

where P_i and ρ_i are the pressure and density of particle i. The notation used by Pelupessy (2005) was adopted so that $W_{ij}(h_i) = W(|r_i - r_j|, h_i)$. The term $\nabla_i W_{ij}(h_i)$ is computed as

$$\nabla_i W_{ij}(h_i) = \frac{r_i - r_j}{|r_i - r_j|} \frac{\partial_i W(r, h_i)}{\partial r}. \tag{4.33}$$

The term $\overline{W}_{ij} = \frac{1}{2}[W_{ij}(h_i) + W_{ij}(h_j)]$ is a symmetrized form of the kernel function, and f_i is given by

$$f_i = \left(1 + \frac{h_i}{3(\rho_i + \tilde{\rho})} \frac{\partial \rho_i}{\partial h_i}\right)^{-1}. \tag{4.34}$$

The term Π_{ij} is an artificial viscosity term which in SPH codes is necessary for capturing shocks. This term is given by

$$\Pi_{ij} = \begin{cases} \dfrac{-\alpha c_{ij}\mu_{ij} + \beta\mu_{ij}^2}{\rho_{ij}} & \text{if } \boldsymbol{v}_{ij} \cdot \boldsymbol{r}_{ij} < 0 \\ 0 & \text{otherwise}, \end{cases} \tag{4.35}$$

with

$$\mu_{ij} = \frac{h_{ij}\boldsymbol{v}_{ij} \cdot \boldsymbol{r}_{ij}}{(r_{ij}^2 + \epsilon h_{ij}^2)}. \tag{4.36}$$

Here h_{ij} is the arithmetic mean of the smoothing lengths of particles i and j. In FI, c_{ij} is taken to be the maximum sound speed among particles i and j, and ρ_{ij} is the minimum density among them. Note that a smoothing term ϵh_{ij}^2 is introduced in Eq.(4.36) in order to prevent a divergence of the viscous force for very small particle separations, with $\epsilon = 0.01$. The parameters α and β regulate the strength of the viscosity and in FI are set to $\alpha = 0.5$, $\beta = 1.0$.

Finally, the energy equation in FI is given by

$$\frac{du_i}{dt} = \frac{1}{2}\sum_{j=1}^{N} m_j \left[f_i \frac{P_i}{\rho_i^2} v_{ij} \cdot \nabla_i W_{ij}(h_i) + f_j \frac{P_j}{\rho_j^2} v_{ij} \cdot \nabla_i W_{ij}(h_j) + \Pi_{ij} v_{ij} \cdot \nabla_i \overline{W}_{ij} \right]. \tag{4.37}$$

There exists the possibility to follow the entropy evolution rather than the internal energy evolution, just like is done in GADGET-2 (Springel, 2005a), and to include additional heating and cooling terms. The internal energy formulation was adopted here and no heating or cooling terms were included in the simulations presented in Chap. 7.

Necessary modifications

In order to carry-on the simulations presented in Chap. 7 it was necessary to modify the code. The first modification described here is related to the adaptation of the momentum equation in order to include the effects of an external pressure. This is necessary to prevent the evaporation of the cloud when using vacuum boundary conditions. Inspired by the work

of Clark et al. (2011b) an additional pressure was included. This pressure effectively acts upon SPH particles that are not surrounded by neighbouring SPH particles, i.e., the particles at the border of the cloud. For this end an additional term P_{ext} was included in Eq.(4.32) as

$$\frac{dv_i}{dt} = -\sum_{j=1}^{N} m_j \left[f_i \frac{(P_i - P_{ext})}{\rho_i^2} \nabla_i W_{ij}(h_i) + f_j \frac{(P_j - P_{ext})}{\rho_j^2} \nabla_i W_{ij}(h_j) + \Pi_{ij} \nabla_i \overline{W}_{ij} \right].$$

(4.38)

These changes must be included in the file `entdot.f90`, which is inside the folder `.../amuse/src/amuse/community/fi/src/`.

The second necessary modification is related to the equation of state adopted by FI. The default values for the AMUSE version of FI are set in such a way that the equation of state is adiabatic with $\gamma = 5/3$, and the entropy evolution is followed instead of the internal energy evolution. The equation of state that needs to be included for this work has the form

$$T = T_0 \left[1 + \left(\frac{\rho}{\rho_c} \right)^{\gamma - 1} \right],$$

(4.39)

so that it is isothermal but changes to an adiabatic EOS for densities higher than ρ_c. As discussed in Sec. 4.3.2 the values $\rho_c = 10^{15}$ g cm^{-3}, and $T_0 = 8000$ K were used. In order to include this modification in FI it was necessary to modify the subroutines that extrapolate the specific thermal energy of the SPH particles.

This modification is particularly easy as one only needs to modify the file `ethstep.f90`. Here, in the subroutines `extrapeth` and `exstep2`, right after the line

```
call exstepp(p,dt,eth,deth,drad,lerad,lhe,imax,jmax)
```

one needs to include the next line

```
eth=a*(1. + (rho(p)/b)**gamma1)
```

where `a` and `b` are the thermal energy per unit mass and critical density, in code units.

4.2.3 SPH and N-body coupling

For the set of simulations presented in Chap. 7 the coupling of an SPH and an N-body code was required. The coupling is easier since both are particle codes, and although the script examples included in AMUSE are a good starting point, adequate numerical modelling of this problem requires extra effort. This section describes the procedure followed for the coupling of the N-body code PH4 and the SPH code FI, using the BRIDGE method.

Coupling strategy

Just like in the classical BRIDGE described in Fujii et al. (2007) one first needs a way of calculating the gravitational interaction between the different particles, in this case the N-body and the SPH particles. AMUSE includes an example script in which a hydrodynamics code is coupled with an N-body code. This example can be found in

<div align="center">

`amuse/examples/simple/gas_in_cluster.py`

</div>

and it models the evolution of an embedded star cluster by coupling the SPH code GADGET-2 with the N-body code HERMITE. The coupling is realized by utilizing the BRIDGE method of AMUSE. This works as follows

- At t_0 calculate the acceleration on each N-body particle due to all SPH particles using the function `get_gravity_at_point(eps,x,y,z)` of the SPH code, with the gravitational softening length `eps`, and the position of each N-body particle.

- At t_0 construct a tree for the N-body particles, and use it to calculate the acceleration on every SPH particle due to all N-body particles by utilizing the function `get_gravity_at_point(eps,x,y,z)`, and setting `eps` to be equal to the smoothing length of each SPH particle.

- Kick the velocity of every particle with the calculated acceleration during half a time-step.

- Drift the particles during a full timestep by updating their positions and velocities with the corresponding code, i.e., the leapfrog algorithm of GADGET-2 for the SPH particles, and the fourth order Hermite algorithm of HERMITE for the N-body particles.

- At $t_0 + \delta t$ calculate the acceleration on each N-body particle using the function `get_gravity_at_point(eps,x,y,z)` of the SPH code with the softening length `eps`, and updated position of every N-body particle.

- At $t_0 + \delta t$ construct a tree for the N-body particles, and use it to calculate the acceleration at the updated position of every SPH particle with the function `get_gravity_at_point(eps,x,y,z)` by setting `eps` equal to the updated smoothing length of the SPH particles.

- Finish the timestep by kicking the particles of each code during a half-timestep with the new accelerations.

The problem with this procedure lies in the method used for the calculation of gravitational interactions between the particles of different codes. When particles have different

gravitational softening lengths an effective softening length should be considered. This effective softening length must maintain a symmetry of the calculated forces and the conservation of momentum.

To better understand the problem introduced by this method consider a pair of point masses, one SPH particle and one N-body particle, with gravitational softening lengths h and ϵ respectively. Consider also the calculation of the gravitational force with Plummer softening. When calculating the force on the N-body particle due to the SPH particle one obtains a force with magnitude

$$F_{\text{SPH},N-\text{body}} = \frac{Gm_{\text{SPH}}m_{N-\text{body}}}{\left(r_{\text{SPH},N-\text{body}}^2 + \epsilon^2\right)^{3/2}}|r_{\text{SPH},N-\text{body}}|. \tag{4.40}$$

On the other hand, when calculating the force on the SPH particle due to the N-body particle, the magnitude of the force is

$$F_{N-\text{body},\text{SPH}} = \frac{Gm_{N-\text{body}}m_{\text{SPH}}}{\left(r_{\text{SPH},N-\text{body}}^2 + h^2\right)^{3/2}}|r_{\text{SPH},N-\text{body}}|. \tag{4.41}$$

When $h \neq \epsilon$ it is evident that

$$F_{\text{SPH},N-\text{body}} \neq F_{N-\text{body},\text{SPH}}. \tag{4.42}$$

This problem is illustrated in Fig. 4.6.

Employing the same gravitational softening length for all the particles would not solve the problem if the codes make use of different softening algorithms for the force calculation. For many SPH codes it is frequent to employ a cubic spline smoothing, whereas for N-body codes the Plummer softening is the preferred choice. The difference in the magnitude of the gravitational force calculated with Plummer softening and a cubic spline kernel is shown in Fig. 4.7.

This problem was tackled by using another code for calculating the gravitational interactions between the SPH and N-body particles. The code chosen is FASTKICK and utilizes a particle-particle force calculation with Plummer softening. For the force calculation a constant softening length of $\epsilon = 0.5$ AU was set, which is equal to the minimum smoothing length among the SPH particles. The new force calculation scheme is illustrated in Fig. 4.8. This constant softening length for the gravitational force calculation is adopted only for the gravitational interaction between N-body and SPH particles. Inside the N-body code PH4, the force between the N-body particles is calculated using Plummer softening with a constant softening length of $\epsilon = 1\,\text{R}_\odot$, which provides the necessary accuracy for treating close encounters between all the particles. On the other hand, the gravitational force calculation in the SPH code (due to self-gravity) is done via a Tree algorithm and employing the cubic spline smoothing as explained in Sec. 4.2.2.
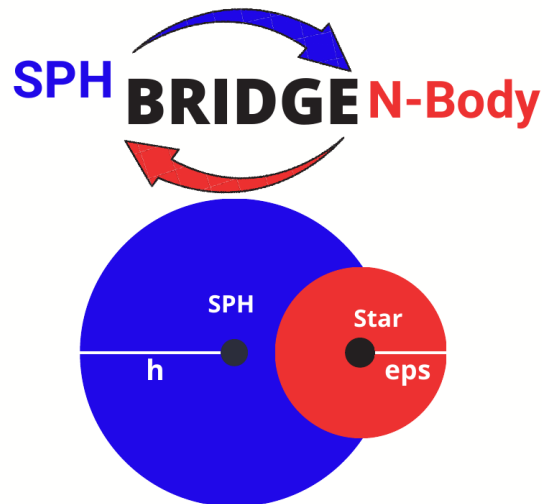
Figure 4.6. Illustration of the usual coupling strategy between SPH and N-body codes employed in AMUSE. Black dots represent the point masses. The blue circle represents the smoothing volume of the SPH particle, with a smoothing length h. The red circle represents the softening volume of the N-body particle, with a softening length eps. The difference in the softening lengths of SPH and N-body particles poses a problem of force asymmetry in the standard AMUSE coupling.
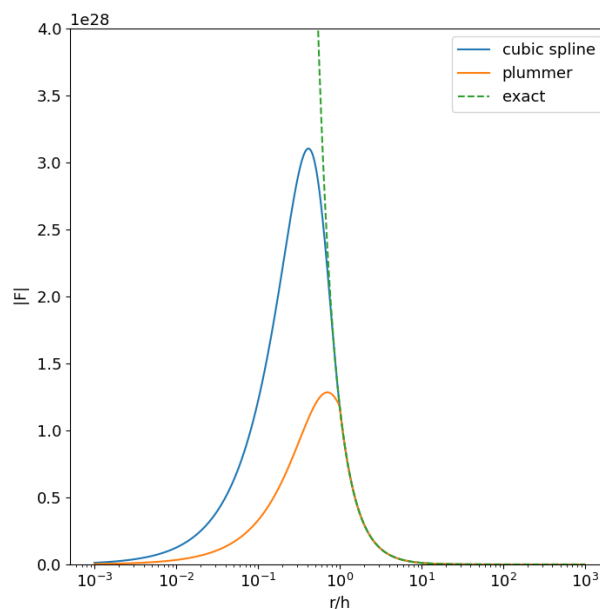
Figure 4.7. Illustration of the difference in the magnitude of the gravitational force between two particles when using a Plummer softening kernel (orange line), a cubic spline (blue line), or no softening at all (green dashed line). The x-axis shows the particle separation in units of the smoothing length. The force in the y-axis is shown in arbitrary units.
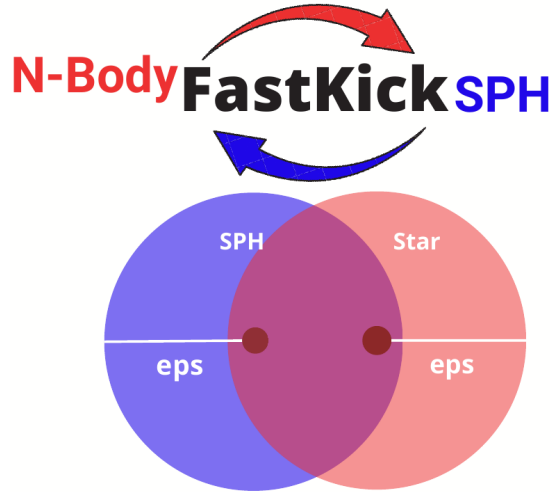
Figure 4.8. Illustration of the new coupling strategy adopted in this work. The black dots represent the point particles. The blue circle represents the smoothing volume of the SPH particle for the force calculation. The red circle represents the softening volume of the N-body particle for the force calculation. A constant softening length eps was adopted for every particle.

The integration scheme

After presenting the improved N-body-SPH coupling described in Sec. 4.2.3, this section continues with a description of the integration scheme adopted in the simulations. The system modelled approximates an embedded star cluster during the early stages of formation, when protostars are still being formed. The system is therefore comprised of a gas cloud (mapped with SPH particles), and a small star cluster of N-body particles, which are called protostars here. One integration step from time t_0 to time $t_0 + \delta t$ is based on the BRIDGE method and therefore consists of a Kick-Drift-Kick scheme that proceeds as follows:

- **Kick the particles:** Calculate the gravitational acceleration $\mathbf{a}_{\mathrm{SPH}, N-\mathrm{body}}$ on each SPH particle due to all protostars by making use of the FASTKICK code with a constant softening length of $\epsilon = 0.5$ AU. Calculate also the gravitational acceleration $\mathbf{a}_{N-\mathrm{body}, \mathrm{SPH}}$ on each protostar due to all SPH particles by making use of the FASTKICK code with a constant softening length of $\epsilon = 0.5$ AU.

  Kick the velocity of each SPH particle for half a timestep by doing $\mathbf{v}_{\mathrm{SPH}} = \mathbf{v}_{\mathrm{SPH}} + 0.5 \times \mathbf{a}_{\mathrm{SPH}, N-\mathrm{body}} \times \delta t$. Kick also the velocity of each protostar for half a timestep by doing $\mathbf{v}_{\mathrm{protostar}} = \mathbf{v}_{\mathrm{protostar}} + 0.5 \times \mathbf{a}_{N-\mathrm{body}, \mathrm{SPH}} \times \delta t$.

- **Drift the particles:** For the SPH set, drift the particles for a full timestep with the FI code (see Sec.4.2.2). For the protostar set, drift the particles for a full timestep with the PH4 code (see Sec.4.2.1). During this step, stellar collisions can occur and are solved as described in Sec. 4.2.1.

- **Kick the particles:** Calculate the gravitational acceleration $\mathbf{a}_{\text{SPH},N-\text{body}}$ on each SPH particle due to all protostars by making use of the FASTKICK code with a constant softening length of $\epsilon = 0.5$ AU. Calculate also the gravitational acceleration $\mathbf{a}_{N-\text{body},\text{SPH}}$ on each protostar due to all SPH particles by making use of the FASTKICK code with a constant softening length of $\epsilon = 0.5$ AU.

  Kick the velocity of each SPH particle for half a timestep by doing $\mathbf{v}_{\text{SPH}} = \mathbf{v}_{\text{SPH}} + 0.5 \times \mathbf{a}_{\text{SPH},N-\text{body}} \times \delta t$. Kick also the velocity of each protostar for half a timestep by doing $\mathbf{v}_{\text{protostar}} = \mathbf{v}_{\text{protostar}} + 0.5 \times \mathbf{a}_{N-\text{body},\text{SPH}} \times \delta t$.

4.2.4   Additional algorithms

Given that the goal of the research presented in Chap. 7 was the modelling of a cluster of accreting protostars while capturing the collisions between them, it was of fundamental importance to include a physically motivated recipe for gas accretion, since the high accretion rates found in that environment have a crucial impact on the size of the protostars as explained in Sec.3.2.2 and 3.5. An adequate treatment of gas accretion, mass-radius relations and collisions was therefore essential. This section describes the additional algorithms employed that allow an adequate treatment of the evolution of this system including these effects.

Gas accretion

An adequate treatment for the mass accretion onto the protostars is crucial when their radii depend on this, which in turn directly affects the collision probability between accreting protostars. Recently Hubber et al. (2013b) developed an algorithm for sink particle creation and gas accretion, which is specially suited for SPH codes. This novel accretion recipe introduces an interaction zone which is the main difference with previous algorithms. This interaction zone consist of a spherical volume around the accreting sink particle. We will refer to the radius of this interaction zone as interaction radius. Inside the interaction zone, the SPH particles contribute to the calculation of two important timescales for mass accretion, namely the radially symmetric accretion timescale t_{rad} and the disk accretion timescale t_{disk}. Each of these timescales is calculated as a weighted mean of the contribution of each SPH particle inside the interaction zone, and the weights are obtained with a kernel function which was chosen here to be the cubic spline from Monaghan and Lattanzio (1985b) as

implemented in FI, and given by

$$W(r,h) = \frac{8}{\pi h^3} \begin{cases} 1 - 6\left(\frac{r}{h}\right)^2 + 6\left(\frac{r}{h}\right)^3, & 0 \le \frac{r}{h} \le \frac{1}{2}, \\ 2\left(1 - \frac{r}{h}\right)^3, & \frac{1}{2} \le \frac{r}{h} \le 1, \\ 0. & \frac{r}{h} > 1. \end{cases} \qquad (4.43)$$

In the following a detailed description of the gas accretion algorithm is presented, as implemented in the simulations.

Spherically symmetric accretion

The mass inflow rate inside a volume delimited by the surface **S** can be calculated as:

$$\frac{dm}{dt} = -\int_S \rho \mathbf{v} \cdot \mathbf{dS}, \qquad (4.44)$$

where $\frac{dm}{dt}$ is the mass inflow rate and ρ is the density of the mass element passing through the surface element $\mathbf{dS}$ with velocity $\mathbf{v}$. Spherical symmetry is assumed in order to derive the expression

$$\dot{M}(r) = -4\pi r^2 \rho(r) v_{\text{rad}}(r). \qquad (4.45)$$

Now following Hubber et al. (2013b), one can compute a weighted mean accretion rate from the SPH particles that lie inside the interaction zone of sink s as

$$\dot{M}_s = -4\pi \sum_j |\Delta r_{js}| \Delta r_{js} \cdot \Delta v_{js} m_j W(|\Delta r_{js}|, R_s), \qquad (4.46)$$

where $\Delta r_{js} = \mathbf{r_j} - \mathbf{r_s}$ is the relative position of the SPH particle j with respect to the sink s, $\Delta v_{js} = \mathbf{v_j} - \mathbf{v_s}$ their relative velocity, and R_s is the interaction radius of the sink s. If one now computes the total mass M_{int} of all the SPH particles inside the interaction zone and divide it by Eq.(4.46), one obtains the timescale in which all that mass would be accreted. The spherically symmetric accretion timescale is then computed as

$$\langle t_{\text{rad}} \rangle = -\frac{\sum_j \{m_j\} W_{\text{norm}}}{4\pi \sum_j |\Delta r_{js}| \Delta r_{js} \cdot \Delta v_{js} m_j W(|\Delta r_{js}|, R_s)}, \qquad (4.47)$$

with

$$W_{\text{norm}} = \frac{\sum_j m_j W(|\Delta r_{js}|, R_s)}{\rho_j}. \qquad (4.48)$$

Disk accretion

One can also calculate a disk accretion timescale using the prescription for viscous disks developed by Shakura and Sunyaev (1973) which is based on the parametrization of the

angular momentum transport mechanisms in a gaseous thin disk by a single parameter α_{SS}. Following Hubber et al. (2013b), one can compute a weighted mean disk accretion timescale form the contribution of all the SPH particles inside the interaction zone and using the kernel function defined in Eq.(4.43). This disk accretion timescale is given by

$$\langle t_{\text{disk}} \rangle = \frac{(GM_s)^{1/2}}{\alpha_{SS} W_{\text{norm}}} \sum_j \left\{ \frac{|\Delta r_{js}|^{1/2} m_j W(|\Delta r_{js}|, R_s)}{\rho_j c_{s,j}^2} \right\}, \tag{4.49}$$

where M_s is the mass of the sink particle, ρ_j is the density of the SPH particle j, and $c_{s,j}$ its sound speed. As in Hubber et al. (2013b) the default value of $\alpha_{SS} = 0.01$ was used.

Timescale for accretion

Once the two timescales have been computed, it is necessary to decide the timescale that will be actually employed for the gas accretion. The timescale is chosen based on a comparison of the rotational energy and the gravitational energy of the SPH particles inside the interaction zone. The timescale for accretion is finally given by

$$t_{\text{acc}} = \langle t_{\text{rad}} \rangle^{(1-f)} \langle t_{\text{disk}} \rangle^f, \tag{4.50}$$

$$f = \min\left(\frac{2E_{\text{rot}}}{|E_{\text{grav}}|}, 1 \right). \tag{4.51}$$

In this case E_{rot} and E_{grav} are the net rotational and gravitational energy of the SPH particles inside the interaction zone, relative to the point mass. These energies are calculated as

$$E_{\text{rot}} = \frac{|\mathbf{L}_{\text{int}}|^4}{2 \sum_j m_j |\Delta \mathbf{r}_{js} \cdot \mathbf{L}_{\text{int}}|^2}, \tag{4.52}$$

$$E_{\text{grav}} = \frac{GM_s}{2} \sum_j m_j \left\{ \phi(|\Delta \mathbf{r}_{js}|, R_s) + \phi(|\Delta \mathbf{r}_{js}|, h_j) \right\}$$
$$+ \frac{G}{4} \sum_j \sum_{j' \neq j} m_j m_{j'} \left\{ \phi(|\Delta \mathbf{r}_{jj'}|, h_j) + \phi(|\Delta \mathbf{r}_{jj'}|, h_{j'}) \right\}, \tag{4.53}$$

where $\mathbf{L}_{\text{int}}$ is the total angular momentum of the the SPH particles inside the interaction zone with respect to the point mass s, and $\phi(|\mathbf{r}|, h)$ is the kernel function for the gravitational potential.

The first term of the gravitational energy makes use of an average of the potential considering two softening lengths, the one of the sink particle R_s and the one of the SPH particle h_j. The same applies to the second term, which takes into account the interaction among all the pairs of SPH particles j and j' inside the interaction zone. The potential is calculated with a formula derived from the kernel function. For the kernel defined in Eq.(4.43), the

gravitational potential is given by (see derivation in Apendix A)

$$
\phi(r, h) = -\frac{32}{h} \begin{cases} \frac{1}{6}\left(\frac{r}{h}\right)^2 - \frac{3}{10}\left(\frac{r}{h}\right)^4 + \frac{1}{5}\left(\frac{r}{h}\right)^5 - \frac{41}{480} & 0 \leq \frac{r}{h} \leq 0.5 \\[2ex] \frac{1}{3}\left(\frac{r}{h}\right)^2 - \frac{1}{2}\left(\frac{r}{h}\right)^3 + \frac{3}{10}\left(\frac{r}{h}\right)^4 - \frac{1}{15}\left(\frac{r}{h}\right)^5 + \frac{1}{240}\left(\frac{h}{r}\right) - \frac{49}{480} & 0.5 < \frac{r}{h} \leq 1 \\[2ex] -\frac{h}{32}\frac{1}{r} & \frac{r}{h} > 1 \end{cases}
$$
(4.54)

The total angular momentum of the SPH particles inside the interaction zone with respect to the point mass s is obtained as

$$
\mathbf{L}_{\text{int}} = \sum_j m_j \Delta \mathbf{r}_{js} \times \Delta \mathbf{v}_{js}.
$$
(4.55)

Taking mass from SPH particles

After the accretion timescale has been defined one can calculate the total amount of mass that must be transferred to the point particle s. At the end of the current timestep, i.e., at time $t + \delta t$, the mass that will be transferred to the point mass is

$$
\delta M_{\text{acc}} = M_{\text{int}} \left[1 - \exp\left(-\frac{\delta t}{t_{\text{acc}}}\right) \right].
$$
(4.56)

First, the mass is taken from the SPH particle that is closest to the point mass. If the mass is less than δM_{acc}, the remaining is taken from the next SPH closest to the point mass and so on until a total of δM_{acc} is taken or all the mass of the interaction zone has been consumed.

Unlike in Hubber et al. (2013b) an additional parameter $m_{\text{SPH,min}}$ was introduced here. The aim of this parameter is to prevent ending up with SPH particles with tiny masses compared to the rest. Therefore, if an SPH particle were going to be left with a mass equal to or less than $m_{\text{SPH,min}}$, the mass of the SPH particle is instead set to zero, and all its mass is transferred to the accreting sink. The value $m_{\text{SPH,min}} = 10^{-4}$ was adopted so that the SPH particles cannot have masses that are less than 10^{-4} times their initial mass.

Note also that Hubber et al. (2013b) describe two instances in which the procedure of mass removal is superseded. In the work presented in Chap. 7 only the first instance was included but in a slightly modified way. The procedure included is:

- If the total mass of SPH particles inside the interaction zone of a sink s exceeds a maximum value M_{max}, then t_{acc} is decreased artificially by a factor $(M_{\text{int}}/M_{\text{max}})^2$, in order to accrete the excess mass more rapidly.

The adopted value was $M_{\text{max}} = 2 \times M_{\text{ini,IZ}}$, where $M_{\text{ini,IZ}}$ is the initial gas mass contained in the interaction zone for each sink, which was set to be equal to the mass of 50 SPH particles, i.e.

$$
M_{\text{max}} = 2 \times M_{\text{ini,IZ}} = 100 \frac{M_{\text{gas}}}{N_{\text{SPH}}}.
$$
(4.57)

Interaction radius

In the mass accretion formulation of Hubber et al. (2013b) the interaction radius R_s is chosen at the moment of sink particle creation and remains fixed throughout the simulation. In this work a variable interaction radius was employed. The radius is adjusted at the beginning of every accretion step in such a way that the amount of mass contained inside the interaction zone remains close to $M_{\mathrm{ini,IZ}}$. A tolerance of 10% around this value is allowed, and the interaction radius is recalculated iteratively (50 iterations maximum) until the enclosed mass falls within the allowed values. In order to prevent extreme values for the interaction radius two limits were imposed. An upper limit of 2000 AU and a lower limit of 10 AU.

Particle ejections

In a dense stellar system as the one modelled in this work, close encounters between protostars can result in strong gravitational kicks that can ultimately eject individual or binary stars. Additionally, studying the ejection of low mass protostars during primordial star formation has important implications for constraining models of Pop. III star formation (Schlaufman et al., 2018), and thus an adequate treatment of these events was necessary.

The simulations keep the record of N-body particles ejected during the evolution of the system by storing the masses and velocities at the moment of ejection. A particle is considered ejected from the system when it fulfills the next three criteria:

- The distance between the particle and the center of mass of the system is $d \geq 10\,\mathrm{R_{gas}}$, with $\mathrm{R_{gas}}$ being the virial radius of the gas cloud at $t = 0$.

- The particle is moving away from the system, i.e., $\mathbf{v}_{\mathrm{particle,COM}} \cdot \mathbf{r}_{\mathrm{particle,COM}} > 0$, where $\mathbf{v}_{\mathrm{particle,COM}}$ is the relative velocity between the particle and the center of mass velocity of the system, and $\mathbf{r}_{\mathrm{particle,COM}}$ is the relative position between the particle and the center of mass of the system.

- The particle is unbound, i.e., the gravitational potential energy plus the kinetic energy of the particle with respect to the center of mass of the system is positive.

Once these criteria are fulfilled, the particle is removed from the simulation and its properties at the time of removal are stored in a file.

4.2.5   Sink particle creation

During the evolution of the system the gas cloud collapse leads to extremely high densities ($\rho \sim 10^{-6}$ g cm^{-3}) reached primarily at the cloud center. Such high density results in SPH particles that are assigned with extremely small timesteps in the order of $\Delta t \sim 10^{-4}$ yr due

to the courant condition for SPH. These small timesteps make the simulation very expensive and in most cases impractical. A solution to this problem is to employ sink particles. Initially invented by Bate et al. (1995) for modelling the formation of binary stars from a collapsing gas cloud, sink particles are meant to represent either individual stars or a collection of stars. A sink particle is created by replacing one (or several) SPH particles by a new particle that interacts only through gravity.

Sink particles are nowadays widely extended in the astrophysical community and have been employed for studies of present-day and primordial star formation. Algorithms for sink particle creation and evolution have been implemented in a diverse set of numerical codes like the RAMSES code (Bleuler and Teyssier, 2014), the SEREN code (Hubber et al., 2011), the ATHENA code (Gong and Ostriker, 2013), the AREPO code (Weinberger et al., 2020), the PHANTOM code (Price et al., 2018), and the GIZMO code (Hopkins, 2015), just to name a few.

The implementation of sink particles differ among the codes, in particular between Mesh codes (like ATHENA or RAMSES), SPH codes (like SEREN or PHANTOM), and hybrid moving-mesh codes (like AREPO or GIZMO). In this work the sink particle formulation introduced by Hubber et al. (2013b) was adopted, which is specially suited for SPH codes.

Conditions for sink particle creation

An SPH particle whose density exceeds a user-defined threshold ρ_{sink} becomes a sink particle candidate. In the work presented in Chap. 7 the adopted value was $\rho_{\text{sink}} = 10^{16}$ cm$^{-3} \simeq 2 \times 10^{-8}$ g cm^{-3}(Becerra et al., 2015). SPH particles with a higher density criterion are considered sink candidates.

A sink candidate i is assigned a radius for its interaction zone of

$$R_s = X_{\text{sink}} h_i, \tag{4.58}$$

where X_{sink} is a user-defined value that was set to $X_{\text{sink}} = 2$. h_i is the smoothing length.

Another criteria to be met by the sink candidate is a no-overlap condition at the moment of creation. The interaction zone of sink particles cannot overlap at the moment of creation, this is

$$|\mathbf{r}_{ij}| > R_{s,i} + R_{s,j}, \tag{4.59}$$

for all existing sinks j. Here $|\mathbf{r}_{ij}|$ is the distance between sink candidate i and sink j, $R_{s,i}$ is the radius of the interaction zone for sink candidate i. $R_{s,j}$ is the radius of the interaction zone of the sink j.

The next criterion is that the candidate sink must be at a minimum of the gravitational potential among its neighbours (Federrath et al., 2010), i.e.,

$$\phi_i < \min\{\phi_j\}, \tag{4.60}$$

for all neighbours j.

The final condition is that the candidate sink must be dense enough to dominate the local gravitational potential. This is important when other sink particles are present. The condition is

$$\rho_i > \rho_{\text{Hill}} = \frac{3X_{\text{Hill}}\left(-\Delta\mathbf{r}_{ij} \cdot \Delta\mathbf{a}_{ij}\right)}{4\pi G|\Delta r_{ij}|^2}, \tag{4.61}$$

where X_{Hill} is a user-defined parameter with default value $X_{\text{Hill}} = 4$, $\Delta\mathbf{r}_{ij} = \mathbf{r}_i - \mathbf{r}_j$ is the relative position of candidate i with respect to existing sink j, and $\Delta\mathbf{a}_{ij}$ is the relative acceleration of candidate i with respect to sink j.

If all these criteria are met, the candidate sink is turned into a sink particle inheriting its properties, with mass $m_{\text{sink}} = m_i$, position $\mathbf{r}_{\text{sink}} = \mathbf{r}_i$, velocity $\mathbf{v}_{\text{sink}} = \mathbf{v}_i$, and a radius for the interaction zone given by Eq.(4.58).

Angular momentum feedback

During mass accretion onto protostars, the inflowing material has high specific angular momentum and forms an accretion disk around an accreting central object. Angular momentum is transferred in the disk, allowing the material to spiral inwards and finally reach the central protostar. Such disks have been revealed with ALMA observations (Yen et al., 2017). In order to prevent that sink particles act as sinks of angular momentum, and to model the effects of an accretion disk around protostars, the angular momentum feedback recipe described in Hubber et al. (2013b) is also included in the simulations. For this, at the end of each timestep Δt, the angular momentum of the point mass is reduced and transferred to the SPH particles existing in its interaction zone. The amount of angular momentum transferred $|\delta\mathbf{L}_s|$ is calculated as

$$|\delta\mathbf{L}_s| = |\mathbf{L}_s|\left\{1 - \exp\left(-\frac{\Delta t}{\langle t_{\text{disk}}\rangle}\right)\right\}, \tag{4.62}$$

where $|\mathbf{L}_s|$ is the angular momentum of sink s. This angular momentum is redistributed among the SPH particles inside the interaction zone of sink s via an impulse-velocity given by

$$\delta\mathbf{v}_j = \frac{|\delta\mathbf{L}_s|\mathbf{L}_s \times \Delta\mathbf{r}_{js}}{|\sum_j\{m_j\Delta\mathbf{r}_{js} \times \mathbf{L}_s \times \Delta\mathbf{r}_{js}\}|}. \tag{4.63}$$

At the same time, the point mass s receives impulses of velocity and angular momentum given by

$$\delta\mathbf{v}_s \;=\; -M_s^{-1}\sum_j m_j\delta\mathbf{v}_j, \tag{4.64}$$

$$\delta\mathbf{L}_s \;=\; -\sum_j m_j\Delta\mathbf{r}_{js}\times\delta\mathbf{v}_j. \tag{4.65}$$

4.3 Generation of the initial conditions

Having described in Sec. 4.2.1 and 4.2.2 the community codes employed in this study, and the coupling strategy adopted in Sec. 4.2.3, this section aims to present the procedure followed in order to produce the initial conditions for the research article presented in Chap. 7.

4.3.1 A Plummer sphere of gas and stars

For generating the initial conditions the example scripts provided with the AMUSE interface were utilized as reference. A convenient strategy is to define a `converter` first, a function that will manage the conversion between different units in the AMUSE script, and that can be passed to the function that generates the initial conditions. For creating the converter one needs the total mass of the system and the virial radius of the Plummer distribution. In particular, for generating a Plummer sphere in virial equilibrium consider the following. For a Plummer model, the velocity dispersion is given by

$$\sigma_p^2(r) = \frac{GM}{6\sqrt{r^2+a^2}}, \tag{4.66}$$

where M is the total mass and a is the Plummer radius. If we consider a position r much larger than a we can simplify the previous relation to

$$\sigma_p^2(r) = \frac{GM}{6r}. \tag{4.67}$$

Therefore, the kinetic energy of a Plummer distribution is given by

$$K = \frac{3}{2}M\sigma_p^2 = \frac{3}{12}\frac{GM^2}{r}. \tag{4.68}$$

The potential energy of a Plummer distribution, again, for the limit in which $r >> a$ is

$$U = -\frac{3\pi}{32}\frac{GM^2}{a}. \tag{4.69}$$

Consider now the virial theorem that relates the kinetic and potential energy of a particle distribution as

$$2K = -U, \tag{4.70}$$

so that we can define a *virial radius* at which the virial theorem holds for a Plummer distribution. This virial radius can be calculated as

$$\frac{1}{2}\frac{GM^2}{r} = \frac{3\pi}{32}\frac{GM^2}{a},$$

$$\frac{16}{3\pi}a = r_v, \tag{4.71}$$

$$r_v \sim 1.7a. \tag{4.72}$$

This virial radius is required for initializing the particle distribution with the function provided by AMUSE.

Define now the converter using the total mass of the system and the virial radius of the Plummer distribution. The virial radius in this case is chosen such that the half-mass radius of the system is 0.1 pc. The half-mass radius of a Plummer distribution is $r_h \sim 1.3a$. Therefore the virial radius is

$$r_v \sim \frac{1.7}{1.3}r_h \sim 0.14 \text{ pc}. \tag{4.73}$$

In AMUSE, the converter is initialized as

```
converter=nbody_system.nbody_to_si(M_tot, R_v),
```

where M_{tot} is the total mass of the system, i.e., gas plus protostars.

After this initialization one can easily generate the initial conditions for the simulations presented in Chap. 7. This is rather straightforward for the N-body particles. The first step is to import the required function into the script. This can be done by writing

```
from amuse.ic import plummer
```

and then generating a plummer distribution by doing

```
proto_stars=plummer.new_plummer_model(N_proto, converter, radius_cutoff=5.,
do_scale=True).
```

Here, N_{proto} is the number of particles to be created, the option `radius_cutoff=5.` is used to truncate the distribution at $5a$, and the option `do_scale=True` is used to scale the results to N-body units in which the total mass is $M = 1$, the kinetic energy is $K = 0.25$ and the gravitational potential energy is $U = -0.25$, all of them in N-body units.

Note that since the converter is defined using the total mass of the system (not only that of the N-body particles), the mass of each N-body particle will be set equal to $M_{\text{tot}}/N_{\text{proto}}$. By doing this the velocities of the N-body particles are set under the assumption of virial equilibrium in a deeper gravitational potential. The only remaining step is to change the masses of the particles as desired. In this case an initial mass of $0.1\,\text{M}_\odot$ was chosen for each of them. This choice of the converter for generating the initial conditions and subsequent change of the masses of the particles results in a set of $0.1\,\text{M}_\odot$ particles that will remain in virial equilibrium when the gas cloud is included. This was checked by running a simulation in which only the N-body particles are evolved under the influence of the gravity of the gas (see Fig. 4.11).

For the the set of SPH particles a Plummer profile was also used for producing the initial conditions. Additionally, an option for including turbulence was set. For this, the AMUSE script used to generate a turbulent uniform cloud was used as a template. The uniform SPH distribution was replaced by a Plummer SPH distribution. In order to generate the turbulent field it is necessary to specify the kinetic energy associated to the turbulent motions. More specifically, one needs as input the ratio of the kinetic energy (associated to turbulence) to the absolute value of the gravitational potential energy. It is customary to express the velocity of the turbulent motions via the Mach number $\mathcal{M}$ defined as

$$\mathcal{M} = \frac{\sigma_v}{c_s}, \tag{4.74}$$

where σ_v is the velocity dispersion of the gas and c_s is the sound speed. Therefore it is convenient to express the ratio $-K/U$ as a function of $\mathcal{M}$. For this, consider first the kinetic energy associated to turbulent motions for a gas cloud of mass M, this is

$$K = \frac{3}{2}M\sigma_v^2, \tag{4.75}$$

and express σ_v as a function of $\mathcal{M}$ using Eq.(4.74) to obtain

$$K = \frac{3}{2}M\mathcal{M}^2 c_s^2. \tag{4.76}$$

Now, for modelling an isothermal cloud, consider the isothermal sound speed

$$c_s = \sqrt{\gamma\frac{kT}{\mu}}, \tag{4.77}$$

where γ is the adiabatic index, k is Boltzmann's constant and μ is the mean molecular weight of the gas. The expression for the kinetic energy associated to turbulent motions is given by

$$K = \frac{3}{2}M\mathcal{M}^2\gamma\frac{kT}{\mu}. \tag{4.78}$$

Now, combine this equation with the expression for the gravitational potential energy of a Plummer distribution (Eq. 4.69) to obtain

$$-\frac{K}{U} = \frac{16\mathcal{M}^2 \gamma k T a}{\pi G M \mu}.$$ (4.79)

It is in principle also necessary to specify the ratio of thermal to gravitational potential energy in order to set the temperature of the gas cloud. For the set of simulations presented in Chap. 7 this was not necessary since the modified equation of state employed automatically set the initial temperature to 8000 K (see Sec. 4.39). Therefore, only for initialization purposes, a value of $E_{\text{th}}/U = 0.5$ is set here.

The method for generating turbulent initial conditions is similar to the one followed by Dubinski et al. (1995) and consists in generating a total of $(2n_f)^3$ shear waves with random propagating directions in Fourier space, whose amplitude is $A \propto k^{p/2}$. The angular wavenumber k spans a range of values between 10^{-15} and $\sqrt{3}n_f$. In this work the value $n_f = 32$ was chosen. This yields a total of $262\,144$ waves. The script for injecting divergence free turbulence is included in AMUSE and can be imported as

```
from amuse.ext.molecular_cloud import molecular_cloud
```

and then the particle set initialized by doing

```
gas = molecular_cloud(nf=32,power=-10./3.,targetN=Nsph,
convert_nbody=converter,ethep_ratio=ratio1,ekep_ratio=ratio2,
seed=turb_seed).result
```

where `power` sets the value of the exponent p and in turn sets the amplitude of the waves in Fourier space ($v_k \propto k^{p/2}$). `targetN` is the number of SPH particles, `convert_nbody` is the converter defined previously, `ethep_ratio` and `ekep_ratio` are the ratios of thermal to potential energy (which for initialization purposes we set to 0.5), and the ratio of kinetic to potential energy defined in Eq.(4.79). Finally, `turb_seed` is the random seed number.

By combining the set of N-body and SPH particles a snapshot of the initial conditions was produced. This is shown in Fig. 4.10.

4.3.2   Gas clouds resulting from the collapse of metal free atomic-cooling halos

The research presented in Chap. 7 describes the results of simulations of the assembly of SMSs in an spherically collapsed atomic cooling halo following fragmentation at sub-parsec
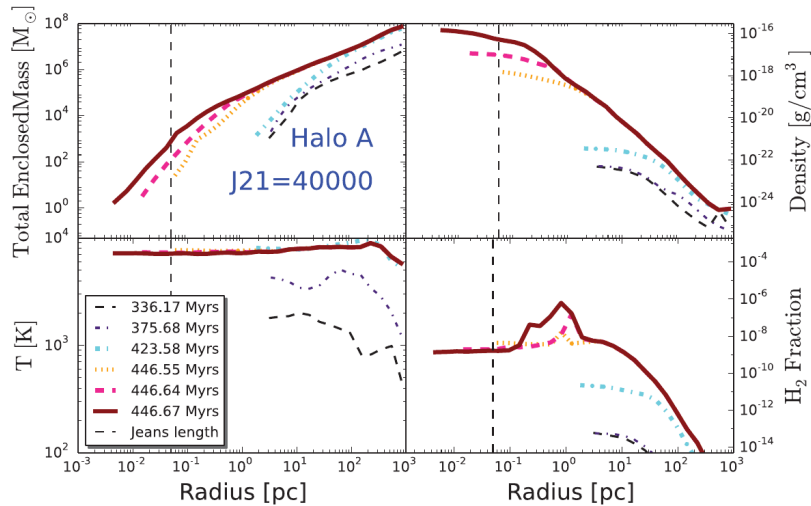
Figure 4.9. Thermodynamical and physical properties of the gas in one of the halos simulated by Latif and Volonteri (2015). From the top left, and in clock-wise direction the panels present the total enclosed mass, the gas density, the H_2 fraction, and the gas temperature, all of them as function of the radius of the cloud. Credits: Latif and Volonteri (2015).

scales. For this end the central 0.14 pc of the collapsed cloud was modelled as a Plummer sphere (Plummer, 1911) since this provides the nearly isothermal density profile ($\rho \sim R^{-2}$) found in large-scale simulations (Chon et al., 2018; Latif et al., 2016a). The typical mass enclosed within such volume was obtained from the work of Latif and Volonteri (2015) who report values of $\sim 10^4$ $M_\odot$ as shown in Fig. 4.9. The values chosen were 10^4 $M_\odot$ and 3×10^4 $M_\odot$ for the mass of the gas clouds.

The temperature of the gas was set to 8000 K and a modified equation of state was employed. This EOS is isothermal below a density of ρ_{ad} and becomes adiabatic at higher densities. The value $\rho_{ad} = 10^{16}$ cm^{-3} was adopted as informed by hydrodynamical numerical simulations that employ chemical networks (Becerra et al., 2018). Therefore, the equation of state employed has the form

$$T = T_0 \left[1 + \left(\frac{\rho}{\rho_{ad}} \right)^{\gamma-1} \right], \tag{4.80}$$

with $T_0 = 8000$ K and $\gamma = 5/3$.

Once the cloud has been relaxed in ten steps during a period of 10% the crossing time, a total of 64^3 waves were injected, with a power spectrum such that $E(k) \propto k^{-5/3}$, corresponding to a Kolmogorov spectrum. The velocities of the SPH particles were then scaled in such a way that the total kinetic energy correspond to Mach=1 turbulence.

The external pressure P_{ext} for the clouds with 10^4 $M_\odot$ and 3×10^4 $M_\odot$ are 7.45×10^{-8} g cm^{-1} s^{-2}, and 1.72×10^{-7} g cm^{-1} s^{-2} respectively. These were the values included in the modified momentum equation for the hydrodynamics code as explained in

Sec. 4.2.2.

Once the gas cloud was initialized, a total of 256 protostars distributed according to a Plummer density distribution were inserted. A snapshot of the initial conditions is presented in Fig. 4.10.
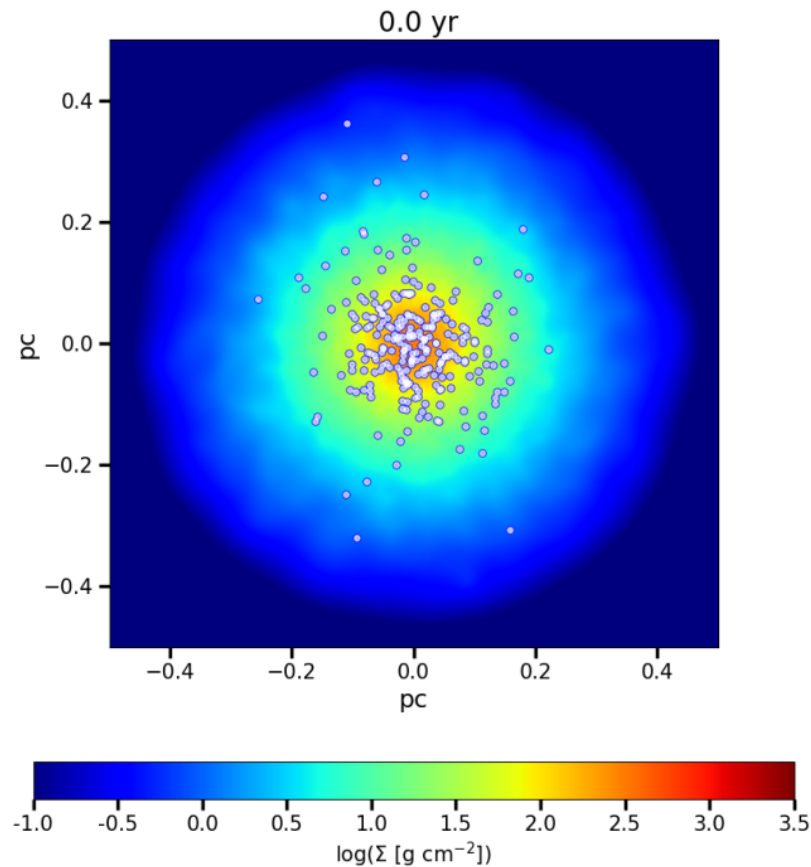
Figure 4.10. Initial conditions for the simulations presented in Chap. 7.

The velocity of the stars were adjusted so that they are in virial equilibrium at the start of the simulation. This was checked by running a simulation evolving the stars only, under the gravitational effects of the gas cloud, which in turn was static. As can be seen in Fig. 4.11, the Lagrangian radii of the distribution of stars maintains a nearly constant value for half a million years. The stars are thus in virial equilibrium.
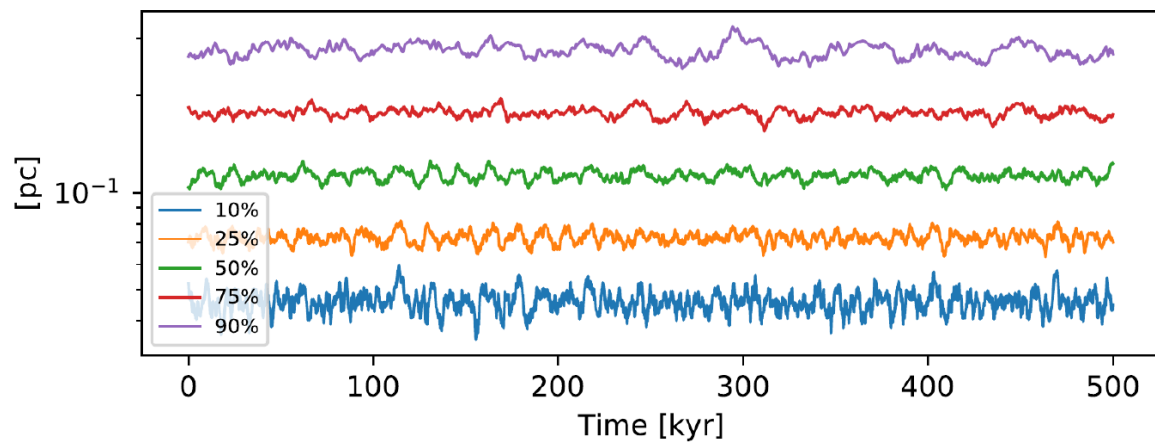
Figure 4.11. Lagrangian radii for a cluster of protostars evolved under the gravitational potential of the gas cloud. The gas cloud remains static in order to check that the protostars are in virial equilibrium.

Chapter 5

The effects of a background potential in star cluster evolution: A delay in the relaxation time-scale and runaway collision processes

5.1   Statement about my contribution

For the research article presented in this chapter my contribution consisted in the modification of the software employed. I also ran the numerical simulations and analyzed them. I created all the tables and figures and wrote the manuscript. All the authors contributed to the discussion and helped with the revision of the manuscript.

Astronomy & Astrophysics

The effects of a background potential in star cluster evolution

A delay in the relaxation time-scale and runaway collision processes

B. Reinoso[1,2], D. R. G. Schleicher[1], M. Fellhauer[1], N. W. C. Leigh[1,3], and R. S. Klessen[2,4]

[1] Departamento de Astronomía, Facultad Ciencias Físicas y Matemáticas, Universidad de Concepción, Av. Esteban Iturra s/n Barrio Universitario, Casilla 160-C, Concepción, Chile
e-mail: breinoso@udec.cl

[2] Universität Heidelberg, Zentrum für Astronomie, Institut für Theoretische Astrophysik, Albert-Ueberle-Str. 2, 69120 Heidelberg, Germany

[3] Department of Astrophysics, American Museum of Natural History, New York, NY 10024, USA

[4] Universität Heidelberg, Interdisziplinäres Zentrum für Wissenschaftliches Rechnen, Im Neuenheimer Feld 205, 69120 Heidelberg, Germany

ABSTRACT

Runaway stellar collisions in dense star clusters are invoked to explain the presence of very massive stars or blue stragglers in the center of those systems. This process has also been explored for the first star clusters in the Universe and shown to yield stars that may collapse at some points into an intermediate mass black hole. Although the early evolution of star clusters requires the explicit modeling of the gas out of which the stars form, these calculations would be extremely time-consuming and often the effects of the gas can be accurately treated by including a background potential to account for the extra gravitational force. We apply this approximation to model the early evolution of the first dense star clusters formed in the Universe by performing N-body simulations, our goal is to understand how the additional gravitational force affects the growth of a very massive star through stellar mergers in the central parts of the star cluster. Our results show that the background potential increases the velocities of the stars, causing an overall delay in the evolution of the clusters and in the runaway growth of a massive star at the center. The population of binary stars is lower due to the increased kinetic energy of the stars, initially reducing the number of stellar collisions, and we show that relaxation processes are also affected. Despite these effects, the external potential enhances the mass of the merger product by a factor ~ 2 if the collisions are maintained for long times.

Key words. galaxies: star clusters: general – galaxies: star formation – binaries: general

1. Introduction

The discovery of supermassive black holes (SMBHs) in the first billion years of the Universe (Fan et al. 2006; Mortlock et al. 2011; Wu et al. 2015; Reed et al. 2019) has led to the study of formation channels for massive black hole seeds early on ($z \sim 10-20$), following the collapse of molecular-cooling halos ($\sim 10^6 \, M_\odot$) or atomic-cooling halos ($\sim 10^8 \, M_\odot$). The direct collapse of protogalactic clouds exposed to a moderate Lyman-Werner flux from neighboring star forming halos produced the most massive seeds ($10^{3-5} \, M_\odot$) (Wise et al. 2019), and recent numerical simulations suggest that contrary to what was previously thought, the UV flux is not that critical anymore in the case of the efficient merger of fragments (Suazo et al. 2019). Another promising mechanism to form massive seeds is the formation of very massive stars (VMS) in the centers of dense stellar systems through stellar mergers (Fujii & Portegies Zwart 2013; Katz et al. 2015; Sakurai et al. 2017; Reinoso et al. 2018), producing either VMSs with several $10^2 \, M_\odot$ or intermediate mass black holes with $\sim 10^3 \, M_\odot$ and potentially up to $10^4 \, M_\odot$. Such massive seeds could be present in the early Universe if accreting population III (Pop. III) protostars can merge before entering the main sequence or if the remaining gas in the cluster can be accreted by the central object (Boekholt et al. 2018). Furthermore, after the formation of a BH in the center of a stellar cluster, additional growth can be expected by tidal disruption events of stars passing close to the black hole (Sakurai et al. 2019; Bonetti et al. 2020).

Although most of these previous studies have focused on mergers in second generation star clusters, that is, clusters that formed from molecular clouds that were polluted by stellar winds or supernovae from the first generation of stars (Katz et al. 2015; Sakurai et al. 2017, 2019), we are mostly interested in the very first star clusters of the Universe given the particular properties of these systems and these stars. Fragmentation occurs at higher densities in primordial gas clouds ($10^9 \, \mathrm{cm^{-3}}$ or higher) (e.g., Clark et al. 2011a; Greif et al. 2011, 2012; Smith et al. 2011, 2012; Latif et al. 2013a), with clusters potentially having half-mass radii of 0.1 pc, especially if dust grains are present in such clouds which trigger fragmentation at high densities (e.g., Omukai et al. 2005; Klessen et al. 2012; Bovino et al. 2016; Latif et al. 2016).

In those environments, the protostellar radii could also be enhanced due to the rapid accretion expected in primordial or low-metallicity gas, which in turn are a consequence of much higher gas temperatures than at present day star formation, and so the protostellar radii are enhanced up to $300 \, R_\odot$ (Stahler et al. 1986; Omukai & Palla 2001, 2003). Moreover, high accretion rates of $\sim 0.1 \, M_\odot \, \mathrm{yr^{-1}}$ have been reported in several simulations for these protostars (Hosokawa et al. 2012, 2013;

Schleicher et al. 2013; Haemmerlé et al. 2018; Woods et al. 2017), implying $\sim 500\,R_\odot$ for a $10\,M_\odot$ star and potentially more than $1000\,R_\odot$ for a $100\,M_\odot$ star. While some models already included the effects of an external potential in the evolution of dense star clusters (e.g., Leigh et al. 2013a,b, 2014; Boekholt et al. 2018; Sakurai et al. 2019) in order to mimic the effects of gas during the embedded phase of the cluster or to account for the dark matter halo, disentangling the effects of the external potential can be tricky because these models also include mass accretion recipes (Boekholt et al. 2018).

In this paper, we present a systematic investigation on how the formation of very massive stars in dense star clusters and the evolution of the clusters themselves are affected when including a background potential in the evolution of the systems. Our work can be used to constraint the parameter space that future, more sophisticated simulations should focus on. Since each physical collision led to a merger in our runs, we use these terms interchangeably. We describe our setup and initial conditions in Sect. 2 and our results are presented in Sect. 3, including the typical evolution of clusters under the influence of a background potential and clusters without a background potential, the number of collisions, the mass of the resulting object, and our model to estimate the number of mergers at different times. We apply our model to population III (Pop.III) star clusters in Sect. 4. A discussion about neglected effects and considerations for future research on this subject is given in Sect. 5 and finally the conclusions are presented in Sect. 6.

2. Simulation setup

To understand the impact of the gas potential on the number of mergers that occur in star clusters, we first performed simulations in which we did not include stellar mergers, and we compared the evolution of these systems without an external potential and when placed in the center of a background potential. Once we addressed the effects of the extra force on the evolution of the clusters, we performed simulations that include stellar mergers in clusters with and without an external potential. To perform the calculations, we used a modified version of NBODY6[1] (Aarseth et al. 2000) to treat collisions, where we switched off the stellar evolution package and instead explicitly specify the stellar radii to perform a parameter study. NBODY6 is a fourth order Hermite integrator, and includes a spatial hierarchy to speed up the calculations: This is referred to as the Ahmad-Cohen scheme (Ahmad & Cohen 1973). It also includes routines to treat tidal capture and tidal circularization of binary systems (Mardling & Aarseth 2001) that we activated in our simulations. Another important routine included is the Kustaanheimo-Stiefel regularization (Kustaanheimo & Stiefel 1965), which is an algorithm that can be used to treat binaries and close two-body encounters more accurately. We performed a total of 344 N-body simulations.

2.1. Simulations without stellar mergers

In order to create a controlled experiment to which we can compare our results including stellar mergers, we first investigated the effects produced by the external potential on the evolution of the star clusters in the absence of collisions. We specifically explored how the mass of the external potential affects the core-collapse, the formation of binary systems, and the evaporation of the clusters. We modeled each cluster as a Plummer (Plummer 1911) distribution of $N = 1000$ and $N = 10\,000$ equal mass particles with a total cluster mass of $M_{\text{stars}} = 10^4\,M_\odot$. Given that

Table 1. Simulations that do not include stellar mergers.

Numbers	N	M_{stars} [$M_\odot$]	$M_{\text{ext}}/M_{\text{stars}}$	R_{v} [pc]	$t_{\text{cc}}/t_{\text{cross}}$
1	1000	10^4	0.0	1.0	456
2	1000	10^4	0.1	1.0	460
3	1000	10^4	0.5	1.0	1 820
4	1000	10^4	1.0	1.0	6 553
5	10 000	10^4	0.0	1.0	2 306[a]
6	10 000	10^4	0.1	1.0	3 377[a]
7	10 000	10^4	0.5	1.0	13 519[a]
8	10 000	10^4	1.0	1.0	51 889[a]

Notes. Summary of simulations that do not include stellar mergers showing the number of particles, the cluster mass, the ratio of external potential to cluster mass, the virial radius and the ratio of core collapse time to crossing time in Cols. 1, 2, 3, 4, 5 and 6 respectively. [a]Crossing time calculated using Eq. (1) with $q = M_{\text{ext}}/M_{\text{stars}} = 1.0$.

we are interested in the overall evolution of the system, and in order to save computational time, we modeled less dense clusters than the ones presented in Sect. 2.2, with a virial radius of $R_{\text{v}} = 1.0$ pc. We then included an analytic background potential that also follows a Plummer density profile with the same virial radius as the stellar distribution $R_{\text{v,ext}} = 1.0$ pc and the mass of the potential was varied as $M_{\text{ext}} = 0.0, 0.1, 0.5$ and $1.0 \times M_{\text{stars}}$. The clusters start in virial equilibrium. We performed a total of eight simulations that do not include stellar mergers and which are listed in Table 1.

2.2. Simulations that include stellar mergers

Our simulations that include stellar mergers aim to model the first stages after the formation of Pop. III star clusters. We modeled a compact cluster in virial equilibrium by also using a Plummer distribution (Plummer 1911) for the stars that are all equal in mass and radius at the beginning of the simulation. We modeled dense clusters with a virial radius of $R_{\text{v}} = 0.14$ pc and a total mass in stars of $M_{\text{stars}} = 10^4\,M_\odot$. We then performed the same set of simulations including an external analytic Plummer potential with $M_{\text{ext}} = 1.0 \times M_{\text{stars}}$ with the same virial radius of $R_{\text{v,ext}} = 0.14$ pc in order to consider at first order the effects of the gas that remains in the cluster after the formation of the stars. Taking the mass of the external potential into account, the crossing time of the clusters were calculated as:

$$t_{\text{cross}} = \sqrt{\frac{R_{\text{v}}^3}{GM_{\text{stars}}}} \frac{1}{1 + q}, \qquad (1)$$

with $q = \frac{M_{\text{ext}}}{M_{\text{stars}}}$ (see Appendix A); this gives a value of $t_{\text{cross}} = 0.0078$ Myr and $t_{\text{cross,ext}} = 0.0039$ Myr for clusters without and with an external potential, respectively. We investigated how the mass of the final merger product depends on the initial number of stars in the cluster N, which we varied as $N = 100, 500, 1000$, and 5000 stars. We also varied the initial stellar radius as $R_{\text{star}} = 20, 50, 100, 200, 500, 1000$, and $5000\,R_\odot$ using equal radii stars in each run. For each of these configurations, we performed simulations with $M_{\text{ext}} = 0.0$ and $1.0 \times M_{\text{stars}}$. Finally, we ran a total of six random simulations per each configuration, which are listed in Table 2. This gives a total of 336 N-body simulations that include stellar mergers.

Table 2. Simulations that include stellar mergers.

Number	N	M_{stars} [$M_\odot$]	M_{ext}/M_{stars}	R_v [pc]	m_{star} [$M_\odot$]	R_{star} [$R_\odot$]	$\overline{M}_{max}$ [$M_\odot$][a]
1	100	10^4	0.0	0.14	100.0	20.0	350 ± 164
2	100	10^4	0.0	0.14	100.0	50.0	466 ± 137
3	100	10^4	0.0	0.14	100.0	100.0	883 ± 237
4	100	10^4	0.0	0.14	100.0	200.0	1050 ± 274
5	100	10^4	0.0	0.14	100.0	500.0	1533 ± 413
6	100	10^4	0.0	0.14	100.0	1000.0	2083 ± 691
7	100	10^4	0.0	0.14	100.0	5000.0	2833 ± 516
8	500	10^4	0.0	0.14	20.0	20.0	390 ± 55
9	500	10^4	0.0	0.14	20.0	50.0	633 ± 120
10	500	10^4	0.0	0.14	20.0	100.0	937 ± 184
11	500	10^4	0.0	0.14	20.0	200.0	1390 ± 170
12	500	10^4	0.0	0.14	20.0	500.0	2056 ± 204
13	500	10^4	0.0	0.14	20.0	1000.0	2756 ± 463
14	500	10^4	0.0	0.14	20.0	5000.0	3013 ± 332
15	1000	10^4	0.0	0.14	10.0	20.0	430 ± 143
16	1000	10^4	0.0	0.14	10.0	50.0	747 ± 173
17	1000	10^4	0.0	0.14	10.0	100.0	1168 ± 132
18	1000	10^4	0.0	0.14	10.0	200.0	1748 ± 188
19	1000	10^4	0.0	0.14	10.0	500.0	2428 ± 150
20	1000	10^4	0.0	0.14	10.0	1000.0	2980 ± 243
21	1000	10^4	0.0	0.14	10.0	5000.0	3217 ± 162
22	5000	10^4	0.0	0.14	2.0	20.0	421 ± 263
23	5000	10^4	0.0	0.14	2.0	50.0	1005 ± 377
24	5000	10^4	0.0	0.14	2.0	100.0	1520 ± 284
25	5000	10^4	0.0	0.14	2.0	200.0	1912 ± 750
26	5000	10^4	0.0	0.14	2.0	500.0	3223 ± 305
27	5000	10^4	0.0	0.14	2.0	1000.0	3495 ± 146
28	5000	10^4	0.0	0.14	2.0	5000.0	4256 ± 366
29	100	10^4	1.0	0.14	100.0	20.0	683 ± 216
30	100	10^4	1.0	0.14	100.0	50.0	983 ± 293
31	100	10^4	1.0	0.14	100.0	100.0	1583 ± 581
32	100	10^4	1.0	0.14	100.0	200.0	2183 ± 382
33	100	10^4	1.0	0.14	100.0	500.0	2800 ± 316
34	100	10^4	1.0	0.14	100.0	1000.0	3367 ± 619
35	100	10^4	1.0	0.14	100.0	5000.0	3700 ± 820
36	500	10^4	1.0	0.14	20.0	20.0	683 ± 159
37	500	10^4	1.0	0.14	20.0	50.0	1180 ± 324
38	500	10^4	1.0	0.14	20.0	100.0	1653 ± 279
39	500	10^4	1.0	0.14	20.0	200.0	2287 ± 348
40	500	10^4	1.0	0.14	20.0	500.0	3310 ± 312
41	500	10^4	1.0	0.14	20.0	1000.0	3987 ± 208
42	500	10^4	1.0	0.14	20.0	5000.0	4027 ± 332
43	1000	10^4	1.0	0.14	10.0	20.0	645 ± 141
44	1000	10^4	1.0	0.14	10.0	50.0	1343 ± 215
45	1000	10^4	1.0	0.14	10.0	100.0	1785 ± 392
46	1000	10^4	1.0	0.14	10.0	200.0	2502 ± 166
47	1000	10^4	1.0	0.14	10.0	500.0	3622 ± 204
48	1000	10^4	1.0	0.14	10.0	1000.0	4092 ± 158
49	1000	10^4	1.0	0.14	10.0	5000.0	4317 ± 267
50	5000	10^4	1.0	0.14	2.0	20.0	181 ± 144[b]
51	5000	10^4	1.0	0.14	2.0	50.0	552 ± 71
52	5000	10^4	1.0	0.14	2.0	100.0	1497 ± 189
53	5000	10^4	1.0	0.14	2.0	200.0	2264 ± 765
54	5000	10^4	1.0	0.14	2.0	500.0	3630 ± 166
55	5000	10^4	1.0	0.14	2.0	1000.0	4084 ± 213
56	5000	10^4	1.0	0.14	2.0	5000.0	5185 ± 236

Notes. Summary of simulations that include stellar mergers showing the number of particles, the cluster mass, the ratio of external potential to cluster mass, the virial radius, the initial stellar masses, the initial stellar radii and the average mass of the most massive star at the end of the simulation. [a]Value obtained as the average from 6 simulations. [b]Simulation run until 5657 $t_{cross} = 22$ Myr.

2.3. Stellar mergers

In our simulations, a merger occurs when two stars are separated by a distance equal to or smaller than the sum of their radii, this is:

$$r \leq R_1 + R_2, \qquad (2)$$

with r being the distance between both stars center of mass, and R_1 and R_2 are the radii of the stars. Given that the stars are physically in contact at this point, we also call this a stellar collision. Additionally, since each collision in our runs led to a merger, we then consider the terms merger and collision to be synonymous. Once this condition was fulfilled, we merged both stars

replacing them by a new star whose total mass is the sum of the masses of the merging stars. Furthermore, the radius was calculated assuming that the star rapidly settles to a stable configuration where the new star has the same density as the previously merging stars, which is consistent with the calculations of Hosokawa et al. (2012) and Haemmerlé et al. (2018). Therefore the new mass and radius of the merger product were calculated as:

$$M_{\text{new}} = M_1 + M_2, \tag{3}$$

$$R_{\text{new}} = R_1 \left(\frac{M_1 + M_2}{M_1} \right)^{1/3}. \tag{4}$$

3. Results

First we present the results of the simulations that do not include stellar mergers and describe the effects introduced by the addition of an external potential and the variation of the potential mass. Then, we present the results of our simulations that include stellar mergers and describe how their evolution and the formation of massive stars due to the runaway merger process are affected by the external potential.

3.1. Simulations without mergers

Here, we describe the main effects of including an external potential on the evolution of our star cluster models in the absence of stellar mergers. Due to the similarities between the runs, here, we only present the results for simulations number 5 and 8 listed in Table 1 with the setup described in Sect. 2.1. However, a description for the remaining simulations listed in Table 1 is included in Appendix B.

The evolution of clusters with $M_{\text{ext}} = 0 \times M_{\text{stars}}$ is well understood and consistent with the results of Spitzer (1987), where the clusters evolve toward core collapse as a result of two-body relaxation. The core then experiences core-oscillations, contracting and expanding again due to the formation of hard binaries that act as an energy source in the core. The core collapse is expected to occur between 10 and 20 half mass relaxation times t_{rh} that we calculated as (Spitzer 1987):

$$t_{\text{rh}} = 0.138 \frac{N}{\ln(\gamma N)} t_{\text{cross}}, \tag{5}$$

with $\gamma = 0.4$ because we used equal mass stars and t_{cross} was calculated with Eq. (1) setting $M_{\text{tot}} = M_{\text{stars}}$. The half mass relaxation time for the cluster with $N = 10\,000$ stars and $M_{\text{ext}} = 0 \times M_{\text{stars}}$ is $t_{\text{rh}} = 166.38\, t_{\text{cross}}$ and core collapse occurs at $2306\, t_{\text{cross}}$ which is $14\, t_{\text{rh}}$. We found the core collapse time by visual inspection and looking for the first drop and subsequent rise in the 10% Lagrangian radius as marked by the vertical green line in Fig. 1.

At the moment of core collapse, the 10% Lagrangian radius drops to 0.087 pc, yielding a mean density of $3.6 \times 10^5\, M_\odot\, \text{pc}^{-3}$. After this phase, the entire cluster begins to expand and the onset of ejections takes place with a total number of ejections of about 1500 until a time of $10\,000\, t_{\text{cross}}$. A star is considered to be ejected from the cluster if its distance to the center of mass of the system is $>20\, R_{\text{v}}$ and its kinetic energy is higher than its potential energy at this location.

When we included an external potential in our simulations, we note first that, since the clusters start virialized, the velocities of the stars are higher compared to clusters without the background potential. This compensates for the extra gravitational
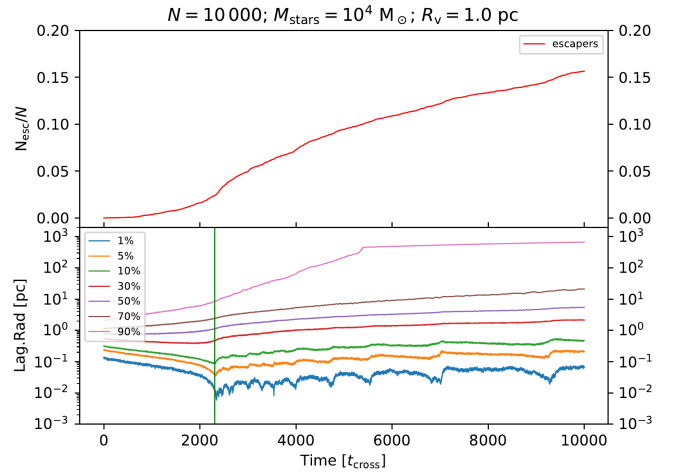
Fig. 1. Evolution of a cluster with $N = 10\,000$ stars with a total stellar mass of $M_{\text{stars}} = 10^4\, M_\odot$ and virial radius $R_{\text{v}} = 1.0\,$pc. *Top panel*: fraction of ejections from the cluster and *bottom panel*: Lagrangian radii of the cluster. The vertical green line marks the moment of core collapse.

Fig. 2. Evolution of a cluster with $N = 10\,000$ stars with a total stellar mass of $M_{\text{stars}} = 10^4\, M_\odot$ and a virial radius of $R_{\text{v}} = 1.0\,$pc in the center of an external analytic potential with $M_{\text{ext}} = 10^4\, M_\odot$. *Top panel*: fraction of ejections from the cluster and *bottom panel*: Lagrangian radii of the cluster. The vertical green line marks the moment of core collapse.
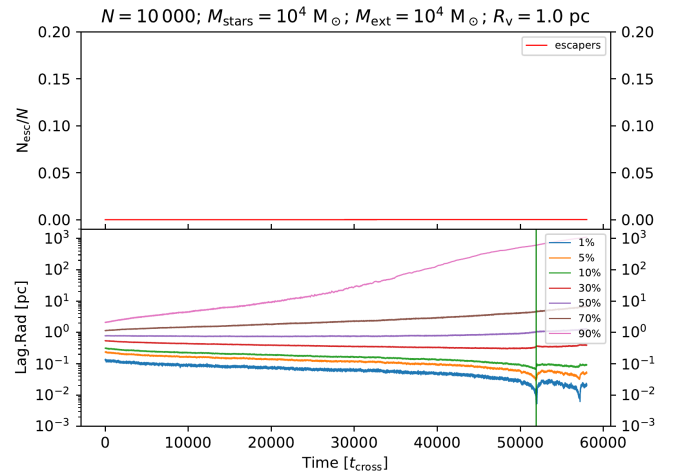
force. Then we had to calculate the crossing time of the cluster using Eq. (1) with $M_{\text{tot}} = M_{\text{stars}} + M_{\text{ext}}$.

We find that all of the clusters behave in a similar way. All of them evolve toward core collapse while there is little expansion of the outer parts (>30% Lagrangian radii) compared to clusters without an external potential (see Fig. 2).

For the case when the mass of the external potential is comparable to the total mass ($M_{\text{ext}} = M_{\text{stars}}$), the core collapse is delayed significantly, which occurs now at $51\,889\, t_{\text{cross}}$ (see green vertical line in bottom panel of Fig. 2). This is 23 times (in units of the cluster crossing time) later than the core collapse time for the cluster without a background potential. The 10% Lagrangian radius at this moment drops to 0.073 pc, which yields a mean density of $6.0 \times 10^5\, M_\odot\, \text{pc}^{-3}$. For this simulation, the time is not long enough to see the contraction expansion phase that follows after core collapse. Finally, in this run, only one star is ejected from the cluster due to the higher escape velocity compared to the cluster without the external potential.
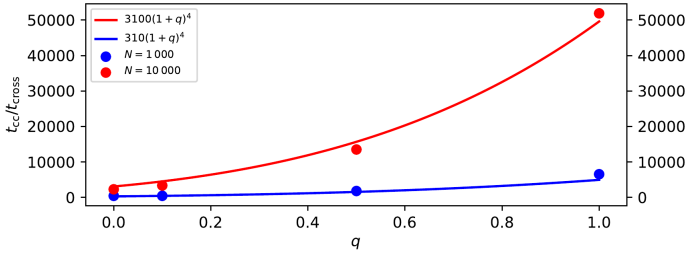
Fig. 3. Core collapse time t_{cc} divided by the crossing time t_{cross} for clusters with $N = 1000$ (blue circles) and $N = 10\,000$ (red circles) as a function of $q = M_{ext}/M_{stars}$. We also plotted two relations that scale as $(1 + q)^4$ which fit our data and therefore suggest that if the core collapse time is proportional to the relaxation time of the cluster, then the relaxation time scales as $(1 + q)^4$, which is the same relation that we derive in Appendix A.
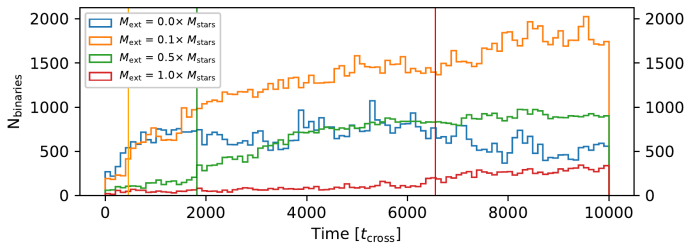

Fig. 4. Number of binary systems as a function of time and for different values for the mass of the external potential M_{ext} for simulations with $N = 1000$ and up to 8000 crossing times. The vertical lines mark the moments of core collapse and coincides with the onset of the formation of binary systems.

In order to understand the delay in the core collapse time when including a background potential, we define the parameter $q = M_{ext}/M_{stars}$ as the ratio between the mass of the external potential and the total mass in stars, then we find that the core collapse time scales as $t_{cc} \propto (1 + q)^4 \, t_{cross}$ as presented in Fig. 3. If we assume, as found by Spitzer (1987) that the core collapse time is proportional to the relaxation time, then according to our data the relaxation time is proportional to $t_{rh} \propto (1 + q)^4$, which is consistent with Eq. (A.12) for which we derived the relaxation time of a cluster in the center of an analytic external potential (see Appendix A):

$$t_{rh} = 0.138 \frac{N(1 + q)^4}{\log{(\gamma N)}} t_{cross}, \tag{6}$$

where the crossing time must be calculated from Eq. (1) with $q = M_{ext}/M_{stars}$ (see the Appendix in Leigh et al. 2013a and Leigh et al. 2014 for similar derivations but slightly modified to consider different cases).

A second important effect that we note is on the binary population. Our results show that in increasing the mass of the background potential, the number of binary systems that form decreases dramatically as shown in Fig. 4 due to the increased mean kinetic energy of the stars. Consequently, we also find that these binaries tend to be more tightly bound (see Fig. 5) given that they form at the hard-soft boundary, which is smaller for higher velocity dispersion (Leigh et al. 2015). This will certainly have an impact on the growth of a massive star through stellar mergers given that collisions are more likely to occur in binary systems.
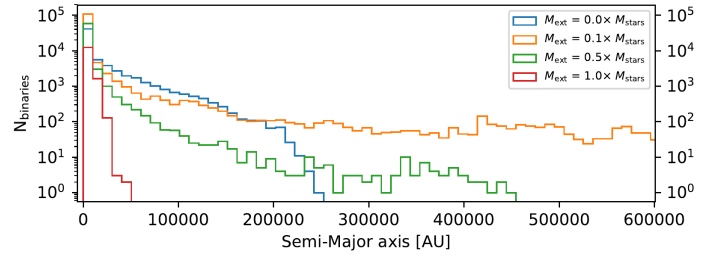

Fig. 5. Distribution of the semi-major axis of the binary population for the set of simulations listed in Table 1. The data clearly shows that increasing the mass of the external potential the formed binaries tend to be more tightly bound. Despite the fact that a low mass of the external potential ($M_{ext} < 1.0 \times M_{stars}$) may promote the formation of wider binaries, these systems tend to be short-lived due to the higher velocities of all the stars. This figure is only intended to show the distribution of the semi-major axis and not the total number of binaries that formed.

3.2. Simulations that include stellar mergers

In the following, we present the results that we obtained when we included stellar mergers in the evolution of star clusters with and without an external Plummer potential. Additionally, we describe the effects introduced by this background potential on the formation of massive merger products. These simulations are listed in Table 2.

The first effect that we note is a delay in the runaway growth of the central object, which is explained by the delay in the core collapse time due to a larger relaxation time when increasing the mass of the potential, as can be seen in Eq. (6). Moreover with this external force, binary systems are harder to form, as shown in Fig. 4 and these binaries tend to be more compact.

Here we describe the time evolution for two clusters with $N = 1000$ stars, with and without an external potential, which correspond to simulations number 17 and 45 in Table 2 and we also present their evolution in Figs. 6 and 7, respectively. These simulations serve as examples of the typical evolution of the runs that include stellar mergers, given that all the simulated clusters follow very similar patterns.

In our runs, we identify three types of mergers: namely hyperbolic mergers, which are mergers that occur between stars that are not gravitationally bound; binary mergers, which occur between stars that are part of a binary system; and chain mergers, which occur between stars that are part of a higher order system, for example, triples. Before the onset of runaway mergers occurs in all of the clusters, there is a nearly constant merger rate for hyperbolic mergers which do not produce a single massive star, but instead several less massive stars that eventually sink to the cluster center, thus finally contributing to the growth of the most massive star. We note that the hyperbolic merger rate in clusters that do not include an external potential is only maintained for short periods of time (see Fig. 6); whereas in clusters that include the extra force, the hyperbolic merger rate is maintained until the end of the simulation (see Fig. 7). Chain mergers are very rare with only a handful having been identified among all of our simulations.

During the period before the rapid growth of the most massive star, relaxation processes drive an energy flow from the central parts of the cluster (inside the half-mass radius) via high velocity stars that migrate to the cluster halo and cause the expansion of the outer parts. All of the clusters evolve toward core collapse, but not all of them reach that stage because for large stellar radii $R_{star} \geq 100\,R_{\odot}$, the growth of the central star
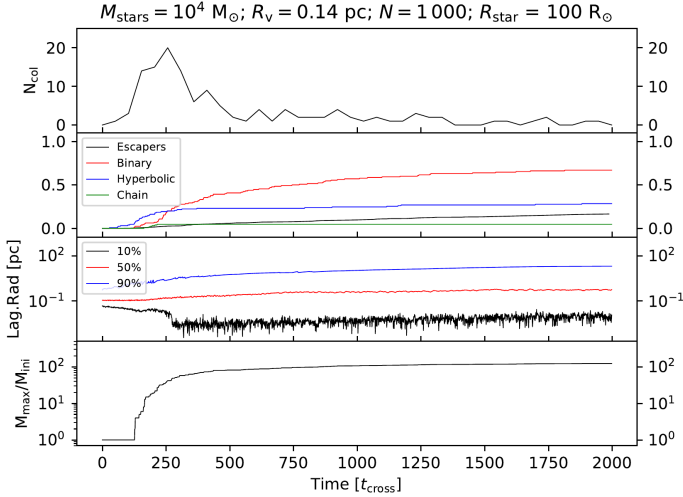
Fig. 6. Evolution of a cluster with $N = 1000$ stars, total mass $M_{stars} = 10^4 \, M_\odot$, $R_v = 0.14 \, pc$, and $R_{star} = 100 \, R_\odot$. *Uppermost panel*: number of mergers as a function of time, the fraction of binary, hyperbolic, and chain mergers in the *second panel* along with the fraction of stars that escape from the cluster. *Third panel*: 10, 50 and 90% Lagrangian radii, and *bottom panel*: mass growth of the most massive object that formed through mergers in the cluster.

Fig. 7. Evolution of a cluster with $N = 1000$ stars, stellar mass $M_{stars} = 10^4 \, M_\odot$, $R_v = 0.14 \, pc$, and $R_{star} = 100 \, R_\odot$ in the center of an external potential with $M_{ext} = 10^4 \, M_\odot$. *Uppermost panel*: number of mergers as a function of time, the fraction of binary, hyperbolic, and chain mergers in the *second panel*, along with the fraction of stars that escape from the cluster. *Third panel*: 10, 50, and 90% Lagrangian radii, and *bottom panel*: mass growth of the most massive object that formed through mergers in the cluster. The drop in the 50% Lagrangian radius toward the end of the simulation suggests that the central object may grow up to 5000 $M_\odot$.

is fast and the drop in the 10% Lagrangian radius that we see in Fig. 6 occurs because the central object has already gathered 10% of the cluster mass, and thus we see the position of the central star rather than a collapsed core. The onset of growth for the central star is also marked by a rapid increase in the merger rate of stars in binary systems despite the presence of an external potential.

An important difference that we note when including the background potential is on the expansion of the clusters and the fraction of escaping stars. In this sense we found that the external potential prevents the evaporation of the cluster (see panel 2 of Fig. 7) and keeps it compact so the mergers can continue for longer periods of time, potentially gathering up to 50% or more of the cluster mass in the central object, as the third panel of Fig. 7 suggests.

3.3. Formation and growth of the most massive star

One important goal of this research is to address the effect of the external potential on the formation of a massive star by stellar mergers. Thus, we present the results regarding the mass growth of the most massive star in our clusters, along with a description of the effects introduced by the background potential.

The first important effect is a delay in the formation of the most massive star due to the increased stellar velocity, which in turn causes relaxation processes to be slower. This then leads to a reduction in the number of binary systems that form, at a given time, if the mass of the external potential is comparable to the total stellar mass. On the other hand, the external potential can also favor the mass growth of the central star by preventing the evaporation and expansion of the cluster.

In the following, we present a model that we used to estimate the mass of the central object at different times for both a cluster with and without an external potential. For this, we followed the same method described in Reinoso et al. (2018).

In the lower panel of Fig. 8, we first present an example of the mass growth of the most massive star, which undergoes a very rapid growth at around 1000–1500 t_{cross}. This coincides with the
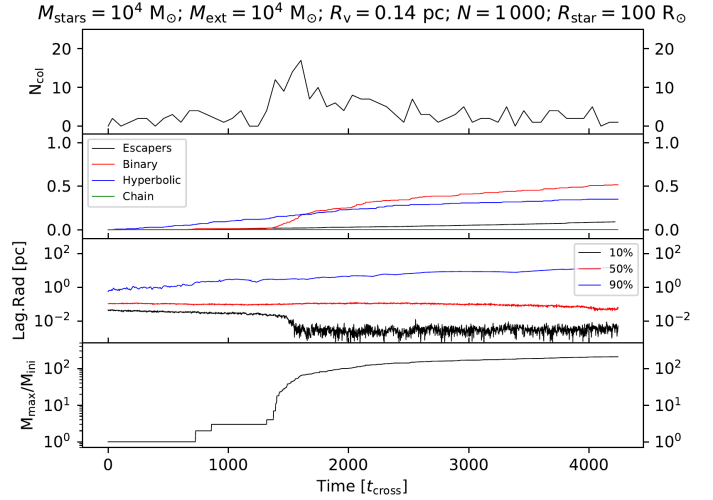

Fig. 8. Example of a Gaussian fit to the number of mergers with the central star for simulation number 45 listed in Table 2. *Top panel*: number of mergers with the most massive star as a function of time (black solid line) along with the Gaussian function that we used to estimate the total number of mergers at different times. The parameters t_{delay} and $t_{duration}$ are also shown in the figure. *Bottom panel*: mass growth of the central star whose rapid growth coincides with the peak in the number of mergers.

peak in the number of mergers with the central object as shown in the top panel of the same figure.

We fit the Gaussian function presented in Eq. (7) to the combined data from the six random realizations for each simulation setup presented in Table 2 in order to get an estimate for the number of mergers with the central object during the rapid growth. Thus, we define the delay time t_{delay} as the time at which the peak in the Gaussian occurs, and the height A of the Gaussian gives us an estimate for the number of mergers at t_{delay}.

Additionally, we define the duration time $t_{\text{duration}} = FWHM/\left(2\sqrt{2\ln 2}\right)$, with FWHM being the full width at half maximum of the Gaussian. An illustration of the fitting formula and two parameters are shown in the top panel of Fig. 8. By doing this, we were able to obtain an estimate for the moment at which there is rapid growth of the most massive star (t_{delay}) and an estimate for the duration of this period (t_{duration}), which we can later combine with A and a normalization factor D to finally obtain the number of mergers experienced by the central star using Eq. (8) and therefore an estimate for its final mass at different times. Furthermore we determined D by comparing our model to the results from our simulations. We also show how well our model reproduces the data of our simulations in Figs. 9 and 10. The total number of mergers at time t can thus be calculated as:

$$N_{\text{merger}}(t) = A \exp\left(-\frac{(t - t_{\text{delay}})^2}{2t_{\text{duration}}^2}\right), \tag{7}$$

and the total number of mergers until a time t_{end} can be calculated as:

$$N_{\text{merger,total}} = AD \int_0^{t_{\text{end}}} \exp\left(-\frac{(t - t_{\text{delay}})^2)}{2t_{\text{duration}}^2}\right)dt. \tag{8}$$

Although the data is not a perfect Gaussian (see Fig. 8), we only need an estimate for the delay time t_{delay}, the duration time t_{duration}, and an estimate for the number of collisions A at t_{delay}. Following this procedure, we first combined the data of the six random realizations per each of the configurations listed in Table 2 and then applied the Gaussian fit of Eq. (7) to find the values of A, t_{delay}, and t_{duration} that we present in Figs. 11 and 12 for clusters with $M_{\text{ext}}/M_{\text{stars}} = 0.0$ (simulations 1–28 in Table 2) and in Fig. 13 for clusters with $M_{\text{ext}}/M_{\text{stars}} = 1.0$ (simulations 29–56 in Table 2). Then we fit these data using an implementation of the nonlinear least-squares Marquardt-Levenberg algorithm in `gnuplot` and obtained Eqs. (9)–(11) for clusters without an external potential and Eqs. (13)–(15) for clusters in a background potential. Using these equations, we were able to compute $N_{\text{merger,total}}$ assuming first $D = 1$ and we compared the calculated values to the real values from the simulations to adjust D and reproduce the results correctly. By doing this, we obtain Eqs. (12) and (16):

$$\log_{10}(A) = [0.104 \log_{10}(R_{\text{star}}) + 0.562]\log_{10}(N)$$
$$+ 0.358 \log_{10}(R_{\text{star}}) - 1.011, \tag{9}$$

$$\log_{10}(t_{\text{delay}}[t_{\text{cross}}]) = [-0.246 \log_{10}(N) + 0.443]\log_{10}(R_{\text{star}})$$
$$+ 0.954 \log_{10}(N) + 0.077, \tag{10}$$

$$\log_{10}(t_{\text{duration}}[t_{\text{cross}}]) = 0.430 \log_{10}(N) + 0.580, \tag{11}$$

$$\log_{10}(D) = -0.227 \log_{10}(R_{\text{star}}) - 1.791, \tag{12}$$

and the parameters for clusters in an external potential:

$$\log_{10}(A_{\text{ext}}) = [3.975 \times 10^{-5}N + 0.606]\log_{10}(R_{\text{star}})$$
$$+ 0.554 \log_{10}(N) - 1.510, \tag{13}$$

$$\log_{10}(t_{\text{delay,ext}}[t_{\text{cross,ext}}]) = [-0.006 \log_{10}(N) + 0.240]\log_{10}(R_{\text{star}})$$
$$+ 0.064 \log_{10}(N) - 1.170 + t_{\text{delay}}, \tag{14}$$

$$\log_{10}(t_{\text{duration,ext}}[t_{\text{cross,ext}}]) = -0.178 N^{0.119}\log_{10}(R_{\text{star}})$$
$$+ 2.163 N^{0.073} + 0.151, \tag{15}$$

$$\log_{10}(D_{\text{ext}}) = 0.053 \log_{10}(R_{\text{star}})$$
$$- 1.879 \times 10^{6.9N/10^6} - 0.778. \tag{16}$$
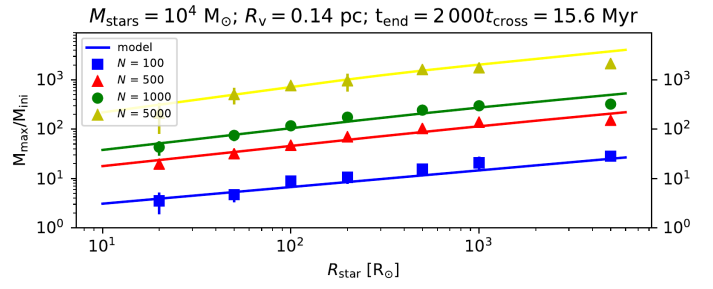
Fig. 9. Mean mass of the most massive star normalized by its initial mass, as a function of N and R_{star} for clusters without an external potential evolved until 2000 $t_{\text{cross}} = 15.6$ Myr. The symbols represent the mean values obtained from six simulations and the solid lines show the results of the calculations with our model presented in Eq. (8) using $t = 15.6$ Myr and the parameters obtained from Eqs. (9)–(12).
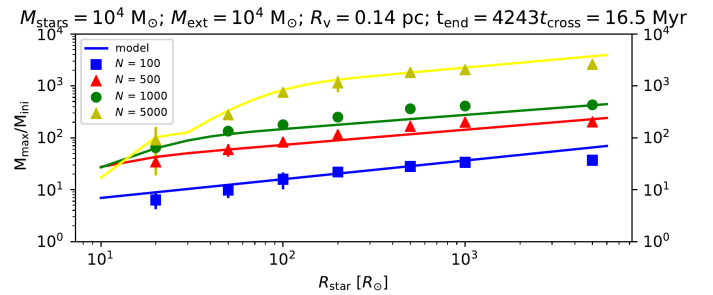
Fig. 10. Mean mass of the most massive star normalized by its initial mass, as a function of N and R_{star} for clusters without an external potential evolved until 3000 $t_{\text{cross}} = 16.5$ Myr, except for the point at $N = 5000$ and $R_{\text{star}} = 20 R_\odot$, which are simulations that were evolved until 4000 $t_{\text{cross}} = 22$ Myr. The symbols represent the mean values obtained from six simulations and the solid lines show the results of the calculations with our model presented in Eq. (8) using $t = 16.5$ Myr ($t = 22$ Myr for $N = 5000$ and $R_{\text{star}} < 50 R_\odot$) and the parameters obtained from Eqs. (13)–(16).

It is important to note that in Eqs. (10) and (11), the delay time t_{delay} and duration time t_{duration} are expressed in units of the crossing time of the cluster defined in Eq. (1) and consequently when calculating the total number of mergers until a time t_{end} using Eq. (8), this time must also be expressed in units of the crossing time t_{cross}. The same principle applies for Eqs. (14) and (15). That is, when calculating the number of mergers until a time t_{end} using Eq. (8), this time must be expressed in units of the cluster crossing time that have been modified by the mass of the external potential $t_{\text{cross,ext}}$, which is defined in Eq. (1).

The delay time for clusters in a background potential is defined in Eq. (14) as $t_{\text{delay,ext}} = t_{\text{delay}} + t_{\text{delay},M_{\text{ext}}=M_{\text{stars}}}$, which is the delay time for clusters without an external potential t_{delay} plus an additional term $t_{\text{delay},M_{\text{ext}}=M_{\text{stars}}} = [-0.006 \log_{10}(N) + 0.240]\log_{10}(R_{\text{star}}) + 0.064 \log_{10}(N) - 1.170$ that, in principle, may depend on the mass of the potential. However we do not examine this potential dependence here.

To help in the reading of the equations, we define a general equation of the form:

$$\log_{10}(x) = \alpha \log_{10}(R_{\text{star}}) + \beta \log_{10}(N) + \gamma \tag{17}$$

and present the parameters α, β, and γ in Table 3. They can be used to recover Eqs. (9)–(16).

Now we can estimate the number of mergers with the central star and thus the mass of this star up to a time t for clusters with different initial conditions, including the presence of an external

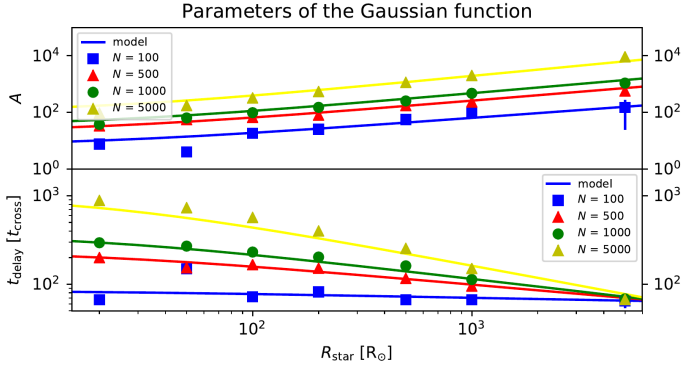**Fig. 11.** Parameters of the Gaussian fit to the number of mergers with the central star for simulations of clusters without an external potential. The data points were obtained after the fit to the combined data of six simulations. *Upper panel*: values of the normalization factor A for different values of N and R_{star} along with our model from Eq. (9). These data points show that the number of mergers increases with both N and R_{star} as expected. *Bottom panel*: different values of t_{delay} in addition to the different values of N and R_{star} along with the fitting function presented in Eq. (10). These points show that t_{delay} decreases with R_{star}, but it increases with N.

Fig. 12. $t_{duration}$ as a function of the number of stars N for clusters without an external potential. We found no clear correlations between $t_{duration}$ and R_{star}. The solid blue line shows the fitting function from Eq. (11).

Fig. 13. Parameters of the Gaussian fit to the number of mergers with the central star for simulations of clusters with an external potential. The data points were obtained after the fit to the combined data of six simulations. *Upper panel*: values of the normalization factor A_{ext} for different values of N and R_{star} along with our model from Eq. (8). These data points show that the number of mergers increases with both N and R_{star} as expected. *Middle panel*: different values of $t_{delay,ext}$ in addition to the different values of N and R_{star} along with the fitting function presented in Eq. (14). These points show that $t_{delay,ext}$ decreases with R_{star}, but it increases with N. Additionally, these values are larger than the values of t_{delay} for clusters without an external potential (see Fig. 11). *Lower panel*: values of $t_{duration,ext}$ along with the fitting function from Eq. (15). We clearly see a positive correlation with N and a negative correlation with R_{star}.

potential that is comparable to the total stellar mass in the cluster. This can be used as a very simplified model of a star cluster, which still contains gas during or shortly after the process of star formation or a nuclear star cluster. In Fig. 14, we show the expected fraction f_{merger} of the stars that merge with a single central object in a cluster without an external potential. In Fig. 15, this is shown for clusters in an external potential, for a broad combination of N and R_{star} after 1, 2, and 10 Myr assuming a cluster with $M_{stars} = 10^4\,M_\odot$, a virial radius of $R_v = 0.14$ pc, and a mass of the external potential $M_{ext} = M_{stars}$ for the second case. We used Eq. (8) for these calculations along with the parameters from Eqs. (9)–(12) to obtain the results presented in Fig. 14, and Eqs. (13)–(16) to obtain the results presented in Fig. 15. Our model gives the total number of stars $N_{merger,total}$ that merge with the central object in a given time interval, and thus assuming that all stars are equal during the time at which most of the collisions occur, we can estimate the mass of the central object as $M_{max} = N_{merger,total}\overline{m} = N_{merger,total}M_{stars}/N = f_{merger}M_{stars}$. Our results indicate that when collisions are maintained for short periods of time only, that is, 1 Myr, then the clusters without an external potential form more massive central stars than clusters with an external potential (see left panels of Figs. 14 and 15). This is due to the fact that the external potential dramatically increases the relaxation time of the cluster, as shown in Eq. (6). In fact the relaxation time depends on the ratio of external potential mass to stellar mass $q = M_{ext}/M_{stars}$ as $t_{relax} \propto q^4$.

As the time limit increases, we see that in both clusters with and without an external potential a more massive star emerges in the center. However, even more massive stars form in the cluster without an external potential for most values of N. However, there is an important difference in clusters that include a background potential, which is that the potential keeps the cluster compact as previously found by Leigh et al. (2014), and thus most of the cluster mass is able to eventually sink to the center at later times. This effect is visible in the left part of the middle panel in Figs. 14 and 15. We also note that for large N and R_{star} for clusters in a background potential and before core collapse, we may also expect mergers with the central star, not binary mergers but hyperbolic, given that in those cases the cross section for collisions is very large and the probability
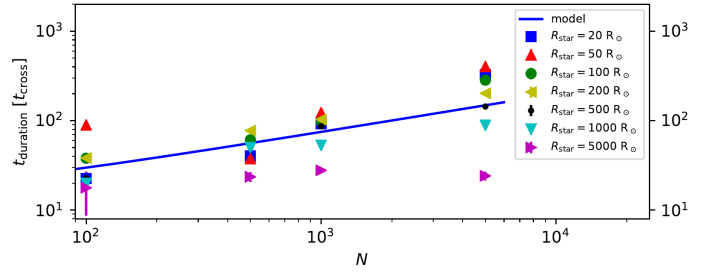
of hyperbolic collisions increases with stellar velocity, that is, if there is an external potential. Finally when the time limit is very long, that is, 10 Myr, we may expect final masses for the central object in the order of 0.3–0.4 M_{stars} for most clusters without an external potential and 0.4–0.7 for clusters in a background potential because the compactness of the cluster is maintained and collisions still occur at an approximately constant rate after the stage of runaway growth of the central star.

4. Implications for primordial clusters

In the following, we explore the implications of our results with respect to primordial star clusters, including both embedded and gas free. Here we particularly distinguish the case of standard Pop. III clusters as expected in a typical minihalo with about $10^6\,M_\odot$.

Table 3. Parameters for Eq. (17).

x	α	β	γ
A	0.358	$0.140 \log_{10}(R_{\text{star}}) + 0.562$	-1.011
$t_{\text{delay}}[t_{\text{cross}}]$	$-0.246 \log_{10}(N) + 0.443$	0.954	0.077
$t_{\text{duration}}[t_{\text{cross}}]$	0	0.430	0.580
D	-0.227	0	-1.791
A_{ext}	$3.975 \times 10^{-5} N + 0.606$	0.554	-1.510
$t_{\text{delay,ext}}[t_{\text{cross,ext}}]$	$-0.006 \log_{10}(N) + 0.240$	0.064	$-1.170 + t_{\text{delay}}[t_{\text{cross}}]$
$t_{\text{duration,ext}}[t_{\text{cross,ext}}]$	$-0.178 N^{0.119}$	0	$2.163 N^{0.073} + 0.151$
D_{ext}	0.053	0	$-1.879 \times 10^{6.9N/10^6} - 0.778$

Notes. Parameters for Eq. (17) that can be used to obtain Eqs. (9)–(16).

4.1. Standard Pop. III clusters (minihalos)

For a typical Pop. III star cluster, we assume a mass of 1000 $M_\odot$, which is consistent with a baryon fraction of about 10% and a star formation efficiency on the order of 1% in a $10^6\,M_\odot$ minihalo. We adopt a virial radius for the cluster on the order of 0.1 pc, which is consistent with the results from simulations and semi-analytic models (Clark et al. 2011a,b; Greif et al. 2011, 2012; Latif et al. 2013b; Latif & Schleicher 2015). We use a stellar radius of $100\,R_\odot$, which is characteristic of primordial protostars with accretion rates on the order of $10^{-3}\,M_\odot\,\text{yr}^{-1}$ (Hosokawa et al. 2012). The crossing time of the cluster then is 0.015 Myr. The number of stars that can be expected in such a cluster is uncertain, but here we adopt an estimate of about $N = 100$. Thus, a stellar mass of $m_{\text{star}} = 10\,M_\odot$. Using the relations that we found, we expect two collisions to occur within 1 Myr which correspond to a final mass of 30 $M_\odot$. If we assume now a lifetime of 10 Myr, we can expect a total of six collisions with the central star which correspond to a final mass of 70 $M_\odot$.

We consider now an embedded and accreting Pop. III star cluster with a stellar mass of 1000 $M_\odot$, a gas mass of 1000 $M_\odot$, a virial radius of 0.1 pc, and a mean stellar radius of $100\,R_\odot$. The crossing time of the cluster, according to Eq. (1), corresponds to 0.007 Myr. We also adopt a number of stars $N = 100$. Then our model predicts that no collisions occur within 1 Myr, but for a lifetime of 10 Myr we expect a total of 15 collisions and hence a central star with 160 $M_\odot$. We expect the lifetime of a massive primordial star to be in between this range, depending on the precise mass, the amount of rotation, and the effects that the collisions may have on the stellar evolution (Maeder & Meynet 2012). We therefore find that a moderate enhancement can be achieved within a normal cluster. We note that the values given here are the expected mean number of mergers. Individual clusters can deviate from these, both towards lower and higher fractions of mergers, potentially including clusters with zero mergers. This is especially the case for typical Pop. III clusters where the number of collisions can be expected to be comparable to the mean value because it is a chaotic collisional dynamical process.

4.2. Massive primordial clusters (atomic cooling halos)

As a next step, we address now the potential impact of collisions in a more massive atomic cooling halo with a total mass of $10^8\,M_\odot$. Under the right conditions and in particular if the cooling on larger scales is regulated by atomic hydrogen (Latif et al. 2014), a rather massive cluster of $10^4\,M_\odot$ can form, which is then exposed to larger accretion rates on the order of $10^{-1}\,M_\odot\,\text{yr}^{-1}$. We assume that the cluster consists of an initial number $N = $

1000 of stars, the virial radius is $R_{\text{v}} = 0.14$ pc, and that the stellar radii are somewhat enhanced compared to the standard Pop. III cluster due to the higher accretion rates, with a typical radius of about $300\,R_\odot$. The crossing time of the cluster according to Eq. (1) with $M_{\text{tot}} = 10^4\,M_\odot$ is then 0.0078 Myr. Using our derived model we expect about 51 collisions in 1 Myr, and about 168 within 10 Myr with a single central star. We again expect the realistic lifetime of the resulting massive star to be in between these extreme cases. In the case of an atomic cooling halo, we thus conclude that a considerable enhancement is possible as a result of stellar mergers. If we take the mean stellar mass, then the expected masses are 520–1690 $M_\odot$ after 1 and 10 Myr, respectively.

If we now consider the same cluster configuration but during the embedded phase, assuming a total mass in gas of $10^4\,M_\odot$, the crossing time of the cluster according to Eq. (1) with $q = M_{\text{ext}}/M_{\text{stars}} = 2$ is then 0.0039 Myr, and we expect a total of 16 collisions to occur within 1 Myr and a total of 199 mergers within 10 Myr. Again, by taking the mean stellar, mass this corresponds to a mass of 170–2000 $M_\odot$ within 1 and 10 Myr, respectively. Also the reported values here correspond to a mean, and there can be deviations to lower and higher merger fractions. Regardless, we expect the number of collisions and hence the final mass to remain within the same order of magnitude.

5. Discussion

We modeled the runaway growth of stars through mergers in the center of dense star clusters by including an analytic external potential in our N-body simulations. Our model relies on computing four parameters that depend on the number of stars N and their stellar radii R_{star}. These parameters are the delay time t_{delay}, the duration time for the collision process t_{duration}, and two normalization factors A and D. We then used these four parameters to integrate a Gaussian function and estimate the mass of the central object up to a time t. Although a Gaussian fit is a good tool to estimate t_{delay}, t_{duration}, and A (see Fig. 8), there is a deviation from this function when we include an external potential. In fact, when we compare the mass growth of the central object in clusters with and without an external potential (see, e.g. Figs. 6 and 7), we see a delay for clusters in an external potential and an initially less dramatic growth until the onset of mergers of stars in binary systems. This growth continues after the runaway growth and is seen as tails of a Gaussian in a plot of N_{mergers} versus time (see top panel of Figs. 9 and 10). This later growth is associated to hyperbolic mergers, that is, mergers of stars that are not bound by gravity, and this type of
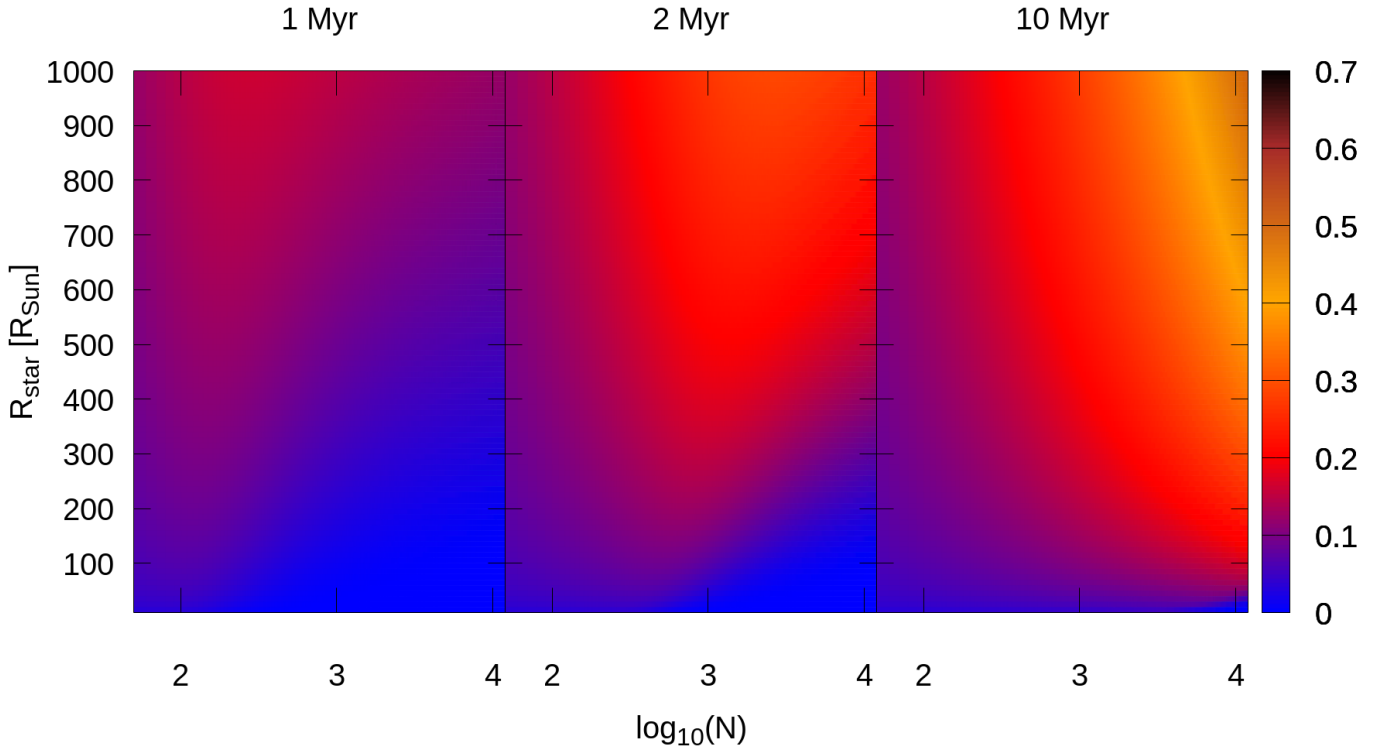
Fig. 14. Fraction of stars f_{merger} that merge with the central star in a cluster with a total stellar mass of $M_{\text{stars}} = 10^4\, M_\odot$ and a virial radius of $R_{\text{v}} = 0.14\,\text{pc}$ after 1 Myr (*left panel*), 2 Myr (*middle panel*), and 10 Myr (*right panel*) for different combinations of the number of stars N and the stellar radius R_{star} calculated using our model presented in Eq. (8). We can see that when the collisions are maintained for short periods of time, that is, 1 Myr, a massive object with $\sim f_{\text{merger}}\, M_{\text{stars}} = 0.15 \times 10^4\, M_\odot = 1500\, M_\odot$ is formed in the cluster center only when N is small (given that t_{delay} becomes larger than the integration time for large N) or large R_{star}. If the time limit is long, that is, 10 Myr, most of the clusters will form stars with $\sim 0.3\, M_{\text{stars}} = 3000\, M_\odot$.

merger becomes important when including an external potential because the cluster remains compact for longer periods of times (Leigh et al. 2014). The onset of collisions is delayed in simulations with an external potential relative to simulations without it.

We also have found a formula for the delay time when we include an external potential $t_{\text{delay,ext}} = t_{\text{delay}} + t_{\text{delay},M_{\text{ext}}=M_{\text{stars}}}$, which is basically the same expression for clusters without the external potential plus an additional term $t_{\text{delay},M_{\text{ext}}=M_{\text{stars}}}$ presented in Eq. (14). We present this parameter in this way so that we can investigate in the future if this can be used in a more general way as a function of the mass of the external field M_{ext} and if it is related to a longer relaxation time by means of its dependence on M_{ext} as suggested by Eq. (6).

The model derived here can be used as a first approximation to obtain the number of stellar mergers in embedded star clusters or to understand the effects of an external potential on the formation of massive merger products, which might also be important for the modelling of nuclear star clusters. Future research in this field will employ hydrodynamic modeling of the gas, which may prevent a large delay in the onset of runaway growth for the central star due to gas accretion and dissipative effects via star-gas or binary-gas interactions. These simulations also need to include realistic mass-radius relations for accreting protostars when aiming for a realistic modeling of the first star clusters in the Universe. By performing these suites of N-body simulations we have covered a large parameter space, and this allows us to provide hints as to which part of this parameter space the future, more sophisticated simulations should be focused on and the

subsequent physics that becomes relevant and often even dominant in these regimes.

Our simulations including mergers adopt a virial radius of $R_{\text{v}} = 0.14\, M_\odot$ and a total stellar mass of $M_{\text{stars}} = 10^4\, M_\odot$, but our results can be rescaled for different sizes and masses by means of the crossing time. In this work, we only consider for the initial conditions equal mass and equal radii stars but allow for the mass and radius to vary due to the mergers according to Eqs. (3) and (4), and in this sense our simulations represent an effective model where an average stellar radius is adopted over the period of time considered. This effective stellar radius should correspond to the typical radius when the majority of mergers are expected to occur.

Our model still lacks a more realistic stellar population, namely an initial mass function (IMF), which would naturally lead to mass segregation and subsequent mergers of the most massive stars in the cluster center. Moreover, we have not included the dissipative effects expected for star-gas interactions in our simulations that include an external potential, which could lead to the formation of more binary systems and hence more mergers (Leigh et al. 2014). In this sense, we do not expect a significant variation in the final mass of the most massive stars if the total mass in the most massive stars is comparable to the final mass obtained in our models, around 30–2000 $M_\odot$. Additionally, including an IMF, three-body encounters and two-body relaxation would cause the ejection of the smallest stars in the cluster, which could be an important source of stellar relics from the first star clusters in the early Universe. Another important way to proceed is a better modeling of the stellar mergers, in
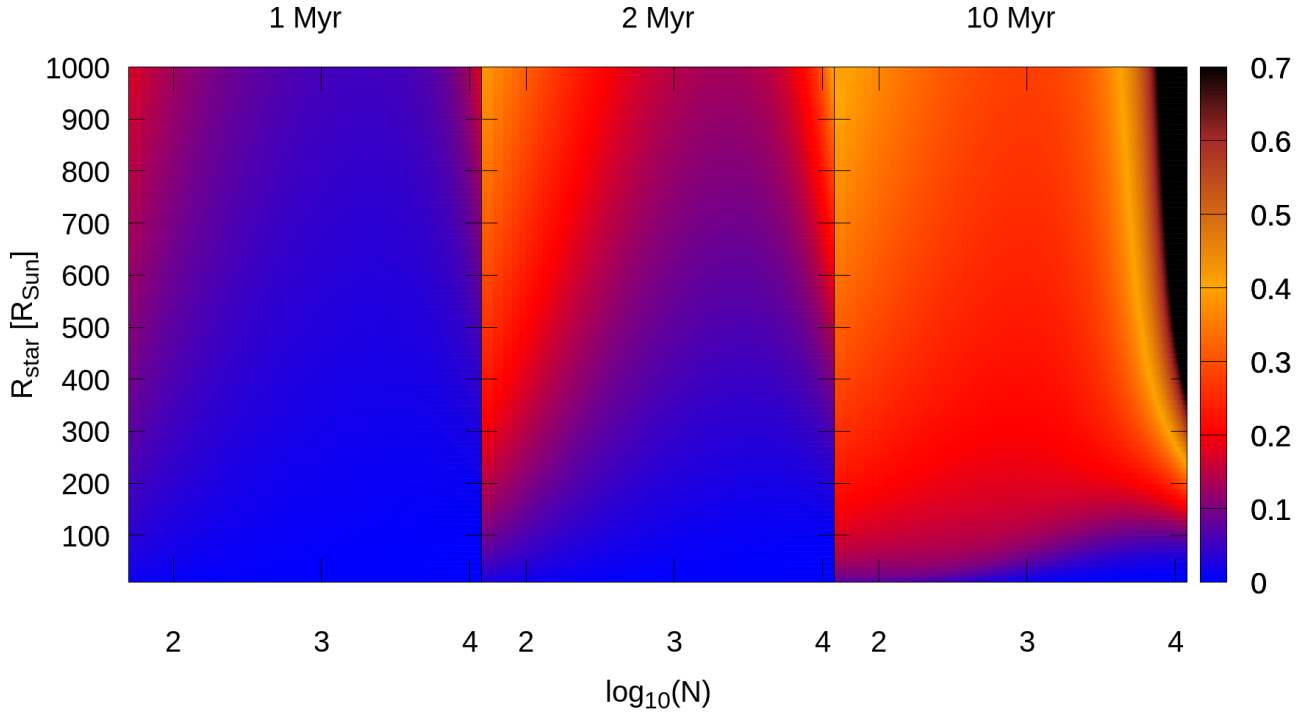
Fig. 15. Fraction of stars f_{merger} that merge with the central star in a cluster with a total stellar mass of $M_{stars} = 10^4 \, M_\odot$, a virial radius of $R_v = 0.14 \, pc$, and an external potential with a mass of $M_{ext} = M_{stars}$ after 1 Myr (*left panel*), 2 Myr (*middle panel*), and 10 Myr (*right panel*) for different combinations of the number of stars N and the stellar radius R_{star} calculated using our model presented in Eq. (8). We can see that when the collisions are maintained for short periods of time, that is, 1 Myr, an object that is not so massive with $\sim f_{merger} \, M_{stars} = 0.1 \times 10^4 \, M_\odot = 1000 \, M_\odot$ is formed in the cluster center only when N is very small (given that t_{delay} becomes larger than the integration time for large N) or when R_{star} is large. If the time limit is 2 Myr (*middle panel*), we expect that clusters with a small N experience core collapse and form a massive central star. However, if the number of stars is large and R_{star} is also large, given the higher velocity of the stars in those clusters compared to clusters without the external potential, there is a larger probability for hyperbolic mergers to occur before core collapse, which we see on the right-hand side of *middle panel*. If the time limit is long, that is, 10 Myr, most of the clusters form stars with $\sim 0.3-0.4 \, M_{stars} = 3000-4000 \, M_\odot$ and even $0.7 \, M_{stars} = 7000 \, M_\odot$ if N is large enough.

particular the mass loss during the stellar collisions which may be up to 25% of the total mass (Gaburov et al. 2010) and the collision product may even receive a kick velocity $>10 \, km \, s^{-1}$. More recent work on the effects of mass loss and its effect on runaway growth of a central star in a cluster shows that considering 5% mass loss in every collision produces objects which are 20–40% less massive at the end of the runaway growth compared to models without mass loss (Glebbeek et al. 2009; Alister Seguel et al. 2020). Thus regarding this, the results presented here should be taken as an upper limit on the mass of the merger product.

6. Conclusions

In this study, we have performed a set of 374 *N*-body simulations of dense, virialized star clusters and clusters in the center of an external potential including stellar mergers in order to understand the effects of the background force on the formation of massive stars and derive a model to estimate the mass enhancement of these objects in embedded star clusters. We find that the presence of an external potential delays the overall evolution of the star cluster and the formation of a massive central star through runaway collisions due to the increased kinetic energy of the stars, which in turn increases the relaxation time. However, the merger products become more massive (if the collision process is maintained for a long time) given that these clusters expand less than clusters without an external potential and so more stars are able to merge with the central star even after the process of runaway growth.

We also find that the increased velocity dispersion for star clusters in an external potential boosts the number of hyperbolic mergers , that is, mergers of stars that are not part of a binary or triple system, with up to 50–60% of the total number of mergers being hyperbolic mergers. Whereas in clusters without an external potential, this percentage is around 30%. This is due to the fact that in presence of a background potential, the clusters remain more compact (Leigh et al. 2013a, 2014) and hyperbolic mergers still may occur. Stellar ejections are highly suppressed in clusters in the center of an external potential.

We find a set of equations that can be used to estimate the mass of the merger product at different times for both clusters with and without an external potential, and we present an example of such calculations in Figs. 14, 15, and in Sect. 4 proving that if the process is not interrupted for long periods of time ($\geq 10 \, Myr$), the external potential enhances the mass of the central object by a factor of ~ 2. However, if the process is interrupted at early times ($\sim 1 \, Myr$), the clusters in a background potential produce objects only half as massive compared to objects formed in clusters without an external potential. When applied to Pop. III star clusters we find, for standard clusters formed in a minihalo, a moderate enhancement for the mass of the most massive star in the range of 10–160 $M_\odot$ within 1 and 10 Myr in embedded clusters. Whereas for a massive Pop. III star cluster that formed in an atomic cooling halo, we find that the mass of the most massive star lies in the range of 170–2000 $M_\odot$ in embedded clusters within 1 and 10 Myr.

References

Aarseth, S. J. 2000, in The Chaotic Universe, eds. V. G. Gurzadyan, & R. Ruffini, 286

Ahmad, A., & Cohen, L. 1973, J. Comput. Phys., 12, 389

Alister Seguel, P. J., Schleicher, D. R. G., Boekholt, T. C. N., Fellhauer, M., & Klessen, R. S. 2020, MNRAS, 493, 2352

Binney, J., & Tremaine, S. 1987, Galactic Dynamics (Princeton, N.J.: Princeton University Press)

Boekholt, T. C. N., Schleicher, D. R. G., Fellhauer, M., et al. 2018, MNRAS, 476, 366

Bonetti, M., Rasskazov, A., Sesana, A., et al. 2020, MNRAS, 493, L114

Bovino, S., Grassi, T., Schleicher, D. R. G., & Banerjee, R. 2016, ApJ, 832, 154

Clark, P. C., Glover, S. C. O., Klessen, R. S., & Bromm, V. 2011a, ApJ, 727, 110

Clark, P. C., Glover, S. C. O., Smith, R. J., et al. 2011b, Science, 331, 1040

Fan, X., Strauss, M. A., Richards, G. T., et al. 2006, AJ, 131, 1203

Fujii, M. S., & Portegies Zwart, S. 2013, MNRAS, 430, 1018

Gaburov, E., Lombardi, J. C., & Portegies Zwart, S. 2010, MNRAS, 402, 105

Glebbeek, E., Gaburov, E., de Mink, S. E., Pols, O. R., & Portegies Zwart, S. F. 2009, A&A, 497, 255

Greif, T. H., Springel, V., White, S. D. M., et al. 2011, ApJ, 737, 75

Greif, T. H., Bromm, V., Clark, P. C., et al. 2012, MNRAS, 424, 399

Haemmerlé, L., Woods, T. E., Klessen, R. S., Heger, A., & Whalen, D. J. 2018, MNRAS, 474, 2757

Hosokawa, T., Omukai, K., & Yorke, H. W. 2012, ApJ, 756, 93

Hosokawa, T., Yorke, H. W., Inayoshi, K., Omukai, K., & Yoshida, N. 2013, ApJ, 778, 178

Katz, H., Sijacki, D., & Haehnelt, M. G. 2015, MNRAS, 451, 2352

Klessen, R. S., Glover, S. C. O., & Clark, P. C. 2012, MNRAS, 421, 3217

Kustaanheimo, P., & Stiefel, E. 1965, J. Reine Angew. Math., 218, 204

Latif, M. A., & Schleicher, D. R. G. 2015, MNRAS, 449, 77

Latif, M. A., Schleicher, D. R. G., Schmidt, W., & Niemeyer, J. 2013a, ApJ, 772, L3

Latif, M. A., Schleicher, D. R. G., Schmidt, W., & Niemeyer, J. C. 2013b, MNRAS, 436, 2989

Latif, M. A., Schleicher, D. R. G., Bovino, S., Grassi, T., & Spaans, M. 2014, ApJ, 792, 78

Latif, M. A., Omukai, K., Habouzit, M., Schleicher, D. R. G., & Volonteri, M. 2016, ApJ, 823, 40

Leigh, N., Sills, A., & Böker, T. 2013a, MNRAS, 433, 1958

Leigh, N. W. C., Böker, T., Maccarone, T. J., & Perets, H. B. 2013b, MNRAS, 429, 2997

Leigh, N. W. C., Mastrobuono-Battisti, A., Perets, H. B., & Böker, T. 2014, MNRAS, 441, 919

Leigh, N. W. C., Giersz, M., Marks, M., et al. 2015, MNRAS, 446, 226

Maeder, A., & Meynet, G. 2012, Rev. Mod. Phys., 84, 25

Mardling, R. A., & Aarseth, S. J. 2001, MNRAS, 321, 398

Mortlock, D. J., Warren, S. J., Venemans, B. P., et al. 2011, Nature, 474, 616

Omukai, K., & Palla, F. 2001, ApJ, 561, L55

Omukai, K., & Palla, F. 2003, ApJ, 589, 677

Omukai, K., Tsuribe, T., Schneider, R., & Ferrara, A. 2005, ApJ, 626, 627

Plummer, H. C. 1911, MNRAS, 71, 460

Reed, S. L., Banerji, M., Becker, G. D., et al. 2019, MNRAS, 487, 1874

Reinoso, B., Schleicher, D. R. G., Fellhauer, M., Klessen, R. S., & Boekholt, T. C. N. 2018, A&A, 614, A14

Sakurai, Y., Yoshida, N., Fujii, M. S., & Hirano, S. 2017, MNRAS, 472, 1677

Sakurai, Y., Yoshida, N., & Fujii, M. S. 2019, MNRAS, 484, 4665

Schleicher, D. R. G., Palla, F., Ferrara, A., Galli, D., & Latif, M. 2013, A&A, 558, A59

Smith, R. J., Glover, S. C. O., Clark, P. C., Greif, T., & Klessen, R. S. 2011, MNRAS, 414, 3633

Smith, R. J., Hosokawa, T., Omukai, K., Glover, S. C. O., & Klessen, R. S. 2012, MNRAS, 424, 457

Spitzer, L. 1987, Dynamical Evolution of Globular Clusters (Princeton, N.J.: Princeton University Press)

Stahler, S. W., Palla, F., & Salpeter, E. E. 1986, ApJ, 302, 590

Suazo, M., Prieto, J., Escala, A., & Schleicher, D. R. G. 2019, ApJ, 885, 127

Wise, J. H., Regan, J. A., O'Shea, B. W., et al. 2019, Nature, 566, 85

Woods, T. E., Heger, A., Whalen, D. J., Haemmerlé, L., & Klessen, R. S. 2017, ApJ, 842, L6

Wu, X.-B., Wang, F., Fan, X., et al. 2015, IAU General Assembly, 29, 2251223

Appendix A: Modification of the half-mass relaxation time-scale

We have seen that when we include an external potential in a star cluster, the overall evolution seems to be delayed, in particular the core collapse times-scale rapidly increases with the mass of the external potential. Until now, we have used the usual half-mass relaxation time-scale defined in Eq. (5) (Spitzer 1987). However, this is probably not adequate when we include an external potential because in that case, considering a virialized cluster, the root mean square (rms) velocity of the stars is higher due to the extra force exerted by the potential and this certainly modifies the time-scale on which stellar encounters are going to modify the higher velocity of the stars. In order to account for this effect, here, we derive a modified relaxation time-scale with the aid of a new parameter $q = M_{\text{ext}}/M_{\text{stars}}$. We begin with the usual derivation of the relaxation time assuming virial equilibrium, a similar derivation can be found in Binney & Tremaine (1987):

$$2T + U = 0. \tag{A.1}$$

We note that $T = \frac{1}{2}M_{\text{stars}}\langle v^2 \rangle$ is the kinetic energy and $|U| = \frac{GM}{2R_v}$ is the potential energy. In this case, M_{stars} is the total mass in stars, $\langle v^2 \rangle$ is the mean velocity squared of the stars, $M = M_{\text{stars}} + M_{\text{ext}}$ is the total mass, that is, the mass in stars plus the mass of the external potential M_{ext}, and R_v is the virial radius of the cluster, which in this case is the same virial radius for the external potential. Now we write the total mass as a function of q:

$$M = M_{\text{stars}} + M_{\text{ext}},$$
$$M = M_{\text{stars}}\left(1 + \frac{M_{\text{ext}}}{M_{\text{stars}}}\right),$$
$$M = M_{\text{stars}}(1 + q). \tag{A.2}$$

We begin now with a derivation for the change of the velocity of a star due to an encounter with another star. The force that one star feels due to the other star is (see Fig. A.1):

$$F = \frac{GMm}{d^2} = \frac{GMm}{b^2 + V^2t^2}, \tag{A.3}$$

where M is the mass of one star and m is the mass of the other star, and d is the impact parameter or distance of closest approach. Now we assume that the velocity change ΔV of the star with mass M in the direction parallel to V is small, and only the perpendicular component of the velocity is changed due to the perpendicular force:

$$F_\perp = F\sin\phi = F \times \frac{b}{d} = \frac{GMmb}{(b^2 + V^2t^2)^{3/2}}, \tag{A.4}$$

$$F_\perp = M\frac{dV_\perp}{dt}. \tag{A.5}$$

Next we want to know the time at which the perpendicular velocity changes by an amount $\Delta V \sim V$, which is the relaxation time-scale. Therefore, we integrate Eq. (A.5) so the final
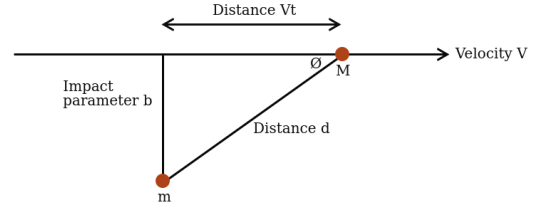

Fig. A.1. Trajectory of a star with mass M that passes close to another star of mass m, which causes a small deflection on the velocity vector V.

perpendicular velocity is:

$$\Delta V = \int_{-\infty}^{\infty} \frac{dV_\perp}{dt}dt,$$
$$= \int_{-\infty}^{\infty} \frac{F_\perp}{M}dt,$$
$$= \int_{-\infty}^{\infty} \frac{Gmb}{(b^2 + V^2t^2)^{3/2}}dt,$$
$$= \frac{2Gm}{bV}.$$

As the star receives many deflections in different directions, we are interested in the mean value of the squares of the velocity kicks $\langle \Delta V_\perp^2 \rangle$ that can be found integrating all the small deflections as:

$$\langle \Delta V_\perp^2 \rangle = \int_{b_{\text{min}}}^{b_{\text{max}}} \left(\frac{2Gm}{bV}\right)^2 dN,$$

where dN is the expected number of encounters that occurs in a time t between impact parameters b and $b + db$ for a star with typical velocity V, this is:

$$dN = n \times Vt \times 2\pi bdb,$$

where n is the number density of stars, then,

$$\langle \Delta V^2 \rangle = \int_{b_{\text{min}}}^{b_{\text{max}}} nVt\left(\frac{2Gm}{bV}\right)^2 2\pi bdb,$$
$$= \frac{8\pi G^2 m^2 nt}{V}\int_{b_{\text{min}}}^{b_{\text{max}}} \frac{db}{b},$$
$$= \frac{8\pi G^2 m^2 nt}{V}\ln\left(\frac{b_{\text{max}}}{b_{\text{min}}}\right). \tag{A.6}$$

After enough time, the perpendicular velocity of one star grows to its original speed, this time is the relaxation time-scale that we can derive using Eq. (A.6):

$$t_{\text{relax}} = \frac{V^3}{8\pi G^2 m^2 n\ln\left(\frac{b_{\text{max}}}{b_{\text{min}}}\right)}. \tag{A.7}$$

The term $\frac{b_{\text{max}}}{b_{\text{min}}}$ is often written as Λ and is the ratio of the size of the system to the "strong encounter distance" $b_{\text{min}} = 2Gm/V^2$, which is the distance at which an encounter with another star would result in a 90 degree deflection. This ratio $\frac{b_{\text{max}}}{b_{\text{min}}}$, for a system of identical N stars is found to be $\frac{b_{\text{max}}}{b_{\text{min}}} = \gamma N$ (Spitzer 1987), with $\gamma = 0.4$. This definition of the relaxation time-scale is useful to estimate the core collapse time, which typically occurs between 15–20 half-mass relaxation times. The problem comes when we include an analytic external potential and evolve the

cluster at the center of this potential. In this case, we have an extra force acting on the stars, and therefore a virialized cluster under the influence of this external potential has a larger potential energy and also a larger kinetic energy compared to a cluster in which there is not an external potential. This should increase the relaxation time-sale as the velocity of the stars increases and the number and masses of stars is kept constant. We now derive the relaxation time for a cluster under the influence of an external potential, assuming that this potential follows the same mass distribution of the stars and with the same virial radius. In Recalling the condition for virial equilibrium from Eq. (A.1) and the total mass for the cluster from Eq. (A.2) we find that:

$$2T + U = 0,$$

$$2\left(\frac{1}{2}NmV^2\right) - \frac{GM_{tot}^2}{R_v} = 0,$$

$$M_{stars}V^2 = \frac{GM_{stars}^2(1+q)^2}{R_v},$$

$$V = \sqrt{\frac{GM_{stars}}{R_v}}(1+q),$$

where V is the rms velocity of the stars, N is the number of stars, m is the mass of a single star, $M = M_{stars} + M_{ext}$ is the total mass, that is, the mass of the stars plus the mass of the external potential, and $q = \left(1 + \frac{M_{ext}}{M_{stars}}\right)$ and R_v is the virial radius of the system. When $q = 0$, we get the typical velocity for stars in a cluster which is in virial equilibrium:

$$V = \sqrt{\frac{GM_{stars}}{R_v}}, \tag{A.8}$$

but for a cluster in virial equilibrium and with a background potential, the typical velocity is modified as:

$$V_{ext} = \sqrt{\frac{GM_{stars}}{R_v}}(1+q),$$
$$V_{ext} = V(1+q), \tag{A.9}$$

where V_{ext} is the rms velocity of the stars in the presence of an external potential and V is the rms velocity of stars without a background potential.

The relaxation time is often expressed as a function of the crossing time t_{cross} of the cluster, which is simply the time it takes for a star with the typical velocity V to cross the system:

$$t_{cross} = \frac{R_v}{V}, \tag{A.10}$$

then, combining Eqs. (A.7) and (A.10) the relaxation time for clusters without an external potential is:

$$t_{relax} = \frac{V^4}{8\pi G^2 m^2 nR_v \ln\left(\frac{b_{max}}{b_{min}}\right)} t_{cross}. \tag{A.11}$$

Now, if we include an external potential, $q \neq 0$, and in substituting Eqs. (A.9) for (A.10), the crossing time for a cluster in an external potential is:

$$t_{cross,ext} = \frac{R_v}{V(1+q)},$$
$$t_{cross,ext} = \frac{t_{cross}}{(1+q)}. \tag{A.12}$$

Subsequently the relaxation time for clusters in an external potential must be:

$$t_{relax,ext} = \frac{V_{ext}^4}{8\pi G^2 m^2 nR_v \ln\left(\frac{b_{max}}{b_{min}}\right)} t_{cross,ext}.$$

Now we replace Eq. (A.9) for Eq. (A.13) and we find:

$$t_{relax,ext} = \frac{V^4(1+q)^4}{8\pi G^2 m^2 nR_v \ln\left(\frac{b_{max}}{b_{min}}\right)} t_{cross,ext}, \tag{A.13}$$

Now in recalling that from the usual definition of the relaxation time we can define the half-mass relaxation time for a cluster of N equal mass stars as (Spitzer 1987):

$$t_{rh} = 0.138\frac{N}{\ln(\gamma N)} t_{cross}$$

then, for comparison purposes, we define the half-mass relaxation time-scale for clusters in an external potential as:

$$t_{rh,ext} = 0.138\frac{N(1+q)^4}{\ln(\gamma N)} t_{cross,ext}, \tag{A.14}$$

with $q = \frac{M_{ext}}{M_{stars}}$ and $\gamma = 0.4$ for equal mass stars.

Appendix B: Evolution of clusters in a background potential

In this section, we describe in more detail the results of our simulations that do not include stellar collisions and which are listed in Table 1. We show the evolution of the clusters with and without an external potential, and we find a delay in the overall evolution when increasing the mass of the external potential.

All of the clusters evolve toward core collapse, which we found upon visual inspection by looking for the first drop and subsequent rise in the 10% Lagrangian radius. The core collapse occurs for the clusters without a background potential at 456 $t_{cross} = 19.78\,t_{rh}$ for the cluster with $N = 1000$ (see Fig. B.1), and for the cluster with $N = 10\,000$ at 2306 $t_{cross} = 13.85\,t_{rh}$ (see Fig. B.1).

As the clusters evolve toward core collapse, the outer parts continually expand which leads, along with the onset of stellar ejections, to the evaporation of the clusters. We also note that the onset of ejections occur just after core collapse when binary systems form in the core and three body interactions lead to the ejection of stars. An ejection occurs if the distance from the center of mass of the cluster to a star is larger than 20 times the virial radius R_v and if the total energy of the star is greater than zero, that is, $E_{star} = E_{kin} + |E_{pot}| > 0$ with E_{kin} and E_{pot} being the kinetic and potential energy, respectively. These results are shown in Figs. 1 and B.1.

When we include a background potential with a low mass compared to the total mass in stars, $M_{ext} = 0.1 \times M_{stars}$ in our simulations with $N = 1000$, the core collapse time is 460 t_{cross}, which is similar to the core collapse time for the cluster without the external potential in terms of the crossing time of the cluster. However, this cluster show less expansion and only one star is ejected (see Fig. B.2).

For the case when the mass of the background potential is half the mass in stars, $M_{ext} = 0.5 \times M_{stars}$ the cluster evolves toward core collapse, which now occurs at 1820 $t_{cross} = 16\,t_{rh}$

Fig. B.1. Evolution of a cluster with $N = 1000$ stars, total mass $M_{stars} = 10^4\,M_\odot$ and $R_v = 1.0$ pc. *Top panel*: fraction of stars that were ejected from the cluster. *Bottom panel*: Lagrangian radius and the vertical green line marks the moment of core collapse. The time is presented in units of the crossing time of the cluster.

Fig. B.3. Evolution of a cluster with $N = 1000$ stars, total mass $M_{stars} = 10^4\,M_\odot$, $R_v = 1.0$ pc in a background potential with mass $M_{ext} = 5 \times 10^3\,M_\odot$. *Top panel*: fraction of stars that were ejected from the cluster. *Bottom panel*: Lagrangian radius and the vertical green line marks the moment of core collapse. The time is presented in units of the crossing time of the cluster.

Fig. B.2. Evolution of a cluster with $N = 1000$ stars, total mass $M_{stars} = 10^4\,M_\odot$ and $R_v = 1.0$ pc in a background potential with mass $M_{ext} = 10^3\,M_\odot$. *Top panel*: fraction of stars that were ejected from the cluster. *Bottom panel*: Lagrangian radius and the vertical green line marks the moment of core collapse. The time is presented in units of the crossing time of the cluster.

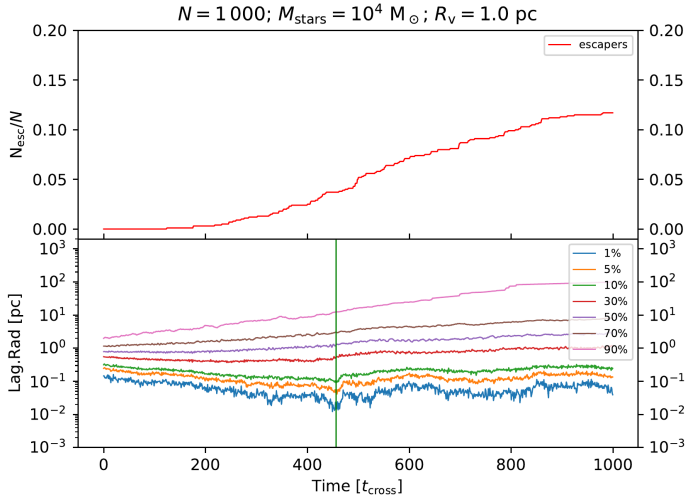**Fig. B.4.** Evolution of a cluster with $N = 1000$ stars, total mass $M_{stars} = 10^4\,M_\odot$, $R_v = 1.0$ pc in a background potential with mass $M_{ext} = 10^4\,M_\odot$. *Top panel*: fraction of stars that were ejected from the cluster. *Bottom panel*: Lagrangian radius and the vertical green line marks the moment of core collapse. The time is presented in units of the crossing time of the cluster.
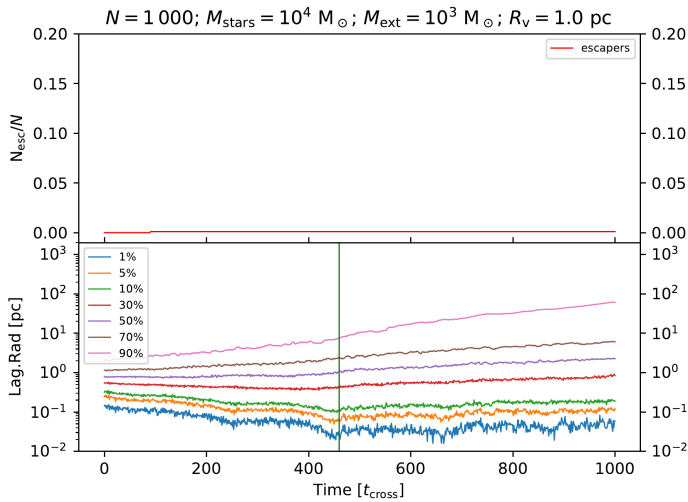
(calculated with Eq. (A.14)). The cluster again shows less expansion than the cluster without the external potential (see Fig.B.1) and only one single star is ejected.

For the case when the mass of the external potential is the same as the total mass in stars $M_{ext} = M_{stars}$, the cluster also evolves toward core collapse. However, this is now delayed now until 6553 t_{cross} as shown by the green vertical line in Fig. B.4.

When the number of stars is $N = 10\,000$, the behavior is essentially the same when we include a background potential; the global evolution is delayed due to the increased velocity of the stars. First, we present the case when the mass of the external potential is low $M_{ext} = 0.1 \times M_{stars}$ compared to the total mass in stars. The cluster also evolves toward core collapse, which now occurs at 3377 t_{cross} as indicated with a green vertical line in the bottom panel of Fig. B.5, which is $\sim 14\,t_{rh}$ (we used Eq. (A.14) to calculate the half mass relaxation time). The mean density inside the 10% Lagrangian radius at this moment is of $4.4 \times 10^5\,M_\odot\,pc^{-3}$, which is higher than the mean density at core collapse for the cluster without a background potential. Moreover the cluster in general shows less expansion when including the external potential.

When the mass of the external potential is half the total mass in stars, that is, $M_{ext} = 0.5 \times M_{stars}$, the core collapse is delayed until 13 519 t_{cross} as marked by the green vertical line in Fig. B.6 which is 16 t_{rh} (we used Eq. (A.14) again to calculate the half mass relaxation time) and during this moment the mean density inside the 10% Lagrangian radius is of $5.5 \times 10^5\,M_\odot\,pc^{-3}$. Our simulation is not long enough to see the expansion of the outer parts. however we do expect even less expansion than for the cluster with $M_{ext} = 0.1 \times M_{stars}$ and again until this time only 1 star has been ejected from the cluster, this was also found in Leigh et al. (2013a, 2014).
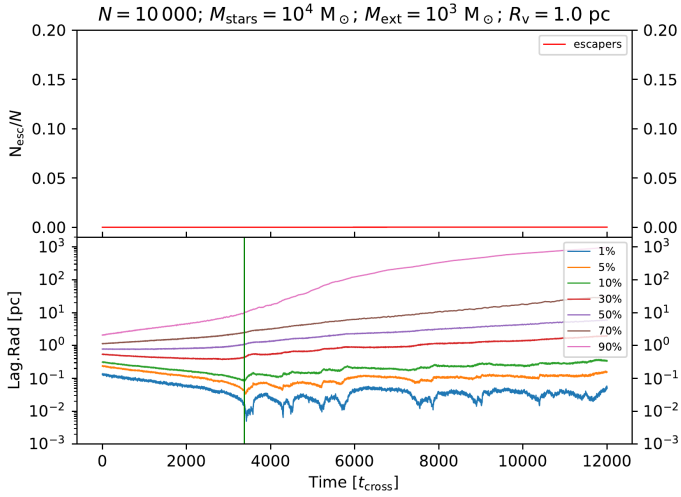
Fig. B.5. Evolution of a cluster with $N = 10\,000$ stars, total mass $M_{stars} = 10^4 M_\odot$ and $R_v = 1.0$ pc under the influence of a background potential with $M_{ext} = 10^3 M_{ext}$. *Top panel*: fraction of stars that were ejected from the cluster, which is negligible since only one star escaped the cluster. *Bottom panel*: Lagrangian radius and the vertical green line marks the moment of core collapse. The time is presented in units of the crossing time of the cluster.
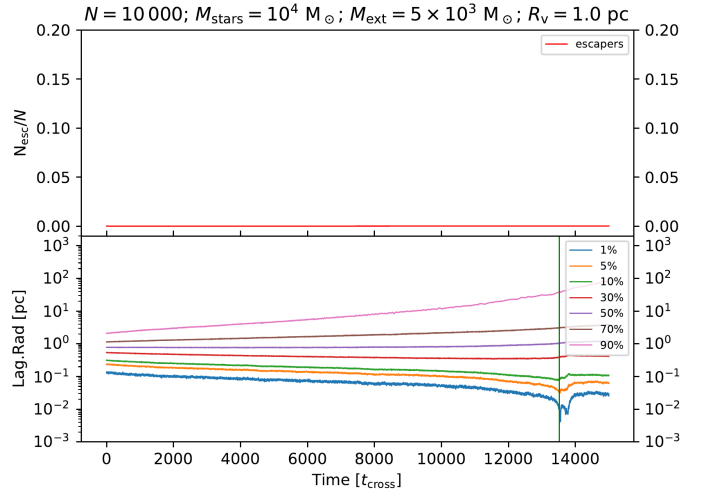
Fig. B.6. Evolution of a cluster with $N = 10\,000$ stars, total mass $M_{stars} = 10^4 M_\odot$ and $R_v = 1.0$ pc under the influence of a background potential with $M_{ext} = 5 \times 10^3 M_{ext}$. *Top panel*: fraction of stars that were ejected from the cluster, which is negligible since only one star escaped the cluster. *Bottom panel*: Lagrangian radius and the vertical green line marks the moment of core collapse. The time is presented in units of the crossing time of the cluster.
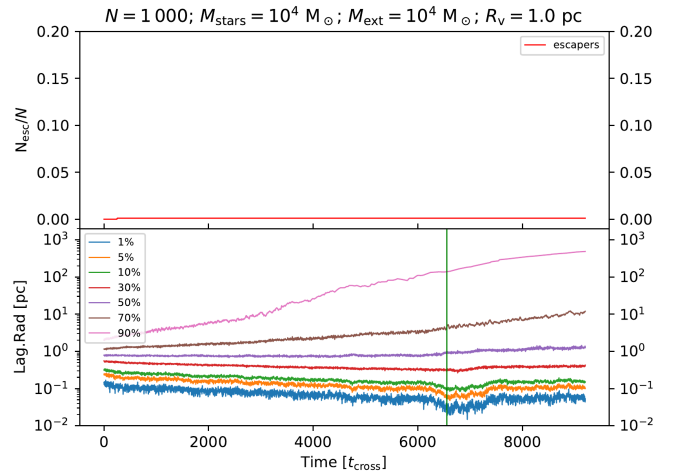
Chapter 6

The mean free path approximation and stellar collisions in star clusters: numerical exploration of the analytic rates and the role of perturbations on binary star mergers

6.1 Statement about my contribution

For the research article presented in this chapter my contribution consisted in the modification of the software employed. I also ran the numerical simulations and analyzed them. I gathered the observation data presented in the paper and modified the analytic collision rates in order to include gravitational focusing effects. I created all the tables and figures and wrote most of the article. All the authors contributed to the discussion and helped with the revision of the manuscript.

The mean free path approximation and stellar collisions in star clusters: numerical exploration of the analytic rates and the role of perturbations on binary star mergers

Bastián Reinoso [1],[*] Nathan W. C. Leigh,[2,3] Carlos M. Barrera-Retamal,[2] Dominik Schleicher,[2] Ralf S. Klessen [1,4] and Amelia M. Stutz[2,5]

[1]*Universität Heidelberg, Zentrum für Astronomie, Institut für Theoretische Astrophysik, Albert-Ueberle-Str. 2, D-69120 Heidelberg, Germany*
[2]*Departamento de Astronomía, Facultad Ciencias Físicas y Matemáticas, Universidad de Concepción, Av. Esteban Iturra s/n Barrio Universitario, Casilla 160-C, Concepción, Chile*
[3]*Department of Astrophysics, American Museum of Natural History, New York, NY 10024, USA*
[4]*Universität Heidelberg, Interdisziplinäres Zentrum für Wissenschaftliches Rechnen, Im Neuenheimer Feld 205, D-69120 Heidelberg, Germany*
[5]*Max-Planck-Institute for Astronomy, Konigstuhl 17, D-69117 Heidelberg, Germany*

ABSTRACT

In this paper, we compute predictions for the number of stellar collisions derived from analytic models based on the mean free path (MFP) approximation and compare them to the results of N-body simulations. Our goal is to identify the cluster conditions under which the MFP approximation remains valid. Adopting a range of particle numbers ($100 \leq N \leq 5000$) and different combinations of particle masses and radii, we explore three different channels leading to stellar collisions, all of which are expected to occur in realistic stellar environments. At high densities, binaries form from isolated three-body interactions of single stars. Hence, we consider collisions between single stars and collisions involving binary stars, after they form in our simulations. For the latter, we consider two channels for mergers, namely direct stellar collisions during chaotic single–binary interactions and perturbation-driven mergers of binaries due to random walks in eccentricity approaching unity. In the densest systems considered here, a very massive object is formed at the cluster centre, causing local stellar orbits to become increasingly Keplerian and the assumptions going into our analytic model to break down. Before reaching this limit, we obtain excellent agreement between our theoretical predictions and the simulations: The analytic rates are typically accurate to within one standard deviation for the entire parameter space considered here, but the agreement is best for short integration times. Our results have direct implications for blue straggler formation in dense star clusters, and stellar mergers in galactic nuclei hosting massive black holes.

Key words: methods: analytical – methods: numerical – globular clusters: general.

1 INTRODUCTION

The mean free path (MFP) approximation has been widely used throughout the field of astrophysical dynamics for centuries. Simple estimates based on the stellar number density, the collisional cross-section, and the stellar velocities ('nσv') for the rate of direct collisions between pairs of particles can be, and very often are, applied to a wide variety of astrophysical problems (e.g. Binney & Tremaine 1987), ranging from direct stellar collisions in star clusters and galactic nuclei (e.g. Fregeau et al. 2004; Portegies Zwart et al. 2004; Naoz et al. 2018), the growth of planetary embryos in protoplanetary discs (e.g. Goldreich & Tremaine 1982), tidal stripping during interactions between pairs of galaxies (e.g. Ogiya 2018), and even atoms and molecules colliding in gas clouds (e.g. Spitzer 1941a,b, 1942). Typically, the 'sticky-star approximation' is adopted to compute the relevant rates and time-scales, where a

collision is defined as occurring when the radii of two or more stars overlap in both time and space.

To date, few studies have considered the accuracy of analytic methods for computing the rates of particle collisions in realistic astrophysical environments (e.g. Hut 1983; Hut & Bahcall 1983; Fregeau et al. 2004). Most of the work that has been done focused on direct collisions between pairs of objects (galaxies, stars, planets, etc.) during isolated small-number chaotic interactions mediated by gravity. For example, Leigh & Geller (2012) studied the probability of collisions occurring during gravitationally bound small-number ($N = 3, 4, 5,$ and 6) chaotic interactions involving identical finite-sized particles. The authors showed that the collision probability scales approximately as N^2, as expected from combinatorics and the MFP approximation (i.e. the collision probability should be proportional to $\binom{N}{2}$). In subsequent studies Leigh & Geller (2015) and Leigh et al. (2017, 2018) expanded the parameter space to consider particles having different masses and radii. Eventually, they were able to build from first principles, on a combinatorics-based back bone, analytic predictions for the relative probabilities

[*] E-mail: bastian.reinoso@uni-heidelberg.de

of different collision scenarios occurring (e.g. multicollision scenarios). Using numerical simulations, they confirmed the validity of their method and demonstrated its robustness for any number of interacting particles with any combinations of particle masses and radii.

Other studies using numerical simulations of collisions involving stars, typically focused on cross-sections, since these can be inserted directly into the standard '$n\sigma v$' time-scales derived using the MFP approximation (e.g. Hut 1983; Hut & Bahcall 1983; Fregeau et al. 2004; Fregeau, Chatterjee & Rasio 2006). But these too only considered small numbers of particles, typically four or less. In a recent study Barrera et al. (2020) compared analytic collision timescales to collision times obtained from *N*-body simulations. They considered a range of particle numbers ($N \sim 10^3$) and included particles with different masses and radii. They showed that the collision times typically agree to within one standard deviation with the simulated results, and that the agreement is better for smaller *N* and a narrow mass spectrum.

In astrophysics, runaway collisions have been first suggested to be relevant in dense young star clusters and globular clusters (GCs; Portegies Zwart & McMillan 2002; Portegies Zwart et al. 2004). Baumgardt & Klessen (2011) explored them particularly in the context of young clusters, as a potential origin of very massive stars. In the early universe, runaway collisions in dense stellar clusters have been considered as a potential origin of massive black hole seeds, employing analytic relations (Devecchi & Volonteri 2009; Devecchi et al. 2012) as well as numerical simulations (Katz, Sijacki & Haehnelt 2015; Sakurai et al. 2017; Sakurai, Yoshida & Fujii 2019; Reinoso et al. 2018, 2020). Collisions in clusters of stellar-mass black holes were suggested to be relevant for the formation of massive black holes by Lupi et al. (2014). Furthermore, the interplay between collisions and accretion appears as a particularly promising mechanism for the formation of the first supermassive black hole (SMBH) seeds (Boekholt et al. 2018; Alister Seguel et al. 2020; Chon & Omukai 2020; Das et al. 2020; Tagawa, Haiman & Kocsis 2020). Stellar collisions are also invoked to explain the formation of exotic stellar populations, such as blue stragglers (BSs) and the S-stars, a group of high-mass stars distributed in a disc-like structure very close ($\lesssim 0.04$ pc) to Sgr A* in the Galactic centre (e.g. Eckart & Genzel 1997; Ghez et al. 2003; Naoz et al. 2018). Both BSs and the S-stars are thought to be products of stellar mergers between main-sequence (MS) stars.

It is important to understand how good is the '$n\sigma v$' approximation in extreme environments where frequent stellar collisions are expected to occur. The approximation may not be valid because cluster conditions are not constant over time. Two-body relaxation causes the core radius to shrink and the central stellar density to increase, and the core velocity dispersion along with it. Slower heavier stars that collide outside the core begin to drift into it via two-body relaxation, populating the cluster centre and subsequently transferring kinetic energy to other stars, having a direct impact on the velocity distribution of stars in both the core and the halo. If collisions are frequent, the mean stellar mass will also change, and more massive collision products have larger cross-sections for collisions. Furthermore, the hard-soft boundary varies as the masses of the binary components change and the core contracts to become hotter with a higher velocity dispersion, which would modify the time-scale for single–binary interactions. It may not be a good approximation to take then the average semimajor axis when computing the single–binary collision time-scale, but the only way to know for sure is to perform the numerical experiments and compare to the analytic theory, as we do in this paper. The presence of

collision products will also change the properties of binary systems since during interactions with single stars, they tend to retain higher mass stars and eject the lightest one. This will cause rapid evolution in the stellar mass function at both the high-mass and low-mass ends.

In this paper, we present a comparison between the number of stellar collisions obtained from *N*-body simulations of dense star clusters and the predicted number of collisions from analytic collision rates. We show that the predicted and simulated values agree to within a factor of order unity. We identify in our simulations collisions of binary stars that occur due to perturbations coming from single stars that pass close to the binary on hyperbolic orbits. We discuss the implications of this process for the formation of stellar exotica in realistic stellar environments.

The manuscript is organized as follows. We describe our *N*-body and analytic models in Section 2, and present the results of their comparisons in Section 3. We discuss the applicability of our results to the formation of stellar exotica in Section 4. A final discussion and summary is presented in Section 5.

2 METHODS

We present in this section the *N*-body models that served as initial conditions for the numerical simulations used in this paper. We also discuss how we count the number of collisions from our simulated data. Then we present the analytic model and describe how we compute the predicted number of stellar collisions. We focus our analysis to the cluster core and thus all the collisions presented in this paper (both from simulations and analytic rates) refer to collisions occuring in the core.

2.1 Initial conditions

In our study, we model compact star clusters assuming a Plummer distribution (Plummer 1911) with virial radius $R_v = 0.14$ pc. Every system is composed of identical stars initially having the same masses and radii, with a total stellar mass of $M_{\text{cluster}} = 10^4$ M$_\odot$. With these properties fixed, we vary the total number of stars *N* and the stellar radius R_{star} to produce 24 different *N*-body models, all of which are listed in Table 1. The initial masses of the stars are decided as $m_{\text{ini}} = M_{\text{cluster}}/N$. For each of the 24 models mentioned above, we run six simulations varying the initial random seed, yielding a total of 144 *N*-body simulations.

Every cluster begins in a state of virial equilibrium, and is left to evolve for 2000 *N*-body time units which equals 15.6 Myr in the lifetimes of our simulated clusters. We are here interested only in the first stages of the cluster evolution, as explained more clearly below (see the fourth column in Table 2).

2.2 Numerical simulations

All the simulations presented in this paper were performed with NBODY6 (Aarseth 2000), a direct *N*-body integrator which makes use of the fourth-order Hermite method, block time-steps, KS regularization for treating close encounters (Kustaanheimo & Stiefel 1965; Mikkola & Aarseth 1998), and a spatial hierarchy for the force computation (Ahmad & Cohen 1973). Stellar collisions are detected once the radii of particles overlap in both space and time during the integration, and they are replaced by a new single particle. This new particle is placed at the centre of mass of the previous configuration. The mass and velocity are computed assuming mass and linear momentum conservation. The new radius

Table 1. Initial conditions for each *N*-body model. We perform six simulations per model.

Model	N	m_{ini} $(M_\odot)$	R_{star} $(R_\odot)$	r_{core} (pc)	v_{rms} (km s^{-1})	n_{core} (10^6 pc^{-3})
1	100	100	20	0.042	17.450	0.318
2	100	100	50	0.042	16.865	0.327
3	100	100	100	0.045	11.818	0.266
4	100	100	200	0.058	12.063	0.124
5	100	100	500	0.061	12.194	0.108
6	100	100	1000	0.054	13.017	0.152
7	500	20	20	0.040	16.618	1.930
8	500	20	50	0.042	15.804	1.579
9	500	20	100	0.045	15.501	1.320
10	500	20	200	0.050	15.673	0.967
11	500	20	500	0.047	15.553	1.126
12	500	20	1000	0.040	15.678	1.864
13	1000	10	20	0.039	15.037	3.886
14	1000	10	50	0.047	15.640	2.252
15	1000	10	100	0.045	15.926	2.550
16	1000	10	200	0.044	15.648	2.751
17	1000	10	500	0.048	15.099	2.190
18	1000	10	1000	0.040	14.941	3.780
19	5000	2	20	0.042	15.099	16.014
20	5000	2	50	0.042	15.120	16.014
21	5000	2	100	0.043	15.095	15.153
22	5000	2	200	0.043	15.116	15.258
23	5000	2	500	0.043	15.117	15.153
24	5000	2	1000	0.043	15.097	15.258

is calculated by assuming that the density of the progenitors and the collision product are the same. For simplicity, we do not include in our simulations stellar evolution nor tidal interactions between stars.

2.3 Counting the number of collisions from the simulations

The majority of the collisions in our simulations happen in the cluster core (see below), or very close to it, therefore we focus our analysis on the central regions of our clusters. We extract the required information about stellar collisions from the output files and snapshots of NBODY6 and select only those collisions occurring inside the 10 per cent Lagrangian radius, which we will henceforth refer to as the core radius r_{core}. The snapshot output frequency is 1 *N*-body unit of time, which corresponds to 7800 yr.

We distinguish between two types of collisions here, according to the classification given by NBODY6. First, we have both hyperbolic collisions or, equivalently, collisions between stars that are not initially gravitationally bound. Second, we have binary–mediated collisions or collisions between two stars that become gravitationally bound before the collision event, and these mergers/collisions can be decomposed into two groups – mergers of the binary system mediated by perturbations from bound single stars, and collisions mediated by perturbations from unbound single stars (sometimes undergoing prolonged chaotic interactions, with the eccentricity doing a random walk to higher and higher values, before a merger occurs when the stellar radii overlap at pericentre).

We present for each *N*-body model, the average number of hyperbolic N_{Hyp} and binary-mediated N_{Bin} collisions in Table 2, as

well as the average total number of collisions $N_{col,sim}$. The errors are computed assuming Poisson statistics.

2.4 The analytic model

The analytic model that we use in this paper is constructed from the mean times or rates between stellar encounters derived from the MFP approximation. In a similar way to Leigh, Sills & Knigge (2011), we include single–single and single–binary interactions via encounter time-scales, but we include the gravitationally focused cross-sections in the derivation (see Appendix A), which are applicable to the cores of star clusters. Consequently, the mean time between single–single encounters in the core is given by

$$\tau_{1+1} = 8.3 \times 10^{13} (1 - f_b - f_t)^{-2} \left(\frac{10^3 \text{ pc}^{-3}}{2n_{core}} \right)^2$$
$$\times \left(\frac{1 \text{ pc}}{r_{core}} \right)^3 \left(\frac{5 \text{ km s}^{-1}}{v_{rms}} \right) \left(\frac{0.5 \text{ R}_\odot}{\langle R \rangle} \right)^2$$
$$\times \left[1 + 7635 \left(\frac{\langle m \rangle}{0.5 \text{ M}_\odot} \right) \left(\frac{0.5 \text{ R}_\odot}{\langle R \rangle} \right) \left(\frac{5 \text{ km s}^{-1}}{v_{rms}} \right)^2 \right]^{-1} \text{ yr,}$$
(1)

where f_b is the fraction of binary systems in the core, defined as $f_b = N_b/N_{core}$, where N_b is the number of binaries in the core and N_{core} is the total number of objects in the core (i.e. including both singles and binaries), r_{core} and n_{core} are the core radius and core number density, v_{rms} is the root-mean-square velocity, $\langle m \rangle$ and $\langle R \rangle$ are the mean stellar mass and mean stellar radius.

The mean time between single–binary interactions is given by

$$\tau_{1+2} = 1.8 \times 10^9 (1 - f_b - f_t)^{-1} f_b^{-1} \left(\frac{10^3 \text{ pc}^{-3}}{2n_{core}} \right)^2$$
$$\times \left(\frac{1 \text{ pc}}{r_{core}} \right)^3 \left(\frac{5 \text{ km s}^{-1}}{v_{rms}} \right) \left(\frac{1 \text{ AU}}{a_b} \right)^2$$
$$\times \left[1 + 53 \left(\frac{\langle m \rangle}{0.5 \text{ M}_\odot} \right) \left(\frac{1 \text{ AU}}{a_b} \right) \left(\frac{5 \text{ km s}^{-1}}{v_{rms}} \right)^2 \right]^{-1} \text{ yr,}$$
(2)

where a_b is the mean semimajor axis for binaries.

We note that binary–binary collisions can be ignored, due to the very low binary fractions in our simulations and the fact that single–binary interactions dominate over binary–binary interactions for $f_b \lesssim 0.1$ (Leigh et al. 2011).

We also attempted a different model in which we use equation (4) to estimate the number of single–single collisions between equal mass stars, combined with the gravitationally focused encounter rate for unequal mass stars presented in Leigh et al. (2017). A similar experiment was done in Barrera et al. (2020). This model, however, overestimates the number of collisions between unequal mass stars by a factor of ~ 2.

2.5 Calculating the predicted number of collisions from the analytic model

The quantities going into equations (1) and (2) are taken directly from our *N*-body simulations. For this purpose, we first choose a simulation time t_{sim} during which the core radius is smoothly decreasing over time, so we avoid going into the stage of core-collapse. The simulation times t_{sim} chosen for each model are listed

Table 2. Numbers and types of collisions for each model. We perform six simulations for each model and calculate the mean number of collisions within t_{sim}, both from our simulations (column 5) and from our analytic model (column 6). The ratio between the simulated and analytic number of collisions is presented in column 7 and plotted in Fig. 3. The number of hyperbolic and binary collisions from the simulations are presented in columns 8 and 10. We also present the number of 1+1 and 1+2 collisions derived from our analytic model in columns 9 and 11.

Model	N	R_{star} $(R_\odot)$	t_{sim} (Myr)	$N_{col, sim}$	$N_{col,analytic}$	$\frac{N_{col,sim}}{N_{col,analytic}}$	N_{Hyp}	N_{1+1}	N_{Bin}	N_{1+2}
1	100	20	0.400	0.333 ± 0.236	0.077	4.308	0.000	0.026	0.333	0.052
2	100	50	0.400	0.333 ± 0.236	0.094	3.559	0.000	0.094	0.333	0.000
3	100	100	0.400	0.500 ± 0.289	0.145	3.439	0.333	0.145	0.167	0.000
4	100	200	0.300	0.667 ± 0.333	0.216	3.085	0.333	0.202	0.333	0.014
5	100	500	0.200	0.667 ± 0.333	0.855	0.780	0.167	0.351	0.500	0.503
6	100	1000	0.150	0.833 ± 0.373	0.579	1.439	0.167	0.544	0.667	0.035
7	500	20	0.500	0.667 ± 0.333	1.444	0.462	0.167	0.254	0.500	1.189
8	500	50	0.900	4.333 ± 0.850	3.292	1.316	1.833	1.323	2.500	1.968
9	500	100	0.600	2.000 ± 0.577	3.027	0.661	1.500	1.581	0.500	1.446
10	500	200	0.530	4.333 ± 0.850	6.302	0.688	3.000	2.637	1.333	3.666
11	500	500	0.400	9.333 ± 1.247	9.205	1.014	6.167	4.909	3.167	4.295
12	500	1000	0.370	11.333 ± 1.374	14.469	0.783	9.500	8.820	1.833	5.649
13	1000	20	1.349	2.667 ± 0.667	2.595	1.028	2.333	1.896	0.333	0.699
14	1000	50	1.349	7.833 ± 1.143	8.741	0.896	5.667	4.780	2.167	3.960
15	1000	100	1.000	7.000 ± 1.080	8.860	0.790	4.167	5.960	2.833	2.901
16	1000	200	0.900	12.000 ± 1.414	14.812	0.810	9.833	10.545	2.167	4.268
17	1000	500	0.700	22.667 ± 1.944	25.634	0.884	17.833	17.521	4.833	8.114
18	1000	1000	0.500	28.667 ± 2.186	45.490	0.630	22.333	27.668	6.333	17.822
19	5000	20	5.316	66.667 ± 3.333	52.655	1.266	55.167	45.064	11.500	7.591
20	5000	50	3.500	75.000 ± 3.536	81.020	0.926	65.333	60.352	9.667	20.668
21	5000	100	3.200	147.500 ± 4.958	113.954	1.294	120.500	105.549	27.000	8.405
22	5000	200	2.200	171.000 ± 5.339	153.362	1.115	148.333	137.331	22.667	16.031
23	5000	500	1.200	164.333 ± 5.233	194.490	0.845	152.667	178.430	11.667	16.060
24	5000	1000	0.700	205.667 ± 5.855	255.998	0.803	190.167	235.863	15.500	20.136

in the fourth column of Table 2. We partition this time into 10 successive intervals, each with a length $\Delta t = 0.1 t_{sim}$ over which we compute the number of collisions expected from our analytic predictions according to averaged cluster core and stellar properties in that interval. This is illustrated for one of our simulations in Fig. 1 where we show in the top panel the evolution of the core radius and the partitioning of the simulation time t_{sim} into 10 smaller intervals via vertical black lines. The horizontal green lines in each interval mark the average core radius in the top panel and the mean binary fraction in the bottom panel. The number of intervals is chosen in such a way that we get representative values for the dynamical properties of the stars in the core by averaging over simulation snapshots, but avoiding large intervals over which the changing properties of the cluster become significant. We check that using 20 intervals does not change our results but using 5 or less intervals leads to lower predicted collision rates.

The total number of collisions expected from our analytic rates is calculated by summing over the number of collisions in each interval i:

$$N_{col,analytic} = \sum_{i=1}^{10} N_{1+1,i} + N_{1+2,i} \,, \tag{3}$$

where we define the number of collisions due to single–single interactions, occurring in the interval i, as

$$N_{1+1,i} = \frac{\Delta t}{\tau_{1+1,i}}. \tag{4}$$
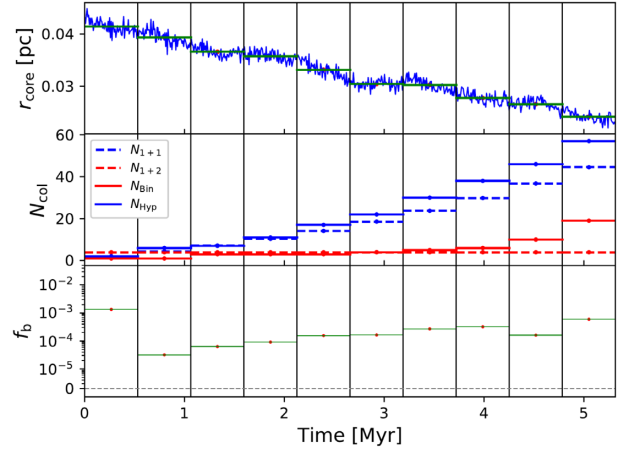
Figure 1. Illustration of the calculation for the number of collisions from our analytic model. We present, in the top panel, the evolution of the core radius. The middle panel shows the number of calculated 1+1 and 1+2 collisions, as described in Section 2.5. We also show the number of hyperbolic and binary collisions counted from the simulation for comparison. The bottom panel shows the fraction of binary systems in the core. The black vertical lines show the partitioning of the simulation time t_{sim} into 10 smaller intervals, each of which contains, on average, 6.8 snapshots. This is one of the simulations of Model 19.

The number of binary mediated collisions, occurring in the interval i, is

$$N_{1+2,i} = \left(f_{\text{dir}} + \frac{f_{\text{pert}}}{n_{\text{pert}}} \right) \frac{\Delta t}{\tau_{1+2,i}}. \tag{5}$$

We illustrate this calculation procedure in the middle panel of Fig. 1 by showing with dashed blue and dashed red lines the accumulated number of 1+1 and 1+2 collisions respectively, calculated according to equation (4) and (5). We also show for comparison the number of hyperbolic and binary collisions counted from the simulations with solid blue and solid red lines respectively. The mean fraction of binaries in the core f_{b} is presented in the bottom panel.

We note in equation (5) the presence of three correction factors. These are included in order to account for two different merger channels as described in Section 2.5.1 and 2.5.2.

We emphasize that, since we study binary interactions in the cluster centre, these correction factors apply only to the core. In order to obtain accurate correction factors outside of this region, we would need to run many more simulations to build up the required statistics, further justifying our choice to focus on the collision rates in the core. The determination of these factors is described in Section 2.5.1.

For the calculation of the collision time-scale given by equation (1) and (2), we compute the values for r_{core}, v_{rms}, n_{core}, $\langle m \rangle$, $\langle R \rangle$, and f_{b} in every snapshot of our simulations. Then we take the average over the number of snapshots in each interval. We illustrate this for the core radius in the top panel of Fig. 1 and for f_{b} in the bottom panel. The semimajor axis a_b is taken to be the mean semimajor axis per binary in the core. Typical initial values for the above mentioned quantities for each of our N-body models, are presented in Table 1 (except for f_{b} and a_{b}).

2.5.1 Calculating the number of collisions due to (bound and unbound) single–binary interactions

The total number of binary mediated stellar collisions is calculated with equation (5) in which we introduce three correction factors. We determine those factors by studying the evolution of the binary systems in our simulations. We note however that studying binary evolution requires very frequent snapshot output in order to capture the chaotic and rapid perturbations that a binary experiences from the moment of its formation until disruption or merger. In order to obtain representatives values for the correction factors that we introduce, but at the same time avoiding excessively large data outputs and long computational runtimes, we re-simulate three sets of the 24 models presented in Table 1, with a higher output frequency of 0.01 N-body units of time or 78 yr. These new data are used to compute the parameters f_{dir}, f_{pert}, and n_{pert}.

During a single–binary encounter, a stellar collision between two gravitationally bound stars can occur. When the collision occurs during a bound interaction with a third body we call this type of event a direct binary collision. In order to account for this in our model, we introduce the factor f_{dir}, calculated as the number of direct binary collisions divided by the total number of distinct binaries formed in the considered time interval. The values of f_{dir} for each model are presented in Table 3.

2.5.2 Unbound or perturbative single–binary interactions

A total of 56 binary collisions in our sample are driven to merger via the cumulative effects of many weak perturbative interactions from passing single stars on hyperbolic orbits relative to the binary

Table 3. Correction factors for direct and perturbed binary collisions.

Model	N	R_{star} (R$_\odot$)	f_{dir}	f_{pert}	n_{pert}
1	100	20	0.006	0.000	–
2	100	50	0.000	0.000	–
3	100	100	0.000	0.000	–
4	100	200	0.000	0.007	3.000
5	100	500	0.122	0.000	–
6	100	1000	0.000	0.037	4.000
7	500	20	0.017	0.000	–
8	500	50	0.014	0.006	2.250
9	500	100	0.017	0.011	11.500
10	500	200	0.042	0.010	1.000
11	500	500	0.040	0.007	1.000
12	500	1000	0.071	0.026	3.75
13	1000	20	0.002	0.002	1.000
14	1000	50	0.016	0.002	2.000
15	1000	100	0.015	0.000	–
16	1000	200	0.017	0.003	1.000
17	1000	500	0.044	0.000	–
18	1000	1000	0.108	0.010	2.667
19	5000	20	0.006	0.001	1.500
20	5000	50	0.015	0.009	14.679
21	5000	100	0.008	0.008	14.382
22	5000	200	0.018	0.001	6.000
23	5000	500	0.020	0.010	16.578
24	5000	1000	0.028	0.005	6.667

centre of mass. This occurs via an exchange of orbital energy and angular momentum with the binary, slowly driving it, via a random walk, to smaller orbital separations and higher eccentricities. This process has been studied by means of Monte Carlo methods and simplified encounter rates with field stars (Krolik, Meiksin & Joss 1984; Portegies Zwart et al. 1997; Kaib & Raymond 2014).

In order to model the perturbation-driven mergers, we study the eccentricity and semimajor axis evolution from the time of binary formation until the time of collision/merger. We define a perturbation as a close encounter in which the distance from the centre of mass of the binary to the closest star is less than, or equal to, three times the semimajor axis. Additionally, the close encounter should cause an eccentricity change equal to or larger than 5 per cent.

We introduce the correction factor f_{pert}, which accounts for the efficiency of this merger channel, and is calculated as the number of binary systems in which more than 50 per cent of the perturbations are caused by an unbound star, divided by the total number of distinct binaries formed in the considered time interval. For these perturbed binary collisions, we define n_{pert} as the number of unbound perturbations. We present the calculated values of f_{pert} and n_{pert} for each model in Table 3.

We show in Fig. 2 two examples of this perturbed binary collision scenario, following the evolution from the time of binary formation until merger. The left panels correspond to a binary with equal mass components perturbed by passing unbound single stars, whereas the right-hand panels correspond to a binary that involves the most massive object in the cluster. In the top panels, we show the time evolution of the eccentricity of the binary orbit. In the bottom panels, we show the time evolution of the semimajor axis with a red line, and the distance from the centre of mass to the closest third star with a green line. We mark with black vertical lines the times at which a perturbation is detected, as described in the previous paragraph. The mean time between perturbations, in the left-hand panels, is 4074 yr.
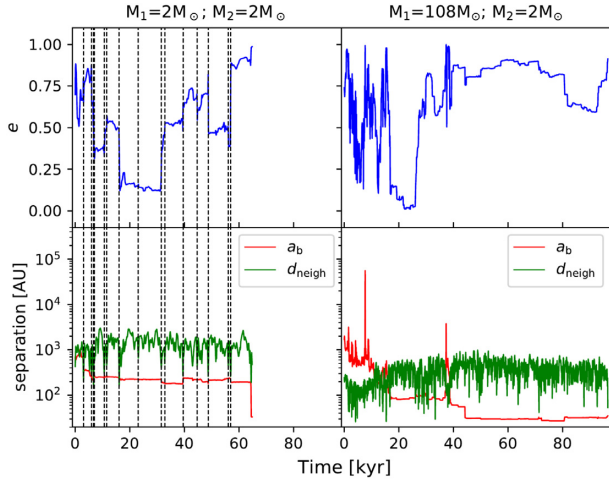
Figure 2. Perturbations to the eccentricity and semimajor axis of two binary systems in our simulations, from the time of binary formation until merger of the binary components. The left-hand panels correspond to a binary with equal mass members whereas the right panels correspond to a binary with the most massive object as a member. The masses are shown at the top of the corresponding panels. We present in the upper panels the time evolution of the eccentricity of the orbit. In the bottom panels, the red line represents the semimajor axis of the binary system and the green line shows the distance separating the binary centre of mass from the closest passing star. The dashed black vertical lines in the left panels mark the perturbations caused by the unbound passing star following the method described in Section 2.5.2. These lines are omitted in the right-hand panels to avoid crowding.

In this case, perturbations are caused by passing stars that are not bound to the binary. In the right-hand panels, perturbations are cause by a third star bound to the binary and are more frequent, with a mean time between perturbations of 367 yr. These perturbations are not shown to avoid crowding of lines.

3 RESULTS

In this section, we confront the predicted number of stellar collisions derived from our analytic model with the simulated number of collisions obtained from our *N*-body runs. Our results indicate that the simulated and predicted numbers of collisions agree to within a factor of $\lesssim 2$ and to within one standard deviation for most of our simulations, as shown in Fig. 3. The number of binary-mediated collisions is not well reproduced at later times due to the formation of a massive object at the cluster centre which tends to grow through binary collisions. This is more important in our simulations with $N = 5000$, in which a very massive object is always present in the cluster centre at late times.

3.1 Hyperbolic collisions

In Fig. 1, we illustrate the calculation procedure for one example simulation. We compare the expected number of collisions over a specified time interval. The middle inset shows the number of simulated hyperbolic, and analytic 1+1 collisions calculated with equation (4), over each time interval. We also present the ratio between simulated and predicted number of single–single collisions in Table 2 and Fig. 3. We find an excellent agreement between the predicted and simulated number of collisions.

Despite the emergence of more massive and larger stars from collisions, the single–single encounter rate is still able to account
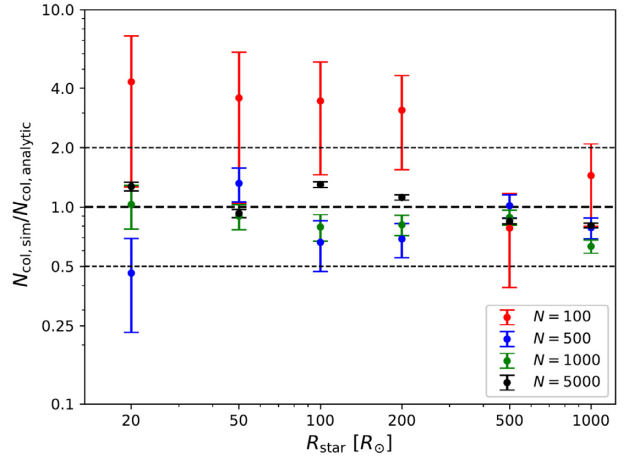

Figure 3. Ratio of simulated to predicted number of collisions as a function of stellar radius. The predicted number of collisions are obtained from our analytic model described in Section 2.3. The simulated number of collisions are obtained from our *N*-body simulations as described in Section 2.5. The data plotted here correspond to the seventh column in Table 2.

for mergers involving unequal mass stars. When compared to the number of single–single collisions only, the analytic model that we use underestimates the simulations results by a factor of 1.04, with a three sigma uncertainty of ± 0.05

3.2 Binary-mediated collisions

We note that in our clusters the density is sufficiently high as to activate the formation of binary stars via close interactions between three isolated single stars. A pair of stars then remain bound in a binary while the third star is ejected, typically taking away more positive kinetic energy than it came in with. This sets the scene for subsequent single–binary interactions to occur, in which three stars undergo a chaotic gravitationally bound interaction within a small volume with a correspondingly high probability of a collision occurring (see Leigh & Geller 2012, 2015; Leigh et al. 2016, 2018, for more details on the expected probabilities). If the collision occurs during an interaction with a third bound star, we classify it as a direct binary collision (see Section 2.5.1). Isolated binaries can also be driven to merger due to perturbative encounters with bound or unbound single stars. We present in Fig. 2 one example for each of these two cases (see Section 2.5.2).

In Fig. 1, we revisit the example simulation considered in the previous section. In the middle panel, the solid and dashed red lines show the simulated and predicted numbers of binary mediated collisions, respectively, as calculated with equation (5). We find that the agreement is better when the number of stars is low $N \leq 1000$, except for $N = 100$ (see columns 10 and 11 in Table 2). For our $N = 100$ simulations, nearly all of the collisions are binary mediated, but there are very few of them. This low number statistics directly impacts the determination of the correction factors $f_{\rm dir}$, $f_{\rm pert}$ and $n_{\rm pert}$ from our higher cadence runs (see Section 2.5.1), such that they become unreliable for these models (see Table 3).

The better agreement for $N = 500$ and 1000 can be explained by the almost unchanged stellar mass distribution. For larger particle numbers (i.e. $N = 5000$), the amount of binary collisions increases dramatically towards the end of the simulated time-span, as can be seen in Fig. 1. We attribute this increased rate of binary mediated collisions to the presence of a very massive object in the cluster core.
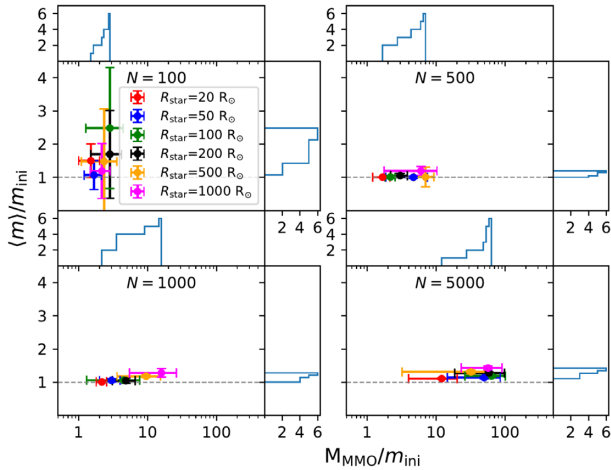
Figure 4. Average stellar mass inside the core as function of the most massive object mass. For low *N* and small R_{star}, there is not a very massive object in the cluster. For larger *N* and R_{star}, the core always contains an object that is much more massive than the rest at the end of the considered time-span. The cumulative histograms at the top and to the right of each panel help to see the widths in the distribution of the mean stellar mass in the core and the MMO mass distribution, respectively.
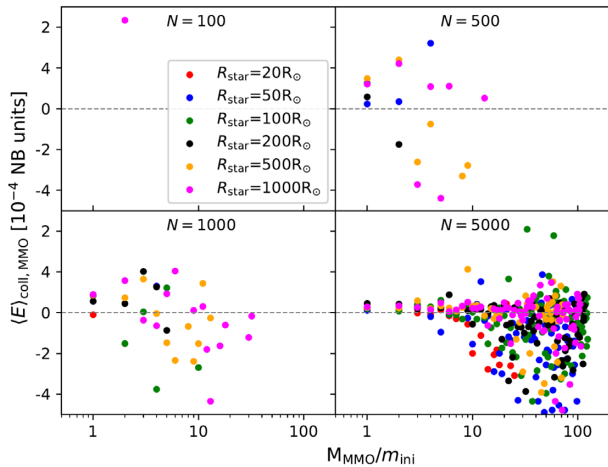

Figure 5. Average kinetic plus potential energy of stars colliding with the most massive object $\langle E \rangle_{coll,MMO}$, as function of the most massive object mass, for different *N* and R_{star}. Hyperbolic collisions are above the dashed grey line whereas binary collisions are below. For larger R_{star} hyperbolic collisions are preferred. Binary collisions are favoured for larger M_{MMO}/m_{ini}, which is specially important at late times for *N* = 5000. For *N* = 100, the rest of the points are around −100 NB units, and thus are not shown here.

In Fig. 4, we plot the average stellar mass inside the cluster core $\langle m \rangle$ as function of the mass of the most massive object (MMO). We exclude the MMO from the calculation of $\langle m \rangle$. We show that for *N* = 5000 there is always a single object in the core that is much more massive than the rest.

In order to illustrate the tendency of the MMO to grow through binary instead of hyperbolic collisions (i.e. single stars that become bound to the MMO on quasi-Keplerian orbits, forming binaries with it), we calculate the average energy of the stars that collide with the MMO as function of its mass. This is done for different values of *N* and R_{star} and shown in Fig. 5. In this figure, hyperbolic collisions are above the dashed grey line and binary collisions below. The energy is presented in *N*-body (NB) units (Heggie & Mathieu 1986). This

figure shows that for *N* = 5000 and $R_{star} \leq 200 R_{\odot}$ the most massive object in the core preferentially grows via binary-mediated collisions. This helps to explain the discrepancy seen in Fig. 1 and in columns 10 and 11 in Table 2.

Summarizing our results so far, the presence of a very massive object in the core causes the assumptions and approximations going into our analytic model to break down, such that the model should be re-visited and re-constructed to account for these alternative collision channels. For example, as the MMO grows in mass, we expect secular analytic theories to agree better with the results of the simulations, as perturbations become less important in the deep potential of a central very massive object.

4 APPLICATIONS TO OBSERVED DATA AND THE FORMATION OF STELLAR EXOTICA

In this section, we quantify what our results are telling us about the dominant merger/collision channels as a function of environment. We then go on to confront our results with observed data from Milky Way GCs, to identify the dominant collision mechanism operating in different star cluster environments. With this information in hand, we move on to making predictions for the properties of stellar exotica that are thought to be the products or progenitors of collisions/mergers, specifically BSs stars and other potential merger products found in galactic nuclei (e.g. the S-stars).

4.1 Collision time-scales and real GCs

We now proceed to compare three different collision rates in the cores of GCs, namely the rate for single–single collisions, the rate for direct single–binary collisions and the rate for binary formation from encounters of three single stars. For the calculation of these rates, we assume that the average mass and average stellar radius correspond to Sun-like stars, and for the cluster core radius we take the mean core radius from the GC sample.

All these rates depend on the number density of stars and on the binary fraction, and we present in Fig. 6 the regions of this space where each of these rates dominates over the others. The time-scales for 1+1 and 1+2 interactions are obtained from equations (1) and (2), whereas the rate for 1+1+1 interactions is obtained from equation (7.11) in Binney & Tremaine (2008) including gravitational focusing. The red line in Fig. 6 marks the limit in which the 1+1+1 and 1+2 rates are equal. The black line marks the limit in which the 1+1+1 and 1+1 rates are equal. The blue line marks the limit in which the 1+1 and 1+2 rates are equal. For computing the 1+2 rate, we use the semimajor axis corresponding to the hard-soft boundary. We assume a velocity dispersion of 5 km s^{-1}.

The GC sample we take from Milone et al. (2012), which contains information about the binary fractions in the cores of the clusters, and we cross-correlate these clusters to the ones in the VizieR Catalogue of Harris (1996). The latter catalogue contains information about the cluster core radius and central luminosity per cubic parsec, which we convert to a core number density n_{core} assuming a mass–luminosity ratio of 1 $M_{\odot}$ $L_{\odot}^{-1}$ and mean stellar mass of 1 $M_{\odot}$.

As can be seen in Fig. 6, the majority of the clusters in this sample fall in the region where binary collisions dominate over hyperbolic collisions. Hence, once binaries begin to form, they become a significant contribution to the overall rate of collisions and mergers. The presence of even a few binaries causes the rates for the binary collision channels to dominate over the hyperbolic collision rates. We also include in this figure the time evolution of two of our simulations (shown by +the green and orange trajectories). For one
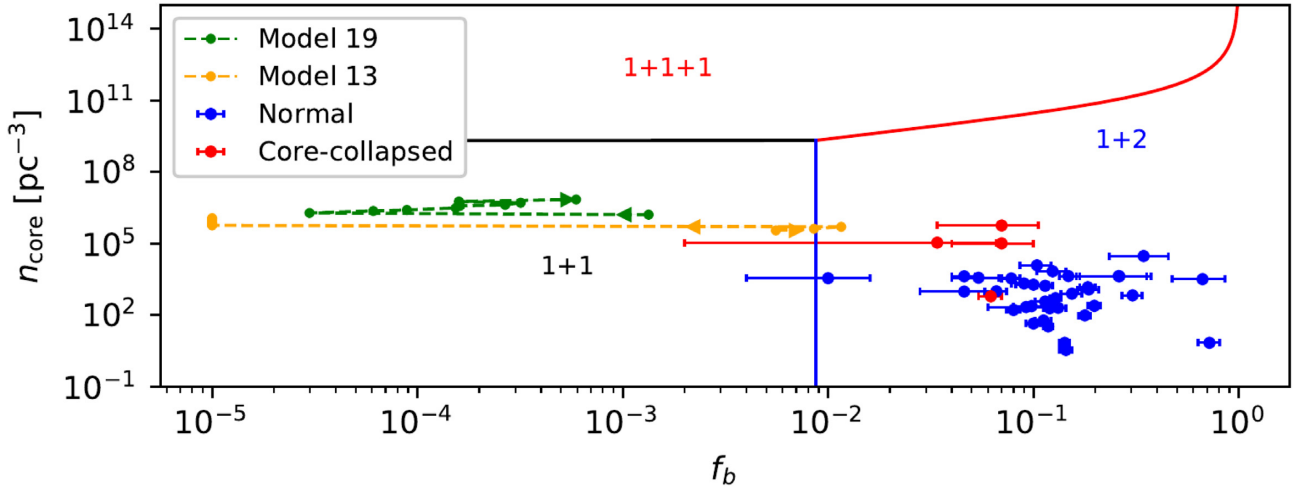
Figure 6. Encounter rates, observed data for GCs and data from two of our simulations. The solid lines separate the regions where each encounter rate dominates over the others, and the regions are labelled accordingly. We overplot real data for Milky Way GCs distinguishing core-collapsed clusters (red points) from the rest (blue points). We also overplot data from one of our simulations for Model 19 and Model 13. The time-scales are calculated assuming a cluster core radius of 2.6 pc (corresponding to the mean of our GC sample) and a mean stellar radius of $1R_\odot$.

of our Model 19 simulations, the cluster always remains in the region dominated by single–single collisions.

For one of our simulations of Model 13, the cluster starts in the region dominated by single–single collisions. Some binaries are formed and f_b increases, thus triggering binary collisions to dominate for a brief time. These are, however, a factor ~ 7 less numerous than hyperbolic collisions. Once a binary forms, it merges or evaporates so quickly that the single–single rate quickly goes back to dominating over the single–binary rate.

Overall, the rate of hyperbolic collisions is higher than the rate for single–binary collisions. Over time, however, the altered mass function helps to promote the formation of binary systems between the surrounding stars and the central most massive object, such that binary collisions tend to involve a massive collision product residing in the centre of the cluster. These binaries tend to merge quickly, due to a perturbation-driven random walk in eccentricity, as shown in the right-hand panel of Fig. 2.

4.2 Blue stragglers

BS stars appear in the cluster colour–magnitude diagram brighter and bluer than the MS turn-off, where isolated stellar evolution predicts that no stars should be present. Two main competing mechanisms have been proposed for their formation, namely direct collisions between MS stars and mass transfer on to an MS star in a binary star system. If most BSs are formed from single–single collisions, then this would predict a correlation between BS numbers and the collision rate, as has been observed for low-mass x-ray binaries (Pooley & Hut 2006). However, there is no clear correlation between BS numbers or relative frequencies, and the collision rate in the cores of GCs (Leigh, Sills & Knigge 2007). This, combined with a correlation between cluster core mass and BS numbers, is indirect evidence supporting a binary evolution origin for BSs (Knigge, Leigh & Sills 2009; Leigh et al. 2011, 2013). Our results suggest that the complexity in the process of collisions/mergers could play an important role when looking for correlations with collision rates.

The process of perturbative single–binary encounters that we see in our simulations could be an important formation mechanism for

isolated BSs (i.e. without binary companions) in GC cores. This motivates the development of analytic models like in Leigh et al. (2011), but more complex as to realistically model the complicated collisional and/or merger processes identified here in high-density clusters with low binary fractions, as illustrated in this paper and Barrera et al. (2020). Taken at face value, our results predict a higher fraction of isolated BSs relative to BSs with binary companions in clusters with high central densities and low binary fractions. This is in contrast to both the binary evolution channel for BS formation and the mechanism proposed in Perets & Fabrycky (2009) for BSs forming from stable hierarchical triples, as they predict BSs with binary companions.

Let the number of isolated BSs be denoted $N_{\rm BS, iso}$ and the number of BSs with binary companions be denoted $N_{\rm BS, bin}$. Our results could predict a correlation between the ratio $N_{\rm BS, iso}/N_{\rm BS, bin}$ and both central density and core binary fraction, with this ratio increasing in denser clusters with lower binary fractions. In principle, this prediction is observationally testable. Recently, tentative evidence for double BS sequences have been identified in the colour–magnitude diagrams of Galactic GCs (Ferraro et al. 2009; Dalessandro et al. 2013; Simunovic, Puzia & Sills 2014). The authors propose that one sequence is due to collisions/mergers which would produce isolated BSs, whereas the other sequence is due to binary evolution which would produce BSs with binary companions. If these double BS sequences are confirmed to be statistically significant, then our results naively predict that the ratio of these two populations should also correlate with central density and core binary fraction. The sample size for observing double BS sequences in GCs is currently of order unity. Hence, a preliminary test of our hypothesis can be done now, but more data would be needed to properly answer the question with statistical significance. Using the WIYN data from the WOCS collaboration (see Mathieu & WOCS Collaboration (2013), for example, for more details) would be ideal for this experiment, since it focuses on old open clusters and, at least for clusters like NGC 188, M67 and a few others, extensive studies have been done over the last several decades to thoroughly quantify the issue of cluster membership, and even provide BS binary fractions in some clusters (e.g. Mathieu & Geller 2009; Geller & Leigh 2015; Rain et al. 2020; Jadhav & Subramaniam 2021). In order to increase

the sample size for the number of clusters with known BS binary fractions, these WIYN data can be combined with the GC data coming from double BS sequences. Both individual samples continue to grow slowly over time. The rate could be accelerated even further by looking for double BS sequences in the WIYN data and using speckle interferometry to search for binary companions to individual BSs in open clusters. Ultimately, however, the data are coming from studies of both open cluster and GC, and it will not be long before we have a reasonable sample size of BS binary fractions to test our prediction that more single BSs should be present in higher density star clusters due to perturbative mergers of binaries. Performing a more detailed comparison by confronting our theoretical predictions with real astronomical data will be the focus of future work.

4.3 The Galactic Centre and the origins of the S-stars

The innermost parsec in the Galactic Centre contains a stellar disc extending out to 0.5 pc (Støstad et al. 2015). This structure is formed by massive young stars with an estimated age of 4–6 Myr and a notably top heavy mass function (Bartko et al. 2010; Mauerhan et al. 2010; Lu et al. 2013; Yelda et al. 2014). The presence of binary systems in the disc whose components merge due to Lidov–Kozai (LK) oscillations could potentially provide an explanation to observed stellar properties and even the peculiar G2 object (Prodan, Antonini & Perets 2015; Stephan et al. 2016). Following the same approach adopted by Prodan et al. (2015), we consider a binary system, which, in turn, is orbiting a central supermassive black hole and we make a crude estimate of the time-scale for LK oscillations to operate by using their equation (2):

$$
T_{\mathrm{Kozai}} \approx 2.5 \times 10^6 \left(\frac{a_{\mathrm{out}}}{0.5\,\mathrm{pc}} \right)^3 \left(\frac{1\,\mathrm{AU}}{a_b} \right)^3 \left(\frac{M_b}{2\,\mathrm{M_\odot}} \right)^{1/2}
$$
$$
\times \left(\frac{4 \times 10^6\,\mathrm{M_\odot}}{M_\bullet} \right) \left(\frac{a_b}{1\,\mathrm{AU}} \right)^{3/2} \left(1 - e_{\mathrm{out}}^2 \right)^{3/2} \mathrm{yr}, \qquad (6)
$$

where a_{out} is the semimajor axis of the binary–SMBH system and e_{out} the eccentricity of the orbit. a_b is the semimajor axis of the binary that orbits the SMBH, M_b is the mass of the binary, and $M_\bullet$ is the mass of the SMBH.

In the Galactic Centre the stellar density follows a power law given by $\rho \propto r^{-\gamma}$, and the gravitational potential is dominated by the central SMBH, thus $v_{\mathrm{rms}} = \sqrt{GM_\bullet/a_{\mathrm{out}}}$. With this, the single binary collision time-scale from equation (2) can be expressed as

$$
\tau_{1+2,\mathrm{GC}} = 4.9 \times 10^7 (1 - f_b)^{-1} f_b^{-1} \left(\frac{a_{\mathrm{out}}}{0.5\,\mathrm{pc}} \right)^{1/2+2\gamma}
$$
$$
\times \left(\frac{10^3\,\mathrm{pc}^{-3}\langle m \rangle}{\rho_0} \right)^2 \left(\frac{1\,\mathrm{pc}}{r_0} \right)^3 \left(\frac{4 \times 10^6\,\mathrm{M_\odot}}{M_\bullet} \right)^{1/2}
$$
$$
\times \left(\frac{1\,\mathrm{AU}}{a_b} \right)^2 \left[1 + 53 \left(\frac{\langle m \rangle}{0.5\,\mathrm{M_\odot}} \right) \left(\frac{1\,\mathrm{AU}}{a_b} \right) \right.
$$
$$
\left. \times \left(\frac{5\,\mathrm{km\,s^{-1}}}{v_{\mathrm{rms},0}} \right)^2 \right]^{-1}, \qquad (7)
$$

where for simplicity, we set $v_{\mathrm{rms},0} = \sqrt{GM_\bullet/0.5\,\mathrm{pc}}$. We use $\rho_0 = 5.2 \times 10^5\,\mathrm{M_\odot\,pc^{-3}}$, $r_0 = 0.5$ pc and $\gamma = 2$ (Prodan et al. 2015). We can now derive the distance from the SMBH at which the time-scale for LK oscillations equals the time-scale for a perturbed binary collision, for different values of a_b. We estimate which time-scale
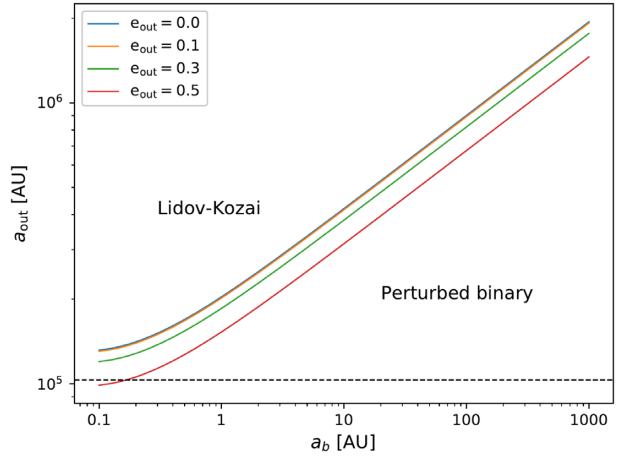
Figure 7. Dominant collisional time-scale for binaries in the central galactic disc. a_{out} is the distance from the Galactic Centre at which the binary orbits, and a_b is the semimajor axis of the binary. The solid coloured lines mark the region where the time-scale for one LK oscillation is equal to the time for perturbed single–binary encounters to produce a merger. Higher eccentricities for the orbit of the binary around the central BH shortens the time-scale for perturbed binary collisions compared to collisions from LK oscillations. The regions where each time-scale dominates are labelled accordingly. The dashed horizontal line marks the edge of the disc at 0.5 pc.

dominates by doing:

$$
\frac{T_{\mathrm{Kozai}}}{0.55} = \frac{\tau_{1+2,\mathrm{GC}}\, n_{\mathrm{pert}}}{f_{\mathrm{pert}}}, \qquad (8)
$$

where we introduced the factor 0.55 to account for the fact that the LK mechanism operates for mutual inclinations $\gtrsim 40°$, that is, we approximate the fraction of triple systems that are in the active LK window as $100°/180°$. We set $f_{\mathrm{pert}} = 0.006$ and $n_{\mathrm{pert}} = 1.500$ that correspond to our simulation with $N = 5000$ and $R_{\mathrm{star}} = 20 R_\odot$ (see Table 3).

As shown in Fig. 7, we find that perturbed binary collisions might be more important than LK oscillation-driven collisions when the binary orbits at a distance ≤ 0.5 pc of the central SMBH, for a wide range of binary semimajor axes. The perturbed binary collision scenario that we find in this work thus provides an alternative merger channel that does not require inclined orbits as in the KL case. This alternative channel requires further investigation to characterize the number of perturbations and the frequency of collisions expected in this environment, which depends sensitively on the assumed density, the mass of the most massive central object and the compactness of the binary. For example, it could occur that only very compact binaries are able to form, and they are relatively insensitive to perturbations. Indeed, the hard–soft boundary depends on distance from the SMBH, when one is present (Leigh et al. 2016).

A more detailed parameter space exploration is required to properly identify how these effects compete in dense environments. Although in Section 3.2, we show that our model is not able to correctly reproduce the number of collisions that involve a central very massive object, we cannot conclude that the model does not work for estimating the number of single–binary interactions for binary systems orbiting such an object. We expect that equation (7) is still able to capture these events, but we aim for a simplified model here that needs to be tested with more sophisticated simulations in the future.

Here, we used the correction factors f_{pert} and n_{pert} for our model that matches better the stellar properties and number density of stars in the Galactic Centre, however, the stellar radii are still too large. We choose not to extrapolate the values of f_{pert} and n_{pert} to smaller radii, and limit ourselves to a very simplified comparison between the two time-scales to avoid overstating the significance of our results (since we have only explored a small subset of the total allowed parameter space of initial conditions).

The take-away message from Fig. 7 is that the S-stars could potentially be explained via three-body binary formation forming binaries near to the central SMBH, which then merge due to perturbations from the surrounding high-density N-body system. Hence, Fig. 7 shows that the time-scale to drive a merger due to perturbations could be shorter than the time-scale for Lidov–Kozai cycles to operate, provided $a_b \lesssim 10$ au and $a_{out} \lesssim 0.5$ pc. In this regime, this scenario predicts a top-heavy mass function for stellar populations in the cores of very dense clusters not just due to mergers, but also because it is usually the least massive object that is ejected during three-body binary formation. The escaping single particle must leave with more kinetic energy than it came in with, such that three-body binary formation would contribute to depleting the central regions of dense environments of lower mass stars. Naively, however, this would not explain a disc-like configuration for the orbits of the S-stars, unless star formation first occurred and only formed isolated single stars, which then formed binaries later via 1+1+1 interactions. To constrain this mechanism, the distribution of orbital eccentricities can be used, since the highly perturbative environment should drive the eccentricity distribution of the S-stars to become supra-thermal. But detailed N-body simulations would first be required to properly quantify the predicted eccentricity distributions for different initial conditions, combinations of BH masses, and so on.

Performing a more rigorous parameter space exploration using sophisticated N-body models to properly quantify the post-scattering time evolution of the orbital diffusion in energy- and angular momentum-space for the S-star population will be the focus of future work. This will be necessary in order to use the observed orbital parameters of the S-star population to test the predictions presented in this section.

5 SUMMARY AND DISCUSSION

In this paper, we perform a comparison between analytic calculations for the rate of stellar collisions, to a set of N-body simulations that include stellar collisions. Our goal is to test the validity and extent of the MFP approximation, in a dense dynamically active star cluster environment. Our simple numerical models initially consist of equal mass and equal radii particles without stellar evolution, and collisions are treated using the 'sticky star approximation'. This allows us to use simple 'nσv' rates for our analytic model and to avoid complicating effects such as tidal capture, mass-loss and tidal disruption. We focus our analysis to the cluster core, where most simulated collisions occur, and take into account single–single and single–binary collisions.

In general, our analytic model works better for larger N systems where most of the collisions are due to hyperbolic encounters, but worsens for longer evolution time-scales as shown in the middle panel of Fig. 1. A longer evolution time produces a larger number of collisions, which in turn promotes the formation of a very massive object in the cluster centre. As this object grows (preferentially through binary collisions, as we show in Fig. 5), our model begins to break down. This should mark the transition from a chaotic

to a more deterministic dynamical evolution, as the contribution from the most massive object to the total gravitational potential increases and the local stellar orbits become increasingly Keplerian. In the limit of large central object masses, the influence radius becomes large (i.e. the distance from the cluster centre of mass to the distance at which point the Keplerian velocity becomes on the order of the local velocity dispersion) and the stellar orbits are typically assumed not to be changing significantly over short time-scales, as occurs for low-number chaotic systems. For our simulations, however, we do not reach this limit, suggesting that perturbative encounters remain important for a large fraction of the parameter space relevant to very dense clusters hosting binary stars (i.e. $n_{core} \gtrsim 10^6$ pc^{-3}; see Fig. 6). In this regime, a loss cone formalism is likely more applicable, but would need to be combined with the standard 'nσv' estimates further out in the cluster where the density is lower and the relevant dynamical time-scales, which cause the cluster structure and mass spectrum to change, are longer.

We include two types of binary collisions in our analytic model, namely direct binary collisions and perturbed binary collisions. The first type of collision occur when all three stars become bound, and two or more stars undergo a direct collision during the interaction. The second type of collision requires that a binary first forms via encounters involving three isolated single stars, but then later merges due to perturbations from the surrounding stellar potential pumping the binary eccentricity to near unity. For the latter type of collisions, close passages of single stars drive the orbital eccentricity to $e \sim 1$ and cause the merger of the binary stars (see Section 2.5.2 for details), as we show in Fig. 2.

A shortcoming of our model for binary mediated collisions comes from the determination of the correction factors that we introduce to account for direct and perturbed binary collisions. Specifically, for our higher cadence simulations with $N = 100$ (see Section 2.5.1), the number of runs is still so low that we have no binary collisions at all, and hence the correction factors are mostly zero (see Table 3). While this problem is most important for our smallest N simulations, we still have to deal with low number statistics when computing the correction factors for the rest of the models. This, combined with a low cadence in snapshot outputs, prevents us from accurately exploring the evolution of every binary system and developing a complete understanding of the competition between the effects of the stellar number density, the stellar radius and mass, and the properties of the central MMO on the two binary collision channels that we identify.

We use GC data taken from the literature to determine which of our rates is dominating in which cluster environments. We obtain core densities from the Harris GC Catalogue (Harris 1996) and core binary fractions from Milone et al. (2012). We plot binary fraction as a function of number density, and segment off those regions of parameter space where each of the 1+1, 1+2 and 1+1+1 rates dominate in Fig. 6, as explained in Section 4.1. As is clear, 1+2 interactions dominate in all the GCs considered here. We also overplot the time evolution of two of our simulations in this parameter space. This indicates that in such dense environments with large radii stars, the single–single collision rate always dominate. Nevertheless, binaries are still created, but merge or are destroyed relatively quickly without ever reaching a sufficiently high binary fraction for a significant period of time such that single–binary collisions dominate.

We suggest that the perturbed binary collisions identified in our simulations could be an alternative merger channel operating efficiently in dense stellar environments where no stable triples

can form. This process would produce isolated BSs as opposed to binary stellar evolution, which instead predicts a white dwarf binary companion (e.g. Gosnell et al. 2014, 2015), potentially producing a correlation between the number of isolated BSs and the stellar density. Specifically, we predict that the ratio of BSs without binary companions to the ratio of BSs with binary companions, or $N_{\rm BS,iso}/N_{\rm BS,bin}$, should increase in denser clusters with lower binary fractions, which offers a possible observational test for this prediction. By means of a simplified comparison of time-scales, we show that perturbed binary collisions could be more important than LK induced collisions in the outer parts of the Milky Way central stellar disc. This could have implications for the formation of the S-stars in the Galactic Centre, which we quantify qualitatively, however, more sophisticated models and simulations are needed to confirm or reject this hypothesis.

Our results have important implications for performing accurate and precise numerical simulations involving collisions and mergers. Consequently, we caution against blindly using independent analytic approximations in very dense stellar systems. For example, in loss cone theory (see Merritt 2013b for a detailed review), an analytic model (e.g. a Boltzmann-based diffusion model) is used to compute the torques orbiting objects exert on each other's orbits and hence the time-scale for resonant relaxation to operate (see Merritt 2013a for a review of resonant relaxation). The model evolves those orbits by computing the rate of energy and angular momentum exchanged between them, which can then be used to compute the time-scale on which stellar orbits diffuse to high eccentricities and pass very close to the system centre of mass, where they would collide with any central massive object. Our results suggest that this could be an oversimplified analytic model, since it ignores perturbations, which become particularly important when the orbiting bodies are at apocentre. At high densities, these perturbations become stronger and more frequent. *N*-body codes are capable of modeling the perturbations and can be used to quantify the competing rates and parameter space. To the best of our knowledge, however, perturbative effects are still not fully included and any contribution from distant perturbers (e.g. stars in the outskirts of a cluster) are entirely neglected in Monte Carlo simulations for star cluster evolution. A detailed parameter space study is needed to better understand when the perturbations can be safely ignored, and when they must be included in any analytic model.

REFERENCES

Aarseth S. J., 2000, The Chaotic Universe NBODY 6: A New Star Cluster Simulation Code. WorldScientific Publishing, Singapore, p. 286
Ahmad A., Cohen L., 1973, J. Comput. Phys., 12, 389
Alister Seguel P. J., Schleicher D. R. G., Boekholt T. C. N., Fellhauer M., Klessen R. S., 2020, MNRAS, 493, 2352
Barrera C., Leigh N. W. C., Reinoso B., Stutz A. M., Schleicher D., 2020, MNRAS, 502, 3374
Bartko H. et al., 2010, ApJ, 708, 834
Baumgardt H., Klessen R. S., 2011, MNRAS, 413, 1810
Binney J., Tremaine S., 1987, Galactic Dynamics. Princeton Univ. Press, Princeton
Binney J., Tremaine S., 2008, Galactic Dynamics: Second Edition. Princeton Univ. Press, Princeton
Boekholt T. C. N., Schleicher D. R. G., Fellhauer M., Klessen R. S., Reinoso B., Stutz A. M., Haemmerlé L., 2018, MNRAS, 476, 366
Chon S., Omukai K., 2020, MNRAS, 494, 2851
Dalessandro E. et al., 2013, ApJ, 778, 135
Das A., Schleicher D. R. G., Leigh N. W. C., Boekholt T. C. N., 2020, MNRAS, 501, 1051
Devecchi B., Volonteri M., 2009, ApJ, 694, 302
Devecchi B., Volonteri M., Rossi E. M., Colpi M., Portegies Zwart S., 2012, MNRAS, 421, 1465
Eckart A., Genzel R., 1997, MNRAS, 284, 576
Ferraro F. R. et al., 2009, Nature, 462, 1028
Fregeau J. M., Chatterjee S., Rasio F. A., 2006, ApJ, 640, 1086
Fregeau J. M., Cheung P., Portegies Zwart S. F., Rasio F. A., 2004, MNRAS, 352, 1
Geller A. M., Leigh N. W. C., 2015, ApJ, 808, L25
Ghez A. M. et al., 2003, ApJ, 586, L127
Goldreich P., Tremaine S., 1982, ARA&A, 20, 249
Gosnell N. M., Mathieu R. D., Geller A. M., Sills A., Leigh N., Knigge C., 2014, ApJ, 783, L8
Gosnell N. M., Mathieu R. D., Geller A. M., Sills A., Leigh N., Knigge C., 2015, ApJ, 814, 163
Harris W. E., 1996, VizieR Online Data Catalog: Globular Clusters in the Milky Way, VII/202
Heggie D. C., Mathieu R. D., 1986, The Use of Supercomputers in Stellar Dynamics, Vol. 267, Springer-Verlag, Berlin, p. 233
Hut P., 1983, ApJ, 268, 342
Hut P., Bahcall J. N., 1983, ApJ, 268, 319
Jadhav V. V., Subramaniam A., 2021, MNRAS, 507, 1699
Kaib N. A., Raymond S. N., 2014, ApJ, 782, 60
Katz H., Sijacki D., Haehnelt M. G., 2015, MNRAS, 451, 2352
Knigge C., Leigh N., Sills A., 2009, Nature, 457, 288
Krolik J. H., Meiksin A., Joss P. C., 1984, ApJ, 282, 466
Kustaanheimo P., Stiefel E., 1965, J. Reine Angew. Math., 218, 204
Leigh N. W. C., Geller A. M., 2015, MNRAS, 450, 1724
Leigh N. W. C., Geller A. M., Shara M. M., Baugher L., Hierro V., Ferreira D., Teperino E., 2018, MNRAS, 480, 3062
Leigh N. W. C., Geller A. M., Shara M. M., Garland J., Clees-Baron H., Ahmed A., 2017, MNRAS, 471, 1830

Leigh N. W. C., Stone N. C., Geller A. M., Shara M. M., Muddu H., Solano-Oropeza D., Thomas Y., 2016, MNRAS, 463, 3311

Leigh N., Geller A. M., 2012, MNRAS, 425, 2369

Leigh N., Knigge C., Sills A., Perets H. B., Sarajedini A., Glebbeek E., 2013, MNRAS, 428, 897

Leigh N., Sills A., Knigge C., 2007, ApJ, 661, 210

Leigh N., Sills A., Knigge C., 2011, MNRAS, 416, 1410

Leonard P. J. T., 1989, AJ, 98, 217

Lu J. R., Do T., Ghez A. M., Morris M. R., Yelda S., Matthews K., 2013, ApJ, 764, 155

Lupi A., Colpi M., Devecchi B., Galanti G., Volonteri M., 2014, MNRAS, 442, 3616

Mathieu R. D., Geller A. M., 2009, Nature, 462, 1032

Mathieu R. D., WOCS Collaboration, 2013, in American Astronomical Society Meeting Abstracts. p. 214.03

Mauerhan J. C., Cotera A., Dong H., Morris M. R., Wang Q. D., Stolovy S. R., Lang C., 2010, ApJ, 725, 188

Merritt D., 2013a, Dynamics and Evolution of Galactic Nuclei. Princeton Univ. Press, Princeton

Merritt D., 2013b, Classical and Quantum Gravity, 30, 244005

Mikkola S., Aarseth S. J., 1998, New Astron., 3, 309

Milone A. P. et al., 2012, A&A, 540, A16

Naoz S., Ghez A. M., Hees A., Do T., Witzel G., Lu J. R., 2018, ApJ, 853, L24

Ogiya G., 2018, MNRAS, 480, L106

Perets H. B., Fabrycky D. C., 2009, ApJ, 697, 1048

Plummer H. C., 1911, MNRAS, 71, 460

Pooley D., Hut P., 2006, ApJ, 646, L143

Portegies Zwart S. F., Baumgardt H., Hut P., Makino J., McMillan S. L. W., 2004, Nature, 428, 724

Portegies Zwart S. F., Hut P., McMillan S. L. W., Verbunt F., 1997, A&A, 328, 143

Portegies Zwart S. F., McMillan S. L. W., 2002, ApJ, 576, 899

Prodan S., Antonini F., Perets H. B., 2015, ApJ, 799, 118

Rain M. J., Carraro G., Ahumada J. A., Villanova S., Boffin H., Monaco L., Beccari G., 2020, AJ, 159, 59

Reinoso B., Schleicher D. R. G., Fellhauer M., Klessen R. S., Boekholt T. C. N., 2018, A&A, 614, A14

Reinoso B., Schleicher D. R. G., Fellhauer M., Leigh N. W. C., Klessen R. S., 2020, A&A, 639, A92

Sakurai Y., Yoshida N., Fujii M. S., 2019, MNRAS, 484, 4665

Sakurai Y., Yoshida N., Fujii M. S., Hirano S., 2017, MNRAS, 472, 1677

Simunovic M., Puzia T. H., Sills A., 2014, ApJ, 795, L10

Spitzer Lyman J., 1941a, ApJ, 93, 369

Spitzer Lyman J., 1941b, ApJ, 94, 232

Spitzer Lyman J., 1942, ApJ, 95, 329

Stephan A. P., Naoz S., Ghez A. M., Witzel G., Sitarski B. N., Do T., Kocsis B., 2016, MNRAS, 460, 3494

Støstad M., Do T., Murray N., Lu J. R., Yelda S., Ghez A., 2015, ApJ, 808, 106

Tagawa H., Haiman Z., Kocsis B., 2020, ApJ, 892, 36

Yelda S., Ghez A. M., Lu J. R., Do T., Meyer L., Morris M. R., Matthews K., 2014, ApJ, 783, 131

APPENDIX A: COLLISION TIME-SCALES WITH GRAVITATIONAL FOCUSING

For deriving the time-scales for single–single collisions (τ_{1+1}) and single–binary collisions (τ_{1+2}), we use the next relations (Leonard 1989):

$$\sigma_{i+j} = \pi p^2 \left[1 + \frac{2G(m_i + m_j)}{p v_{\rm rel}^2} \right], \qquad (A1)$$

$$\Gamma_{i+j} = N_i n_j \sigma_{i+j} v_{\rm rel}, \qquad (A2)$$

$$\tau_{i+j} = \Gamma_{i+j}^{-1}, \qquad (A3)$$

$$N_{\rm core} = \frac{2}{3} \pi n_0 r_{\rm core}^3, \qquad (A4)$$

$$n_{\rm core} = \frac{n_0}{2}. \qquad (A5)$$

Here, σ_{i+j}, is the gravitationally focused cross-section for the interaction between particles i and j, p is the pericenter distance for a physical collision, m_i and m_j are the masses of the colliding particles, N_i and n_j are the core number and core number density of particles i and j, respectively, $v_{\rm rel}$ is the relative velocity at infinity, n_0 is the number density of particles in the cluster centre, $r_{\rm core}$ is the core radius, $n_{\rm core}$ is the mean number density of particles in the core, and $N_{\rm core}$ is the total number of particles in the core.

A1 Single–single collision time-scale

Consider a physical collision between two single particles with the same mass and radius, m and R, respectively. The gravitationally focused cross-section for such an interaction as calculated with equation (A1) is

$$\sigma_{1+1} = 4\pi R^2 \left[1 + \frac{Gm}{R v_{\rm rms}^2} \right], \qquad (A6)$$

where for a Maxwellian velocity distribution the relative velocity between the two particles is equal to the square root of two multiplied by the root mean square velocity of the particles, i.e, $v_{\rm rel} = \sqrt{2} v_{\rm rms}$. The number of single stars in the core is $N_s = N_{\rm core}(1 - f_b - f_t)$, where f_b and f_t are the fraction of binary and triple systems in the core, i.e. the number of binary and triple systems in the core, divided by the number of single stars, plus binary systems, plus triple systems in the core. By using equations (A4) and (A5), we can show that

$$N_s n_s = N_{\rm core}^2 (1 - f_b - f_t)^2 \frac{3}{4\pi r_{\rm core}^3},$$

$$N_s n_s = \frac{\pi}{3} n_0^2 r_{\rm core}^3 (1 - f_b - f_t)^2. \qquad (A7)$$

Now, combining equation (A2), (A6), (A7), and setting $v_{\rm rel} = \sqrt{2} v_{\rm rms}$ we obtain

$$\Gamma_{1+1} = \sqrt{2} \frac{4\pi^2}{3} (1 - f_b - f_t)^2 n_0^2 r_{\rm core}^3 R^2 v_{\rm rms} \left[1 + \frac{Gm}{R v_{\rm rms}^2} \right]. \qquad (A8)$$

Finally, inverting equation (A8), inserting some typical values for star clusters, and using $n_{\rm core}$ instead of n_0, we get

$$\tau_{1+1} = 8.3 \times 10^{13} (1 - f_b - f_t)^{-2} \left(\frac{10^3 \text{ pc}^{-3}}{2 n_{\rm core}} \right)^2$$

$$\times \left(\frac{1 \text{ pc}}{r_{\rm core}} \right)^3 \left(\frac{5 \text{ km s}^{-1}}{v_{\rm rms}} \right) \left(\frac{0.5 \ R_\odot}{R} \right)^2$$

$$\times \left[1 + 7635 \left(\frac{m}{0.5 \ M_\odot} \right) \left(\frac{0.5 R_\odot}{R} \right) \left(\frac{5 \text{ km s}^{-1}}{v_{\rm rms}} \right)^2 \right]^{-1} \text{ yr.}$$

A2 Time-scale for single–binary collisions

Consider now an encounter between a single star and a binary system, with all the stars having the same mass m and radius R. The gravitationally focused cross-section for such an interaction, assuming a pericenter distance equal to the semi major axis of the binary $p = a_{\rm b}$, as calculated with equation (A1) is

$$\sigma_{1+2} = \pi a_b^2 \left[1 + \frac{3Gm}{a_b v_{\rm rms}^2} \right], \qquad (A9)$$

where for a Maxwellian velocity distribution the relative velocity between the two particles is equal to the square root of two multiplied by the root mean square velocity of the particles, i.e, $v_{rel} = \sqrt{2}v_{rms}$. The number of single stars in the core is $N_s = N_{core}(1 - f_b - f_t)$ and the number of binary systems in the core is $N_b = N_{core}f_b$, where f_b and f_t are the fraction of binary and triple systems in the core. By using equation (A4) and equation (A5), we can show that

$$N_s n_b = N_{core}^2 (1 - f_b - f_t) f_b \frac{3}{4\pi r_{core}^3},$$

$$N_s n_b = \frac{\pi}{3} n_0^2 r_{core}^3 (1 - f_b - f_t) f_b. \tag{A10}$$

Now, combining equation (A2), (A9), (A10), and setting $v_{rel} = \sqrt{2}v_{rms}$ we obtain

$$\Gamma_{1+2} = \sqrt{2}\frac{\pi^2}{3}(1 - f_b - f_t) f_b\, n_0^2\, r_{core}^3\, a_b^2 v_{rms} \left[1 + \frac{3Gm}{a_b v_{rms}^2}\right]. \tag{A11}$$

Finally, inverting equation (A11), inserting some typical values for star clusters, and using n_{core} instead of n_0, we get

$$\tau_{1+2} = 1.8 \times 10^9 \, (1 - f_b - f_t)^{-1} \, f_b^{-1} \left(\frac{10^3 \text{ pc}^{-3}}{2n_{core}}\right)^2$$

$$\times \left(\frac{1 \text{ pc}}{r_{core}}\right)^3 \left(\frac{5 \text{ km s}^{-1}}{v_{rms}}\right) \left(\frac{1 \text{ AU}}{a_b}\right)^2$$

$$\times \left[1 + 53 \left(\frac{m}{0.5 \text{ M}_\odot}\right) \left(\frac{1 \text{ AU}}{a_b}\right) \left(\frac{5 \text{ km s}^{-1}}{v_{rms}}\right)^2\right]^{-1} \text{ yr.}$$

This paper has been typeset from a TEX/LATEX file prepared by the author.

Chapter 7

Formation of supermassive stars in the first star clusters

7.1 Statement about my contribution

For the research article presented in this chapter my contribution consisted in the development of the numerical implementation used to run the simulations. I ran the numerical simulations and analyzed them. I obtained the parametrization of the mass-radius relationships included in the appendix. I created all the tables and figures and wrote the article. All the authors contributed to the discussion and helped with the revision of the manuscript.

Formation of supermassive stars in the first star clusters

Bastián Reinoso [○],[1][★] Ralf S. Klessen [○],[1,2] Dominik Schleicher,[3] Simon C. O. Glover [○][1] and P. Solar[3]

[1]*Universität Heidelberg, Zentrum für Astronomie, Institut für Theoretische Astrophysik, Albert-Ueberle-Str 2, D-69120 Heidelberg, Germany*
[2]*Universität Heidelberg, Interdisziplinäres Zentrum für Wissenschaftliches Rechnen, Im Neuenheimer Feld 205, D-69120 Heidelberg, Germany*
[3]*Departamento de Astronomía, Facultad Ciencias Físicas y Matemáticas, Universidad de Concepción, Av. Esteban Iturra s/n Barrio Universitario, Casilla 160-C, Concepción, Chile*

ABSTRACT

The formation of supermassive stars is believed to be an essential intermediate step for the formation of the massive black hole seeds that become the supermassive black holes powering the quasars observed in the early Universe. Numerical simulations have shown that supermassive stars can form in atomic-cooling haloes when protostars reach accretion rates higher than $\sim 10^{-2}\,M_\odot\,yr^{-1}$ and fragmentation is suppressed on pc scales. It is, however, still uncertain if a supermassive star still emerges when fragmentation occurs at smaller scales and a cluster of stars is formed instead. In this work, we explore the problem of massive object formation due to the interplay of collisions and accretion in star clusters at low metallicity. We model a small embedded cluster of accreting protostars following subparsec scale fragmentation during the collapse of a primordial gas cloud, and follow its evolution by performing N-body plus hydrodynamical simulations. Our results show that supermassive stars with 10^3 and $10^4\,M_\odot$ are always formed due to the interplay of collisions and accretion, and in some cases these objects are part of a binary system. The resulting supermassive star is surrounded by tens of smaller stars with typical masses in the range 1–$100\,M_\odot$.

Key words: methods: numerical – stars: formation – quasars: supermassive black holes – stars: Population III – early Universe.

1 INTRODUCTION

As of today, more than 200 quasars have been detected at redshift $z > 5.7$ (Fan et al. 2006; Mortlock et al. 2011; Wu et al. 2015; Bañados et al. 2018; Onoue et al. 2019; Reed et al. 2019; Bañados et al. 2021; Wang et al. 2021), with masses larger than $10^9\,M_\odot$, and notably, more than $10^{10}\,M_\odot$ for SDSS J010013.02 + 280225.8 (Wu et al. 2015). Explaining the formation and growth of the supermassive black holes (SMBHs) powering those quasars, at an age of the Universe of less than a billion years, is still an important open problem in astrophysics (see the reviews by Volonteri 2010; Woods et al. 2019). A natural approach to solve this problem is to find and study the processes capable of yielding massive black holes (BHs) early in the history of the Universe. These early-formed massive BHs are the seeds that grow further by accreting matter, continuous mergers, or both, becoming finally the most distant quasars observed today.

The most straightforward path that yields massive BH seeds comes from the death of massive population III stars (Abel, Bryan & Norman 2002; Heger & Woosley 2002; Heger et al. 2003; Klessen 2019), whose initial mass function (IMF) is believed to be heavy as supported by recent numerical simulations (Stacy, Bromm & Lee 2016; Fraser et al. 2017; Riaz et al. 2018; Sharda, Federrath & Krumholz 2020). This scenario, however, faces important limitations, as the formed seeds are still too light ($\lesssim 10^2\,M_\odot$). In addition, because massive Pop III stars are very effective at expelling gas from the low-mass haloes, in which they form the black holes formed from them are 'born starving' in regions of low-gas density, and thus cannot grow efficiently by gas accretion (Johnson & Bromm

2007; Smith et al. 2018). An alternative pathway for massive black hole seed formation is the runaway growth of a single star due to stellar collisions in very dense star clusters (Omukai, Schneider & Haiman 2008; Katz, Sijacki & Haehnelt 2015; Sakurai et al. 2017; Reinoso et al. 2018; Sakurai, Yoshida & Fujii 2019; Reinoso et al. 2020; Vergara et al. 2021), or black hole mergers in dense black hole clusters (Davies, Miller & Bellovary 2011; Lupi et al. 2014). This channel yields massive objects with typical masses of $10^3\,M_\odot$. These BHs could grow to $10^9\,M_\odot$ by $z \sim 7$ if they accreted continuously at the Eddington limit, but this is an unlikely scenario considering the environment in which those seeds emerge. A recent work by Escala (2021) suggests that a runaway collision process in nuclear star clusters could produce BHs with masses up to $10^9\,M_\odot$.

The pathway that yields the most massive BH seeds is the so-called direct collapse black hole (DCBH) scenario, and as of today, it seems the most plausible explanation for the highest redshift quasars observed. Initially proposed by Rees (1984), this formation channel consists of the accumulation of a huge amount of matter in a sufficiently small volume, following the collapse of a pristine gas cloud. This process yields a supermassive star (SMS) that collapses to a BH due to the post-Newtonian instability (Chandrasekhar 1964).

Stellar structure calculations show that SMSs are inflated objects, with effective temperatures of $10^4\,K$, that can reach final masses of $10^5\,M_\odot$ before collapsing due to the post-Newtonian instability (Chandrasekhar 1964; Hosokawa, Omukai & Yorke 2012; Hosokawa et al. 2013; Schleicher et al. 2013; Woods et al. 2017; Haemmerlé et al. 2018; Haemmerlé 2021). Given their low effective temperature, they are unable to produce ionizing photons that may terminate accretion due to radiative feedback. Furthermore, considering the gas-rich environments, in which those objects form, they are promising

★ E-mail: bastian.reinoso@uni-heidelberg.de

candidates to produce the massive BH seeds that can grow further by mass accretion.

Recent numerical simulations explored the collapse of pristine gas clouds in the early Universe, and found that an essential condition for the formation of SMSs in such environments is the suppression of molecular hydrogen cooling, which would otherwise lead to fragmentation of the cloud and the formation of population III stars. Preventing the cooling due to molecular hydrogen requires a decrease of its abundance by photodetachement of the H^- ion and the destruction of the H_2 molecule. This can be achieved in the presence of a strong radiation background that carries photons in the Lyman–Werner bands ($11.2\,eV \leq h\nu \leq 13.6\,eV$), and dissociates the H_2 molecule along with infrared photons ($h\nu \geq 0.76\,eV$) that lower the abundance of H^-, a catalyst for H_2 formation. This can occur if two pristine haloes remain at a small separation such that once star formation begins in one of them, the other is exposed to a high Lyman–Werner radiation intensity, thus suppressing molecular hydrogen cooling. This is termed as the 'synchronized pairs' scenario (Dijkstra et al. 2008; Visbal, Haiman & Bryan 2014; Chon, Hosokawa & Yoshida 2018). Once molecular hydrogen cooling has been suppressed, cooling occurs primarily via collisional excitation of hydrogen atoms, provided that the gas temperature is high enough to make this process efficient. Haloes, in which this is the case, are often referred to as atomic-cooling halo.

The radiation intensity needed to suppress molecular hydrogen cooling is usually expressed in units of J_{21}, where $J_{21} = 1$ corresponds to a radiation intensity of $10^{-21}\,erg\,cm^{-2}\,s^{-1}\,sr^{-1}\,Hz^{-1}$ at the Lyman limit (see e.g. Omukai 2001; Latif et al. 2015). The required radiation intensity on the atomic-cooling halo could be as high as $J_{21} = 1000$ (Regan, Johansson & Wise 2014; Latif et al. 2015), or even higher when considering an X-ray background (Inayoshi & Tanaka 2015; Glover 2016), and the true value has important implications for the number density of DCBHs (Dijkstra, Ferrara & Mesinger 2014; Inayoshi & Tanaka 2015; Chon et al. 2016; Chon et al. 2018).

It has been suggested (Wise et al. 2019) that extremely high radiation intensities are not a necessary condition as long as the dark matter halo grows rapidly through mergers. The dynamical heating induced by this period of rapid growth, combined with a moderate Lyman–Werner flux of $J_{21} \sim 3$ can still produce accretion rates of the order of 0.1–$1\,M_\odot\,yr^{-1}$ onto the central object. Once the right conditions are met and high accretion rates achieved ($>0.04\,M_\odot\,yr^{-1}$), an SMS can still emerge.

The ideal places for the emergence of DCBHs are overdense regions in the early Universe, as they provide intense radiation backgrounds and rapid halo growth. This has been investigated via semi-analytic models by Lupi, Haiman & Volonteri (2021), suggesting that the 'synchronized pairs' channel as well as the dynamically heated haloes can produce several BH seeds in these environments.

Although, a single object forms initially in idealized scenarios of pristine atomic-cooling haloes irradiated by a high-intensity LW background, it is important to follow its evolution for longer times in order to place constraints on its final mass. High resolution numerical simulations have shown that fragmentation is unavoidable in the accretion disc for the high accretion rates expected in these environments, and fragmentation is seen on $\sim$au scales (Clark et al. 2011; Greif et al. 2012; Latif, Schleicher & Hartwig 2016; Becerra et al. 2018; Suazo et al. 2019; Patrick et al. 2020; Wollenberg et al. 2020; Latif et al. 2021; Jaura et al. 2022; Prole et al. 2022a, b). It is therefore important to understand the fate of the haloes that failed to remain metal-free and/or of the ones, in which an important degree of fragmentation is expected. This scenario is now being explored,

and various models, both numerical and analytical, have shown that SMSs with $10^{4-5}\,M_\odot$ might still be able to form (Boekholt et al. 2018; Alister Seguel et al. 2020; Tagawa, Haiman & Kocsis 2020; Das et al. 2021; Schleicher et al. 2022). These results seem to be confirmed by the more sophisticated simulations of Chon & Omukai (2020) and Regan et al. (2020). Additionally, Sassano et al. (2021) showed that under Eddington-limited accretion, the heavy black hole seeds ($\sim10^5\,M_\odot$) are able to produce $10^9\,M_\odot$ BHs at $z \sim 6$ (see also Trinca et al. 2022 for a similar analysis involving light BH seeds and Kohri et al. 2022 for seed growth under super-Eddington accretion).

In this paper, we present a set of *N*-body plus hydrodynamics simulations that include mass accretion, mass-radius parametrizations, and stellar mergers to model the central region of a collapsed primordial cloud, in which multiple protostars are present. We explore two environments similar to the ones expected in atomic-cooling haloes to assess the impact of fragmentation at sub parsec scales during the assembly of DCBHs. We describe our simulation set-up in Section 2, then present our results in Section 3 and a discussion in Section 4.

2 SETUP

In this section, we describe the initial conditions for our models, the numerical codes used, and additional algorithms that we include in our simulations.

2.1 Initial conditions

The clusters are modelled to consist of a combination of gas and protostars, the former represented by SPH particles and the latter by particles that interact only through gravity, which we also refer to as *N*-body particles throughout this paper. We model two clusters that differ only in the total mass being 10 025.6 in one case and 30 025.6 $M_\odot$ in the other. In both cases, we start with a total mass of 25.6 $M_\odot$ in protostars, so the initial gas masses are 10 000 and 30 000 $M_\odot$, respectively. The initial number of protostars is 256 and each of them has a mass of 0.1 $M_\odot$, which is consistent with the mass of protostars formed in atomic-cooling haloes (Becerra et al. 2015). The gas is sampled with 2^{18} SPH particles. For each set of particles (SPH and protostars), the positions are sampled from a Plummer distribution (Plummer 1911) with a Plummer radius $R_p \sim 0.077\,pc$ such that the half-mass radius is $R_h \sim 1.3R_p = 0.1\,pc$, and we impose a cut-off radius of 5 Plummer radii for each model such that all the mass is enclosed within $\sim 0.4\,pc$. This yields an initial number density for protostars of 956 pc^{-3}. We adopt this distribution for simplicity, as the precise distribution of gas and protostars will be unknown. However, it ensures a meaningful behaviour of both quantities in the central region, where the density profile will be flat, while the behaviour in the outer parts will approximately resemble the behaviour found in cosmological simulations (e.g. Latif et al. 2015). The velocities of the protostars are obtained by imposing virial equilibrium condition. We relax the Plummer distribution of SPH particles, and then inject a spectrum of non-compressive Kolmogorov turbulence with Mach number $\mathcal{M} = 1$ as found in numerical simulations by Latif et al. (2013).

2.2 Numerical simulations

To run our simulations, we use the Astrophsyical MUlti-purpose Software Environment (AMUSE[1]; see Portegies Zwart et al. 2009; Pelupessy et al. 2013; Portegies Zwart et al. 2013; Portegies Zwart & McMillan 2018), a PYTHON interface designed to couple existing numerical codes offering great flexibility, and allowing us to relatively easily include new algorithms such as mass accretion onto the protostars, sink particle creation, a treatment for stellar collisions, and mass radius relations for the protostars, all of them described in the next subsections.

2.3 N-body-SPH coupling

We couple the pure *N*-body code PH4 (McMillan & Hut 1996) and the SPH code FI (Hernquist & Katz 1989; Gerritsen & Icke 1997; Pelupessy, van der Werf & Icke 2004) by means of the BRIDGE method (Fujii et al. 2007) via the *bridge* class included in AMUSE. This method consists of calculating the gravitational acceleration at the position of the *N*-body particles using the SPH particles and vice versa, i.e. the particles in one code kick the particles in the other code. To ensure that the coupling does not violate Newton's third law, we use the code FastKick to perform the kicks, with a constant gravitational smoothing length of 0.5 au, approximately equal to the smallest smoothing length among all the SPH particles. By doing so, we employ the same gravitational smoothing kernel for both sets of particles, and make sure that the gravitational forces among them are symmetric.

For evolving the particles in the *N*-body code, we use a smoothing length of $1\,R_\odot$ in order to accurately solve gravitational interactions between the protostars. We include an external pressure floor in the SPH code by modifying the momentum equation in an analogous way as done in Benz (1990); Clark et al. (2011). This external pressure is equal to the pressure of the cloud at the cut-off radius, and corresponds to $\sim 1.72 \times 10^{-7}\,\mathrm{g\,cm^{-1}\,s^{-2}}$ for the most massive cloud and $\sim 7.45 \times 10^{-8}\,\mathrm{g\,cm^{-1}\,s^{-2}}$ for the less massive cloud. The external pressure is required to stabilize the clouds against vacuum boundary conditions.

Finally, we modified the code FI to include a modified equation of state of the form

$$T = T_0 \left[1 + \left(\frac{\rho}{\rho_c} \right)^{\gamma - 1} \right], \tag{1}$$

so that the gas behaves isothermally, with a temperature $T_0 = 8000\,\mathrm{K}$ at low densities, but becomes adiabatic at densities above $\rho_c = 10^{15}\,\mathrm{cm^{-3}}$, as found in 1D and 3D models including detailed chemical networks (Omukai et al. 2008; Becerra et al. 2015). We use an adiabatic index $\gamma = 5/3$.

The treatment of stellar collisions (described in Section 2.9) as well as the mass radius relations are implemented at the PYTHON level. The mass accretion (see Section 2.6) and sink particle creation (see Section 2.7) algorithms are written in FORTRAN and included as PYTHON functions via F2PY for adequate performance. This offers the advantage of easily replacing any of the codes used without having to re-write these routines.

The time integration consists sequentially of the Kick-Drift-Kick (KDK) integration with *bridge* during which stellar collisions and sink particle creation are solved, followed by the computation of accretion onto the protostars, and the treatment of stellar ejections.
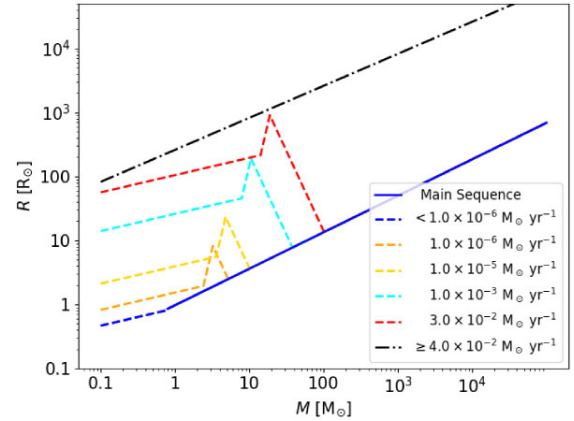
Figure 1. The adopted mass radius relations for accreting protostars in our models.

We impose a maximum time-step of 5 yr for *bridge* in order to perform the accretion steps rather frequently, given the rapid accretion rates expected in this environment.

The densest gas is typically found around accreting protostars and thus it is often accreted after every accretion step. Nevertheless, there are regions where the gas becomes very dense, and thus the associated free-fall time can be of the order of 10^{-4} yr. Because of this, we implemented an adaptive time-stepping algorithm for *bridge*, such that the time-step is reduced by factors of 2 until becoming smaller than the shortest free-fall time. The time-step can increase by a factor of 2 after each time-step only if the shortest free-fall time is more than twice the current time-step.

2.4 Protostars and stars

The *N*-body particles in our simulations are meant to represent, in an approximate way, protostars and stars, but they interact here only through gravity and we do not include any type of feedback. By taking advantage of the particle sets provided by AMUSE, we assign additional properties to our *N*-body particles such as: *stage* and *luminosity*. The *stage* property indicates if an *N*-body particle has already entered the main sequence phase or if it is still in the protostellar phase. This distinction is important as inflated protostars can still contract to the main-sequence phase, and thus will follow different mass-radius relations. A correct determination of the size of the particles is an essential feature needed in this very dense collisional environment. For the determination of the radius of each *N*-body particle, we incorporate new PYTHON functions without the need to modify any code. The mass radius parametrization that we use is briefly described in Section 2.5, and further details are provided in Appendix A.

2.5 Mass-radius parametrization

We use a parametrization of the mass-radius relation based on the works by Hosokawa & Omukai (2009), Hosokawa et al. (2012), and Hosokawa et al. (2013). This implementation is simplified by the use of the *stage* property for our *N*-body particles. We define three stages in which an *N*-body particle can be. The possible stages are the *protostar*, *star*, and *supermassive star* stages.

For a particle in the *protostar* stage, the mass–radius relation depends on its mass and accretion rate. We present in Fig. 1, with

dashed lines, the mass radius relations for protostars accreting at different rates. The implementation is described in Appendix A.

For a particle in the *star* stage, the mass-radius relation is given by:

$$R_* = 0.97 \left(\frac{M_*}{M_\odot} \right)^{0.57} R_\odot. \tag{2}$$

It is used once the protostars enter in the main-sequence stage, and corresponds to the blue solid line, onto which most of the other lines converge in Fig. 1.

An *N*-body particle enters into the *supermassive star* stage if it is still on the *protostar* stage and if its accretion rate becomes larger than a critical accretion rate $\dot{M}_{crit}$. The mass-radius relation for these particles is given by:

$$R_* = 2600 \left(\frac{M_*}{100\, M_\odot} \right)^{1/2} R_\odot. \tag{3}$$

It is shown with a dot–dashed line in Fig. 1.

We note that an *N*-body particle in the *protostar* stage will eventually contract to the main sequence after becoming massive enough. Similarly, an *N*-body particle in the *supermassive star* stage can also contract to the main sequence if its accretion rate drops below a critical value $\dot{M}_{crit}$ for a time longer than the Kelvin–Helmholtz (KH) time-scale t_{KH}. We adopt here $\dot{M}_{crit} = 0.04\, M_\odot\, yr^{-1}$ (Hosokawa et al. 2013).

Due to the structure of supermassive stars, the relevant time-scale for contraction is the Kelvin–Helmholtz time-scale evaluated at the stellar surface $t_{KH,\,surf}$ (Schleicher et al. 2013; Sakurai et al. 2015). The value of the KH time-scale at the surface for these objects can be approximated as 10–$100\, t_{KH}$ (Sakurai et al. 2015). We explore here these two extreme values, namely $t_{KH,\,surf} = 10\, t_{KH}$ and $100\, t_{KH}$. The first case is the most pessimistic case for stellar collisions to occur, whereas the second is the most optimistic case. In consequence, in our simulations, an *N*-body particle in the *supermassive star* stage will contract if its accretion rate falls below $\dot{M}_{crit}$ for a time longer than $t_{KH,\,surf}$ given by:

$$t_{KH,surf} = X\, t_{KH} = X \frac{GM^2}{RL}, \tag{4}$$

with $X = 10$ or 100.

In order to calculate $t_{KH,\,surf}$, we make use of the *luminosity* property of our *N*-body particles. Luminosites are calculated based on the works by Hosokawa & Omukai (2009), Hosokawa et al. (2012), and Hosokawa et al. (2013) as described in Appendix A.

Finally, we also assume that a stellar merger will perturb the new object in such a way that the resulting object has to start over the relaxation process. This means that stellar mergers help to keep the protostars inflated in our simulations.

2.6 Gas accretion

After every KDK step, we calculate the gas accretion onto the protostars. We model the gas accretion by employing the algorithm developed by Hubber, Walch & Whitworth (2013). For every *N*-body particle, we define a spherical volume called the interaction zone, with radius $R_{I.Z.}$. Inside this region, the weighted average gas flux onto the central point mass is computed, with the weight calculated via a cubic spline kernel function.

The radius of the interaction zone is adjusted iteratively before every accretion calculation, with a maximum of 50 iterations per particle, to maintain a constant gas mass of $M_{int,\,max} = 50\, M_{gas}/N_{SPH}$ (the mass corresponding to 50 SPH particles). We impose lower and

upper limits to the radius of the interaction zone of $r_{min} = \max(10\, au, 2R_{star})$ and $r_{max} = 500\, au$, respectively, so that the interaction zone cannot be smaller than the protostars. We also impose the angular momentum conservation condition for the accreted gas and the angular momentum feedback from the point particle as described in Hubber et al. (2013), as well as the prescriptions for spherical or disc accretion.

Once the accretion step has been completed, we update the radius of each star particle according to the mass–radius parametrization described in Section 2.5 and in Appendix A.

2.7 Sink particles

Given the high densities reached in our simulations, we decided to include sink particle creation to avoid prohibitively small time-steps. Based on the work by Hubber et al. (2013), specifically on their 'NewSink' algorithm, we create sink particles whenever an SPH particle reaches a density higher than $10^{16}\, cm^{-3}$ (Becerra et al. 2015), it sits in a minimum of the gravitational potential among its neighbours, it does not overlap existing sinks, and fulfills the density criterion:

$$\rho_i > \rho_{Hill} \equiv \frac{3 X_{Hill}(-\Delta \mathbf{r}_{is'} \cdot \Delta \mathbf{a}_{is'})}{4\pi G |\Delta \mathbf{r}_{is'}|^2}, \tag{5}$$

for all existing sinks s' for a given SPH particle i. Here, $\Delta \mathbf{r}_{is'}$ and $\Delta \mathbf{a}_{is'}$ are the relative position and acceleration of sink candidate i with respect to existing sink s'. We set $X_{Hill} = 4$. This Hill sphere criterion ensures that an SPH particle turns into a sink particle in the vicinity of another sink only if the density peak dominates the local gravitational potential. Once the previous conditions are fulfilled, we remove the SPH particle from FI and insert a new *N*-body particle in PH4. The mass, position, and velocity of the new particle are the same as the ones of the removed SPH particle. The radius of the protostar is initialized to $0.1\, R_\odot$, but is recalculated after every accretion step according to the mass–radius parametrization described in Section 2.5.

The Jeans mass scales as

$$M_J \propto \left(\frac{T^3}{n} \right)^{1/2}, \tag{6}$$

with n being the number density of the gas. In our simulations, the minimum Jeans mass is $\sim 3.96\, M_\odot$. The mass resolution is equal to twice the mass contained inside the smoothing length of an SPH particle. In our case this is

$$M_{res} = 2 N_{neigh} \frac{M_{gas}}{N_{SPH}}, \tag{7}$$

where $N_{neigh} = 64$ is the number of neighbours for one SPH particle as adopted in the code FI, M_{gas} is the initial cloud mass, and N_{SPH} is the number of SPH particles.

In order to avoid artificial fragmentation, our simulations need to resolve the Jeans mass (Bate & Burkert 1997). We achieve the mass resolution by using $N_{SPH} = 1\,048\,576$ for all our simulations.

2.8 Ejections

The *N*-body particles can also be ejected from the cluster. A particle is considered to have been ejected once it fulfills three criteria: its distance to the centre of mass of the system is $\geq 1.4\, pc$; its gravitational potential energy plus kinetic energy per unit mass is positive; and it is moving away from the cluster, i.e. $\mathbf{r} \cdot \mathbf{v} > 0$. Ejected particles are removed from the simulation.

2.9 Collisions

A collision between two particles occurs once the radii of two *N*-body particles overlap during the *N*-body integration. This is implemented in AMUSE with the help of the *stopping conditions*. We activate the *stopping condition* that detects the overlap of two particle's radii in PH4, i.e. a collision occurs when

$$d \leq R_1 + R_2,$$

where *d* is the separation between the particles and R_1 and R_2 are their radii. Once the condition is fulfilled, the integration is interrupted, and then, by implementation at the PYTHON level, we replace the overlapping particles by a new particle that is placed at the centre of mass of the previous configuration, and the new velocity is calculated assuming linear momentum conservation. We assume no mass loss to occur, and thus the new mass is the sum of the masses of the colliding particles, i.e.

$$M_{\text{new}} = M_1 + M_2.$$

In order to determine the new radius of the merger product, we first determine the stage in which the new particle will be, according to the outcomes shown in Table B1; and the new track, in case the resulting stage is *protostar*, is assigned as shown in Table B2. Subsequently, the new radius is obtained from the corresponding mass–radius relation. Further details are provided in Appendix B. After determining the evolutionary stage of the particle, the luminosity is calculated as explained in Appendix A.

3 RESULTS

In this section, we describe the results obtained from our simulations. We begin by describing the general behaviour of the simulated systems, in which we set $t_{\text{KH, surf}} = 100 \, t_{\text{KH}}$ (see Section 2.5). We describe the emergence of massive objects and characterize the final state of the clusters. We do so first for the simulations with $M_{\text{gas}} = 10^4 \, \text{M}_\odot$, and then for simulations with $M_{\text{gas}} = 3 \times 10^4 \, \text{M}_\odot$. We then show the impact of setting $t_{\text{KH, surf}} = 10 \, t_{\text{KH}}$ on the final masses of the most massive objects. All the uncertainties reported correspond to the one sigma interval assuming a normal distribution.

3.1 Clusters with $M_{\text{gas}} = 10^4 \, \text{M}_\odot$

3.1.1 Cluster evolution

By the time that we stop our simulations, most of the gas accretion has already occurred as depicted in Fig. 2. The initial phase of the evolution is marked by a contraction of the inner parts of the gas cloud on a free-fall time-scale. We see the contraction of the inner parts of the cloud, up to the radius at which 25 per cent of the total mass is enclosed, i.e. the 25 per cent Lagrangian radius. This takes place at around 6000 yr, and marks the beginning of the short-time-span during which most of the gas accretion takes place.

During this contraction, turbulence does not significantly affect the cloud evolution as no substructures appear and we observe a spherical collapse, which in turn causes high accretion rates onto a central object around which a gaseous disc is formed. This object quickly becomes the most massive object (MMO) of the cluster.

By the end of the simulations, the total accreted mass reaches typical values of $4612 \pm 798 \, \text{M}_\odot$, i.e. ~$46 \pm 8$ per cent of the initial mass, and the mean total mass in stars that are still bound to the cluster is $4131 \pm 791 \, \text{M}_\odot$. The mean mass in ejected stars is $481 \pm 338 \, \text{M}_\odot$.
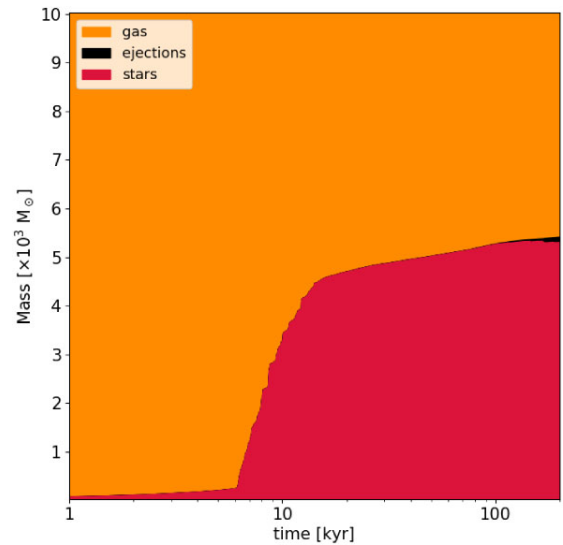

Figure 2. Mass of the gas, bound stars, and ejected stars during the evolution of the system for one of our simulations with $M_{\text{gas}} = 10^4 \, \text{M}_\odot$ (M1_t100_1).

3.1.2 Emergence of very massive objects

In most of our simulations, we see the formation of a single object that contains most of the accreted mass. The typical mass of the MMO is $3729 \pm 792 \, \text{M}_\odot$. We define a parameter ϵ to asses the efficiency of the formation of a massive object. It is defined as $\epsilon = M_{\text{MMO}}/M_{\text{gas}}$ and shown for each simulation in Table 1. We find a mean efficiency $\epsilon = 0.37 \pm 0.08$.

We also see that in one third of the simulations, the MMO is in a binary system with another very massive object. We define a pair of bound stars to be in a binary system if they follow a Keplerian orbit and the mass ratio $q = M_1/M_2$ is less than 7. This choice for this mass ratio is arbitrary but allow us to select high mass stars that are in a binary system with the MMO, which are the binary systems in which we are interested.

We show the properties of the binary systems in Table 2, and we note that in simulations with a binary outcome, there are fewer stars in the final stellar system due to more collisions occurring and more ejections due to three body interactions (see columns 11, 12, and 13 in Table 1).

The overall contraction of the gas cloud causes a strong inflow and therefore a high accretion rate onto one of the central protostars. We show the evolution of this object that becomes the MMO in Fig. 3. The maximum accretion rates in the simulations are a few $\text{M}_\odot \, \text{yr}^{-1}$, surpassing during some time, the critical accretion rate of $\dot{M}_{\text{crit}} = 0.04 \, \text{M}_\odot \, \text{yr}^{-1}$, and thus creating an MMO that emerges in the cloud centre and evolves as a supermassive star. This moment can be distinguished in the second panel of Fig. 3 at the point when the solid orange line first crosses the grey-dashed line. Because of this, the star inflates up to around $2 \times 10^4 \, R_\odot$, i.e. ~93 au as it now follows the mass–radius relation shown with a black dot–dashed line in Fig. 1. The increased cross section of the central star results in a period of runaway collisions with the MMO. The collision rate reaches a maximum of 0.1 collisions per year just after the MMO has inflated in radius, but starts to decline as the number of protostars decreases, as shown in the middle panel of Fig. 4. The mass accretion rate due to collisions can reach very high values of up to $2 \, \text{M}_\odot \, \text{yr}^{-1}$.

Additionally, we see that huge gas densities ($\rho \sim 10^{-8} \, \text{g cm}^{-3}$) around the MMO trigger the formation of ~217 new sink particles

Table 1. Summary of simulation outcomes. We present for each simulation the initial gas mass, the final time, the quiescent time adopted for contraction to the main sequence for supermassive stars, the simulation outcome, the total accreted mass, the final stellar mass bound to the most massive object, the mass of the most massive object, the efficiency of massive object formation, the total mass in ejected stars, the number of stars bound to the MMO, the number of ejections and the number of collisions.

Simulation	M_{gas} [M$_\odot$]	t_{end} [yr]	$t_{KH, surf}$ [t_{KH}]	outcome	$M_{accreted}$ [M$_\odot$]	$M_{stellar, bound}$ [M$_\odot$]	M_{MMO} [M$_\odot$]	ϵ	$M_{ejected}$ [M$_\odot$]	N_{stars}	$N_{ejections}$	N_{col}
M1_t100_1	10^4	200 015	100	single	5414	5305	5197	0.52	109	56	70	256
M1_t100_2	10^4	200 005	100	single	3815	3482	3311	0.33	333	62	112	288
M1_t100_3	10^4	200 043	100	single	4709	4539	3893	0.39	170	56	77	341
M1_t100_4	10^4	200 023	100	single	3730	3315	3048	0.30	415	48	153	291
M1_t100_5	10^4	200 017	100	binary	5854	4821	4096	0.41	1033	6	141	369
M1_t100_6	10^4	200 050	100	binary	4150	3326	2831	0.28	824	15	196	300
M1_t10_1	10^4	200 024	10	single	5397	4952	4326	0.43	445	66	83	343
M1_t10_2	10^4	120 045	10	single	4548	4377	4156	0.42	171	88	79	375
M1_t10_3	10^4	200 022	10	binary	6057	5297	4064	0.41	760	65	147	364
M1_t10_4	10^4	200 029	10	binary	5262	4468	2901	0.29	794	86	141	456
M1_t10_5	10^4	200 036	10	single	6804	6256	4858	0.49	548	89	53	412
M1_t10_6	10^4	112 701	10	single	4617	4255	4135	0.41	362	56	119	301
M3_t100_1	3×10^4	200 021	100	single	26 108	25 808	24 418	0.81	300	13	42	1892
M3_t100_2	3×10^4	200 043	100	single	26 939	26 898	26 890	0.90	41	10	19	1842
M3_t100_3	3×10^4	200 009	100	single	26 388	26 211	24 577	0.82	177	11	34	2547
M3_t100_4	3×10^4	200 038	100	single	23 312	22 850	20 365	0.68	462	36	53	1844
M3_t100_5	3×10^4	200 034	100	single	23 070	22 973	22 618	0.75	97	12	50	2215
M3_t100_6	3×10^4	200 035	100	single	26 966	26 851	24 375	0.81	115	3	29	2522
M3_t10_1	3×10^4	200 008	10	single	20 981	20 831	20 435	0.68	150	13	70	2283
M3_t10_2	3×10^4	200 026	10	single	23 451	23 063	20 776	0.69	388	32	61	1807
M3_t10_3	3×10^4	200 048	10	single	25 871	25 413	22 267	0.74	458	6	50	2354
M3_t10_4	3×10^4	200 014	10	single	22 585	21 889	21 733	0.72	696	10	89	2445
M3_t10_5	3×10^4	200 039	10	single	20 778	20 481	20 368	0.68	297	6	96	2297
M3_t10_6	3×10^4	200 011	10	single	27 051	26 846	26 746	0.89	205	7	42	3514

Table 2. Properties of binary systems. We present the mass of the most and less massive object M_1 and M_2, respectively, the semimajor axis a and the eccentricity e.

Simulation	M_1 [M$_\odot$]	M_2 [M$_\odot$]	a [au]	e
M1_t100_5	4096	688	355	0.126
M1_t100_6	2831	464	240	0.375
M1_t10_3	4064	831	472	0.394
M1_t10_4	2901	1224	120	0.077

on average. Almost all (95.4 ± 1.7 per cent) of these new sinks merge with other objects, but only 34 ± 7 per cent of them merge with the MMO. We show the mass distribution of the particles that merge with the MMO in Fig. 5.

Despite the accretion rate falling below the critical accretion rate $\dot{M}_{crit}$, the frequent stellar collisions prevent the contraction of the MMO. We note that the mass contributed by collisions to this object is around 60 per cent of its final mass as shown in Fig. 6.

3.1.3 Final cluster properties

The typical outcome of our simulations is a small cluster of stars with almost no gas left. This final stellar cluster in most simulations is made up of ~50 stars with typical masses in the range 1–10 M$_\odot$ surrounding the MMO. No more significant gas accretion is taking place at 200 kyr, and we would expect radiative feedback from the stars to efficiently evaporate the remaining gas. The final mass functions are similar in shape as well as the number of remaining and ejected stars, although a few clusters contain a binary system and

fewer stars remain bound due to the increased number of collisions and three body interactions effectively ejecting lower mass objects.

We present the combined mass distribution at the end of simulations M1_t100_1–6 in Fig. 7, and the combined mass distribution of ejected particles in Fig. 8. Individual mass distributions of bound and ejected particles for each simulation are presented in Figs D1 and D2.

3.2 Clusters with $M_{gas} = 3 \times 10^4$ M$_\odot$

In this section, we describe the general evolution of the clusters with 3×10^4 M$_\odot$ in gas, and mention the differences with the less massive clusters.

3.2.1 Cluster evolution

The initial behaviour of the gas cloud is the same for all the simulations, and also very similar to the behaviour in the less massive clusters. We see that most of the gas is accreted early on in the cloud evolution as depicted in Fig. 9. During the initial evolution, the inner parts of the cloud experience an overall contraction. Specifically, we see a contraction of the 25 per cent Lagrangian radius, which leads to a rapid inflow of gas to the central parts of the cluster in a free-fall time, i.e. ~3000 yr. Unlike in the less massive clusters, we also see a contraction at the 50 per cent Lagrangian radius.

Turbulence seems to have a negligible role here, as no substructure appears during the initial contraction and a spherical collapse proceeds. During the rapid mass inflow, either a central object starts to accrete most of the mass, or a new sink particle is created at the centre due to the high gas densities. This central particle reaches accretion rates of several 10 M$_\odot$ yr^{-1}, and the average efficiency

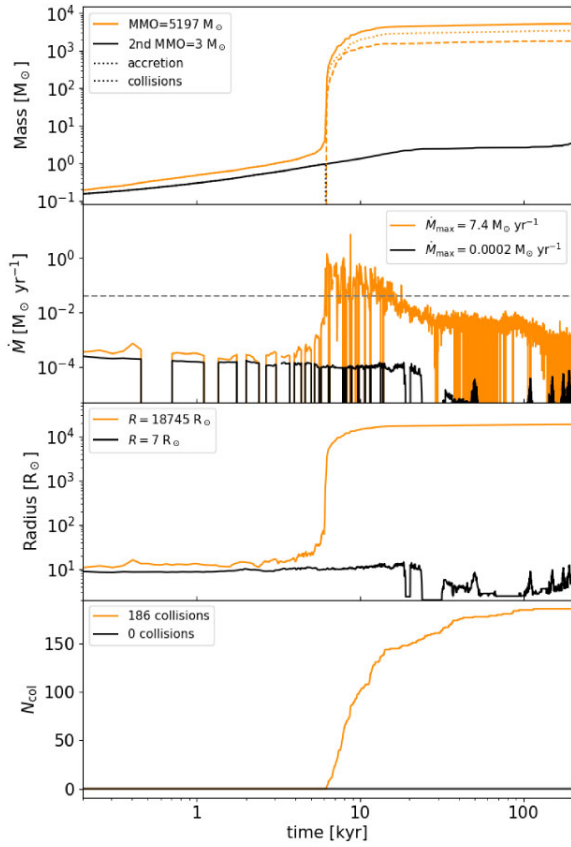**Figure 3.** Evolution of the mass M, accretion rate $\dot{M}$, and radius R for the MMO and second MMO in one of our simulations (M1_t100_2), along with the number of collisions N_{col} as functions of time.
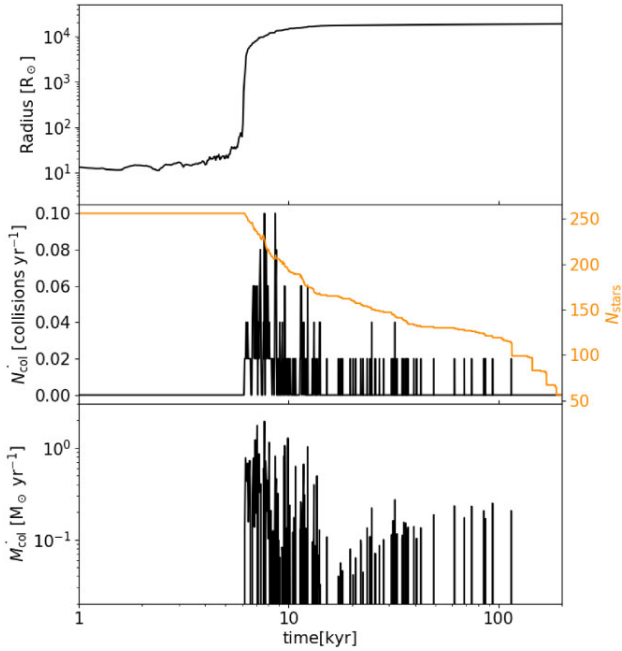

Figure 4. Radius of the MMO, collision rate along with the number of protostars, and mass accretion rate due to collisions as functions of time for one of our simulations (M1_t100_1).
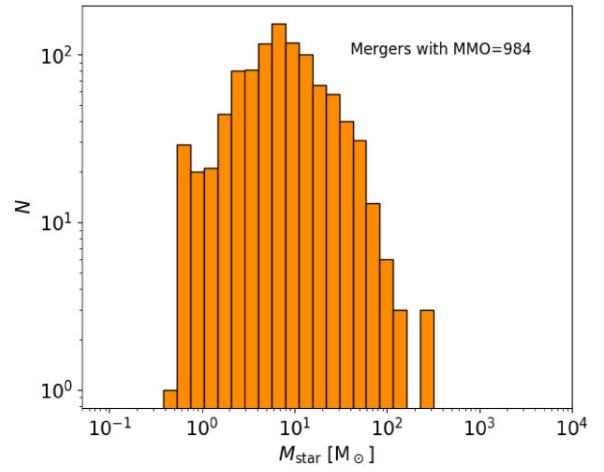

Figure 5. Mass distribution of the particles that merge with the MMO for simulation M1_t100_1–6.
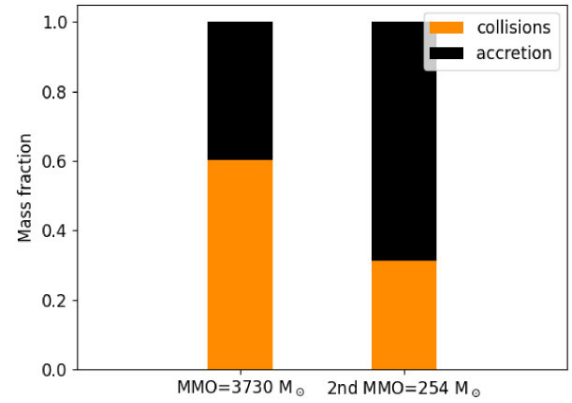

Figure 6. Average mass fraction gained through collisions and accretion, and average masses for the MMO and second MMO for simulations M1_t100_1–6.
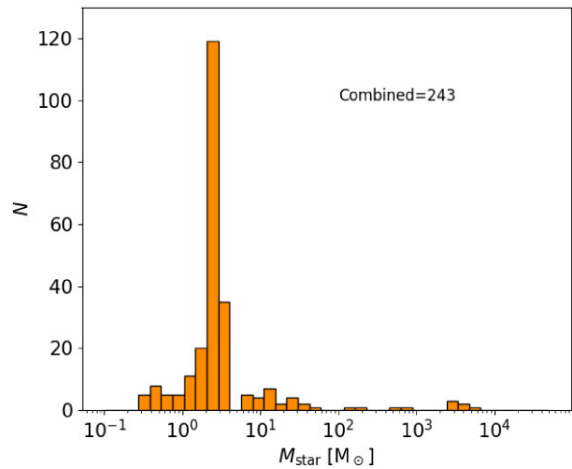

Figure 7. Combined mass distribution for stars bound to the cluster at the end of simulations M1_t100_1–6.
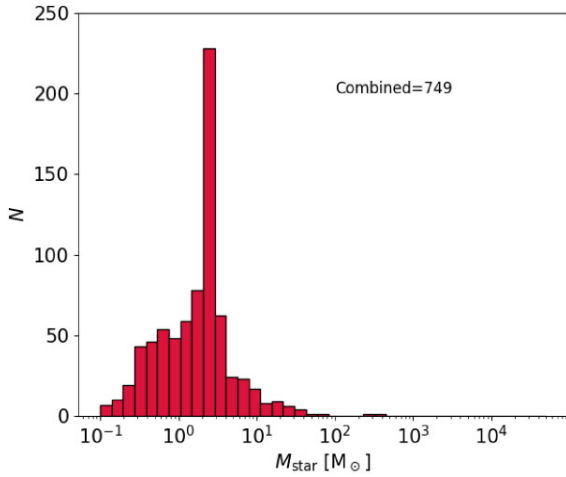
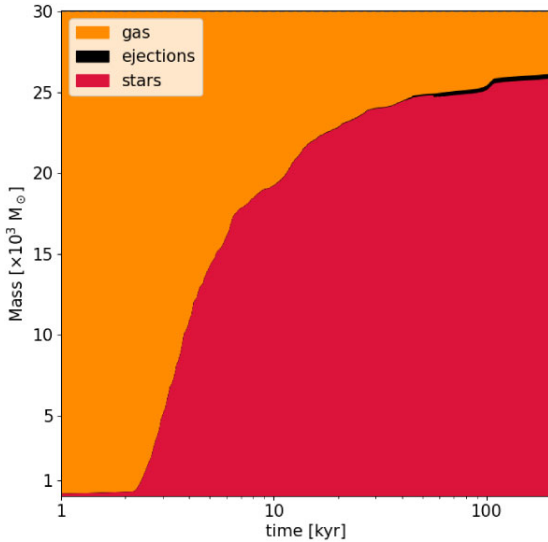**Figure 8.** Combined mass distribution of ejected stars at the end of simulations M1_t100_1–6.

Figure 9. Same as Fig. 2 but for a cluster with $M_{gas} = 3 \times 10^4 \, M_\odot$.

$\epsilon = 0.80 \pm 0.07$ means that this single object gathers on average 80 ± 7 per cent of the total mass of the cloud.

3.2.2 Emergence of very massive objects

In all our simulations with $M_{gas} = 3 \times 10^4 \, M_\odot$, we see the formation of a single object that contains on average 80 ± 7 per cent of the initial cluster mass at 200 kyr. This means that the average mass of the MMO is $23\,873 \pm 2001 \, M_\odot$. We present in Fig. 10 some of the properties of the MMO, like the mass, accretion rate, radius, and number of collisions it experiences during the evolution of the system. This particle also evolves as a supermassive star due to the high accretion rates that it reaches, and grows both by accretion of gas and stellar collisions. The mass growth by mergers with other protostars contributes on average 46 per cent of its final mass as shown in Fig. 11. Unlike the less massive clusters, here higher accretion rates are reached, and they last for longer. We also see that stellar collisions contribute with a smaller mass fraction to the final mass of the MMO. This is simply due to the fact that in the
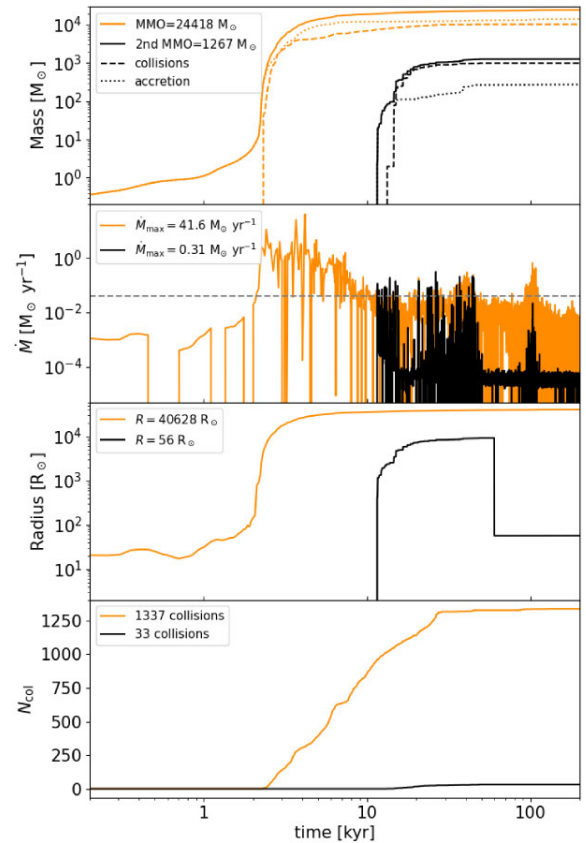

Figure 10. Same as Fig. 3 but for a cluster with $M_{gas} = 3 \times 10^4 \, M_\odot$.
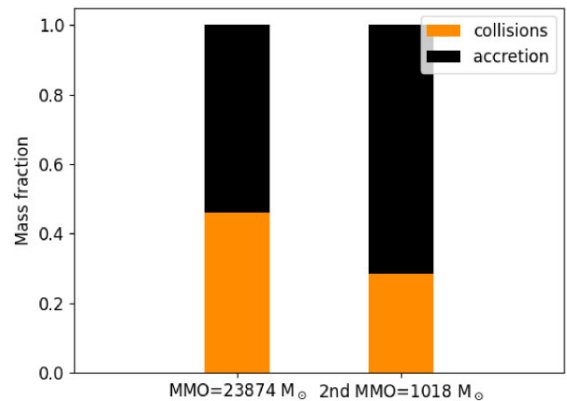
Figure 11. Average mass fractions gained through collisions and accretion, and average final masses for the MMO and the second MMO for simulations M3_t100_1–6.

simulations with $M_{gas} = 3 \times 10^4 \, M_\odot$, the MMO gains much more mass by gas accretion.

Gas accretion peaks on average at $10 \, M_\odot \, yr^{-1}$ and remains above the critical accretion rate during the initial 8000 yr after the initial cloud contraction. This is sufficient to cause the protostar to evolve as an inflated object that quickly reaches a radius of more than 100 au, which in turn causes many stellar collisions to occur. We see in Fig. 12, the collision rate peaks just after the MMO inflates in radius, reaching a peak of more than 0.3 collisions per year, a factor 3 higher than the lower mass cloud simulations. The mass accretion due to

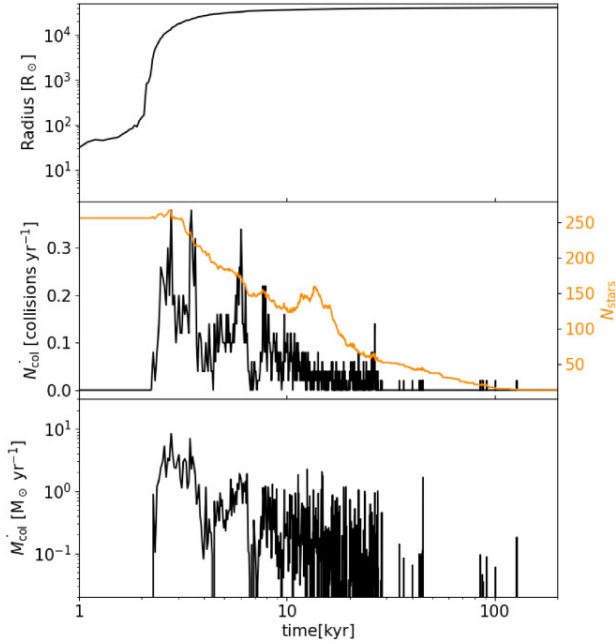**Figure 12.** Same as Fig. 4 but for a cluster with $M_{\mathrm{gas}} = 3 \times 10^4 \, \mathrm{M}_\odot$.

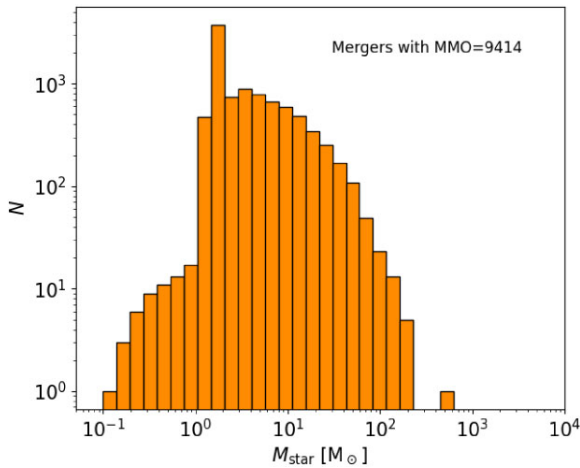**Figure 13.** Mass distribution of the particles that merge with the MMO for simulation M3_t100_1.

collisions reaches peaks of $\sim 10 \, \mathrm{M}_\odot \, \mathrm{yr}^{-1}$, a factor 10 higher than for the less massive cloud simulations. The collision rate then decreases with the number of protostars.

Additionally, the huge gas densities ($\rho \sim 10^{-8} \, \mathrm{g \, cm}^{-3}$) found around the MMO trigger, the formation of sink particles, 1950 new sink particles on average. Nearly all of these sink particles ($\sim 99 \pm 0.2$ per cent) merge with other objects, notably, 70 ± 5 per cent of the sinks merge with the MMO, and most of them do so shortly after they are created when they have accreted only 1–2 $\mathrm{M}_\odot$. Sink particles in this mass range that merge with the MMO represent 52 ± 9 per cent of the total number of mergers, but they contribute on average only 11 ± 4 per cent of the total mass gained through mergers. We show the mass distribution of the sink particles that merge with the MMO in Fig. 13.
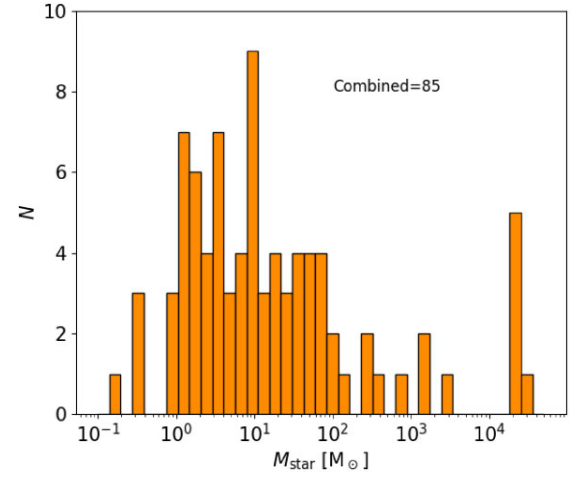

Figure 14. Combined mass distribution for stars bound to the cluster at the end of simulations M3_t100_1–6.
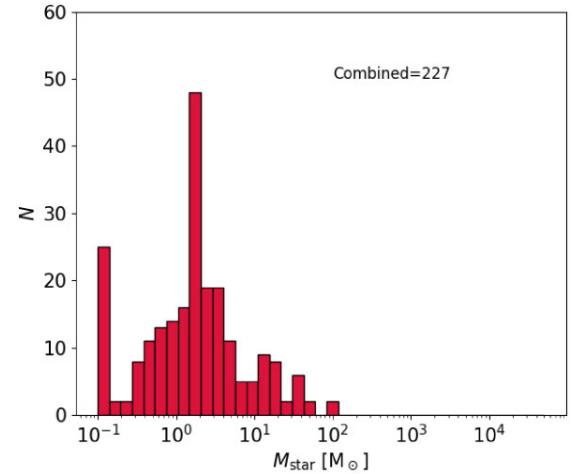
Figure 15. Combined mass distribution for stars ejected from the cluster at the end of simulations M3_t100_1–6.

3.2.3 Final cluster properties

At the end of our simulations, the remaining stellar systems consist of, on average, only 14 ± 10 particles with an average of 38 ± 12 ejected ones. Little to no gas is left, and the final cluster is essentially comprised of an MMO with $\sim 2 \times 10^4 \, \mathrm{M}_\odot$ that is orbited by a few other stars, most of them with masses in the range 1–10 $\mathrm{M}_\odot$. In three simulations, the second most massive object reaches more than $1000 \, \mathrm{M}_\odot$ and is orbiting the MMO in a close Keplerian orbit, but since the mass ratio $q = M_1/M_2$ is too high (>20), we do not mark them as binary systems.

We show the combined mass distribution of the particles that remain bound to the MMO for simulations M3_t100_1–6 in Fig. 14. Comparing this mass distribution to the mass distribution of less massive clusters shown in Fig. 7, the immediate difference that we note is that now we do not have a prominent peak. Instead the mass distribution looks flat in the mass range 1–100 $\mathrm{M}_\odot$.

We also show the combined mass distribution of ejected particles for these simulations in Fig. 15. This looks more similar to the one for less massive clusters, but with an additional peak at $\sim 0.1 \, \mathrm{M}_\odot$. While the shape of the mass function is maintained, it now peaks

in between 1–$2\,\mathrm{M}_\odot$ instead of 2–$3\,\mathrm{M}_\odot$ as observed for less massive clusters.

We present the individual mass distribution of bound and ejected particles for each of these simulations in Figs D3 and D4, respectively.

3.3 Impact of a reduced $t_{\mathrm{KH,\,surf}}$

As explained at the end of Section 2.5, the time it takes for an inflated SMS to contract to the main sequence after its accretion rate falls below $\dot{M}_{\mathrm{cirt}}$ (i.e. $t_{\mathrm{KH,\,surf}}$) ranges in between 10–$100\,t_{\mathrm{KH}}$ (Sakurai et al. 2015). So far we have assumed $t_{\mathrm{KH,\,surf}} = 100\,t_{\mathrm{KH}}$, and found that the MMOs in our simulations reach an average mass of $3729\,\mathrm{M}_\odot$ for clusters with $M_{\mathrm{gas}} = 10^4$ and $23\,873\,\mathrm{M}_\odot$ for clusters with $M_{\mathrm{gas}} = 3 \times 10^4\,\mathrm{M}_\odot$.

In principle, a shorter $t_{\mathrm{KH,\,surf}}$ would cause an earlier contraction to the main sequence and this could impact the formation of an MMO via two effects. The first one is related to the growth via stellar collisions. An earlier contraction to the main sequence implies that the protostars that evolve as SMSs will not maintain a high cross-section for long enough times compared to simulations with $t_{\mathrm{KH,\,surf}} = 100\,t_{\mathrm{KH}}$. The second effect is a reduction of the mass of the stars that evolve as SMSs, given that gas accretion should terminate once the star contracts to the main sequence. Because of this, the simulations with $t_{\mathrm{KH,\,surf}} = 10\,t_{\mathrm{KH}}$ would have the highest impact on the final mass of the MMO.

In order to explore the effects of a reduced $t_{\mathrm{KH,\,surf}}$ on the final masses of the MMOs, we ran simulations with $t_{\mathrm{KH,\,surf}} = 10\,t_{\mathrm{KH}}$ for our two different cluster models (see Table 1), and compare the results to the ones from our simulations with $t_{\mathrm{KH,\,surf}} = 100\,t_{\mathrm{KH}}$. This gives us an idea of how much a reduced $t_{\mathrm{KH,\,surf}}$ would impact the formation of an MMO through stellar collisions. Then in order to get an idea of how our results would change when including radiation feedback, we post process the snapshots of our simulations with $t_{\mathrm{KH,\,surf}} = 10\,t_{\mathrm{KH}}$. For this, we stop the mass growth of all particles once they contract to the main sequence and use the existing merger history, but now with the modified masses to obtain a new estimate for the final mass of the MMO.

3.3.1 Clusters with $\mathrm{M}_{gas} = 10^4\,\mathrm{M}_\odot$

For the set of simulations with $M_{\mathrm{gas}} = 10^4\,\mathrm{M}_\odot$ (M1_t100_1–6 and M1_t10_1–6), by comparing the final masses of the MMOs (column 7), we find that the average values are consistent within one sigma errors. In fact, for simulations with $t_{\mathrm{KH,\,surf}} = 100\,t_{\mathrm{KH}}$, the average mass of the MMO is $\sim 3700 \pm 800$, whereas for simulations with $t_{\mathrm{KH,\,surf}} = 10\,t_{\mathrm{KH}}$, the average mass of the MMO is $\sim 4000 \pm 600$. Therefore, we find that an earlier contraction to the main sequence has no impact on the growth of the MMO via stellar collisions and that the different values that we find here are the result of the intrinsic variability among different simulations.

The MMO does not contract to the main sequence but this is not due to very frequent stellar collisions, the mean time between collisions ($\sim 2700\,\mathrm{yr}$) is actually slightly longer than $10\,t_{\mathrm{KH}}$ ($\sim 1700\,\mathrm{yr}$). We attribute this behaviour to very short accretion bursts that surpass $\dot{M}_{\mathrm{crit}}$ during a brief period of time ($<50\,\mathrm{yr}$) not captured in Fig. 3, since the cadence for data output is $50\,\mathrm{yr}$.

Subsequently, after including an approximate effect of feedback (i.e. stopping the mass growth of a star once it enters the main sequence), we find very little reduction of the stellar masses. For simulations with $t_{\mathrm{KH,surf}} = 10\,t_{\mathrm{KH}}$, the average final mass of the
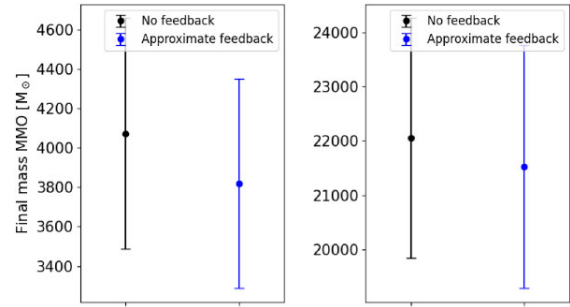

Figure 16. Estimate for the approximate effects of radiation feedback on the final mass of the MMO obtained from post-processing of our simulations. *Left-hand panel:* Average final mass of the MMO with one sigma errorbars for simulations with $M_{\mathrm{gas}} = 10^4\,\mathrm{M}_\odot$ and $t_{\mathrm{KH,\,surf}} = 10\,t_{\mathrm{KH}}$. *Right-hand panel:* Same as left-hand panel but for simulations with $M_{\mathrm{gas}} = 3 \times 10^4\,\mathrm{M}_\odot$ and $t_{\mathrm{KH,\,surf}} = 10\,t_{\mathrm{KH}}$.

MMO goes down to $\sim 3800 \pm 500\,\mathrm{M}_\odot$ after post-processing. This is still within the one sigma error of the value obtained without any type of feedback. We show the comparison of the final masses of the MMOs in the case without feedback, and in the case with approximate feedback in the left-hand panel of Fig. 16.

Finally, we also note that the same holds true for the binary systems formed in these simulations. We find a reduction of only 10 per cent for the masses of the primary and secondary stars, and the mass ratios remain the same.

3.3.2 Clusters with $\mathrm{M}_{gas} = 3 \times 10^4\,\mathrm{M}_\odot$

We first compare the final mass of the MMO for simulations with $t_{\mathrm{KH,\,surf}} = 100\,t_{\mathrm{KH}}$ and $t_{\mathrm{KH,\,surf}} = 10\,t_{\mathrm{KH}}$. For the first case, the average mass of the MMO is $\sim 23\,800 \pm 2000\,\mathrm{M}_\odot$, and for the second case, the average mass of the MMO is $\sim 22\,000 \pm 2200\,\mathrm{M}_\odot$. Thus, we find again that an earlier contraction to the main sequence will not reduce the final mass of the MMO due to collisions appreciably. The MMO still remains inflated due to frequent mergers, and this is the main driver of stellar collisions. The different values that we find here are a result of the intrinsic simulation to simulation variation.

When we post-process our simulations to account for the approximate effect of radiation feedback, we find that the average mass of the MMO is reduced to $\sim 21\,500 \pm 2200\,\mathrm{M}_\odot$, which again is within the one sigma error of the average mass of the MMO when no feedback is considered. We thus conclude that radiation feedback would not appreciably reduce the mass of the MMO. We show the final average masses of the MMOs when no feedback is included and with approximate feedback in the right-hand panel of Fig. 16.

We find, however, that the mass of the second most massive object is severely affected. On average, the post-processing reduces the mass of the second MMO by a factor of four, and in one case even a factor of six. This occurs because in the simulations, where a higher density is reached in the cloud centre, many protostars initially evolve as SMSs as they surpass the critical accretion rate. They however cannot maintain the high accretion rates for long times and eventually contract to the main sequence. In the simulations with high $t_{\mathrm{KH,\,surf}}$, this time span of lower accretion rates is not long enough for the stars to contract to the main sequence, but in post-processing when $t_{\mathrm{KH,surf}}$ is lower they contract and their masses are fixed at that point.

3.3.3 Possible impact of feedback from surrounding stars

Regarding the formation and growth of the MMO, we try to understand if once another protostar close to the MMO contracts to the main sequence, it would appreciably impact the final mass of the MMO. For this purpose, we calculate the Strömgren radius of the first star that enters the main sequence in our simulations, and that is close enough to influence the growth of the MMO. We find that the first star enters the main sequence once the MMO has already gathered more than 80 per cent of its final mass, and the typical separation between these objects is around 500 au, but the Strömgren radius for the main sequence star (as calculated in Appendix C) is usually around 6 au. Therefore, we conclude that the surrounding stars that enter the main sequence will not appreciably impact the final mass of the MMO, which can also still grow through stellar mergers.

4 DISCUSSION AND CONCLUSIONS

In this work, we address the problem of massive object formation, considering the evolution of a protostellar cluster embedded in a massive gas cloud at very low metallicity following fragmentation at subparsec scales, during the collapse of an atomic-cooling halo. We perform a suite of hydrodynamical plus *N*-body simulations including sink particle creation, gas accretion, pseudo (proto-)stellar evolution, and stellar collisions. Our calculations start from a Plummer distribution of protostars embedded in a gas cloud that follows a Plummer density profile as well, and to which we impose a turbulent velocity field with Mach number equal to one, resembling the centre of a spherically collapsing atomic-cooling halo as found in cosmological hydrodynamical simulations (Chon et al. 2018). We note that spherical collapse is not always the case, and elongated clouds are also found in these simulations, so it will be desirable to begin with initial conditions taken directly from cosmological simulations in the future. Despite this, no fragmentation at parsec-scales is seen during these simulations, and we expect that fragmentation at smaller scales, as studied here, will not impede the formation of a supermassive star with $10^4 \, \mathrm{M_\odot}$.

Our simulations include (proto)-stellar evolution in the sense that the stellar radius and luminosity change with the mass and accretion rate of the protostar. Therefore, the protostars are allowed to contract to the main sequence, and thus reduce the cross-section for collisions. This is essential because survival, ejection, and merger rates depend sensitively on the object size. One caveat in our simulations comes from the fact that we do not include stellar feedback. We estimate the possible impact of radiation feedback on the final mass of the MMO in Section 3.3. For this purpose, we post-processed our simulations and stop mass accretion once the object enters the main sequence, at which point we assume that strong UV radiation may remove gas from the surrounding. In this extreme model, further mass growth is only possible via collisions. We find that this modification has negligible impact on the final masses of the MMO, and similar holds for the binary systems when present. We also calculate the Strömgren radius of surrounding stars that enter the main sequence but find that they do so once the MMO has already gathered more than 80 per cent of its final mass and these stars are not close enough to affect the growth of the MMO. We find, however, that the masses of the second most massive object could be affected in simulations with $M_{\mathrm{gas}} = 3 \times 10^4 \, \mathrm{M_\odot}$. This indicates that in order to fully characterize the final stellar masses in such systems, simulations that include radiation feedback are required.

The simulation results presented here agree with the study by Chon & Omukai (2020), where they find what they termed a 'super-

competitive accretion', in which a single massive object dominates the growth by gas accretion. The conditions under which this scenario emerges were recently studied by means of analytical arguments by Schleicher, Reinoso & Klessen (2023). They demonstrate that self-gravity induced accretion will initially dominate the mass growth of an object that will become the most massive object in the cluster, and this does not depend on the number of protostars present. Only after the gas accretion mode shifts from self-gravity to Bondi–Hoyle, due to lower gas densities, could the fragments around the MMO interfere with gas accretion onto it, however, the moment at which this occurs depends only on the square root of the number of protostars. We conclude that in the context of atomic cooling haloes as studied here, in an initially Jeans-unstable cloud, varying the initial number of protostars will have little to no impact on the mass growth through accretion.

We note that we model systems with a high initial number density of protostars (see Section 2.1). We tried to estimate the effect that a lower initial number density of protostars would have on the final mass of the MMOs. For this purpose, we consider the extreme scenario, in which no initial protostars are present and post-process the collision histories to remove all the mass contributed by these protostars to the MMO. In this extreme scenario, in which that mass would be lost from the system we find that for our simulations with $10^4 \, \mathrm{M_\odot}$ in gas, the mass of the MMO decreases by 36 per cent; and in our simulations with $3 \times 10^4 \, \mathrm{M_\odot}$ in gas, the mass is reduced by 11 per cent. This reduction in mass would still leave MMOs that can collapse to produce massive black holes seeds.

Since we consider protostars forming in a pristine gas cloud, the stars that are formed in our simulations resemble primordial stars, in particular the so-called Population III stars. These stars, once on the main sequence do not lose significant mass due to stellar winds because of their low metallicity (Krtička & Kubát 2006), therefore including mass loss due to stellar winds will not change our results.

Moreover, the MMOs formed in our simulations evolve as supermassive stars because of the high accretion rate they reach (Hosokawa et al. 2013; Schleicher et al. 2013; Haemmerlé et al. 2018; Haemmerlé 2021). Again, due to their low metallicity, no mass loss is expected from stellar winds. Furthermore, Hosokawa et al. (2013) demonstrated that mass loss due to the pulsational instability reaches a maximum of $\sim 5 \times 10^{-3} \, \mathrm{M_\odot \, yr^{-1}}$, much lower than the accretion rates that these objects experience. It is thus safe also to ignore mass loss for our MMOs. Note that mass loss due to stellar winds is relevant for higher metallicity stars when considering the formation of massive objects due to stellar collisions as explored in the context of nuclear star clusters by Das et al. (2021).

Finally, we note that the sink particles we consider resemble protostars but eventually some of them reach the zero-age main sequence (ZAMS) and turn into stars. The point at which this typically occurs is around 30 kyr when protostars accreting at high rates reach the Kelvin–Helmholtz contraction phase (Hosokawa & Omukai 2009). At this moment, the MMO has gathered more than 80 per cent of its final mass. The typical mass for stars that reach the ZAMS is around $20 \, \mathrm{M_\odot}$. Stellar evolution models for these type of stars show main sequence lifetimes in the order of Myr even for very massive stars (Tanikawa et al. 2020; Murphy et al. 2021) therefore no supernova explosion can occur during the time-span of our simulations.

We have not considered mass loss during stellar collisions. This effect has been studied in the context of blue straggler formation (Sills & Bailyn 1999; Sills et al. 2000), and in the context of local star clusters. For this purpose, fitting functions depending on the mass ratio of the collision (Lombardi James C. et al. 2002) and the stellar structure (Glebbeek & Pols 2008; Glebbeek, Pols & Hurley 2008)

have been obtained for stars colliding at different stages during their evolution (Glebbeek et al. 2013). Armed with these functions, Alister Seguel et al. (2020) found that including mass loss could reduce the mass of the MMO by 20–40 per cent in a similar environment to the one studied here. Applied to our simulations, we conclude that the run-away formation of the MMO cannot be prevented. However, we note that it is not clear how well these analytical estimates can be applied to the collision between an SMS and its surrounding stars. More work is required to reduce the uncertainty in these estimates.

The formation of very massive objects that can collapse to produce massive black hole seeds has also been investigated in the context of star cluster formation in non-primordial clouds (Sakurai et al. 2017; Sakurai et al. 2019; Das et al. 2021). In these models different mass-radius relations are used as the accretion rates experienced in these environments are much lower. In particular in these studies, the stars never evolve as the inflated SMSs produced in our simulations. This lead to important differences in the masses of the objects formed and the time-scales involved. Even in presence of a much larger gas reservoir ($10^5\,M_\odot$), the most massive objects reach typical masses of $10^3\,M_\odot$ (Sakurai et al. 2019; Das et al. 2021).

According to previous simulations investigating the formation of SMSs in atomic cooling haloes, mass inflows of $0.5\,M_\odot\,\mathrm{yr}^{-1}$ are reported at scales similar to the ones simulated here (Wise et al. 2019). At this constant rate, the flow can be maintained for about 1 Myr, which is comparable to the lifetime of the most massive stars formed in our simulations. Assuming that a total of $10^6\,M_\odot$ have concentrated in the inner 1 pc of the DM halo, we estimate a binding energy of $\sim 5 \times 10^{52}$ erg. On the other hand, the binding energy of a $150\,M_\odot$ Population III star (a typical massive star formed in our simulations) is around 1.7×10^{52} erg. These estimates yield similar quantities therefore it is very uncertain to say that a supernova explosion will or not be able to eject the remaining gas, it is important to know how much mass is concentrated inside which volume and the final masses of the stars. If the gas is not ejected after the supernova explosion, another episode of star formation could occur in the halo but this time producing second generation stars due to the metal enrichment of the ejecta.

In our simulations, we find that a massive central object is always formed and experiences run-away growth via collisions with other protostars in the cluster. The mass growth is typically dominated by one single object, as found in previous studies (Latif et al. 2013; Inayoshi & Haiman 2014; Sakurai et al. 2016; Matsukoba et al. 2019; Chon & Omukai 2020) and explained by analytical arguments by Schleicher et al. (2023). Additionally, the fragmentation process does not fully suppress the high-mass flow towards the centre and so the MMO continues to grow via gas accretion as well. The MMO begins to grow once the cloud collapses on a free-fall time-scale (around 3000 yr), and by 10 000 yr it already contains 37 per cent of the initial gas mass for clusters with $M_{\mathrm{gas}} = 10^4\,M_\odot$, and 80 per cent of the initial gas mass for clusters with $M_{\mathrm{gas}} = 3 \times 10^4\,M_\odot$. 50 to 60 per cent of the mass of the MMO is gained through collisions. In a third of the simulations with $M_{\mathrm{gas}} = 10^4\,M_\odot$, we find that the MMO is in a binary system with another massive object with mass ratios in between 1:2 and 1:7. Radiation feedback is unable to reduce the mass of the MMO significantly. The final outcome is therefore a small group of tens of stars with typical masses in the range 1–$100\,M_\odot$ orbiting a single object with 10^3 or $10^4\,M_\odot$. In one third of the cases, the group of stars orbits a pair of massive objects ($\sim 10^3\,M_\odot$) in a binary configuration.

DATA AVAILABILITY

The data underlying this article will be shared on reasonable request to the corresponding author.

REFERENCES

Abel T., Bryan G. L., Norman M. L., 2002, Science, 295, 93
Alister Seguel P. J., Schleicher D. R. G., Boekholt T. C. N., Fellhauer M., Klessen R. S., 2020, MNRAS, 493, 2352
Bañados E. et al., 2018, Nature, 553, 473
Bañados E. et al., 2021, ApJ, 909, 80
Bate M. R., Burkert A., 1997, MNRAS, 288, 1060
Becerra F., Greif T. H., Springel V., Hernquist L. E., 2015, MNRAS, 446, 2380
Becerra F., Marinacci F., Bromm V., Hernquist L. E., 2018, MNRAS, 480, 5029
Benz W., 1990, in Buchler J. R.ed., Proc. NATO Advanced Research Workshop, Numerical Modelling of Nonlinear Stellar Pulsations Problems and Prospects. Kluwer Academic Publishers, Dordrecht, p. 269
Boekholt T. C. N., Schleicher D. R. G., Fellhauer M., Klessen R. S., Reinoso B., Stutz A. M., Haemmerlé L., 2018, MNRAS, 476, 366
Chandrasekhar S., 1964, ApJ, 140, 417
Chon S., Hirano S., Hosokawa T., Yoshida N., 2016, ApJ, 832, 134
Chon S., Hosokawa T., Yoshida N., 2018, MNRAS, 475, 4104
Chon S., Omukai K., 2020, MNRAS, 494, 2851
Clark P. C., Glover S. C. O., Smith R. J., Greif T. H., Klessen R. S., Bromm V., 2011, Science, 331, 1040
Das A., Schleicher D. R. G., Leigh N. W. C., Boekholt T. C. N., 2021, MNRAS, 503, 1051
Davies M. B., Miller M. C., Bellovary J. M., 2011, ApJ, 740, L42
Dijkstra M., Ferrara A., Mesinger A., 2014, MNRAS, 442, 2036
Dijkstra M., Haiman Z., Mesinger A., Wyithe J. S. B., 2008, MNRAS, 391, 1961
Escala A., 2021, ApJ, 908, 57

Fan X. et al., 2006, AJ, 131, 1203

Fraser M., Casey A. R., Gilmore G., Heger A., Chan C., 2017, MNRAS, 468, 418

Fujii M., Iwasawa M., Funato Y., Makino J., 2007, PASJ, 59, 1095

Gerritsen J. P. E., Icke V., 1997, A&A, 325, 972

Glebbeek E., Gaburov E., Portegies Zwart S., Pols O. R., 2013, MNRAS, 434, 3497

Glebbeek E., Pols O. R., 2008, A&A, 488, 1017

Glebbeek E., Pols O. R., Hurley J. R., 2008, A&A, 488, 1007

Glover S. C. O., 2016, preprint (arXiv:1610.05679)

Greif T. H., Bromm V., Clark P. C., Glover S. C. O., Smith R. J., Klessen R. S., Yoshida N., Springel V., 2012, MNRAS, 424, 399

Haemmerlé L., 2021, A&A, 647, A83

Haemmerlé L., Woods T. E., Klessen R. S., Heger A., Whalen D. J., 2018, MNRAS, 474, 2757

Heger A., Fryer C. L., Woosley S. E., Langer N., Hartmann D. H., 2003, ApJ, 591, 288

Heger A., Woosley S. E., 2002, ApJ, 567, 532

Hernquist L., Katz N., 1989, ApJS, 70, 419

Hosokawa T., Omukai K., 2009, ApJ, 703, 1810

Hosokawa T., Omukai K., Yorke H. W., 2012, ApJ, 756, 93

Hosokawa T., Yorke H. W., Inayoshi K., Omukai K., Yoshida N., 2013, ApJ, 778, 178

Hubber D. A., Walch S., Whitworth A. P., 2013, MNRAS, 430, 3261

Inayoshi K., Haiman Z., 2014, MNRAS, 445, 1549

Inayoshi K., Tanaka T. L., 2015, MNRAS, 450, 4350

Jaura O., Glover S. C. O., Wollenberg K. M. J., Klessen R. S., Geen S., Haemmerlé L., 2022, MNRAS, 512, 116

Johnson J. L., Bromm V., 2007, MNRAS, 374, 1557

Katz H., Sijacki D., Haehnelt M. G., 2015, MNRAS, 451, 2352

Klessen R., 2019, in Latif M., Schleicher D., Formation of the first stars. World Scientific Publishing Co., Singapore

KohriK.,Sekiguchi T.,Wang S.,2022, Physical Review D , 106

Krtička J., Kubát J., 2006, A&A, 446, 1039

Latif M. A., Bovino S., Grassi T., Schleicher D. R. G., Spaans M., 2015, MNRAS, 446, 3163

Latif M. A., Khochfar S., Schleicher D., Whalen D. J., 2021, MNRAS, 508, 1756

Latif M. A., Schleicher D. R. G., Hartwig T., 2016, MNRAS, 458, 233

Latif M. A., Schleicher D. R. G., Schmidt W., Niemeyer J., 2013, MNRAS, 433, 1607

Lombardi James C.J., Warren J. S., Rasio F. A., Sills A., Warren A. R., 2002, ApJ, 568, 939

Lupi A., Colpi M., Devecchi B., Galanti G., Volonteri M., 2014, MNRAS, 442, 3616

Lupi A., Haiman Z., Volonteri M., 2021, MNRAS, 503, 5046

Matsukoba R., Takahashi S. Z., Sugimura K., Omukai K., 2019, MNRAS, 484, 2605

McMillan S. L. W., Hut P., 1996, ApJ, 467, 348

Mortlock D. J. et al., 2011, Nature, 474, 616

Murphy L. J. et al., 2021, MNRAS, 501, 2745

Omukai K., 2001, ApJ, 546, 635

Omukai K., Schneider R., Haiman Z., 2008, ApJ, 686, 801

Onoue M. et al., 2019, ApJ, 880, 77

Patrick S. J., Whalen D. J., Elford J. S., Latif M. A., 2020, preprint (arXiv:2012.11612)

Pelupessy F. I., van der Werf P. P., Icke V., 2004, A&A, 422, 55

Pelupessy F. I., van Elteren A., de Vries N., McMillan S. L. W., Drost N., Portegies Zwart S. F., 2013, A&A, 557, A84

Plummer H. C., 1911, MNRAS, 71, 460

Portegies Zwart S. et al., 2009, New A, 14, 369

Portegies Zwart S., McMillan S. L. W., van Elteren E., Pelupessy I., de Vries N., 2013, Comput. Phys. Commun., 184, 456

Portegies Zwart S., McMillan S., 2018, Astrophysical Recipes: The art of AMUSE, IOP Publishing, Bristol

Prole L. R., Clark P. C., Klessen R. S., Glover S. C. O., 2022a, MNRAS, 510, 4019

Prole L. R., Clark P. C., Klessen R. S., Glover S. C. O., Pakmor R., 2022b, MNRAS, 516, 2223

Reed S. L. et al., 2019, MNRAS, 487, 1874

Rees M. J., 1984, ARA&A, 22, 471

Regan J. A., Johansson P. H., Wise J. H., 2014, ApJ, 795, 137

Regan J. A. et al. 2020, The Open Journal of Astrophysics, 3, 15

Reinoso B., Schleicher D. R. G., Fellhauer M., Klessen R. S., Boekholt T. C. N., 2018, A&A, 614, A14

Reinoso B., Schleicher D. R. G., Fellhauer M., Leigh N. W. C., Klessen R. S., 2020, A&A, 639, A92

Riaz R., Bovino S., Vanaverbeke S., Schleicher D. R. G., 2018, MNRAS, 479, 667

Sakurai Y., Hosokawa T., Yoshida N., Yorke H. W., 2015, MNRAS, 452, 755

Sakurai Y., Vorobyov E. I., Hosokawa T., Yoshida N., Omukai K., Yorke H. W., 2016, MNRAS, 459, 1137

Sakurai Y., Yoshida N., Fujii M. S., 2019, MNRAS, 484, 4665

Sakurai Y., Yoshida N., Fujii M. S., Hirano S., 2017, MNRAS, 472, 1677

Sassano F., Schneider R., Valiante R., Inayoshi K., Chon S., Omukai K., Mayer L., Capelo P. R., 2021, MNRAS, 506, 613

Schleicher D. R. G. et al., 2022, MNRAS, 512, 6192

Schleicher D. R. G., Palla F., Ferrara A., Galli D., Latif M., 2013, A&A, 558, A59

Schleicher D. R. G., Reinoso B., Klessen R. S., 2023, MNRAS, submitted

Sharda P., Federrath C., Krumholz M. R., 2020, MNRAS, 497, 336

Sills A., Bailyn C. D., 1999, ApJ, 513, 428

Sills A., Bailyn C. D., Edmonds P. D., Gilliland R. L., 2000, ApJ, 535, 298

Smith B. D., Regan J. A., Downes T. P., Norman M. L., O'Shea B. W., Wise J. H., 2018, MNRAS, 480, 3762

Stacy A., Bromm V., Lee A. T., 2016, MNRAS, 462, 1307

Suazo M., Prieto J., Escala A., Schleicher D. R. G., 2019, ApJ, 885, 127

Tagawa H., Haiman Z., Kocsis B., 2020, ApJ, 892, 36

Tanikawa A., Yoshida T., Kinugawa T., Takahashi K., Umeda H., 2020, MNRAS, 495, 4170

Trinca A., Schneider R., Valiante R., Graziani L., Zappacosta L., Shankar F., 2022, MNRAS, 511, 616

Vergara M. Z. C., Schleicher D. R. G., Boekholt T. C. N., Reinoso B., Fellhauer M., Klessen R. S., Leigh N. W. C., 2021, A&A, 649, A160

Visbal E., Haiman Z., Bryan G. L., 2014, MNRAS, 445, 1056

Volonteri M., 2010, A&A Rev., 18, 279

Wang F. et al., 2021, ApJ, 907, L1

Wise J. H., Regan J. A., O'Shea B. W., Norman M. L., Downes T. P., Xu H., 2019, Nature, 566, 85

Wollenberg K. M. J., Glover S. C. O., Clark P. C., Klessen R. S., 2020, MNRAS, 494, 1871

Woods T. E. et al., 2019, Publ. Astron. Soc. Aust., 36, e027

Woods T. E., Heger A., Whalen D. J., Haemmerlé L., Klessen R. S., 2017, ApJ, 842, L6

Wu X.-B. et al., 2015, Nature, 518, 512

APPENDIX A: MASS RADIUS PARAMETRIZATION

We use different mass-radius (M–R) relations depending on the accretion rate of the protostar and on its evolutionary stage. We also calculate associated quantities such as the luminosity and the Kelvin Helmholtz (KH) time-scale. All these properties are calculated after every accretion step. We define three evolutionary stages, namely *protostar*, *star*, and *supermassive star*. The M–R relations for each stage are described below.

A1 *Protostar*

Every particle in our simulations begins in the *protostar* stage. The M–R parametrizations that we use for them are based on the works of Hosokawa & Omukai (2009), Hosokawa et al. (2012), and Hosokawa et al. (2013). We calculate the properties of each *protostar*

by classifying them into three different tracks. The classification depends on the accretion rate $\dot{M}$. We therefore have the 'SMS' track, 'VMS' track, and 'NORMAL' track. Each track is described in the next subsections.

A1.1 'SMS' track

There is a critical accretion rate above which the accreting protostars remain inflated, and their radii always increase with the mass. A *protostar* whose accretion rate is higher than this critical accretion rate is in the 'SMS' track. The critical accretion rate in our simulations is set to $\dot{M}_{\mathrm{crit}} = 0.04\,\mathrm{M}_\odot\,\mathrm{yr}^{-1}$ taken from Hosokawa et al. (2013). For every *protostar* in the 'SMS' track, the radius is computed as:

$$R_* = 2600 \left(\frac{M_*}{100\,\mathrm{M}_\odot} \right)^{1/2} R_\odot. \tag{A1}$$

The *protostar* will follow this relation unless the accretion rate $\dot{M}$ remains below $\dot{M}_{\mathrm{crit}}$ for more than 10–$100\,t_{\mathrm{KH}}$ (Schleicher et al. 2013; Sakurai et al. 2015), where the KH time-scale t_{KH} is calculated as:

$$t_{\mathrm{KH}} = \frac{GM^2}{RL}, \tag{A2}$$

with M, R, and L, being the mass, radius, and luminosity of the protostar. For the calculation of the KH time-scale, we need the luminosity of the *protostar*. As long as the mass is $\leq 10\,\mathrm{M}_\odot$, the luminosity is calculated as (Hosokawa & Omukai 2009):

$$L_* = 0.6 \left(\frac{M_*}{\mathrm{M}_\odot} \right)^{11/2} \left(\frac{R_*}{R_\odot} \right)^{-1/2} L_\odot, \tag{A3}$$

whereas for $M_* > 10\,\mathrm{M}_\odot$, the luminosity is given by:

$$L_* = 10 \left(\frac{M_*}{\mathrm{M}_\odot} \right)^3 L_\odot, \tag{A4}$$

and for $M_* > 70\,\mathrm{M}_\odot$, the luminosity approaches the Eddington limit and is calculated as:

$$L_* = 3.8 \times 10^6 \left(\frac{M_*}{100\,\mathrm{M}_\odot} \right) L_\odot. \tag{A5}$$

Finally, once the *protostar* reaches a mass of $600\,\mathrm{M}_\odot$, it enters the *supermassive star* stage. In case the accretion rate $\dot{M}$ of a *protostar* in the 'SMS' track remains below $\dot{M}_{\mathrm{crit}}$ for more than a 10–$100\,\mathrm{KH}$ time-scales, the *protostar* will enter a new evolutionary track according to its last value for $\dot{M}$. We note that the time during which a protostar in the 'SMS' track remains inflated after its accretion rate falls below $\dot{M}_{\mathrm{crit}}$ can vary between 10–$100\,\mathrm{KH}$ time-scales (Sakurai et al. 2015). We consider both extreme values for the KH time-scales in this work.

A1.2 'VMS' track

Every *protostar* whose accretion rate is in the range $[10^{-6}, 0.04]\,\mathrm{M}_\odot\,\mathrm{yr}^{-1}$ is in the 'VMS' track. In this track, we distinguish three phases, the *adiabatic accretion phase*, the *swelling*, and the *Kelvin Helmholtz contraction* as described in Hosokawa & Omukai (2009). The *adiabatic accretion phase* holds as long as the mass of the *protostar* is $\leq M_{\mathrm{ad}}$, which is given by:

$$M_{\mathrm{ad}} = 0.9 \left[\left(\frac{\dot{M}}{4.2 \times 10^{-8}\,\mathrm{M}_\odot\,\mathrm{yr}^{-1}} \right) \left(\frac{\dot{M}}{10^{-3}\,\mathrm{M}_\odot\,\mathrm{yr}^{-1}} \right)^{(-0.41/2)} \right]^{(2/9.27)} \mathrm{M}_\odot. \tag{A6}$$

In this phase, the luminosity is calculated from equation (A3) and the radius as:

$$R_* = 26 \left(\frac{M_*}{\mathrm{M}_\odot} \right)^{0.27} \left(\frac{\dot{M}}{10^{-3}\,\mathrm{M}_\odot\,\mathrm{yr}^{-1}} \right)^{0.41} R_\odot. \tag{A7}$$

Now, it is useful to define two parameters α and β:

$$\alpha = 26 \left(\frac{M_{\mathrm{ad}}}{\mathrm{M}_\odot} \right)^{-4.73} \left(\frac{\dot{M}}{10^{-3}\,\mathrm{M}_\odot\,\mathrm{yr}^{-1}} \right)^{0.41}, \tag{A8}$$

$$\beta = \alpha \left(1.2 \frac{M_{\mathrm{ad}}}{\mathrm{M}_\odot} \right)^{7.5}. \tag{A9}$$

The *swelling* phase holds for *protostars* whose mass is in the range $[M_{\mathrm{ad}}, 1.2M_{\mathrm{ad}}]$. In this phase, the luminosity is given by equation (A3), and the radius as:

$$R_* = \alpha \left(\frac{M_*}{\mathrm{M}_\odot} \right)^5 R_\odot. \tag{A10}$$

The *Kelvin Helmholtz contraction* phase holds for *protostars* whose mass is in the range $[1.2M_{\mathrm{ad}}, M_{\mathrm{ms}}]$, with M_{ms} given by:

$$M_{\mathrm{ms}} = \left(\frac{\beta}{0.97} \right)^{1/3.07}. \tag{A11}$$

The luminosity in this phase is given by equation (A4) and the radius by:

$$R_* = \beta \left(\frac{M_*}{\mathrm{M}_\odot} \right)^{-2.5} R_\odot. \tag{A12}$$

If the mass of a *protostar* in the 'VMS' track is larger than M_{ms}, it enters the *star* stage, i.e. it contracts to the main sequence. In case the accretion rate $\dot{M}$ of a *protostar* in the 'VMS' track remains below $10^{-6}\,\mathrm{M}_\odot\,\mathrm{yr}^{-1}$ for more than a KH time-scale, the *protostar* will enter the 'NORMAL' track.

A1.3 'NORMAL' track

The *protostars* whose accretion rate is $\dot{M} < 10^{-6}\,\mathrm{M}_\odot\,\mathrm{yr}^{-1}$ are in the 'NORMAL' evolutionary track. As long as their mass is $<0.8\,\mathrm{M}_\odot$, the luminosity is given by equation (A3), and their radius is given by:

$$R_* = 0.86 \left(\frac{M_*}{\mathrm{M}_\odot} \right)^{0.27} R_\odot. \tag{A13}$$

If the mass is $\geq 0.8\,\mathrm{M}_\odot$, the *protostar* enters the *star* stage.

As long as a particle is in the *protostar* stage, it can move between the three tracks described above. There is a hierarchy for the tracks, with the 'SMS' track having the highest hierarchy, and the 'NORMAL' track having the lowest hierarchy. A *protostar* can move to a track with higher hierarchy if the accretion rate $\dot{M}$ is high enough, but it will only move to a lower hierarchy track if the accretion rate $\dot{M}$ remains lower than the critical accretion rate for the current track during a time longer than a KH time-scale.

A2 Star

When a particle is in the *star* stage, the radius and luminosity are those for a star in the main sequence. Therefore, the luminosity is given by equation (A5) and the radius is calculated as:

$$R_* = 0.97 \left(\frac{M_*}{\mathrm{M}_\odot} \right)^{0.57} R_\odot. \tag{A14}$$

Table B1. Determination of the evolutionary stage for a merger product.

progenitor's stage	*protostar*	*star*	*supermassive star*
protostar	*protostar*	*protostar*	*supermassive star*
star	–	*star*	*supermassive star*
supermassive star	–	–	*supermassive star*

We assume that a particle in the *star* stage will not inflate in radius even if the accretion rate is $\dot{M} \geq 0.04\,\mathrm{M}_\odot\,\mathrm{yr}^{-1}$, therefore once a star particle has entered the *star* stage, it will always follow the same M–R relation.

A3 *Supermassive star*

When a particle is in the *supermassive star* stage, the luminosity is given by equation (A5) and the radius is given by equation (A1). It is worth noting that even after a star particle has entered the *supermassive star* stage, it can still contract if the accretion rate falls below the critical accretion rate for more than 10–100 KH time-scales. If that occurs, then the star particle will enter the *star* stage, and will follow the mass radius relation given by equation (A14).

APPENDIX B: PROPERTIES OF THE MERGER PRODUCT

In our simulations, the star particles have not only mass and radius, but also an interaction zone radius, angular momentum, an evolutionary stage, and track (see Appendix A). We describe here the method that we follow to determine the new properties for the merger product.

We make the assumption that the mass is conserved and the mass of the merger product is the sum of the masses of the progenitors. We do the same for the angular momentum. For the radius of the interaction zone, we select the largest value among the two progenitors.

B1 Stage

Determining the stage of the merger product is important to decide the new radius. Given that particles can be in three different stages, we have six combinations for the merging particles as presented in Table B1.

B2 Track

When the stage of the merger product is decided to be a *protostar*, there are six possibilities for the *track* in which it can be, as shown in Table B2.

If the merging particles happen to be in the *protostar* and *star* stage, then the track of the merger product is simply the track of the *protostar*.

For deciding the radius of the merger product, we need to determine the accretion rate. We do this by assigning the highest accretion rate among the progenitors to the merger product. Once the stage, the track, and the accretion rate of the merger product have been decided, the radius is calculated as described in Section A, and a new luminosity and KH time-scale are also computed.

Table B2. Determination of the evolution track for a merger product in the *protostar* stage.

progenitor's track	NORMAL	VMS	SMS
NORMAL	NORMAL	VMS	SMS
VMS	–	VMS	SMS
SMS	–	–	SMS

APPENDIX C: STRÖMGREN RADIUS CALCULATION

In order to provide an estimate for the impact of the stars that contract to the main sequence during the cluster evolution, we provide our calculations of the Strömgren radius at the moment when a star

enters the main sequence for the first time in one of our simulations, specifically simulation M1_t100_1.

The Strömgren radius is given by

$$R_{\rm s} = \left(\frac{3}{4\pi} \frac{Q_\star}{n_{\rm H}^2 \beta_2(T)} \right)^{1/3}, \tag{C1}$$

where $Q_\star$ is the number of hydrogen ionizing photons ($h\nu \geq$ 13.6 eV) per unit time, $n_{\rm H}$ is the hydrogen nuclei number density, and $\beta_2(T)$ is the case B volume recombination rate for hydrogen, which is $\sim 2 \times 10^{-13}$ cm^{-3} s^{-1} at 10^4 K. We adopt this value here. The number of ionizing photons can be estimated by using Planck's function as

$$Q_\star = \int_{\nu_1}^\infty \frac{L_\nu}{h\nu}\, {\rm d}\nu = \frac{8\pi^2 R^2}{c^2} \int_{\nu_1}^\infty \frac{\nu^2}{{\rm e}^{\frac{h\nu}{kT}} - 1}, \tag{C2}$$

where $h\nu_1 = 13.6$ eV and R is the radius of the star. Now, in this specific simulation, the masses of the first star that enters the MS is around $7.5\,M_\odot$, this implies a radius of $R \sim 3\,R_\odot$, luminosity of $\sim 285\,363\,L_\odot$, and $T_{\rm eff} \sim 76\,316$ K. With these values, we obtain $\frac{h\nu_1}{kT} \sim 2.1$, so we can approximate the integral in eq.(C2) as

$$\int_{\nu_1}^\infty \frac{\nu^2}{{\rm e}^{\frac{h\nu}{kT}} - 1}\, {\rm d}\nu \sim \int_{\nu_1}^\infty \frac{\nu^2}{{\rm e}^{\frac{h\nu}{kT}}}\, {\rm d}\nu = \left(\frac{kT}{h} \right)^3 \int_{x_1}^\infty \frac{x^2}{{\rm e}^x}\, {\rm d}x, \tag{C3}$$
$$= \left(\frac{kT}{h} \right)^3 (x_1^2 + 2x_1 + 2){\rm e}^{-x},$$

where $x = \frac{h\nu}{kT}$.

By doing so, we obtain

$$Q_\star = \frac{8\pi^2 R^2}{c^2} \left(\frac{kT}{h} \right)^3 \left[\left(\frac{h\nu_1}{kT} \right)^2 + 2\frac{h\nu_1}{kT} + 2 \right] {\rm e}^{-\left(\frac{h\nu_1}{kT} \right)}. \tag{C4}$$

Inserting the numerical values we obtain

$$Q_\star \sim 2 \times 10^{49}\,{\rm s}^{-1}. \tag{C5}$$

For estimating the number density of hydrogen atoms, we take the mean density inside a sphere with radius 200 au, centred on the radiation source, and obtain $n_{\rm H} = 5.6 \times 10^9$ cm^{-3}, so the Strömgren radius is

$$R_s = 6\,{\rm au}. \tag{C6}$$

We note that the separation between this star and the accreting MMO is 734 au at this moment, thus this star would be unable to stop further accretion onto the MMO.

APPENDIX D: MASS DISTRIBUTIONS

In this appendix, we present the mass distribution of bound and ejected stars, at the end of, and for each of our simulations with $t_{\rm KH, surf} = 100 t_{\rm KH}$.

D1 Clusters with $M_{\rm gas} = 10^4\,M_\odot$

D2 Clusters with $M_{\rm gas} = 3 \times 10^4\,M_\odot$

Figure D1. Mass distribution of bound stars at the end of our simulations M1_t100_1–4.

Figure D2. Mass distribution of ejected stars at the end of our simulations M1_t100_1–4.
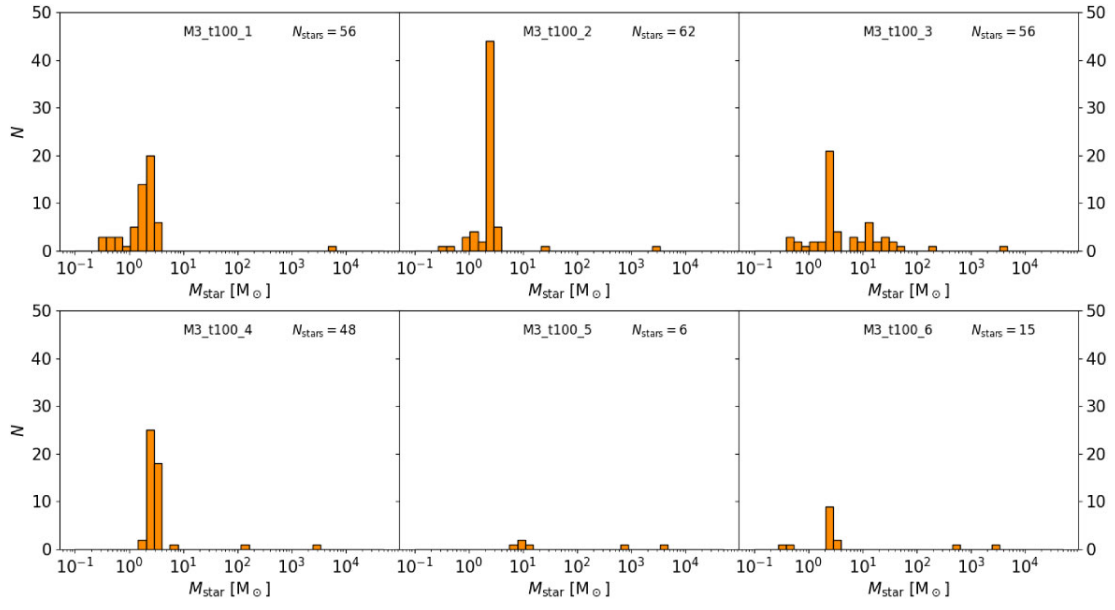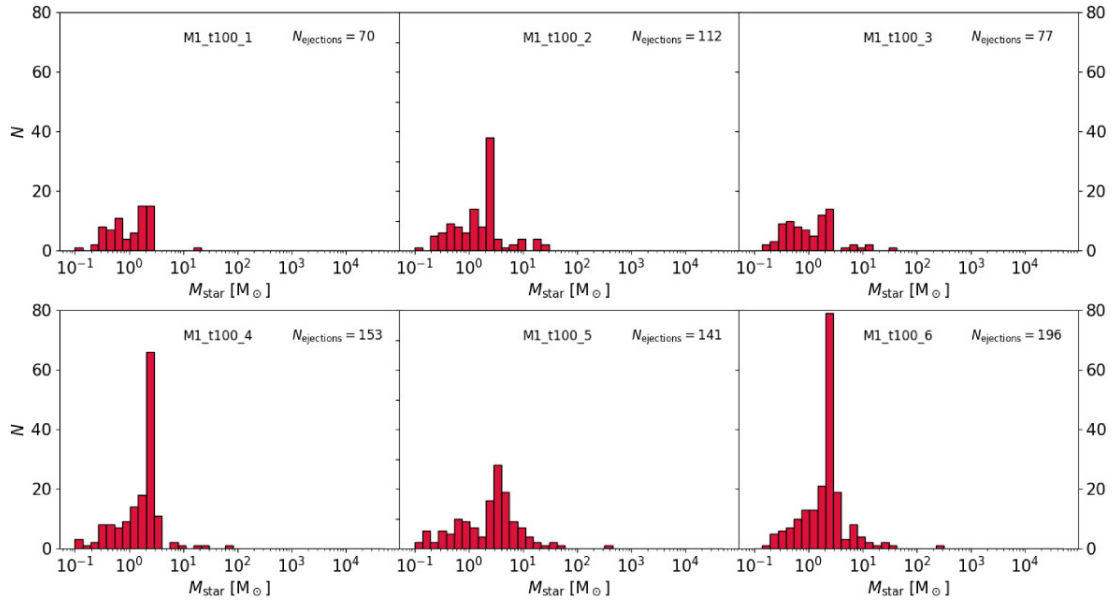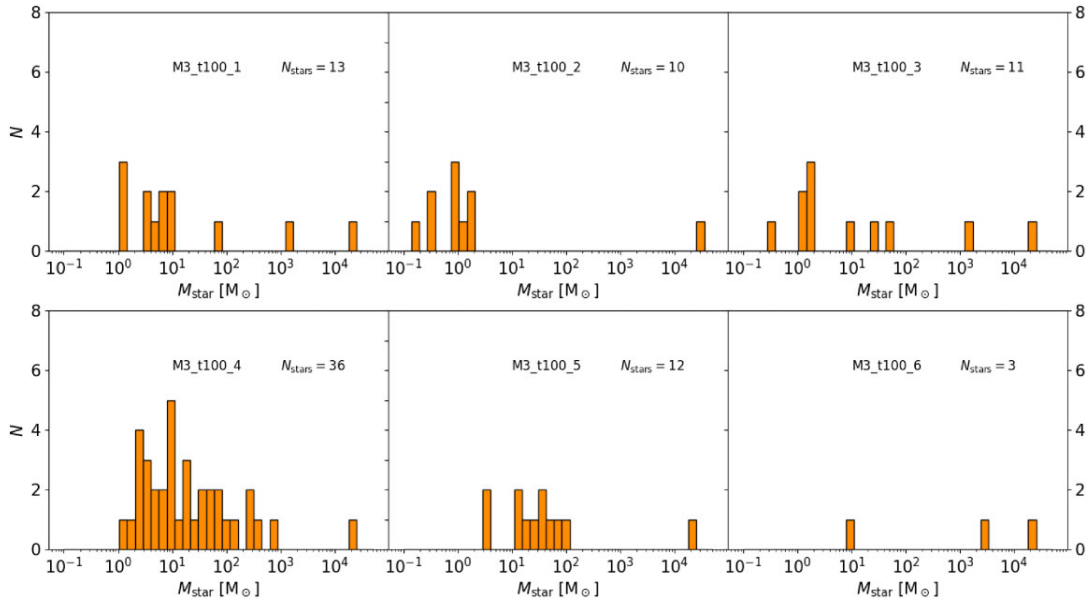
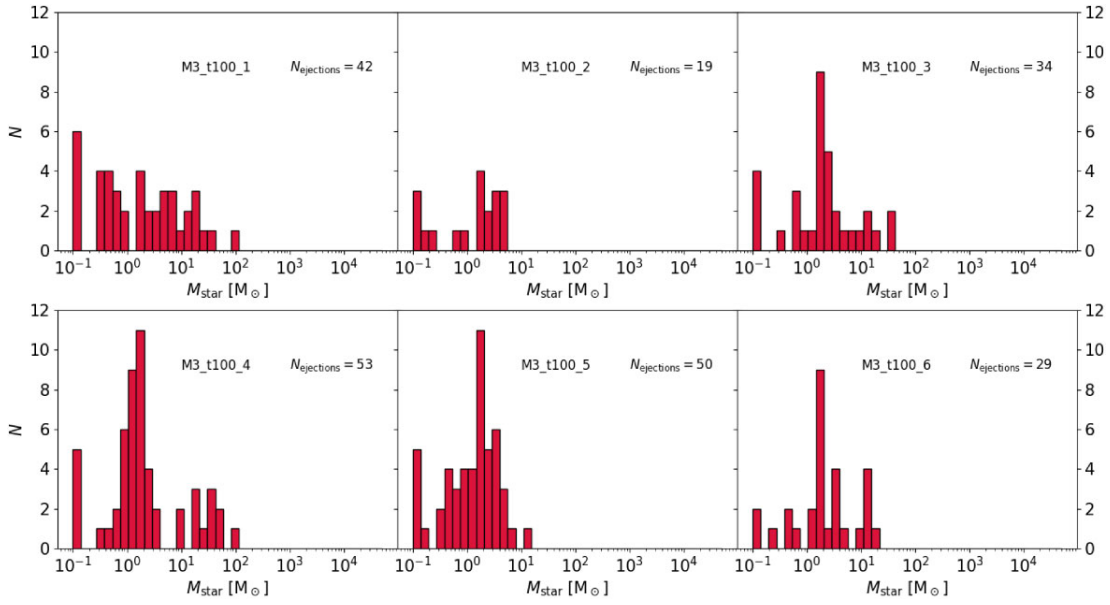**Figure D3.** Mass distribution of bound stars at the end of our simulations M3_t100_1–6.

Figure D4. Mass distribution of ejected stars at the end of our simulations M3_t100_1–6.

This paper has been typeset from a TEX/LATEX file prepared by the author.

Chapter 8

Discussion and conclusions

In this work the origin of the supermassive black holes powering the highest redshift quasars has been explored by means of numerical simulations. The research presented in this thesis focused on two channels for massive black hole seed formation: runaway stellar collisions in dense star clusters, and the interplay of gas accretion and stellar collisions in dense embedded clusters formed in metal free atomic-cooling halos. In the following, a summary is presented for each manuscripts included in this thesis, along with a discussion and comments on the future work needed to improve the models presented.

8.1 Runaway collisions in dense star clusters and formation of massive black hole seeds

The research presented in Chap. 5 revisits the models presented in Reinoso et al. (2018) but including the effects of an external potential to mimic the effects of the gas in embedded Pop. III star clusters. An additional effort is dedicated to understanding how this external potential affects the evolution of the clusters and the runaway collision process. The results of this research demonstrate that in this case the scaling of the velocities that is needed to produce virialized clusters directly impacts the formation of binary systems and the evolution of the cluster. The higher velocities effectively modify the hard-soft boundary and the formed binaries are more tightly bound. Additionally, the relaxation process is also affected, leading to longer timescales for the onset of core collapse. The external potential works against the evaporation of the cluster by helping to keep the cluster compact, in particular in the inner parts. This is an important difference compared to previous gas-free models (Portegies Zwart et al., 1999; Reinoso et al., 2018; Sakurai et al., 2017; Vergara et al., 2021). In this case a larger fraction of the cluster contracts (potentially up to the 20% lagrangian radius), and the final masses of the collision product are enhanced by a factor of

two. The simplified modelling allowed for a better understanding of the effects introduced by the external potential, but the effects of an IMF or stellar evolution were not accounted for. The addition of an external potential causes a delay in the runaway collision process and this might work against the production of massive black hole seeds because of the short lifetimes of massive stars which impose an upper limit to the duration of the runaway collision process. However other factors can still play a role. Based on the study by Portegies Zwart and McMillan (2002) one might expect that an IMF would accelerate the process of core collapse due to mass segregation. The current uncertainty in the mass limits as well as on the star formation efficiency of Pop. III star clusters would require the exploration of a large parameter space in this case. Moreover, the effects of stellar rejuvenation following a stellar merger have not been included yet. This mechanism could be significant for the runaway collision process (Schneider et al., 2016), providing extra time for growing the central massive star. More importantly, in real systems the gas would not remain static and star-gas interactions could help to promote mass segregation through gaseous dynamical friction. In addition, the modelling of embedded star clusters that self-consistently model the gas has shown that the stars effectively transfer kinetic energy to the gas, causing it to expand whereas the stellar component contracts (Hubber et al., 2013a). This would certainly help to accelerate core collapse in this case.

As a summary, for the runaway collision scenario applied to the formation of massive black hole seeds in the early Universe, including the effects of the gas in the clusters has the potential to increase the final BH masses by a factor > 2. However it will be necessary to improve on the numerical modelling of the systems in order to adequately characterize the expected black hole masses. In particular, for the modelling of Pop. III clusters the initial conditions are still uncertain in terms of star formation efficiency, the IMF, and the expected sizes of the clusters. The inclusion of gas would help to boost the masses of the BHs formed through this channel provided the core collapse occurs before the most massive stars explode as supernova. It is important to adequately treat gaseous dynamical friction, the exchange of kinetic energy between the stellar and gaseous component, the rejuvenation of the collision product, and to include an IMF. All of these effects will help to produce more massive objects in a sorter timespan. The expected masses should be at least $1000 \, \mathrm{M_\odot}$ in sufficiently dense clusters, and possibly $> 2000 \, \mathrm{M_\odot}$ if the effects previously mentioned are included. Narrowing down on the conditions required and the masses of the BHs produced will be important for proving this mechanism with gravitational wave detectors such as LISA and the Einstein Telescope.

8.2   Collision rates in dense star clusters and perturbations on binary systems

The article presented in Chap. 6 provides a comparison of analytic collision rates with collisions obtained from N-body simulations of dense star clusters. The confrontation of the two reveals that the analytic rates derived for hyperbolic collisions are in perfect agreement with the numerical simulations, and that this collision channel dominates during the initial stages of cluster evolution. On the other hand the collision of stars that are part of a binary system is underestimated by the analytic rates, and becomes unreliable once a very massive object is formed at the cluster center. A different formalism should be adopted past that stage.

Apart from revealing the difficulties in the analytic modelling of this process, this article reports the identification of a new mechanism that triggers the collision of stars that are part of a binary system. The identified mechanism occurs when encounters with single stars cause a perturbation of the orbital parameters of the binary, resulting in a random walk of the eccentricity towards unity, ultimately causing the collision of the stars. The identified process is different to the Lidov-Kozai (LK) mechanism as it does not require the formation of a triple system. The analysis presented in this research indicates that this new mechanism could operate more efficiently than the LK mechanism in the central stellar disk of the Milky Way. This hypothesis would need to be tested with detailed numerical simulations in realistic environments with an adequate snapshot output frequency that can capture the evolution of the eccentricity in binary systems. Analytic collision rates that include this new collision channel can be refined by performing simulations with the aim of calibrating the parameters that control the process. These parameters are the number of perturbations needed and the fraction of binary systems that experience the perturbation-driven merger.

Another possible effect of this collision channel would be the production of isolated blue stragglers $N_{\mathrm{BS,iso}}$ in star clusters instead of blue stragglers in binary systems $N_{\mathrm{BS,bin}}$ as predicted for the LK mechanism or for mass transfer in binary systems (Gosnell et al., 2014, 2015). A possible indication of the operation of this channel would be a correlation between the ratio $N_{\mathrm{BS,iso}}/N_{\mathrm{BS,bin}}$ and the density of the cluster. This could be tested with future observations of dense globular and open clusters. Follow up studies should focus in refining the analytic rates presented here in order to better understand the environments in which this new collision channel could be proved.

8.3   Formation of supermassive stars in the first star clusters

The research article presented in Chap. 7 explores the formation of supermassive stars in dense stellar systems embedded in gas by self-consistently modelling the stellar and gas dynamics. The scenario arises when the gas in a metal free atomic-cooling halo fragments at subparsec scales. This is an important step in confirming the plausibility of the direct collapse black hole scenario at scales inaccessible for large scale cosmological simulations (Chon et al., 2018; Latif et al., 2014b; Regan and Haehnelt, 2009a). This work demonstrated that the presence of additional fragments does not prevent the emergence of SMSs since one single object is always favoured with high accretion rates, consistent with similar works (Chon and Omukai, 2020; Regan et al., 2020). The high accretion rates onto this object cause it to evolve as an inflated SMS which in turn triggers a large number of collisions with other fragments. Despite the intermittent accretion, the collisions help to maintain an inflated envelope for this star, preventing the production of ionizing photons that could halt further growth. Interestingly, in the less massive systems explored, not only single but also binary SMSs emerged. The fate of the SMSs formed in these simulations is their collapse to massive black holes with $10^3 - 10^4$ M$_\odot$ surrounded by tens of stars with typical masses in the range $1 - 10$ M$_\odot$. These BH seeds are ideal candidates to explain the rapid emergence of the highest redshift quasars observed to date. The binary BHs expected from this process will be detectable by LISA if they merge (Amaro-Seoane et al., 2023).

The initial conditions chosen for the simulations were motivated by previous works of large scale structure formation (Chon et al., 2018). The work presented here considered one of the outcomes of such simulations, but the exploration of collapsed metal free atomic-cooling halos with a different morphology should also be investigated. In particular, the work by Chon et al. (2018) indicates that the proximity of star forming galaxies needed for preventing H$_2$ cooling can indeed tidally deform the collapsing clouds, and assuming a spherical morphology is not valid in this case. Additionally, by including turbulence with a mach number of 1, the slightly modified channel of Wise et al. (2019) is not taken into account, since rapid halo assembly would produce more turbulence, possibly leading to multiple high density sites and thus a higher multiplicity of SMSs. One possibility for improving on this is to take the output of cosmological simulations and map the resulting gas distributions into a set of SPH particles to study the assembly of SMSs with the numerical implementation presented in Sec. 4.2. Additionally, zoom-in simulations of individual atomic-cooling halos could be an alternative.

The effects of mass loss in stellar collisions was also neglected in this study, however the work by Alister Seguel et al. (2020) suggests that including this effect would not reduce the

mass of the SMSs by more than 10%. Nevertheless it is very important to mention that the result obtained by Alister Seguel et al. (2020) makes use of mass loss recipes that might not be applicable to the scenario explored here. The mass loss included in that study comes from the calculations of Glebbeek et al. (2013) which are adequate for evolved MS stars at solar metallicity. These stars have a different structure when compared to the Pop. III protostars described in Sec.3.2.2 and the SMSs described in Sec. 3.5. Understanding the real outcome expected in those situations will require the modelling of stellar collisions as done in Freitag and Benz (2005) and Glebbeek et al. (2013). An important difference is that very massive and inflated stars need to be modelled in this case, which might only be possible for masses below $1000\,\mathrm{M}_\odot$. Nevertheless this will provide invaluable insight into the runaway collision process in these environments, and help to inform what is the amount of mass loss expected for different combinations of impact velocities, masses, and impact parameters, as well as the disturbance caused to the remnant of the collision in terms of structure and lifetime.

Regarding the numerical implementation used for this study, there is still room for improvement in the coupling of the N-body and SPH codes described in Sec. 4.2.3. While the article presented in Chap. 7 solved the problems described in those sections, moving away from a fixed softening length and using instead the variable smoothing length of SPH particles is advised for future studies. This will improve the energy conservation and better capture the gas fragmentation (Bate and Burkert, 1997; Price and Monaghan, 2007).

The simulations presented in Chap. 7 did not encounter the problem of tight binaries that reduce the efficiency of the N-body integrator. This is due to the presence of an inflated SMSs with a radius of $10^4\,\mathrm{R}_\odot$ and the sticky star approximation included as collision criteria. When applying this method to study different types of embedded star clusters this problem will inevitably appear. One possible solution is to use a different N-body integrator. A good candidate at the moment is the PETAR code (Wang et al., 2020) that includes regularization for treating tight binaries (see Sec. 4.1.4), however it will be necessary to include the detection of stellar collisions in the code during the integration of the particles. The work by Polak et al. (2023) demonstrates this approach.

One of the processes that was not explicitly considered in this study was that of radiation feedback. On one hand the assembly of an SMS occurs in a timescale of $30\,000$ yr so that not even the surrounding high mass protostars have enough time to reach the ZAMS by then. On the other hand the existence of periods of low accretion rate onto the SMS should cause a gradual contraction of the stellar envelope which could trigger the emission of ionizing radiation (Sakurai et al., 2015). In principle the variation of the stellar radius associated to the low accretion rate periods can be easily included in future simulations. How to include the effects of ionizing radiation is still not so clear, and this is in general true for the studies of star formation in similar environments (Jaura et al., 2022; Klessen and Glover, 2023).

In summary, the formation of supermassive stars in dense embedded star clusters is inevitable. This indicates that fragmentation at subparsec scales during the DCBH scenario does not prevent the emergence of 10^4 M$_\odot$ SMSs, at least in gas cloud with a spherical morphology and moderate levels of turbulence. The combination of high accretion rates and the high amount of collisions favour the formation of a single SMS. The large scale fragmentation expected in tidally deformed clouds or in environments with higher levels of turbulence could yield multiple formation sites for SMSs, but would not prevent their formation. Modelling the contraction of SMSs during quiescent phases is necessary for future studies. Understanding the outcomes of collisions that involve an SMS and the expected amount of mass loss associated is critical for placing stronger constraints for the black hole mass expected from this seeding mechanism. Confirming the frequency of binary SMSs formation in this scenario is a promising route for testing the occurrence of this process via gravitational wave detection with LISA.

Appendix A

Gravitational force and potential with a softening kernel

When simulating systems comprised of SPH plus N-body particles it is necessary to introduce a softening for the gravitational force between the particles to avoid numerical artifacts. When doing this, the gravitational potential at position $\mathbf{r}$ produced by a set of N particles is given by

$$\Phi(\mathbf{r}) = -G \sum_{i=1}^{N} m_i \phi(|\mathbf{r} - \mathbf{r}_i|, h), \qquad (A.1)$$

where ϕ is the potential softening kernel, which depends on the distance to a particle $|\mathbf{r} - \mathbf{r}_i|$ and its softening length h.

It is common to use a Plummer force softening kernel in N-body codes, from which the potential softening kernel can be derived. For SPH codes, one can derive the softening kernel from the density smoothing kernel as

$$\phi(r, h) = -4\pi \left(-\frac{1}{r} \int_0^r W r'^2 dr' + \int_0^r W r' dr' + C \right), \qquad (A.2)$$

where W is the density smoothing kernel, and C is a constant that guarantees the continuity of the function. There are several options for the density smoothing kernel even for the same SPH code. We derive here the potential softening kernel from the cubic spline kernel used in the GADGET-2 code as well as on the FI code. The cubic spline kernel is given by

$$W(r, h) = \frac{8}{\pi h^3} \begin{cases} 1 - 6 \left(\frac{r}{h}\right)^2 + 6 \left(\frac{r}{h}\right)^3 & 0 \leq \frac{r}{h} \leq 0.5 \\ 2 \left(1 - \frac{r}{h}\right)^3 & 0.5 < \frac{r}{h} \leq 1 \\ 0 & \frac{r}{h} > 1. \end{cases} \qquad (A.3)$$

In the following, a step-by-step derivation of the softening kernel is presented, for the calculation of the gravitational potential and the gravitational force.

A.1 Softened gravitational potential

The derivation of the potential softening kernel begins by considering first the case $\frac{r}{h} \leq 0.5$. Also, for simplicity, the factor $\frac{8}{\pi h^3}$ in Eq.(A.3) is ignored during the derivation. The first term in Eq.(A.2) is therefore

$$
\begin{aligned}
-\frac{1}{r} \int_0^r W r'^2 dr' &= -\frac{1}{r} \int_0^r \left[1 - 6 \left(\frac{r'}{h}\right)^2 + 6 \left(\frac{r'}{h}\right)^3 \right] r'^2 dr' \\
&= -\frac{1}{r} \int_0^r \left[r'^2 - 6 \frac{r'^4}{h^2} + 6 \frac{r'^5}{h^3} \right] dr' \\
&= -\frac{1}{r} \left(\frac{1}{3} r'^3 - \frac{6}{5} \frac{r'^5}{h^2} + \frac{r'^6}{h^3} \right) \Big|_0^r \\
&= -\frac{1}{r} \left(\frac{1}{3} r^3 - \frac{6}{5} \frac{r^5}{h^2} + \frac{r^6}{h^3} \right) \\
&= -\frac{1}{3} r^2 + \frac{6}{5} \frac{r^4}{h^2} - \frac{r^5}{h^3}.
\end{aligned}
\tag{A.4}
$$

Now the second term in Eq.(A.2) is

$$
\begin{aligned}
\int_0^r W r' dr' &= \int_0^r \left[1 - 6 \left(\frac{r'}{h}\right)^2 + 6 \left(\frac{r'}{h}\right)^3 \right] r' dr' \\
&= \int_0^r \left[r' - 6 \frac{r'^3}{h^2} + 6 \frac{r'^4}{h^3} \right] dr' \\
&= \left(\frac{1}{2} r'^2 - \frac{6}{4} \frac{r'^4}{h^2} + \frac{6}{5} \frac{r'^5}{h^3} \right) \Big|_0^r \\
&= \frac{1}{2} r^2 - \frac{6}{4} \frac{r^4}{h^2} + \frac{6}{5} \frac{r^5}{h^3}.
\end{aligned}
\tag{A.5}
$$

Now consider the second interval of the smoothing kernel in Eq.(A.3). For this interval the first term in Eq.(A.2) is

$$
\begin{aligned}
-\frac{1}{r} \int_0^r W r'^2 dr' &= -\frac{1}{r} \int_0^r 2 \left(1 - \frac{r'}{h} \right)^3 r'^2 dr' \\
&= -\frac{1}{r} \int_0^r 2 \left(1 - 3 \frac{r'}{h} + 3 \frac{r'^2}{h^2} - \frac{r'^3}{h^3} \right) r'^2 dr' \\
&= -\frac{1}{r} \int_0^r 2 \left(r'^2 - 3 \frac{r'^3}{h} + 3 \frac{r'^4}{h^2} - \frac{r'^5}{h^3} \right) dr' \\
&= -\frac{1}{r} 2 \left(\frac{1}{3} r'^3 - \frac{3}{4} \frac{r'^4}{h} + \frac{3}{5} \frac{r'^5}{h^2} - \frac{1}{6} \frac{r'^6}{h^3} \right) \Big|_0^r \\
&= -\frac{1}{r} 2 \left(\frac{1}{3} r^3 - \frac{3}{4} \frac{r^4}{h} + \frac{3}{5} \frac{r^5}{h^2} - \frac{1}{6} \frac{r^6}{h^3} \right) \\
&= -\frac{2}{3} r^2 + \frac{3}{2} \frac{r^3}{h} - \frac{6}{5} \frac{r^4}{h^2} + \frac{1}{3} \frac{r^5}{h^3},
\end{aligned}
\tag{A.6}
$$

and the second term in Eq.(A.2) is

$$
\begin{aligned}
\int_0^r W r' dr' &= \int_0^r 2\left(1 - \frac{r'}{h}\right)^3 r' dr' \\
&= \int_0^r 2\left(1 - 3\frac{r'}{h} + 3\frac{r'^2}{h^2} - \frac{r'^3}{h^3}\right) r' dr' \\
&= \int_0^r 2\left(r' - 3\frac{r'^2}{h} + 3\frac{r'^3}{h^2} - \frac{r'^4}{h^3}\right) dr' \\
&= 2\left(\frac{1}{2}r'^2 - \frac{r'^3}{h} + \frac{3}{4}\frac{r'^4}{h^2} - \frac{1}{5}\frac{r'^5}{h^3}\right)\bigg|_0^r \\
&= 2\left(\frac{1}{2}r^2 - \frac{r^3}{h} + \frac{3}{4}\frac{r^4}{h^2} - \frac{1}{5}\frac{r^5}{h^3}\right) \\
&= r^2 - 2\frac{r^3}{h} + \frac{3}{2}\frac{r^4}{h^2} - \frac{2}{5}\frac{r^5}{h^3}.
\end{aligned}
\tag{A.7}
$$

Therefore, from Eq.(A.2), and using Eqs.(A.4), and (A.5), one finds that the softening kernel, in the interval $0 \leq \frac{r}{h} \leq 0.5$ is given by

$$
\phi(r, h) = -\frac{8}{\pi h^3} 4\pi \left(\frac{1}{6}r^2 - \frac{3}{10}\frac{r^4}{h^2} + \frac{1}{5}\frac{r^5}{h^3} + c_1\right), \qquad 0 \leq \frac{r}{h} \leq 0.5
\tag{A.8}
$$

$$
\phi(r, h) = -\frac{32}{h}\left[\frac{1}{6}\left(\frac{r}{h}\right)^2 - \frac{3}{10}\left(\frac{r}{h}\right)^4 + \frac{1}{5}\left(\frac{r}{h}\right)^5 + c_1\right], \qquad 0 \leq \frac{r}{h} \leq 0.5,
\tag{A.9}
$$

where the factor $\frac{8}{\pi h^3}$ has been reincorporated.

Next, for the interval $0.5 < \frac{r}{h} \leq 1$, and by combining Eqs.(A.2), (A.6), and (A.7), the softening kernel is given by

$$
\phi(r, h) = -\frac{8}{\pi h^3} 4\pi \left(\frac{1}{3}r^2 - \frac{1}{2}\frac{r^3}{h} + \frac{3}{10}\frac{r^4}{h^2} - \frac{1}{15}\frac{r^5}{h^3} + c_2\right), \qquad 0.5 < \frac{r}{h} \leq 1
$$

$$
\phi(r, h) = -\frac{32}{h}\left[\frac{1}{3}\left(\frac{r}{h}\right)^2 - \frac{1}{2}\left(\frac{r}{h}\right)^3 + \frac{3}{10}\left(\frac{r}{h}\right)^4 - \frac{1}{15}\left(\frac{r}{h}\right)^5 + c_2\right], \qquad 0.5 < \frac{r}{h} \leq 1
\tag{A.10}
$$

The factor $\frac{8}{\pi h^3}$ has been also reincorporated in this case.

Note that the potential must be proportional to $-\frac{1}{r}$ for $\frac{r}{h} > 1$, therefore the softening potential is given by

$$
\phi(r, h) = -\frac{32}{h}
\begin{cases}
\frac{1}{6}\left(\frac{r}{h}\right)^2 - \frac{3}{10}\left(\frac{r}{h}\right)^4 + \frac{1}{5}\left(\frac{r}{h}\right)^5 + c_1 & 0 \leq \frac{r}{h} \leq 0.5 \\[2ex]
\frac{1}{3}\left(\frac{r}{h}\right)^2 - \frac{1}{2}\left(\frac{r}{h}\right)^3 + \frac{3}{10}\left(\frac{r}{h}\right)^4 - \frac{1}{15}\left(\frac{r}{h}\right)^5 + c_2 & 0.5 < \frac{r}{h} \leq 1 \\[2ex]
-\frac{h}{32}\frac{1}{r} & \frac{r}{h} > 1
\end{cases}
\tag{A.11}
$$

Now it is necessary to find the constants c_1 and c_2 by imposing the condition of continuity of the smoothing kernel. For the constant c_2 the condition $\phi(r, h) \to -\frac{1}{h}$ for $r = h$ must be

fulfilled. This means that

$$\frac{1}{3} - \frac{1}{2} + \frac{3}{10} - \frac{1}{15} + c_2 = -\frac{1}{32}$$

$$c_2 = -\frac{47}{480}.$$

Now for the case when $r/h = 0.5$ the continuity condition leads to

$$\frac{1}{24} - \frac{3}{160} + \frac{1}{160} + c_1 = \frac{1}{12} - \frac{1}{16} + \frac{3}{160} - \frac{1}{480} + c2$$

$$c_1 = -\frac{43}{480}$$

Finally the smoothing kernel is given by

$$\phi(r,h) = -\frac{32}{h} \begin{cases} \frac{1}{6}\left(\frac{r}{h}\right)^2 - \frac{3}{10}\left(\frac{r}{h}\right)^4 + \frac{1}{5}\left(\frac{r}{h}\right)^5 - \frac{41}{480} & 0 \leq \frac{r}{h} \leq 0.5 \\[2ex] \frac{1}{3}\left(\frac{r}{h}\right)^2 - \frac{1}{2}\left(\frac{r}{h}\right)^3 + \frac{3}{10}\left(\frac{r}{h}\right)^4 - \frac{1}{15}\left(\frac{r}{h}\right)^5 + \frac{1}{240}\left(\frac{h}{r}\right) - \frac{49}{480} & 0.5 < \frac{r}{h} \leq 1 \\[2ex] -\frac{h}{32}\frac{1}{r} & \frac{r}{h} > 1 \end{cases}$$

$$(A.12)$$

The potential of a 1 M$_\odot$ mass calculated with the smoothing kernel and the exact $1/r$ potential is shown in Fig. A.1.
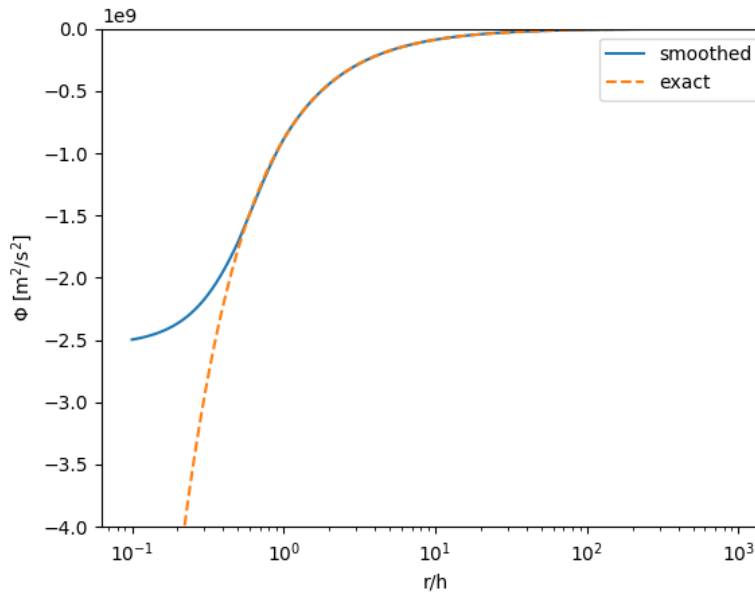

Figure A.1. Comparison of the gravitational potential produced by a 1 M$_\odot$ point mass at different distances calculated with the exact point-mass potential formula (orange dashed line), and with Eq.(A.1) employing a softening kernel based on the cubic spline kernel (blue solid line). Distance is shown in units of the smoothing length.

A.2   Softened gravitational force

The gravitational force between two particles is obtained as

$$\mathbf{F} = -Gm_1m_2\phi'(r_{12}, h)\hat{\mathbf{r}}_{12}, \tag{A.13}$$

with m_1 and m_2 being the masses of the particles, r_{12} their separation, h the softening length, and ϕ' the force softening kernel.

After having derived the potential softening kernel it is a straightforward task to compute the force softening kernel as

$$\phi' = -\frac{\partial\phi}{\partial r}. \tag{A.14}$$

By doing so (and ensuring the continuity of the function) one arrives at the force softening kernel

$$\phi'(r, h) = \frac{32}{h^2} \begin{cases} \frac{1}{3}\left(\frac{r}{h}\right) - \frac{6}{5}\left(\frac{r}{h}\right)^3 + \left(\frac{r}{h}\right)^4 & 0 \leq \frac{r}{h} \leq 0.5 \\[2ex] \frac{2}{3}\left(\frac{r}{h}\right) - \frac{3}{2}\left(\frac{r}{h}\right)^2 + \frac{6}{5}\left(\frac{r}{h}\right)^3 - \frac{1}{3}\left(\frac{r}{h}\right)^4 - \frac{1}{480}\left(\frac{h}{r}\right)^2 & 0.5 < \frac{r}{h} \leq 1 \\[2ex] \frac{h^2}{32}\frac{1}{r^2} & \frac{r}{h} > 1 \end{cases} \tag{A.15}$$

Note that the force softening kernel is always positive. Fig. A.2 shows the magnitude of the gravitational force between two 1 $M_\odot$ particles computed with the force softening kernel and the exact $1/r^2$ force dependence.
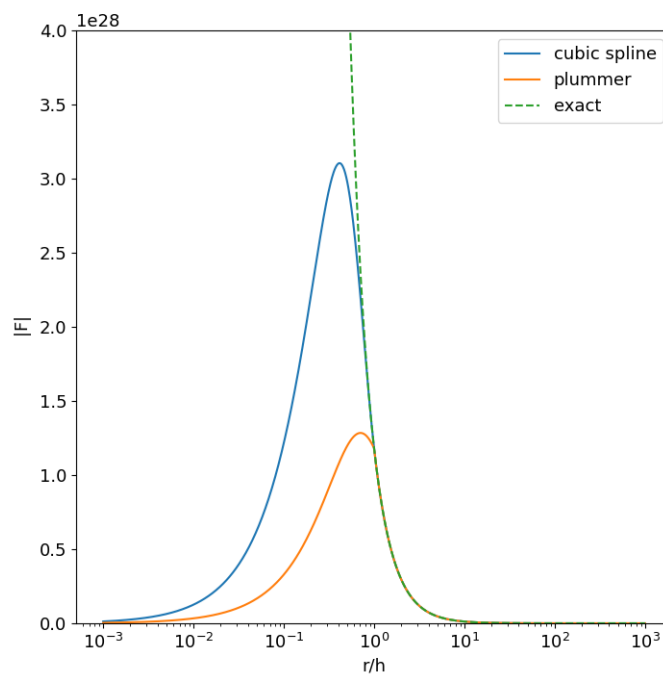
Figure A.2. Magnitude of the gravitational force between two 1 $M_\odot$ point-masses as a function of the distance in units of the smoothing length. The green dashed line shows the force as calculated with the exact point-mass gravitational force. The blue line shows the force as calculated with a cubic spline force smoothing kernel. The orange line shows the magnitude of the force as calculated with a Plummer softening kernel.

Acknowledgements

Bibliography

Aarseth, S. J. (1999). From NBODY1 to NBODY6: The Growth of an Industry. *PASP*, 111(765):1333–1346. https://ui.adsabs.harvard.edu/abs/1999PASP..111.1333.

Aarseth, S. J. (2000). NBODY 6: A New Star Cluster Simulation Code. In Gurzadyan, V. G. and Ruffini, R., editors, *The Chaotic Universe*, pages 286–287. https://ui.adsabs.harvard.edu/abs/2000chun.proc..286A.

Aarseth, S. J., Henon, M., and Wielen, R. (1974). A Comparison of Numerical Methods for the Study of Star Cluster Dynamics. *A&A*, 37(1):183–187. https://ui.adsabs.harvard.edu/abs/1974A&A....37..183A.

Abbott, B. P., Abbott, R., Abbott, T. D., Abernathy, M. R., Acernese, F., Ackley, K., Adams, C., Adams, T., Addesso, P., Adhikari, R. X., Adya, V. B., Affeldt, C., Agathos, M., Agatsuma, K., Aggarwal, N., Aguiar, O. D., Aiello, L., Ain, A., Ajith, P., Allen, B., Allocca, A., Altin, P. A., Anderson, S. B., Anderson, W. G., Arai, K., Arain, M. A., Araya, M. C., Arceneaux, C. C., Areeda, J. S., Arnaud, N., Arun, K. G., Ascenzi, S., Ashton, G., Ast, M., Aston, S. M., Astone, P., Aufmuth, P., Aulbert, C., Babak, S., Bacon, P., Bader, M. K. M., Baker, P. T., Baldaccini, F., Ballardin, G., Ballmer, S. W., Barayoga, J. C., Barclay, S. E., Barish, B. C., Barker, D., Barone, F., Barr, B., Barsotti, L., Barsuglia, M., Barta, D., Bartlett, J., Barton, M. A., Bartos, I., Bassiri, R., Basti, A., Batch, J. C., Baune, C., Bavigadda, V., Bazzan, M., Behnke, B., Bejger, M., Belczynski, C., Bell, A. S., Bell, C. J., Berger, B. K., Bergman, J., Bergmann, G., Berry, C. P. L., Bersanetti, D., Bertolini, A., Betzwieser, J., Bhagwat, S., Bhandare, R., Bilenko, I. A., Billingsley, G., Birch, J., Birney, R., Birnholtz, O., Biscans, S., Bisht, A., Bitossi, M., Biwer, C., Bizouard, M. A., Blackburn, J. K., Blair, C. D., Blair, D. G., Blair, R. M., Bloemen, S., Bock, O., Bodiya, T. P., Boer, M., Bogaert, G., Bogan, C., Bohe, A., Bojtos, P., Bond, C., Bondu, F., Bonnand, R., Boom, B. A., Bork, R., Boschi, V., Bose, S., Bouffanais, Y., Bozzi, A., Bradaschia, C., Brady, P. R., Braginsky, V. B., Branchesi, M., Brau, J. E.,

171

Briant, T., Brillet, A., Brinkmann, M., Brisson, V., Brockill, P., Brooks, A. F., Brown, D. A., Brown, D. D., Brown, N. M., Buchanan, C. C., Buikema, A., Bulik, T., Bulten, H. J., Buonanno, A., Buskulic, D., Buy, C., Byer, R. L., Cabero, M., Cadonati, L., Cagnoli, G., Cahillane, C., Bustillo, J. C., Callister, T., Calloni, E., Camp, J. B., Cannon, K. C., Cao, J., Capano, C. D., Capocasa, E., Carbognani, F., Caride, S., Casanueva Diaz, J., Casentini, C., Caudill, S., Cavaglià, M., Cavalier, F., Cavalieri, R., Cella, G., Cepeda, C. B., Baiardi, L. C., Cerretani, G., Cesarini, E., Chakraborty, R., Chalermsongsak, T., Chamberlin, S. J., Chan, M., Chao, S., Charlton, P., Chassande-Mottin, E., Chen, H. Y., Chen, Y., Cheng, C., Chincarini, A., Chiummo, A., Cho, H. S., Cho, M., Chow, J. H., Christensen, N., Chu, Q., Chua, S., Chung, S., Ciani, G., Clara, F., Clark, J. A., Cleva, F., Coccia, E., Cohadon, P. F., Colla, A., Collette, C. G., Cominsky, L., Constancio, M., Conte, A., Conti, L., Cook, D., Corbitt, T. R., Cornish, N., Corsi, A., Cortese, S., Costa, C. A., Coughlin, M. W., Coughlin, S. B., Coulon, J. P., Countryman, S. T., Couvares, P., Cowan, E. E., Coward, D. M., Cowart, M. J., Coyne, D. C., Coyne, R., Craig, K., Creighton, J. D. E., Creighton, T. D., Cripe, J., Crowder, S. G., Cruise, A. M., Cumming, A., Cunningham, L., Cuoco, E., Dal Canton, T., Danilishin, S. L., D'Antonio, S., Danzmann, K., Darman, N. S., Da Silva Costa, C. F., Dattilo, V., Dave, I., Daveloza, H. P., Davier, M., Davies, G. S., Daw, E. J., Day, R., De, S., DeBra, D., Debreczeni, G., Degallaix, J., De Laurentis, M., Deléglise, S., Del Pozzo, W., Denker, T., Dent, T., Dereli, H., Dergachev, V., DeRosa, R. T., De Rosa, R., DeSalvo, R., Dhurandhar, S., Díaz, M. C., Di Fiore, L., Di Giovanni, M., Di Lieto, A., Di Pace, S., Di Palma, I., Di Virgilio, A., Dojcinoski, G., Dolique, V., Donovan, F., Dooley, K. L., Doravari, S., Douglas, R., Downes, T. P., Drago, M., Drever, R. W. P., Driggers, J. C., Du, Z., Ducrot, M., Dwyer, S. E., Edo, T. B., Edwards, M. C., Effler, A., Eggenstein, H. B., Ehrens, P., Eichholz, J., Eikenberry, S. S., Engels, W., Essick, R. C., Etzel, T., Evans, M., Evans, T. M., Everett, R., Factourovich, M., Fafone, V., Fair, H., Fairhurst, S., Fan, X., Fang, Q., Farinon, S., Farr, B., Farr, W. M., Favata, M., Fays, M., Fehrmann, H., Fejer, M. M., Feldbaum, D., Ferrante, I., Ferreira, E. C., Ferrini, F., Fidecaro, F., Finn, L. S., Fiori, I., Fiorucci, D., Fisher, R. P., Flaminio, R., Fletcher, M., Fong, H., Fournier, J. D., Franco, S., Frasca, S., Frasconi, F., Frede, M., Frei, Z., Freise, A., Frey, R., Frey, V., Fricke, T. T., Fritschel, P., Frolov, V. V., Fulda, P., Fyffe, M., Gabbard, H. A. G., Gair, J. R., Gammaitoni, L., Gaonkar, S. G., Garufi, F., Gatto, A., Gaur, G., Gehrels, N., Gemme, G., Gendre, B., Genin, E., Gennai, A., George, J., Gergely, L., Germain, V., Ghosh, A., Ghosh, A., Ghosh, S., Giaime, J. A., Giardina, K. D., Giazotto, A., Gill, K., Glaefke, A., Gleason, J. R., Goetz, E., Goetz, R., Gondan, L., González, G., Castro, J. M. G., Gopakumar, A., Gordon, N. A., Gorodetsky, M. L., Gossan, S. E., Gosselin, M., Gouaty, R., Graef, C., Graff, P. B., Granata, M., Grant, A., Gras, S., Gray, C., Greco, G., Green,

A. C., Greenhalgh, R. J. S., Groot, P., Grote, H., Grunewald, S., Guidi, G. M., Guo, X., Gupta, A., Gupta, M. K., Gushwa, K. E., Gustafson, E. K., Gustafson, R., Hacker, J. J., Hall, B. R., Hall, E. D., Hammond, G., Haney, M., Hanke, M. M., Hanks, J., Hanna, C., Hannam, M. D., Hanson, J., Hardwick, T., Harms, J., Harry, G. M., Harry, I. W., Hart, M. J., Hartman, M. T., Haster, C. J., Haughian, K., Healy, J., Heefner, J., Heidmann, A., Heintze, M. C., Heinzel, G., Heitmann, H., Hello, P., Hemming, G., Hendry, M., Heng, I. S., Hennig, J., Heptonstall, A. W., Heurs, M., Hild, S., Hoak, D., Hodge, K. A., Hofman, D., Hollitt, S. E., Holt, K., Holz, D. E., Hopkins, P., Hosken, D. J., Hough, J., Houston, E. A., Howell, E. J., Hu, Y. M., Huang, S., Huerta, E. A., Huet, D., Hughey, B., Husa, S., Huttner, S. H., Huynh-Dinh, T., Idrisy, A., Indik, N., Ingram, D. R., Inta, R., Isa, H. N., Isac, J. M., Isi, M., Islas, G., Isogai, T., Iyer, B. R., Izumi, K., Jacobson, M. B., Jacqmin, T., Jang, H., Jani, K., Jaranowski, P., Jawahar, S., Jiménez-Forteza, F., Johnson, W. W., Johnson-McDaniel, N. K., Jones, D. I., Jones, R., Jonker, R. J. G., Ju, L., Haris, K., Kalaghatgi, C. V., Kalogera, V., Kandhasamy, S., Kang, G., Kanner, J. B., Karki, S., Kasprzack, M., Katsavounidis, E., Katzman, W., Kaufer, S., Kaur, T., Kawabe, K., Kawazoe, F., Kéfélian, F., Kehl, M. S., Keitel, D., Kelley, D. B., Kells, W., Kennedy, R., Keppel, D. G., Key, J. S., Khalaidovski, A., Khalili, F. Y., Khan, I., Khan, S., Khan, Z., Khazanov, E. A., Kijbunchoo, N., Kim, C., Kim, J., Kim, K., Kim, N.-G., Kim, N., Kim, Y. M., King, E. J., King, P. J., Kinzel, D. L., Kissel, J. S., Kleybolte, L., Klimenko, S., Koehlenbeck, S. M., Kokeyama, K., Koley, S., Kondrashov, V., Kontos, A., Koranda, S., Korobko, M., Korth, W. Z., Kowalska, I., Kozak, D. B., Kringel, V., Krishnan, B., Królak, A., Krueger, C., Kuehn, G., Kumar, P., Kumar, R., Kuo, L., Kutynia, A., Kwee, P., Lackey, B. D., Landry, M., Lange, J., Lantz, B., Lasky, P. D., Lazzarini, A., Lazzaro, C., Leaci, P., Leavey, S., Lebigot, E. O., Lee, C. H., Lee, H. K., Lee, H. M., Lee, K., Lenon, A., Leonardi, M., Leong, J. R., Leroy, N., Letendre, N., Levin, Y., Levine, B. M., Li, T. G. F., Libson, A., Littenberg, T. B., Lockerbie, N. A., Logue, J., Lombardi, A. L., London, L. T., Lord, J. E., Lorenzini, M., Loriette, V., Lormand, M., Losurdo, G., Lough, J. D., Lousto, C. O., Lovelace, G., Lück, H., Lundgren, A. P., Luo, J., Lynch, R., Ma, Y., MacDonald, T., Machenschalk, B., MacInnis, M., Macleod, D. M., Magaña-Sandoval, F., Magee, R. M., Mageswaran, M., Majorana, E., Maksimovic, I., Malvezzi, V., Man, N., Mandel, I., Mandic, V., Mangano, V., Mansell, G. L., Manske, M., Mantovani, M., Marchesoni, F., Marion, F., Márka, S., Márka, Z., Markosyan, A. S., Maros, E., Martelli, F., Martellini, L., Martin, I. W., Martin, R. M., Martynov, D. V., Marx, J. N., Mason, K., Masserot, A., Massinger, T. J., Masso-Reid, M., Matichard, F., Matone, L., Maval-vala, N., Mazumder, N., Mazzolo, G., McCarthy, R., McClelland, D. E., McCormick, S., McGuire, S. C., McIntyre, G., McIver, J., McManus, D. J., McWilliams, S. T., Meacher, D., Meadors, G. D., Meidam, J., Melatos, A., Mendell, G., Mendoza-Gandara, D., Mer-

cer, R. A., Merilh, E., Merzougui, M., Meshkov, S., Messenger, C., Messick, C., Meyers, P. M., Mezzani, F., Miao, H., Michel, C., Middleton, H., Mikhailov, E. E., Milano, L., Miller, J., Millhouse, M., Minenkov, Y., Ming, J., Mirshekari, S., Mishra, C., Mitra, S., Mitrofanov, V. P., Mitselmakher, G., Mittleman, R., Moggi, A., Mohan, M., Mohapatra, S. R. P., Montani, M., Moore, B. C., Moore, C. J., Moraru, D., Moreno, G., Morriss, S. R., Mossavi, K., Mours, B., Mow-Lowry, C. M., Mueller, C. L., Mueller, G., Muir, A. W., Mukherjee, A., Mukherjee, D., Mukherjee, S., Mukund, N., Mullavey, A., Munch, J., Murphy, D. J., Murray, P. G., Mytidis, A., Nardecchia, I., Naticchioni, L., Nayak, R. K., Necula, V., Nedkova, K., Nelemans, G., Neri, M., Neunzert, A., Newton, G., Nguyen, T. T., Nielsen, A. B., Nissanke, S., Nitz, A., Nocera, F., Nolting, D., Normandin, M. E. N., Nuttall, L. K., Oberling, J., Ochsner, E., O'Dell, J., Oelker, E., Ogin, G. H., Oh, J. J., Oh, S. H., Ohme, F., Oliver, M., Oppermann, P., Oram, R. J., O'Reilly, B., O'Shaughnessy, R., Ott, C. D., Ottaway, D. J., Ottens, R. S., Overmier, H., Owen, B. J., Pai, A., Pai, S. A., Palamos, J. R., Palashov, O., Palomba, C., Pal-Singh, A., Pan, H., Pan, Y., Pankow, C., Pannarale, F., Pant, B. C., Paoletti, F., Paoli, A., Papa, M. A., Paris, H. R., Parker, W., Pascucci, D., Pasqualetti, A., Passaquieti, R., Passuello, D., Patricelli, B., Patrick, Z., Pearlstone, B. L., Pedraza, M., Pedurand, R., Pekowsky, L., Pele, A., Penn, S., Perreca, A., Pfeiffer, H. P., Phelps, M., Piccinni, O., Pichot, M., Pickenpack, M., Piergiovanni, F., Pierro, V., Pillant, G., Pinard, L., Pinto, I. M., Pitkin, M., Poeld, J. H., Poggiani, R., Popolizio, P., Post, A., Powell, J., Prasad, J., Predoi, V., Premachandra, S. S., Prestegard, T., Price, L. R., Prijatelj, M., Principe, M., Privitera, S., Prix, R., Prodi, G. A., Prokhorov, L., Puncken, O., Punturo, M., Puppo, P., Pürrer, M., Qi, H., Qin, J., Quetschke, V., Quintero, E. A., Quitzow-James, R., Raab, F. J., Rabeling, D. S., Radkins, H., Raffai, P., Raja, S., Rakhmanov, M., Ramet, C. R., Rapagnani, P., Raymond, V., Razzano, M., Re, V., Read, J., Reed, C. M., Regimbau, T., Rei, L., Reid, S., Reitze, D. H., Rew, H., Reyes, S. D., Ricci, F., Riles, K., Robertson, N. A., Robie, R., Robinet, F., Rocchi, A., Rolland, L., Rollins, J. G., Roma, V. J., Romano, J. D., Romano, R., Romanov, G., Romie, J. H., Rosińska, D., Rowan, S., Rüdiger, A., Ruggi, P., Ryan, K., Sachdev, S., Sadecki, T., Sadeghian, L., Salconi, L., Saleem, M., Salemi, F., Samajdar, A., Sammut, L., Sampson, L. M., Sanchez, E. J., Sandberg, V., Sandeen, B., Sanders, G. H., Sanders, J. R., Sassolas, B., Sathyaprakash, B. S., Saulson, P. R., Sauter, O., Savage, R. L., Sawadsky, A., Schale, P., Schilling, R., Schmidt, J., Schmidt, P., Schnabel, R., Schofield, R. M. S., Schönbeck, A., Schreiber, E., Schuette, D., Schutz, B. F., Scott, J., Scott, S. M., Sellers, D., Sengupta, A. S., Sentenac, D., Sequino, V., Sergeev, A., Serna, G., Setyawati, Y., Sevigny, A., Shaddock, D. A., Shaffer, T., Shah, S., Shahriar, M. S., Shaltev, M., Shao, Z., Shapiro, B., Shawhan, P., Sheperd, A., Shoemaker, D. H., Shoemaker, D. M., Siellez, K., Siemens, X., Sigg, D., Silva, A. D., Simakov, D., Singer, A., Singer, L. P.,

Singh, A., Singh, R., Singhal, A., Sintes, A. M., Slagmolen, B. J. J., Smith, J. R., Smith, M. R., Smith, N. D., Smith, R. J. E., Son, E. J., Sorazu, B., Sorrentino, F., Souradeep, T., Srivastava, A. K., Staley, A., Steinke, M., Steinlechner, J., Steinlechner, S., Steinmeyer, D., Stephens, B. C., Stevenson, S. P., Stone, R., Strain, K. A., Straniero, N., Stratta, G., Strauss, N. A., Strigin, S., Sturani, R., Stuver, A. L., Summerscales, T. Z., Sun, L., Sutton, P. J., Swinkels, B. L., Szczepańczyk, M. J., Tacca, M., Talukder, D., Tanner, D. B., Tápai, M., Tarabrin, S. P., Taracchini, A., Taylor, R., Theeg, T., Thirugnanasambandam, M. P., Thomas, E. G., Thomas, M., Thomas, P., Thorne, K. A., Thorne, K. S., Thrane, E., Tiwari, S., Tiwari, V., Tokmakov, K. V., Tomlinson, C., Tonelli, M., Torres, C. V., Torrie, C. I., Töyrä, D., Travasso, F., Traylor, G., Trifirò, D., Tringali, M. C., Trozzo, L., Tse, M., Turconi, M., Tuyenbayev, D., Ugolini, D., Unnikrishnan, C. S., Urban, A. L., Usman, S. A., Vahlbruch, H., Vajente, G., Valdes, G., Vallisneri, M., van Bakel, N., van Beuzekom, M., van den Brand, J. F. J., Van Den Broeck, C., Vander-Hyde, D. C., van der Schaaf, L., van Heijningen, J. V., van Veggel, A. A., Vardaro, M., Vass, S., Vasúth, M., Vaulin, R., Vecchio, A., Vedovato, G., Veitch, J., Veitch, P. J., Venkateswara, K., Verkindt, D., Vetrano, F., Viceré, A., Vinciguerra, S., Vine, D. J., Vinet, J. Y., Vitale, S., Vo, T., Vocca, H., Vorvick, C., Voss, D., Vousden, W. D., Vyatchanin, S. P., Wade, A. R., Wade, L. E., Wade, M., Waldman, S. J., Walker, M., Wallace, L., Walsh, S., Wang, G., Wang, H., Wang, M., Wang, X., Wang, Y., Ward, H., Ward, R. L., Warner, J., Was, M., Weaver, B., Wei, L. W., Weinert, M., Weinstein, A. J., Weiss, R., Welborn, T., Wen, L., Weßels, P., Westphal, T., Wette, K., Whelan, J. T., Whitcomb, S. E., White, D. J., Whiting, B. F., Wiesner, K., Wilkinson, C., Willems, P. A., Williams, L., Williams, R. D., Williamson, A. R., Willis, J. L., Willke, B., Wimmer, M. H., Winkelmann, L., Winkler, W., Wipf, C. C., Wiseman, A. G., Wittel, H., Woan, G., Worden, J., Wright, J. L., Wu, G., Yablon, J., Yakushin, I., Yam, W., Yamamoto, H., Yancey, C. C., Yap, M. J., Yu, H., Yvert, M., Zadrożny, A., Zangrando, L., Zanolin, M., Zendri, J. P., Zevin, M., Zhang, F., Zhang, L., Zhang, M., Zhang, Y., Zhao, C., Zhou, M., Zhou, Z., Zhu, X. J., Zucker, M. E., Zuraw, S. E., Zweizig, J., LIGO Scientific Collaboration, and Virgo Collaboration (2016). Observation of Gravitational Waves from a Binary Black Hole Merger. *Phys. Rev. Lett.*, 116(6):061102. https://ui.adsabs.harvard.edu/abs/2016PhRvL.116f1102A.

Abel, T., Bryan, G. L., and Norman, M. L. (2000). The Formation and Fragmentation of Primordial Molecular Clouds. *ApJ*, 540(1):39–44. https://ui.adsabs.harvard.edu/abs/2000ApJ...540...39A.

Agarwal, B., Dalla Vecchia, C., Johnson, J. L., Khochfar, S., and Paardekooper, J.-P. (2014). The First Billion Years project: birthplaces of direct collapse black holes. *MNRAS*, 443(1):648–657. https://ui.adsabs.harvard.edu/abs/2014MNRAS.443..648A.

Agarwal, B., Khochfar, S., Johnson, J. L., Neistein, E., Dalla Vecchia, C., and Livio, M. (2012). Ubiquitous seeding of supermassive black holes by direct collapse. *MN-RAS*, 425(4):2854–2871. https://ui.adsabs.harvard.edu/abs/2012MNRAS.425.2854A.

Agrawal, P., Cyr-Racine, F.-Y., Pinner, D., and Randall, L. (2023). Rock 'n' roll solutions to the Hubble tension. *Physics of the Dark Universe*, 42:101347. https://ui.adsabs.harvard.edu/abs/2023PDU....4201347A.

Ahn, C. P., Alexandroff, R., Allende Prieto, C., Anderson, S. F., Anderton, T., Andrews, B. H., Aubourg, É., Bailey, S., Balbinot, E., Barnes, R., Bautista, J., Beers, T. C., Beifiori, A., Berlind, A. A., Bhardwaj, V., Bizyaev, D., Blake, C. H., Blanton, M. R., Blomqvist, M., Bochanski, J. J., Bolton, A. S., Borde, A., Bovy, J., Brandt, W. N., Brinkmann, J., Brown, P. J., Brownstein, J. R., Bundy, K., Busca, N. G., Carithers, W., Carnero, A. R., Carr, M. A., Casetti-Dinescu, D. I., Chen, Y., Chiappini, C., Comparat, J., Connolly, N., Crepp, J. R., Cristiani, S., Croft, R. A. C., Cuesta, A. J., da Costa, L. N., Davenport, J. R. A., Dawson, K. S., de Putter, R., De Lee, N., Delubac, T., Dhital, S., Ealet, A., Ebelke, G. L., Edmondson, E. M., Eisenstein, D. J., Escoffier, S., Esposito, M., Evans, M. L., Fan, X., Femenía Castellá, B., Fernández Alvar, E., Ferreira, L. D., Filiz Ak, N., Finley, H., Fleming, S. W., Font-Ribera, A., Frinchaboy, P. M., García-Hernández, D. A., García Pérez, A. E., Ge, J., Génova-Santos, R., Gillespie, B. A., Girardi, L., González Hernández, J. I., Grebel, E. K., Gunn, J. E., Guo, H., Haggard, D., Hamilton, J.-C., Harris, D. W., Hawley, S. L., Hearty, F. R., Ho, S., Hogg, D. W., Holtzman, J. A., Honscheid, K., Huehnerhoff, J., Ivans, I. I., Ivezić, Ž., Jacobson, H. R., Jiang, L., Johansson, J., Johnson, J. A., Kauffmann, G., Kirkby, D., Kirkpatrick, J. A., Klaene, M. A., Knapp, G. R., Kneib, J.-P., Le Goff, J.-M., Leauthaud, A., Lee, K.-G., Lee, Y. S., Long, D. C., Loomis, C. P., Lucatello, S., Lundgren, B., Lupton, R. H., Ma, B., Ma, Z., MacDonald, N., Mack, C. E., Mahadevan, S., Maia, M. A. G., Majewski, S. R., Makler, M., Malanushenko, E., Malanushenko, V., Manchado, A., Mandelbaum, R., Manera, M., Maraston, C., Margala, D., Martell, S. L., McBride, C. K., McGreer, I. D., McMahon, R. G., Ménard, B., Meszaros, S., Miralda-Escudé, J., Montero-Dorta, A. D., Montesano, F., Morrison, H. L., Muna, D., Munn, J. A., Murayama, H., Myers, A. D., Neto, A. F., Nguyen, D. C., Nichol, R. C., Nidever, D. L., Noterdaeme, P., Nuza, S. E., Ogando, R. L. C., Olmstead, M. D., Oravetz, D. J., Owen, R., Padmanabhan, N., Palanque-Delabrouille, N., Pan, K., Parejko, J. K., Parihar, P., Pâris, I., Pattarakijwanich, P., Pepper, J., Percival, W. J., Pérez-Fournon, I., Pérez-Ràfols, I., Petitjean, P., Pforr, J., Pieri, M. M., Pinsonneault, M. H., Porto de Mello, G. F., Prada, F., Price-Whelan, A. M., Raddick, M. J., Rebolo, R., Rich, J., Richards, G. T., Robin, A. C., Rocha-Pinto, H. J.,

Rockosi, C. M., Roe, N. A., Ross, A. J., Ross, N. P., Rossi, G., Rubiño-Martin, J. A., Samushia, L., Sanchez Almeida, J., Sánchez, A. G., Santiago, B., Sayres, C., Schlegel, D. J., Schlesinger, K. J., Schmidt, S. J., Schneider, D. P., Schultheis, M., Schwope, A. D., Scóccola, C. G., Seljak, U., Sheldon, E., Shen, Y., Shu, Y., Simmerer, J., Simmons, A. E., Skibba, R. A., Skrutskie, M. F., Slosar, A., Sobreira, F., Sobeck, J. S., Stassun, K. G., Steele, O., Steinmetz, M., Strauss, M. A., Streblyanska, A., Suzuki, N., Swanson, M. E. C., Tal, T., Thakar, A. R., Thomas, D., Thompson, B. A., Tinker, J. L., Tojeiro, R., Tremonti, C. A., Vargas Magaña, M., Verde, L., Viel, M., Vikas, S. K., Vogt, N. P., Wake, D. A., Wang, J., Weaver, B. A., Weinberg, D. H., Weiner, B. J., West, A. A., White, M., Wilson, J. C., Wisniewski, J. P., Wood-Vasey, W. M., Yanny, B., Yèche, C., York, D. G., Zamora, O., Zasowski, G., Zehavi, I., Zhao, G.-B., Zheng, Z., Zhu, G., and Zinn, J. C. (2012). The Ninth Data Release of the Sloan Digital Sky Survey: First Spectroscopic Data from the SDSS-III Baryon Oscillation Spectroscopic Survey. *ApJS*, 203(2):21. https://ui.adsabs.harvard.edu/abs/2012ApJS..203...21A.

Alister Seguel, P. J., Schleicher, D. R. G., Boekholt, T. C. N., Fellhauer, M., and Klessen, R. S. (2020). Formation of SMBH seeds in Population III star clusters through collisions: the importance of mass loss. *MNRAS*, 493(2):2352–2362. https://ui.adsabs.harvard.edu/abs/2020MNRAS.493.2352A.

Amaro-Seoane, P., Andrews, J., Arca Sedda, M., Askar, A., Baghi, Q., Balasov, R., Bartos, I., Bavera, S. S., Bellovary, J., Berry, C. P. L., Berti, E., Bianchi, S., Blecha, L., Blondin, S., Bogdanović, T., Boissier, S., Bonetti, M., Bonoli, S., Bortolas, E., Breivik, K., Capelo, P. R., Caramete, L., Cattorini, F., Charisi, M., Chaty, S., Chen, X., Chruślińska, M., Chua, A. J. K., Church, R., Colpi, M., D'Orazio, D., Danielski, C., Davies, M. B., Dayal, P., De Rosa, A., Derdzinski, A., Destounis, K., Dotti, M., Dutan, I., Dvorkin, I., Fabj, G., Foglizzo, T., Ford, S., Fouvry, J.-B., Franchini, A., Fragos, T., Fryer, C., Gaspari, M., Gerosa, D., Graziani, L., Groot, P., Habouzit, M., Haggard, D., Haiman, Z., Han, W.-B., Istrate, A., Johansson, P. H., Khan, F. M., Kimpson, T., Kokkotas, K., Kong, A., Korol, V., Kremer, K., Kupfer, T., Lamberts, A., Larson, S., Lau, M., Liu, D., Lloyd-Ronning, N., Lodato, G., Lupi, A., Ma, C.-P., Maccarone, T., Mandel, I., Mangiagli, A., Mapelli, M., Mathis, S., Mayer, L., McGee, S., McKernan, B., Miller, M. C., Mota, D. F., Mumpower, M., Nasim, S. S., Nelemans, G., Noble, S., Pacucci, F., Panessa, F., Paschalidis, V., Pfister, H., Porquet, D., Quenby, J., Ricarte, A., Röpke, F. K., Regan, J., Rosswog, S., Ruiter, A., Ruiz, M., Runnoe, J., Schneider, R., Schnittman, J., Secunda, A., Sesana, A., Seto, N., Shao, L., Shapiro, S., Sopuerta, C., Stone, N. C., Suvorov, A., Tamanini, N., Tamfal, T., Tauris, T., Temmink, K., Tomsick, J., Toonen, S., Torres-Orjuela, A., Toscani, M., Tsokaros, A., Unal, C., Vázquez-Aceves, V., Valiante, R., van

Putten, M., van Roestel, J., Vignali, C., Volonteri, M., Wu, K., Younsi, Z., Yu, S., Zane, S., Zwick, L., Antonini, F., Baibhav, V., Barausse, E., Bonilla Rivera, A., Branchesi, M., Branduardi-Raymont, G., Burdge, K., Chakraborty, S., Cuadra, J., Dage, K., Davis, B., de Mink, S. E., Decarli, R., Doneva, D., Escoffier, S., Gandhi, P., Haardt, F., Lousto, C. O., Nissanke, S., Nordhaus, J., O'Shaughnessy, R., Portegies Zwart, S., Pound, A., Schussler, F., Sergijenko, O., Spallicci, A., Vernieri, D., and Vigna-Gómez, A. (2023). Astrophysics with the Laser Interferometer Space Antenna. *Living Reviews in Relativity*, 26(1):2. https://ui.adsabs.harvard.edu/abs/2023LRR....26....2A.

Bañados, E., Venemans, B. P., Mazzucchelli, C., Farina, E. P., Walter, F., Wang, F., Decarli, R., Stern, D., Fan, X., Davies, F. B., Hennawi, J. F., Simcoe, R. A., Turner, M. L., Rix, H.-W., Yang, J., Kelson, D. D., Rudie, G. C., and Winters, J. M. (2018). An 800-million-solar-mass black hole in a significantly neutral Universe at a redshift of 7.5. *Nature*, 553(7689):473–476. https://ui.adsabs.harvard.edu/abs/2018Natur.553..473B.

Baade, W. and Minkowski, R. (1954). Identification of the Radio Sources in Cassiopeia, Cygnus A, and Puppis A. *ApJ*, 119:206. https://ui.adsabs.harvard.edu/abs/1954ApJ...119..206B.

Barnes, J. and Hut, P. (1986). A hierarchical O(N log N) force-calculation algorithm. *Nature*, 324(6096):446–449. https://ui.adsabs.harvard.edu/abs/1986Natur.324..446B.

Bate, M. R., Bonnell, I. A., and Bromm, V. (2003). The formation of a star cluster: predicting the properties of stars and brown dwarfs. *MNRAS*, 339(3):577–599. https://ui.adsabs.harvard.edu/abs/2003MNRAS.339..577B.

Bate, M. R., Bonnell, I. A., and Price, N. M. (1995). Modelling accretion in protobinary systems. *MNRAS*, 277(2):362–376. https://ui.adsabs.harvard.edu/abs/1995MNRAS.277..362B.

Bate, M. R. and Burkert, A. (1997). Resolution requirements for smoothed particle hydrodynamics calculations with self-gravity. *MNRAS*, 288(4):1060–1072. https://ui.adsabs.harvard.edu/abs/1997MNRAS.288.1060B.

Becerra, F., Greif, T. H., Springel, V., and Hernquist, L. E. (2015). Formation of massive protostars in atomic cooling haloes. *MNRAS*, 446(3):2380–2393. https://ui.adsabs.harvard.edu/abs/2015MNRAS.446.2380B.

Becerra, F., Marinacci, F., Bromm, V., and Hernquist, L. E. (2018). Assembly of supermassive black hole seeds. *Monthly Notices of the Royal Astronomical Society*, 480(4):5029–5045. https://doi.org/10.1093/mnras/sty2210.

Becerra, F., Marinacci, F., Inayoshi, K., Bromm, V., and Hernquist, L. E. (2018). Opacity Limit for Supermassive Protostars. *ApJ*, 857(2):138. https://ui.adsabs.harvard.edu/abs/2018ApJ...857..138B.

Begelman, M. C., Rossi, E. M., and Armitage, P. J. (2008). Quasi-stars: accreting black holes inside massive envelopes. *MNRAS*, 387(4):1649–1659. https://ui.adsabs.harvard.edu/abs/2008MNRAS.387.1649B.

Belczynski, K., Bulik, T., Fryer, C. L., Ruiter, A., Valsecchi, F., Vink, J. S., and Hurley, J. R. (2010). On the Maximum Mass of Stellar Black Holes. *ApJ*, 714(2):1217–1226. https://ui.adsabs.harvard.ed/abs/2010ApJ...714.1217B.

Bennett, A. S. (1962). The revised 3C catalogue of radio sources. *Mem. RAS*, 68:163. https://ui.adsabs.harvard.edu/abs/1962MmRAS..68..163B.

Bennett, C. L., Larson, D., Weiland, J. L., Jarosik, N., Hinshaw, G., Odegard, N., Smith, K. M., Hill, R. S., Gold, B., Halpern, M., Komatsu, E., Nolta, M. R., Page, L., Spergel, D. N., Wollack, E., Dunkley, J., Kogut, A., Limon, M., Meyer, S. S., Tucker, G. S., and Wright, E. L. (2013). Nine-year Wilkinson Microwave Anisotropy Probe (WMAP) Observations: Final Maps and Results. *ApJS*, 208(2):20. https://ui.adsabs.harvard.edu/abs/2013ApJS..208...20B.

Bentz, M. C., Peterson, B. M., Netzer, H., Pogge, R. W., and Vestergaard, M. (2009). The Radius-Luminosity Relationship for Active Galactic Nuclei: The Effect of Host-Galaxy Starlight on Luminosity Measurements. II. The Full Sample of Reverberation-Mapped AGNs. *ApJ*, 697(1):160–181. https://ui.adsabs.harvard.edu/abs/2009ApJ...697..160B.

Binney, J. and Tremaine, S. (1987). *Galactic dynamics*. https://ui.adsabs.harvard.edu/abs/1987gady.book.....B.

Blandford, R. D. and McKee, C. F. (1982). Reverberation mapping of the emission line regions of Seyfert galaxies and quasars. *ApJ*, 255:419–439. https://ui.adsabs.harvard.edu/abs/1982ApJ...255..419B.

Bleuler, A. and Teyssier, R. (2014). Towards a more realistic sink particle algorithm for the RAMSES CODE. *MNRAS*, 445(4):4015–4036. https://ui.adsabs.harvard.edu/abs/2014MNRAS.445.4015B.

Boekholt, T. C. N., Schleicher, D. R. G., Fellhauer, M., Klessen, R. S., Reinoso, B., Stutz, A. M., and Haemmerlé, L. (2018). Formation of massive seed black holes via collisions and accretion. *MNRAS*, 476(1):366–380. https://ui.adsabs.harvard.edu/abs/2018MNRAS.476..366B.

Bolton, C. T. (1972). Identification of Cygnus X-1 with HDE 226868. *Nature*, 235(5336):271–273. https://ui.adsabs.harvard.edu/abs/1972Natur.235..271B.

Bonnell, I. A., Bate, M. R., and Vine, S. G. (2003). The hierarchical formation of a stellar cluster. *Monthly Notices of the Royal Astronomical Society*, 343(2):413–418. https://doi.org/10.1046/j.1365-8711.2003.06687.x.

Booth, C. M. and Schaye, J. (2009). Cosmological simulations of the growth of supermassive black holes and feedback from active galactic nuclei: method and tests. *MNRAS*, 398(1):53–74. https://ui.adsabs.harvard.edu/abs/2009MNRAS.398...53B.

Bowyer, S., Byram, E. T., Chubb, T. A., and Friedman, H. (1965). Cosmic x-ray sources. *Science*, 147(3656):394–398. http://www.jstor.org/stable/1715673.

Bromm, V., Coppi, P. S., and Larson, R. B. (1999). Forming the First Stars in the Universe: The Fragmentation of Primordial Gas. *ApJ*, 527(1):L5–L8. https://ui.adsabs.harvard.edu/abs/1999ApJ...527L...5B.

Bromm, V., Coppi, P. S., and Larson, R. B. (2002). The Formation of the First Stars. I. The Primordial Star-forming Cloud. *ApJ*, 564(1):23–51. https://ui.adsabs.harvard.edu/abs/2002ApJ...564...23B.

Bromm, V. and Loeb, A. (2003). Formation of the First Supermassive Black Holes. *ApJ*, 596(1):34–46. https://ui.adsabs.harvard.edu/abs/2003ApJ...596...34B.

Chandrasekhar, S. (1964). The Dynamical Instability of Gaseous Masses Approaching the Schwarzschild Limit in General Relativity. *ApJ*, 140:417. https://ui.adsabs.harvard.edu/abs/1964ApJ...140..417C.

Chilingarian, I. V., Katkov, I. Y., Zolotukhin, I. Y., Grishin, K. A., Beletsky, Y., Boutsia, K., and Osip, D. J. (2018). A Population of Bona Fide Intermediate-mass Black Holes Identified as Low-luminosity Active Galactic Nuclei. *ApJ*, 863(1):1. https://ui.adsabs.harvard.edu/abs/2018ApJ...863....1C.

Chiou, Y. S., Naoz, S., Marinacci, F., and Vogelsberger, M. (2018). The Supersonic Project: rotational effects of supersonic motions on the first structures in the Universe. *Monthly*

Notices of the Royal Astronomical Society, 481(3):3108–3117. `https://doi.org/10.1093/mnras/sty2480`.

Chiu, H.-Y. (1964). Gravitational Collapse. *Physics Today*, 17(5):21. `https://ui.adsabs.harvard.edu/abs/1964PhT....17e..21C`.

Chon, S., Hirano, S., Hosokawa, T., and Yoshida, N. (2016). Cosmological Simulations of Early Black Hole Formation: Halo Mergers, Tidal Disruption, and the Conditions for Direct Collapse. *ApJ*, 832(2):134. `https://ui.adsabs.harvard.edu/abs/2016ApJ...832..134C`.

Chon, S., Hosokawa, T., and Yoshida, N. (2018). Radiation hydrodynamics simulations of the formation of direct-collapse supermassive stellar systems. *MNRAS*, 475(3):4104–4121. `https://ui.adsabs.harvard.edu/abs/2018MNRAS.475.4104C`.

Chon, S. and Omukai, K. (2020). Supermassive star formation via super competitive accretion in slightly metal-enriched clouds. *MNRAS*, 494(2):2851–2860. `https://ui.adsabs.harvard.edu/abs/2020MNRAS.494.2851C`.

Clark, P. C., Glover, S. C. O., Klessen, R. S., and Bromm, V. (2011a). Gravitational Fragmentation in Turbulent Primordial Gas and the Initial Mass Function of Population III Stars. *ApJ*, 727(2):110. `https://ui.adsabs.harvard.edu/abs/2011ApJ...727..110C`.

Clark, P. C., Glover, S. C. O., Smith, R. J., Greif, T. H., Klessen, R. S., and Bromm, V. (2011b). The Formation and Fragmentation of Disks Around Primordial Protostars. *Science*, 331(6020):1040. `https://ui.adsabs.harvard.edu/abs/2011Sci...331.1040C`.

Das, A., Schleicher, D. R. G., Leigh, N. W. C., and Boekholt, T. C. N. (2021). Formation of supermassive black hole seeds in nuclear star clusters via gas accretion and runaway collisions. *MNRAS*, 503(1):1051–1069. `https://ui.adsabs.harvard.edu/abs/2021MNRAS.503.1051D`.

Di Matteo, T., Colberg, J., Springel, V., Hernquist, L., and Sijacki, D. (2008). Direct Cosmological Simulations of the Growth of Black Holes and Galaxies. *ApJ*, 676(1):33–53. `https://ui.adsabs.harvard.edu/abs/2008ApJ...676...33D`.

Dijkstra, M., Ferrara, A., and Mesinger, A. (2014). Feedback-regulated supermassive black hole seed formation. *MNRAS*, 442(3):2036–2047. `https://ui.adsabs.harvard.edu/abs/2014MNRAS.442.2036D`.

Dijkstra, M., Haiman, Z., Mesinger, A., and Wyithe, J. S. B. (2008). Fluctuations in the high-redshift Lyman-Werner background: close halo pairs as the origin of supermassive black holes. *MNRAS*, 391(4):1961–1972. https://ui.adsabs.harvard.edu/abs/2008MNRAS.391.1961D.

Dubinski, J., Narayan, R., and Phillips, T. G. (1995). Turbulence in Molecular Clouds. *ApJ*, 448:226. https://ui.adsabs.harvard.edu/abs/1995ApJ...448..226D.

Edge, D. O., Shakeshaft, J. R., McAdam, W. B., Baldwin, J. E., and Archer, S. (1959). A survey of radio sources at a frequency of 159 Mc/s. *Mem. RAS*, 68:37–60. https://ui.adsabs.harvard.edu/abs/1959MmRAS..68...37E.

Elizalde, E. (2020). *Cosmología moderna desde sus orígenes*. ISBN 978-84-1352-125-1, http://hdl.handle.net/10261/238526.

Elvis, M., Wilkes, B. J., McDowell, J. C., Green, R. F., Bechtold, J., Willner, S. P., Oey, M. S., Polomski, E., and Cutri, R. (1994). Atlas of Quasar Energy Distributions. *ApJS*, 95:1. https://ui.adsabs.harvard.edu/abs/1994ApJS...95....1E.

Escala, A. (2021). Observational Support for Massive Black Hole Formation Driven by Runaway Stellar Collisions in Galactic Nuclei. *ApJ*, 908(1):57. https://ui.adsabs.harvard.edu/abs/2021ApJ...908...57E.

Euclid Collaboration, Barnett, R., Warren, S. J., Mortlock, D. J., Cuby, J. G., Conselice, C., Hewett, P. C., Willott, C. J., Auricchio, N., Balaguera-Antolínez, A., Baldi, M., Bardelli, S., Bellagamba, F., Bender, R., Biviano, A., Bonino, D., Bozzo, E., Branchini, E., Brescia, M., Brinchmann, J., Burigana, C., Camera, S., Capobianco, V., Carbone, C., Carretero, J., Carvalho, C. S., Castander, F. J., Castellano, M., Cavuoti, S., Cimatti, A., Clédassou, R., Congedo, G., Conversi, L., Copin, Y., Corcione, L., Coupon, J., Courtois, H. M., Cropper, M., Da Silva, A., Duncan, C. A. J., Dusini, S., Ealet, A., Farrens, S., Fosalba, P., Fotopoulou, S., Fourmanoit, N., Frailis, M., Fumana, M., Galeotta, S., Garilli, B., Gillard, W., Gillis, B. R., Graciá-Carpio, J., Grupp, F., Hoekstra, H., Hormuth, F., Israel, H., Jahnke, K., Kermiche, S., Kilbinger, M., Kirkpatrick, C. C., Kitching, T., Kohley, R., Kubik, B., Kunz, M., Kurki-Suonio, H., Laureijs, R., Ligori, S., Lilje, P. B., Lloro, I., Maiorano, E., Mansutti, O., Marggraf, O., Martinet, N., Marulli, F., Massey, R., Mauri, N., Medinaceli, E., Mei, S., Mellier, Y., Metcalf, R. B., Metge, J. J., Meylan, G., Moresco, M., Moscardini, L., Munari, E., Neissner, C., Niemi, S. M., Nutma, T., Padilla, C., Paltani, S., Pasian, F., Paykari, P., Percival, W. J., Pettorino, V., Polenta, G., Poncet, M., Pozzetti, L., Raison, F., Renzi, A., Rhodes, J., Rix, H. W., Romelli, E., Roncarelli, M., Rossetti, E., Saglia, R., Sapone, D., Scaramella, R., Schneider, P., Scottez, V., Secroun, A., Serrano, S.,

Sirri, G., Stanco, L., Sureau, F., Tallada-Crespí, P., Tavagnacco, D., Taylor, A. N., Tenti, M., Tereno, I., Toledo-Moreo, R., Torradeflot, F., Valenziano, L., Vassallo, T., Wang, Y., Zacchei, A., Zamorani, G., Zoubian, J., and Zucca, E. (2019). Euclid preparation. V. Predicted yield of redshift 7 < z < 9 quasars from the wide survey. *A&A*, 631:A85. https://ui.adsabs.harvard.edu/abs/2019A&A...631A..85E.

Event Horizon Telescope Collaboration, Akiyama, K., Alberdi, A., Alef, W., Asada, K., Azulay, R., Baczko, A.-K., Ball, D., Baloković, M., Barrett, J., Bintley, D., Blackburn, L., Boland, W., Bouman, K. L., Bower, G. C., Bremer, M., Brinkerink, C. D., Brissenden, R., Britzen, S., Broderick, A. E., Broguiere, D., Bronzwaer, T., Byun, D.-Y., Carlstrom, J. E., Chael, A., Chan, C.-k., Chatterjee, S., Chatterjee, K., Chen, M.-T., Chen, Y., Cho, I., Christian, P., Conway, J. E., Cordes, J. M., Crew, G. B., Cui, Y., Davelaar, J., De Laurentis, M., Deane, R., Dempsey, J., Desvignes, G., Dexter, J., Doeleman, S. S., Eatough, R. P., Falcke, H., Fish, V. L., Fomalont, E., Fraga-Encinas, R., Freeman, W. T., Friberg, P., Fromm, C. M., Gómez, J. L., Galison, P., Gammie, C. F., García, R., Gentaz, O., Georgiev, B., Goddi, C., Gold, R., Gu, M., Gurwell, M., Hada, K., Hecht, M. H., Hesper, R., Ho, L. C., Ho, P., Honma, M., Huang, C.-W. L., Huang, L., Hughes, D. H., Ikeda, S., Inoue, M., Issaoun, S., James, D. J., Jannuzi, B. T., Janssen, M., Jeter, B., Jiang, W., Johnson, M. D., Jorstad, S., Jung, T., Karami, M., Karuppusamy, R., Kawashima, T., Keating, G. K., Kettenis, M., Kim, J.-Y., Kim, J., Kim, J., Kino, M., Koay, J. Y., Koch, P. M., Koyama, S., Kramer, M., Kramer, C., Krichbaum, T. P., Kuo, C.-Y., Lauer, T. R., Lee, S.-S., Li, Y.-R., Li, Z., Lindqvist, M., Liu, K., Liuzzo, E., Lo, W.-P., Lobanov, A. P., Loinard, L., Lonsdale, C., Lu, R.-S., MacDonald, N. R., Mao, J., Markoff, S., Marrone, D. P., Marscher, A. P., Martí-Vidal, I., Matsushita, S., Matthews, L. D., Medeiros, L., Menten, K. M., Mizuno, Y., Mizuno, I., Moran, J. M., Moriyama, K., Moscibrodzka, M., Müller, C., Nagai, H., Nagar, N. M., Nakamura, M., Narayan, R., Narayanan, G., Natarajan, I., Neri, R., Ni, C., Noutsos, A., Okino, H., Olivares, H., Ortiz-León, G. N., Oyama, T., Özel, F., Palumbo, D. C. M., Patel, N., Pen, U.-L., Pesce, D. W., Piétu, V., Plambeck, R., PopStefanija, A., Porth, O., Prather, B., Preciado-López, J. A., Psaltis, D., Pu, H.-Y., Ramakrishnan, V., Rao, R., Rawlings, M. G., Raymond, A. W., Rezzolla, L., Ripperda, B., Roelofs, F., Rogers, A., Ros, E., Rose, M., Roshanineshat, A., Rottmann, H., Roy, A. L., Ruszczyk, C., Ryan, B. R., Rygl, K. L. J., Sánchez, S., Sánchez-Arguelles, D., Sasada, M., Savolainen, T., Schloerb, F. P., Schuster, K.-F., Shao, L., Shen, Z., Small, D., Sohn, B. W., SooHoo, J., Tazaki, F., Tiede, P., Tilanus, R. P. J., Titus, M., Toma, K., Torne, P., Trent, T., Trippe, S., Tsuda, S., van Bemmel, I., van Langevelde, H. J., van Rossum, D. R., Wagner, J., Wardle, J., Weintroub, J., Wex, N., Wharton, R., Wielgus, M., Wong, G. N., Wu, Q., Young, K., Young, A., Younsi, Z., Yuan, F., Yuan, Y.-F., Zensus, J. A., Zhao, G., Zhao, S.-S., Zhu, Z., Algaba, J.-C., Allardi, A., Amestica, R., Anczarski, J., Bach, U.,

Baganoff, F. K., Beaudoin, C., Benson, B. A., Berthold, R., Blanchard, J. M., Blundell, R., Bustamente, S., Cappallo, R., Castillo-Domínguez, E., Chang, C.-C., Chang, S.-H., Chang, S.-C., Chen, C.-C., Chilson, R., Chuter, T. C., Córdova Rosado, R., Coulson, I. M., Crawford, T. M., Crowley, J., David, J., Derome, M., Dexter, M., Dornbusch, S., Dudevoir, K. A., Dzib, S. A., Eckart, A., Eckert, C., Erickson, N. R., Everett, W. B., Faber, A., Farah, J. R., Fath, V., Folkers, T. W., Forbes, D. C., Freund, R., Gómez-Ruiz, A. I., Gale, D. M., Gao, F., Geertsema, G., Graham, D. A., Greer, C. H., Grosslein, R., Gueth, F., Haggard, D., Halverson, N. W., Han, C.-C., Han, K.-C., Hao, J., Hasegawa, Y., Henning, J. W., Hernández-Gómez, A., Herrero-Illana, R., Heyminck, S., Hirota, A., Hoge, J., Huang, Y.-D., Impellizzeri, C. M. V., Jiang, H., Kamble, A., Keisler, R., Kimura, K., Kono, Y., Kubo, D., Kuroda, J., Lacasse, R., Laing, R. A., Leitch, E. M., Li, C.-T., Lin, L. C. C., Liu, C.-T., Liu, K.-Y., Lu, L.-M., Marson, R. G., Martin-Cocher, P. L., Massingill, K. D., Matulonis, C., McColl, M. P., McWhirter, S. R., Messias, H., Meyer-Zhao, Z., Michalik, D., Montaña, A., Montgomerie, W., Mora-Klein, M., Muders, D., Nadolski, A., Navarro, S., Neilsen, J., Nguyen, C. H., Nishioka, H., Norton, T., Nowak, M. A., Nystrom, G., Ogawa, H., Oshiro, P., Oyama, T., Parsons, H., Paine, S. N., Peñalver, J., Phillips, N. M., Poirier, M., Pradel, N., Primiani, R. A., Raffin, P. A., Rahlin, A. S., Reiland, G., Risacher, C., Ruiz, I., Sáez-Madaín, A. F., Sassella, R., Schellart, P., Shaw, P., Silva, K. M., Shiokawa, H., Smith, D. R., Snow, W., Souccar, K., Sousa, D., Sridharan, T. K., Srinivasan, R., Stahm, W., Stark, A. A., Story, K., Timmer, S. T., Vertatschitsch, L., Walther, C., Wei, T.-S., Whitehorn, N., Whitney, A. R., Woody, D. P., Wouterloot, J. G. A., Wright, M., Yamaguchi, P., Yu, C.-Y., Zeballos, M., Zhang, S., and Ziurys, L. (2019a). First M87 Event Horizon Telescope Results. I. The Shadow of the Supermassive Black Hole. *ApJ*, 875(1):L1. https://ui.adsabs.harvard.edu/abs/2019ApJ...875L...1E.

Event Horizon Telescope Collaboration, Akiyama, K., Alberdi, A., Alef, W., Asada, K., Azulay, R., Baczko, A.-K., Ball, D., Baloković, M., Barrett, J., Bintley, D., Blackburn, L., Boland, W., Bouman, K. L., Bower, G. C., Bremer, M., Brinkerink, C. D., Brissenden, R., Britzen, S., Broderick, A. E., Broguiere, D., Bronzwaer, T., Byun, D.-Y., Carlstrom, J. E., Chael, A., Chan, C.-k., Chatterjee, S., Chatterjee, K., Chen, M.-T., Chen, Y., Cho, I., Christian, P., Conway, J. E., Cordes, J. M., Crew, G. B., Cui, Y., Davelaar, J., De Laurentis, M., Deane, R., Dempsey, J., Desvignes, G., Dexter, J., Doeleman, S. S., Eatough, R. P., Falcke, H., Fish, V. L., Fomalont, E., Fraga-Encinas, R., Freeman, W. T., Friberg, P., Fromm, C. M., Gómez, J. L., Galison, P., Gammie, C. F., García, R., Gentaz, O., Georgiev, B., Goddi, C., Gold, R., Gu, M., Gurwell, M., Hada, K., Hecht, M. H., Hesper, R., Ho, L. C., Ho, P., Honma, M., Huang, C.-W. L., Huang, L., Hughes, D. H., Ikeda, S., Inoue, M., Issaoun, S., James, D. J., Jannuzi, B. T., Janssen, M., Jeter, B., Jiang, W., Johnson,

M. D., Jorstad, S., Jung, T., Karami, M., Karuppusamy, R., Kawashima, T., Keating, G. K., Kettenis, M., Kim, J.-Y., Kim, J., Kim, J., Kino, M., Koay, J. Y., Koch, P. M., Koyama, S., Kramer, M., Kramer, C., Krichbaum, T. P., Kuo, C.-Y., Lauer, T. R., Lee, S.-S., Li, Y.-R., Li, Z., Lindqvist, M., Liu, K., Liuzzo, E., Lo, W.-P., Lobanov, A. P., Loinard, L., Lonsdale, C., Lu, R.-S., MacDonald, N. R., Mao, J., Markoff, S., Marrone, D. P., Marscher, A. P., Martí-Vidal, I., Matsushita, S., Matthews, L. D., Medeiros, L., Menten, K. M., Mizuno, Y., Mizuno, I., Moran, J. M., Moriyama, K., Moscibrodzka, M., Müller, C., Nagai, H., Nagar, N. M., Nakamura, M., Narayan, R., Narayanan, G., Natarajan, I., Neri, R., Ni, C., Noutsos, A., Okino, H., Olivares, H., Ortiz-León, G. N., Oyama, T., Özel, F., Palumbo, D. C. M., Patel, N., Pen, U.-L., Pesce, D. W., Piétu, V., Plambeck, R., PopStefanija, A., Porth, O., Prather, B., Preciado-López, J. A., Psaltis, D., Pu, H.-Y., Ramakrishnan, V., Rao, R., Rawlings, M. G., Raymond, A. W., Rezzolla, L., Ripperda, B., Roelofs, F., Rogers, A., Ros, E., Rose, M., Roshanineshat, A., Rottmann, H., Roy, A. L., Ruszczyk, C., Ryan, B. R., Rygl, K. L. J., Sánchez, S., Sánchez-Arguelles, D., Sasada, M., Savolainen, T., Schloerb, F. P., Schuster, K.-F., Shao, L., Shen, Z., Small, D., Sohn, B. W., SooHoo, J., Tazaki, F., Tiede, P., Tilanus, R. P. J., Titus, M., Toma, K., Torne, P., Trent, T., Trippe, S., Tsuda, S., van Bemmel, I., van Langevelde, H. J., van Rossum, D. R., Wagner, J., Wardle, J., Weintroub, J., Wex, N., Wharton, R., Wielgus, M., Wong, G. N., Wu, Q., Young, K., Young, A., Younsi, Z., Yuan, F., Yuan, Y.-F., Zensus, J. A., Zhao, G., Zhao, S.-S., Zhu, Z., Algaba, J.-C., Allardi, A., Amestica, R., Anczarski, J., Bach, U., Baganoff, F. K., Beaudoin, C., Benson, B. A., Berthold, R., Blanchard, J. M., Blundell, R., Bustamente, S., Cappallo, R., Castillo-Domínguez, E., Chang, C.-C., Chang, S.-H., Chang, S.-C., Chen, C.-C., Chilson, R., Chuter, T. C., Córdova Rosado, R., Coulson, I. M., Crawford, T. M., Crowley, J., David, J., Derome, M., Dexter, M., Dornbusch, S., Dudevoir, K. A., Dzib, S. A., Eckart, A., Eckert, C., Erickson, N. R., Everett, W. B., Faber, A., Farah, J. R., Fath, V., Folkers, T. W., Forbes, D. C., Freund, R., Gómez-Ruiz, A. I., Gale, D. M., Gao, F., Geertsema, G., Graham, D. A., Greer, C. H., Grosslein, R., Gueth, F., Haggard, D., Halverson, N. W., Han, C.-C., Han, K.-C., Hao, J., Hasegawa, Y., Henning, J. W., Hernández-Gómez, A., Herrero-Illana, R., Heyminck, S., Hirota, A., Hoge, J., Huang, Y.-D., Impellizzeri, C. M. V., Jiang, H., Kamble, A., Keisler, R., Kimura, K., Kono, Y., Kubo, D., Kuroda, J., Lacasse, R., Laing, R. A., Leitch, E. M., Li, C.-T., Lin, L. C. C., Liu, C.-T., Liu, K.-Y., Lu, L.-M., Marson, R. G., Martin-Cocher, P. L., Massingill, K. D., Matulonis, C., McColl, M. P., McWhirter, S. R., Messias, H., Meyer-Zhao, Z., Michalik, D., Montaña, A., Montgomerie, W., Mora-Klein, M., Muders, D., Nadolski, A., Navarro, S., Neilsen, J., Nguyen, C. H., Nishioka, H., Norton, T., Nowak, M. A., Nystrom, G., Ogawa, H., Oshiro, P., Oyama, T., Parsons, H., Paine, S. N., Peñalver, J., Phillips, N. M., Poirier, M., Pradel, N., Primiani, R. A., Raffin, P. A., Rahlin, A. S.,

Reiland, G., Risacher, C., Ruiz, I., Sáez-Madaín, A. F., Sassella, R., Schellart, P., Shaw, P., Silva, K. M., Shiokawa, H., Smith, D. R., Snow, W., Souccar, K., Sousa, D., Sridharan, T. K., Srinivasan, R., Stahm, W., Stark, A. A., Story, K., Timmer, S. T., Vertatschitsch, L., Walther, C., Wei, T.-S., Whitehorn, N., Whitney, A. R., Woody, D. P., Wouterloot, J. G. A., Wright, M., Yamaguchi, P., Yu, C.-Y., Zeballos, M., Zhang, S., and Ziurys, L. (2019b). First M87 Event Horizon Telescope Results. I. The Shadow of the Supermassive Black Hole. *ApJ*, 875(1):L1. https://ui.adsabs.harvard.edu/abs/2019ApJ...875L...1E.

Fan, X. (2006). Evolution of high-redshift quasars. *New Astron. Rev.*, 50(9-10):665–671. https://ui.adsabs.harvard.edu/abs/2006NewAR..50..665F.

Fan, X., Bañados, E., and Simcoe, R. A. (2023). Quasars and the Intergalactic Medium at Cosmic Dawn. *ARA&A*, 61:373–426. https://ui.adsabs.harvard.edu/abs/2023ARA&A..61..373F.

Fan, X., Hennawi, J. F., Richards, G. T., Strauss, M. A., Schneider, D. P., Donley, J. L., Young, J. E., Annis, J., Lin, H., Lampeitl, H., Lupton, R. H., Gunn, J. E., Knapp, G. R., Brandt, W. N., Anderson, S., Bahcall, N. A., Brinkmann, J., Brunner, R. J., Fukugita, M., Szalay, A. S., Szokoly, G. P., and York, D. G. (2004). A Survey of z>5.7 Quasars in the Sloan Digital Sky Survey. III. Discovery of Five Additional Quasars. *AJ*, 128(2):515–522. https://ui.adsabs.harvard.edu/abs/2004AJ....128..515F.

Fan, X., Narayanan, V. K., Lupton, R. H., Strauss, M. A., Knapp, G. R., Becker, R. H., White, R. L., Pentericci, L., Leggett, S. K., Haiman, Z., Gunn, J. E., Ivezić, Ž., Schneider, D. P., Anderson, S. F., Brinkmann, J., Bahcall, N. A., Connolly, A. J., Csabai, I., Doi, M., Fukugita, M., Geballe, T., Grebel, E. K., Harbeck, D., Hennessy, G., Lamb, D. Q., Miknaitis, G., Munn, J. A., Nichol, R., Okamura, S., Pier, J. R., Prada, F., Richards, G. T., Szalay, A., and York, D. G. (2001a). A Survey of z>5.8 Quasars in the Sloan Digital Sky Survey. I. Discovery of Three New Quasars and the Spatial Density of Luminous Quasars at z~6. *AJ*, 122(6):2833–2849. https://ui.adsabs.harvard.edu/abs/2001AJ....122.2833F.

Fan, X., Narayanan, V. K., Strauss, M. A., White, R. L., Becker, R. H., Pentericci, L., and Rix, H.-W. (2002). Evolution of the Ionizing Background and the Epoch of Reionization from the Spectra of z~6 Quasars. *AJ*, 123(3):1247–1257. https://ui.adsabs.harvard.edu/abs/2002AJ....123.1247F.

Fan, X., Strauss, M. A., Schneider, D. P., Becker, R. H., White, R. L., Haiman, Z., Gregg, M., Pentericci, L., Grebel, E. K., Narayanan, V. K., Loh, Y.-S., Richards, G. T., Gunn, J. E.,

Lupton, R. H., Knapp, G. R., Ivezić, Ž., Brandt, W. N., Collinge, M., Hao, L., Harbeck, D., Prada, F., Schaye, J., Strateva, I., Zakamska, N., Anderson, S., Brinkmann, J., Bahcall, N. A., Lamb, D. Q., Okamura, S., Szalay, A., and York, D. G. (2003). A Survey of z>5.7 Quasars in the Sloan Digital Sky Survey. II. Discovery of Three Additional Quasars at z>6. *AJ*, 125(4):1649–1659. https://ui.adsabs.harvard.edu/abs/2003AJ... .125.1649F.

Fan, X., Strauss, M. A., Schneider, D. P., Gunn, J. E., Lupton, R. H., Becker, R. H., Davis, M., Newman, J. A., Richards, G. T., White, R. L., Anderson, John E., J., Annis, J., Bahcall, N. A., Brunner, R. J., Csabai, I., Hennessy, G. S., Hindsley, R. B., Fukugita, M., Kunszt, P. Z., Ivezić, Ž., Knapp, G. R., McKay, T. A., Munn, J. A., Pier, J. R., Szalay, A. S., and York, D. G. (2001b). High-Redshift Quasars Found in Sloan Digital Sky Survey Commissioning Data. IV. Luminosity Function from the Fall Equatorial Stripe Sample. *AJ*, 121(1):54–65. https://ui.adsabs.harvard.edu/abs/2001AJ....121...54F.

Fan, X., White, R. L., Davis, M., Becker, R. H., Strauss, M. A., Haiman, Z., Schneider, D. P., Gregg, M. D., Gunn, J. E., Knapp, G. R., Lupton, R. H., Anderson, John E., J., Anderson, S. F., Annis, J., Bahcall, N. A., Boroski, W. N., Brunner, R. J., Chen, B., Connolly, A. J., Csabai, I., Doi, M., Fukugita, M., Hennessy, G. S., Hindsley, R. B., Ichikawa, T., Ivezić, Ž., Loveday, J., Meiksin, A., McKay, T. A., Munn, J. A., Newberg, H. J., Nichol, R., Okamura, S., Pier, J. R., Sekiguchi, M., Shimasaku, K., Stoughton, C., Szalay, A. S., Szokoly, G. P., Thakar, A. R., Vogeley, M. S., and York, D. G. (2000). The Discovery of a Luminous Z=5.80 Quasar from the Sloan Digital Sky Survey. *AJ*, 120(3):1167–1174. https://ui.adsabs.harvard.edu/abs/2000AJ....120.1167F.

Fath, E. A. (1909). The spectra of some spiral nebulae and globular star clusters. *Lick Observatory Bulletin*, 149:71–77. https://ui.adsabs.harvard.edu/abs/1909LicOB. ..5...71F.

Federrath, C., Banerjee, R., Clark, P. C., and Klessen, R. S. (2010). Modeling Collapse and Accretion in Turbulent Gas Clouds: Implementation and Comparison of Sink Particles in AMR and SPH. *ApJ*, 713(1):269–290. https://ui.adsabs.harvard.edu/abs/ 2010ApJ...713..269F.

Ferrarese, L. and Merritt, D. (2000). A Fundamental Relation between Supermassive Black Holes and Their Host Galaxies. *ApJ*, 539(1):L9–L12. https://ui.adsabs.harvard. edu/abs/2000ApJ...539L...9F.

Freitag, M. and Benz, W. (2005). A comprehensive set of simulations of high-velocity colli-

sions between main-sequence stars. *MNRAS*, 358(4):1133–1158. https://ui.adsabs.harvard.edu/abs/2005MNRAS.358.1133F.

Freitag, M., Gürkan, M. A., and Rasio, F. A. (2006). Runaway collisions in young star clusters - II. Numerical results. *MNRAS*, 368(1):141–161. https://ui.adsabs.harvard.edu/abs/2006MNRAS.368..141F.

Fryer, C. L., Woosley, S. E., and Heger, A. (2001). Pair-Instability Supernovae, Gravity Waves, and Gamma-Ray Transients. *ApJ*, 550(1):372–382. https://ui.adsabs.harvard.edu/abs/2001ApJ...550..372F.

Fujii, M., Iwasawa, M., Funato, Y., and Makino, J. (2007). BRIDGE: A Direct-Tree Hybrid N-Body Algorithm for Fully Self-Consistent Simulations of Star Clusters and Their Parent Galaxies. *PASJ*, 59:1095. https://ui.adsabs.harvard.edu/abs/2007PASJ..59.1095F.

Fujii, M. S. and Portegies Zwart, S. (2014). The moment of core collapse in star clusters with a mass function. *MNRAS*, 439(1):1003–1014. https://ui.adsabs.harvard.edu/abs/2014MNRAS.439.1003F.

Fuller, G. M., Woosley, S. E., and Weaver, T. A. (1986). The Evolution of Radiation-dominated Stars. I. Nonrotating Supermassive Stars. *ApJ*, 307:675. https://ui.adsabs.harvard.edu/abs/1986ApJ...307..675F.

Gebhardt, K., Bender, R., Bower, G., Dressler, A., Faber, S. M., Filippenko, A. V., Green, R., Grillmair, C., Ho, L. C., Kormendy, J., Lauer, T. R., Magorrian, J., Pinkney, J., Richstone, D., and Tremaine, S. (2000). A Relationship between Nuclear Black Hole Mass and Galaxy Velocity Dispersion. *ApJ*, 539(1):L13–L16. https://ui.adsabs.harvard.edu/abs/2000ApJ...539L..13G.

Gerritsen, J. P. E. and Icke, V. (1997). Star formation in N-body simulations. I. The impact of the stellar ultraviolet radiation on star formation. *A&A*, 325:972–986. https://ui.adsabs.harvard.edu/abs/1997A&A...325..972G.

Gieles, M., Charbonnel, C., Krause, M. G. H., Hénault-Brunet, V., Agertz, O., Lamers, H. J. G. L. M., Bastian, N., Gualandris, A., Zocchi, A., and Petts, J. A. (2018). Concurrent formation of supermassive stars and globular clusters: implications for early self-enrichment. *MNRAS*, 478(2):2461–2479. https://ui.adsabs.harvard.edu/abs/2018MNRAS.478.2461G.

Gingold, R. A. and Monaghan, J. J. (1977). Smoothed particle hydrodynamics: theory and application to non-spherical stars. *MNRAS*, 181:375–389. https://ui.adsabs.harvard.edu/abs/1977MNRAS.181..375G.

Glebbeek, E., Gaburov, E., Portegies Zwart, S., and Pols, O. R. (2013). Structure and evolution of high-mass stellar mergers. *MNRAS*, 434(4):3497–3510. https://ui.adsabs.harvard.edu/abs/2013MNRAS.434.3497G.

Glover, S. (2013). The First Stars. In Wiklind, T., Mobasher, B., and Bromm, V., editors, *The First Galaxies*, volume 396 of *Astrophysics and Space Science Library*, page 103. https://ui.adsabs.harvard.edu/abs/2013ASSL..396..103G.

Glover, S. C. O. (2016). Simulating the formation of massive seed black holes in the early Universe. III: The influence of X-rays. *arXiv e-prints*, page arXiv:1610.05679. https://ui.adsabs.harvard.edu/abs/2016arXiv161005679G.

Gong, H. and Ostriker, E. C. (2013). Implementation of Sink Particles in the Athena Code. *ApJS*, 204(1):8. https://ui.adsabs.harvard.edu/abs/2013ApJS..204....8G.

Gosnell, N. M., Mathieu, R. D., Geller, A. M., Sills, A., Leigh, N., and Knigge, C. (2014). Detection of white dwarf companions to blue stragglers in the open cluster ngc 188: Direct evidence for recent mass transfer. *The Astrophysical Journal Letters*, 783(1):L8. https://dx.doi.org/10.1088/2041-8205/783/1/L8.

Gosnell, N. M., Mathieu, R. D., Geller, A. M., Sills, A., Leigh, N., and Knigge, C. (2015). Implications for the formation of blue straggler stars from hst ultraviolet observations of ngc 188*. *The Astrophysical Journal*, 814(2):163. https://dx.doi.org/10.1088/0004-637X/814/2/163.

GRAVITY Collaboration, Abuter, R., Amorim, A., Bauböck, M., Berger, J. P., Bonnet, H., Brandner, W., Clénet, Y., Coudé Du Foresto, V., de Zeeuw, P. T., Dexter, J., Duvert, G., Eckart, A., Eisenhauer, F., Förster Schreiber, N. M., Garcia, P., Gao, F., Gendron, E., Genzel, R., Gerhard, O., Gillessen, S., Habibi, M., Haubois, X., Henning, T., Hippler, S., Horrobin, M., Jiménez-Rosales, A., Jocou, L., Kervella, P., Lacour, S., Lapeyrère, V., Le Bouquin, J. B., Léna, P., Ott, T., Paumard, T., Perraut, K., Perrin, G., Pfuhl, O., Rabien, S., Rodriguez Coira, G., Rousset, G., Scheithauer, S., Sternberg, A., Straub, O., Straubmeier, C., Sturm, E., Tacconi, L. J., Vincent, F., von Fellenberg, S., Waisberg, I., Widmann, F., Wieprecht, E., Wiezorrek, E., Woillez, J., and Yazici, S. (2019). A geometric distance measurement to the Galactic center black hole with 0.3% uncertainty. *A&A*, 625:L10. https://ui.adsabs.harvard.edu/abs/2019A&A...625L..10G.

Greenhill, L. J., Jiang, D. R., Moran, J. M., Reid, M. J., Lo, K. Y., and Claussen, M. J. (1995). Detection of a Subparsec Diameter Disk in the Nucleus of NGC 4258. *ApJ*, 440:619. https://ui.adsabs.harvard.edu/abs/1995ApJ...440..619G.

Greenstein, J. L. (1963). Red-Shift of the Unusual Radio Source: 3C 48. *Nature*, 197(4872):1041–1042. https://ui.adsabs.harvard.edu/abs/1963Natur.197.1041G.

Greenstein, J. L. and Schmidt, M. (1964). The Quasi-Stellar Radio Sources 3C 48 and 3C 273. *ApJ*, 140:1. https://ui.adsabs.harvard.edu/abs/1964ApJ...140....1G.

Greif, T. H., Bromm, V., Clark, P. C., Glover, S. C. O., Smith, R. J., Klessen, R. S., Yoshida, N., and Springel, V. (2012). Formation and evolution of primordial protostellar systems. *Monthly Notices of the Royal Astronomical Society*, 424(1):399–415. https://doi.org/10.1111/j.1365-2966.2012.21212.x.

Greif, T. H., Johnson, J. L., Klessen, R. S., and Bromm, V. (2008). The first galaxies: assembly, cooling and the onset of turbulence. *MNRAS*, 387(3):1021–1036. https://ui.adsabs.harvard.edu/abs/2008MNRAS.387.1021G.

Greif, T. H., Springel, V., White, S. D. M., Glover, S. C. O., Clark, P. C., Smith, R. J., Klessen, R. S., and Bromm, V. (2011). Simulations on a Moving Mesh: The Clustered Formation of Population III Protostars. *ApJ*, 737(2):75. https://ui.adsabs.harvard.edu/abs/2011ApJ...737...75G.

Gunn, J. E. and Peterson, B. A. (1965). On the Density of Neutral Hydrogen in Intergalactic Space. *ApJ*, 142:1633–1636. https://ui.adsabs.harvard.edu/abs/1965ApJ...142.1633G.

Gürkan, M. A., Freitag, M., and Rasio, F. A. (2004). Formation of Massive Black Holes in Dense Star Clusters. I. Mass Segregation and Core Collapse. *ApJ*, 604(2):632–652. https://ui.adsabs.harvard.edu/abs/2004ApJ...604..632G.

Habouzit, M., Volonteri, M., Latif, M., Dubois, Y., and Peirani, S. (2016). On the number density of 'direct collapse' black hole seeds. *MNRAS*, 463(1):529–540. https://ui.adsabs.harvard.edu/abs/2016MNRAS.463..529H.

Haemmerlé, L., Woods, T. E., Klessen, R. S., Heger, A., and Whalen, D. J. (2018). The evolution of supermassive Population III stars. *MNRAS*, 474(2):2757–2773. https://ui.adsabs.harvard.edu/abs/2018MNRAS.474.2757H.

Hanbury Brown, R., Jennison, R. C., and Gupta, M. K. D. (1952). Apparent Angular Sizes of Discrete Radio Sources: Observations at Jodrell Bank, Manchester. *Nature*, 170(4338):1061–1063. https://ui.adsabs.harvard.edu/abs/1952Natur.170.1061H.

Hazard, C., Mackey, M. B., and Shimmins, A. J. (1963). Investigation of the Radio Source 3C 273 By The Method of Lunar Occultations. *Nature*, 197(4872):1037–1039. https://ui.adsabs.harvard.edu/abs/1963Natur.197.1037H.

Heger, A., Fryer, C. L., Woosley, S. E., Langer, N., and Hartmann, D. H. (2003). How massive single stars end their life. *The Astrophysical Journal*, 591(1):288. https://dx.doi.org/10.1086/375341.

Heger, A. and Woosley, S. E. (2010). Nucleosynthesis and Evolution of Massive Metal-free Stars. *ApJ*, 724(1):341–373. https://ui.adsabs.harvard.edu/abs/2010ApJ...724..341H.

Hernquist, L. and Katz, N. (1989). TREESPH: A Unification of SPH with the Hierarchical Tree Method. *ApJS*, 70:419. https://ui.adsabs.harvard.edu/abs/1989ApJS...70..419H.

Herrington, N. P., Whalen, D. J., and Woods, T. E. (2023). Modelling supermassive primordial stars with MESA. *MNRAS*, 521(1):463–473. https://ui.adsabs.harvard.edu/abs/2023MNRAS.521..463H.

Hey, J. S., Parsons, S. J., and Phillips, J. W. (1946). Fluctuations in Cosmic Radiation at Radio-Frequencies. *Nature*, 158(4007):234. https://ui.adsabs.harvard.edu/abs/1946Natur.158..234H.

Hirano, S., Hosokawa, T., Yoshida, N., Omukai, K., and Yorke, H. W. (2015). Primordial star formation under the influence of far ultraviolet radiation: 1540 cosmological haloes and the stellar mass distribution. *MNRAS*, 448(1):568–587. https://ui.adsabs.harvard.edu/abs/2015MNRAS.448..568H.

Hirano, S., Hosokawa, T., Yoshida, N., Umeda, H., Omukai, K., Chiaki, G., and Yorke, H. W. (2014). One Hundred First Stars: Protostellar Evolution and the Final Masses. *ApJ*, 781(2):60. https://ui.adsabs.harvard.edu/abs/2014ApJ...781...60H.

Hopkins, P. F. (2015). A new class of accurate, mesh-free hydrodynamic simulation methods. *MNRAS*, 450(1):53–110. https://ui.adsabs.harvard.edu/abs/2015MNRAS.450...53H.

Hosokawa, T., Hirano, S., Kuiper, R., Yorke, H. W., Omukai, K., and Yoshida, N. (2016). Formation of Massive Primordial Stars: Intermittent UV Feedback with Episodic Mass Accretion. *ApJ*, 824(2):119. https://ui.adsabs.harvard.edu/abs/2016ApJ...824..119H.

Hosokawa, T. and Omukai, K. (2009). Evolution of Massive Protostars with High Accretion Rates. *ApJ*, 691(1):823–846. https://ui.adsabs.harvard.edu/abs/2009ApJ...691..823H.

Hosokawa, T., Omukai, K., and Yorke, H. W. (2012). Rapidly Accreting Supergiant Protostars: Embryos of Supermassive Black Holes? *ApJ*, 756(1):93. https://ui.adsabs.harvard.edu/abs/2012ApJ...756...93H.

Hosokawa, T., Yorke, H. W., Inayoshi, K., Omukai, K., and Yoshida, N. (2013). Formation of Primordial Supermassive Stars by Rapid Mass Accretion. *ApJ*, 778(2):178. https://ui.adsabs.harvard.edu/abs/2013ApJ...778..178H.

Hoyle, F. and Fowler, W. A. (1963a). Nature of Strong Radio Sources. *Nature*, 197(4867):533–535. https://ui.adsabs.harvard.edu/abs/1963Natur.197..533H.

Hoyle, F. and Fowler, W. A. (1963b). On the nature of strong radio sources. *MNRAS*, 125:169. https://ui.adsabs.harvard.edu/abs/1963MNRAS.125..169H.

Hubbell, J. H. (2006). Electron positron pair production by photons: A historical overview. *Radiation Physics and Chemistry*, 75(6):614–623. https://ui.adsabs.harvard.edu/abs/2006RaPC...75..614H.

Hubber, D. A., Allison, R. J., Smith, R., and Goodwin, S. P. (2013a). A hybrid SPH/N-body method for star cluster simulations. *MNRAS*, 430(3):1599–1616. https://ui.adsabs.harvard.edu/abs/2013MNRAS.430.1599H.

Hubber, D. A., Batty, C. P., McLeod, A., and Whitworth, A. P. (2011). SEREN - a new SPH code for star and planet formation simulations. Algorithms and tests. *A&A*, 529:A27. https://ui.adsabs.harvard.edu/abs/2011A&A...529A..27H.

Hubber, D. A., Walch, S., and Whitworth, A. P. (2013b). An improved sink particle algorithm for SPH simulations. *MNRAS*, 430(4):3261–3275. https://ui.adsabs.harvard.edu/abs/2013MNRAS.430.3261H.

Hubble, E. P. (1926). Extragalactic nebulae. *ApJ*, 64:321–369. https://ui.adsabs.harvard.edu/abs/1926ApJ....64..321H.

Hurley, J. R., Pols, O. R., and Tout, C. A. (2000). Comprehensive analytic formulae for stellar evolution as a function of mass and metallicity. *MNRAS*, 315(3):543–569. https://ui.adsabs.harvard.edu/abs/2000MNRAS.315..543H.

Inayoshi, K. and Tanaka, T. L. (2015). The suppression of direct collapse black hole formation by soft X-ray irradiation. *MNRAS*, 450(4):4350–4363. https://ui.adsabs.harvard.edu/abs/2015MNRAS.450.4350I.

Inayoshi, K., Visbal, E., and Haiman, Z. (2020). The Assembly of the First Massive Black Holes. *ARA&A*, 58:27–97. https://ui.adsabs.harvard.edu/abs/2020ARA&A..58...27I.

Ivezić, Ž., Brandt, W. N., Fan, X., MacLeod, C. L., Richards, G. T., and Yoachim, P. (2014). Optical selection of quasars: SDSS and LSST. In Mickaelian, A. M. and Sanders, D. B., editors, *Multiwavelength AGN Surveys and Studies*, volume 304, pages 11–17. https://ui.adsabs.harvard.edu/abs/2014IAUS..304...11I.

Jaura, O., Glover, S. C. O., Wollenberg, K. M. J., Klessen, R. S., Geen, S., and Haemmerlé, L. (2022). Trapping of H II regions in Population III star formation. *MNRAS*, 512(1):116–136. https://ui.adsabs.harvard.edu/abs/2022MNRAS.512..116J.

Johnson, J. L. and Bromm, V. (2007). The aftermath of the first stars: massive black holes. *MNRAS*, 374(4):1557–1568. https://ui.adsabs.harvard.edu/abs/2007MNRAS.374.1557J.

Johnson, J. L., Greif, T. H., and Bromm, V. (2008). Occurrence of metal-free galaxies in the early Universe. *MNRAS*, 388(1):26–38. https://ui.adsabs.harvard.edu/abs/2008MNRAS.388...26J.

Johnson, J. L., Whalen, D. J., Li, H., and Holz, D. E. (2013). Supermassive Seeds for Supermassive Black Holes. *ApJ*, 771(2):116. https://ui.adsabs.harvard.edu/abs/2013ApJ...771..116J.

Kaspi, S., Smith, P. S., Netzer, H., Maoz, D., Jannuzi, B. T., and Giveon, U. (2000). Reverberation Measurements for 17 Quasars and the Size-Mass-Luminosity Relations in Active Galactic Nuclei. *ApJ*, 533(2):631–649. https://ui.adsabs.harvard.edu/abs/2000ApJ...533..631K.

Katz, H., Sijacki, D., and Haehnelt, M. G. (2015). Seeding high-redshift QSOs by collisional runaway in primordial star clusters. *MNRAS*, 451(3):2352–2369. https://ui.adsabs.harvard.edu/abs/2015MNRAS.451.2352K.

Kiepenheuer, K. O. (1950). Cosmic Rays as the Source of General Galactic Radio Emission. *Physical Review*, 79(4):738–739. https://ui.adsabs.harvard.edu/abs/1950PhRv...79..738K.

King, A. (2003). Black Holes, Galaxy Formation, and the M_{BH}-σ Relation. *ApJ*, 596(1):L27–L29. https://ui.adsabs.harvard.edu/abs/2003ApJ...596L..27K.

Kitsionas, S., Federrath, C., Klessen, R. S., Schmidt, W., Price, D. J., Dursi, L. J., Gritschneder, M., Walch, S., Piontek, R., Kim, J., Jappsen, A. K., Ciecielag, P., and Mac Low, M. M. (2009). Algorithmic comparisons of decaying, isothermal, supersonic turbulence. *A&A*, 508(1):541–560. https://ui.adsabs.harvard.edu/abs/2009A&A...508..541K.

Kitsionas, S. and Whitworth, A. P. (2002). Smoothed Particle Hydrodynamics with particle splitting, applied to self-gravitating collapse. *MNRAS*, 330(1):129–136. https://ui.adsabs.harvard.edu/abs/2002MNRAS.330..129K.

Klessen, R. S. and Glover, S. C. O. (2023). The First Stars: Formation, Properties, and Impact. *ARA&A*, 61:65–130. https://ui.adsabs.harvard.edu/abs/2023ARA&A..61...65K.

Kochanek, C. S. (1992). The Dynamical Evolution of Tidal Capture Binaries. *ApJ*, 385:604. https://ui.adsabs.harvard.edu/abs/1992ApJ...385..604K.

Kormendy, J. and Richstone, D. (1992). Evidence for a Supermassive Black Hole in NGC 3115. *ApJ*, 393:559. http://doi.org/10.1086/171528.

Kreisch, C. D., Cyr-Racine, F.-Y., and Doré, O. (2020). Neutrino puzzle: Anomalies, interactions, and cosmological tensions. *Phys. Rev. D*, 101(12):123505. https://ui.adsabs.harvard.edu/abs/2020PhRvD.101l3505K.

Kudritzki, R. P. (2002). Line-driven Winds, Ionizing Fluxes, and Ultraviolet Spectra of Hot Stars at Extremely Low Metallicity. I. Very Massive O Stars. *ApJ*, 577(1):389–408. https://ui.adsabs.harvard.edu/abs/2002ApJ...577..389K.

Kustaanheimo, P. and Stiefel, E. (1965). Perturbation theory of Kepler motion based on spinor regularization. *J. Reine Angew. Math.*, 218:204–219. https://cds.cern.ch/record/419610.

Latif, M. A., Bovino, S., Grassi, T., Schleicher, D. R. G., and Spaans, M. (2015). How realistic UV spectra and X-rays suppress the abundance of direct collapse black holes. *MNRAS*, 446(3):3163–3177. https://ui.adsabs.harvard.edu/abs/2015MNRAS.446.3163L.

Latif, M. A., Bovino, S., Van Borm, C., Grassi, T., Schleicher, D. R. G., and Spaans, M. (2014a). A UV flux constraint on the formation of direct collapse black holes. *MN-RAS*, 443(3):1979–1987. https://ui.adsabs.harvard.edu/abs/2014MNRAS.443.1979L.

Latif, M. A., Omukai, K., Habouzit, M., Schleicher, D. R. G., and Volonteri, M. (2016a). Impact of Dust Cooling on Direct-collapse Black Hole Formation. *ApJ*, 823(1):40. https://ui.adsabs.harvard.edu/abs/2016ApJ...823...40L.

Latif, M. A., Omukai, K., Habouzit, M., Schleicher, D. R. G., and Volonteri, M. (2016b). Impact of Dust Cooling on Direct-collapse Black Hole Formation. *ApJ*, 823(1):40. https://ui.adsabs.harvard.edu/abs/2016ApJ...823...40L.

Latif, M. A. and Schleicher, D. R. G. (2015). Disc fragmentation and the formation of Population III stars. *Monthly Notices of the Royal Astronomical Society*, 449(1):77–87. https://doi.org/10.1093/mnras/stu2573.

Latif, M. A., Schleicher, D. R. G., Bovino, S., Grassi, T., and Spaans, M. (2014b). The Formation of Massive Primordial Stars in the Presence of Moderate UV Backgrounds. *ApJ*, 792(1):78. https://ui.adsabs.harvard.edu/abs/2014ApJ...792...78L.

Latif, M. A., Schleicher, D. R. G., and Hartwig, T. (2016c). Witnessing the birth of a supermassive protostar. *MNRAS*, 458(1):233–241. https://ui.adsabs.harvard.edu/abs/2016MNRAS.458..233L.

Latif, M. A., Schleicher, D. R. G., and Schmidt, W. (2014c). Magnetic fields during the formation of supermassive black holes. *MNRAS*, 440(2):1551–1561. https://ui.adsabs.harvard.edu/abs/2014MNRAS.440.1551L.

Latif, M. A., Schleicher, D. R. G., Schmidt, W., and Niemeyer, J. (2013). Black hole formation in the early Universe. *MNRAS*, 433(2):1607–1618. https://ui.adsabs.harvard.edu/abs/2013MNRAS.433.1607L.

Latif, M. A., Schleicher, D. R. G., Spaans, M., and Zaroubi, S. (2011). Lyman alpha emission from the first galaxies: implications of UV backgrounds and the formation of molecules. *A&A*, 532:A66. https://ui.adsabs.harvard.edu/abs/2011A&A...532A..66L.

Latif, M. A. and Volonteri, M. (2015). Assessing inflow rates in atomic cooling haloes: implications for direct collapse black holes. *MNRAS*, 452(1):1026–1044. https://ui.adsabs.harvard.edu/abs/2015MNRAS.452.1026L.

Latif, M. A., Whalen, D., and Khochfar, S. (2022). The birth mass function of population iii stars. *The Astrophysical Journal*, 925(1):28. https://dx.doi.org/10.3847/1538-4357/ac3916.

Lawrence, A., Warren, S. J., Almaini, O., Edge, A. C., Hambly, N. C., Jameson, R. F., Lucas, P., Casali, M., Adamson, A., Dye, S., Emerson, J. P., Foucaud, S., Hewett, P., Hirst, P., Hodgkin, S. T., Irwin, M. J., Lodieu, N., McMahon, R. G., Simpson, C., Smail, I., Mortlock, D., and Folger, M. (2007). The UKIRT Infrared Deep Sky Survey (UKIDSS). *MNRAS*, 379(4):1599–1617. https://ui.adsabs.harvard.edu/abs/2007MNRAS.379.1599L.

Laycock, D. and Sills, A. (2005). Simulations of Stellar Collisions Involving Pre-Main-Sequence Stars. *ApJ*, 627(1):277–285. https://ui.adsabs.harvard.edu/abs/2005ApJ...627..277L.

Lee, H. M. (1994). *Dynamics of Dense Stellar Systems Including the Effects of Stellar Collisions*, pages 335–342. Springer Netherlands, Dordrecht. https://doi.org/10.1007/978-94-011-0752-5_41.

Lewin, W. and Goldstein, W. (2011). *For the Love of Physics: From the End of the Rainbow to the Edge Of Time - A Journey Through the Wonders of Physics*. Free Press. https://books.google.de/books?id=5vFRlAEACAAJ.

Liu, B., Sibony, Y., Meynet, G., and Bromm, V. (2021). Stellar winds and metal enrichment from fast-rotating Population III stars. *MNRAS*, 506(4):5247–5267. https://ui.adsabs.harvard.edu/abs/2021MNRAS.506.5247L.

Lo, K. Y. (2005). Mega-Masers and Galaxies. *ARA&A*, 43(1):625–676. http://doi.org/10.1146/annurev.astro.41.011802.094927.

Loeb, A. and Rasio, F. A. (1994). Collapse of Primordial Gas Clouds and the Formation of Quasar Black Holes. *ApJ*, 432:52. https://ui.adsabs.harvard.edu/abs/1994ApJ...432...52L.

Lucy, L. B. (1977). A numerical approach to the testing of the fission hypothesis. *AJ*, 82:1013–1024. https://ui.adsabs.harvard.edu/abs/1977AJ.....82.1013L.

Lupi, A., Haiman, Z., and Volonteri, M. (2021). Forming massive seed black holes in high-redshift quasar host progenitors. *MNRAS*, 503(4):5046–5060. https://ui.adsabs.harvard.edu/abs/2021MNRAS.503.5046L.

Lynden-Bell, D. and Eggleton, P. P. (1980). On the consequences of the gravothermal catastrophe. *MNRAS*, 191:483–498. https://ui.adsabs.harvard.edu/abs/1980MNRAS.191..483L.

Machida, M. N., Omukai, K., Matsumoto, T., and Inutsuka, S.-i. (2008). Conditions for the Formation of First-Star Binaries. *ApJ*, 677(2):813–827. https://ui.adsabs.harvard.edu/abs/2008ApJ...677..813M.

Madau, P., Haardt, F., and Dotti, M. (2014). Super-critical Growth of Massive Black Holes from Stellar-mass Seeds. *ApJ*, 784(2):L38. https://ui.adsabs.harvard.edu/abs/2014ApJ...784L..38M.

Martins, F., Schaerer, D., Haemmerlé, L., and Charbonnel, C. (2020). Spectral properties and detectability of supermassive stars in protoglobular clusters at high redshift. *A&A*, 633:A9. https://ui.adsabs.harvard.edu/abs/2020A&A...633A...9M.

Mayer, L. (2019). Super-Eddington accretion; flow regimes and conditions in high-z galaxies. In Latif, M. and Schleicher, D., editors, *Formation of the First Black Holes*, pages 195–222. https://ui.adsabs.harvard.edu/abs/2019ffbh.book..195M.

McConnell, N. J., Ma, C.-P., Gebhardt, K., Wright, S. A., Murphy, J. D., Lauer, T. R., Graham, J. R., and Richstone, D. O. (2011). Two ten-billion-solar-mass black holes at the centres of giant elliptical galaxies. *Nature*, 480(7376):215–218. https://ui.adsabs.harvard.edu/abs/2011Natur.480..215M.

Minkowski, R. (1960). A New Distant Cluster of Galaxies. *ApJ*, 132:908–910. https://ui.adsabs.harvard.edu/abs/1960ApJ...132..908M.

Miyoshi, M., Moran, J., Herrnstein, J., Greenhill, L., Nakai, N., Diamond, P., and Inoue, M. (1995). Evidence for a black hole from high rotation velocities in a sub-parsec region of NGC4258. *Nature*, 373(6510):127–129. https://ui.adsabs.harvard.edu/abs/1995Natur.373..127M.

Monaghan, J. J. and Lattanzio, J. C. (1985a). A refined particle method for astrophysical problems. *A&A*, 149(1):135–143. https://ui.adsabs.harvard.edu/abs/1985A&A...149..135M.

Monaghan, J. J. and Lattanzio, J. C. (1985b). A refined particle method for astrophysical problems. *A&A*, 149(1):135–143. https://ui.adsabs.harvard.edu/abs/1985A&A...149..135M.

Moran, J., Greenhill, L., Herrnstein, J., Diamond, P., Miyoshi, M., Nakai, N., and Inque, M. (1995). Probing Active Galactic Nuclei with H_2O Megamasers. *Proceedings of the National Academy of Science*, 92(25):11427–11433. https://ui.adsabs.harvard.edu/abs/1995PNAS...9211427M.

Mortlock, D. J., Warren, S. J., Venemans, B. P., Patel, M., Hewett, P. C., McMahon, R. G., Simpson, C., Theuns, T., Gonzáles-Solares, E. A., Adamson, A., Dye, S., Hambly, N. C., Hirst, P., Irwin, M. J., Kuiper, E., Lawrence, A., and Röttgering, H. J. A. (2011). A luminous quasar at a redshift of z = 7.085. *Nature*, 474(7353):616–619. https://ui.adsabs.harvard.edu/abs/2011Natur.474..616M.

Natarajan, P. (2014). Seeds to monsters: tracing the growth of black holes in the universe. *General Relativity and Gravitation*, 46:1702. https://ui.adsabs.harvard.edu/abs/2014GReGr..46.1702N.

Natarajan, P. and Volonteri, M. (2012). The mass function of black holes 1<z<4.5: comparison of models with observations. *MNRAS*, 422(3):2051–2057. https://ui.adsabs.harvard.edu/abs/2012MNRAS.422.2051N.

Nishi, R. and Susa, H. (1999). Formation and Disruption of Cosmological Low-Mass Objects. *ApJ*, 523(2):L103–L107. https://ui.adsabs.harvard.edu/abs/1999ApJ...523L.103N.

Nitadori, K. and Aarseth, S. J. (2012). Accelerating NBODY6 with graphics processing units. *MNRAS*, 424(1):545–552. https://ui.adsabs.harvard.edu/abs/2012MNRAS.424..545N.

Ohkubo, T., Nomoto, K., Umeda, H., Yoshida, N., and Tsuruta, S. (2009). Evolution of very massive population iii stars with mass accretion from pre-main sequence to collapse. *The Astrophysical Journal*, 706(2):1184. https://dx.doi.org/10.1088/0004-637X/706/2/1184.

Oke, J. B. (1963). Absolute Energy Distribution in the Optical Spectrum of 3C 273. *Nature*, 197(4872):1040–1041. https://ui.adsabs.harvard.edu/abs/1963Natur.197.1040O.

Omukai, K. (2001). Primordial Star Formation under Far-Ultraviolet Radiation. *ApJ*, 546(2):635–651. https://ui.adsabs.harvard.edu/abs/2001ApJ...546..635O.

Omukai, K., Hosokawa, T., and Yoshida, N. (2010). Low-metallicity Star Formation: Prestellar Collapse and Protostellar Accretion in the Spherical Symmetry.

ApJ, 722(2):1793–1815. https://ui.adsabs.harvard.edu/abs/2010ApJ...722.
17930.

Omukai, K., Schneider, R., and Haiman, Z. (2008). Can Supermassive Black Holes Form
in Metal-enriched High-Redshift Protogalaxies? *ApJ*, 686(2):801–814. https://ui.
adsabs.harvard.edu/abs/2008ApJ...686..8010.

Omukai, K. and Yoshii, Y. (2003). The Mass Spectrum of Metal-free Stars Resulting from
Photodissociation Feedback: A Scenario for the Formation of Low-Mass Population III
Stars. *ApJ*, 599(2):746–758. https://ui.adsabs.harvard.edu/abs/2003ApJ...
599..7460.

Oppenheimer, J. R. and Volkoff, G. M. (1939). On Massive Neutron Cores. *Physical Review*,
55(4):374–381. https://ui.adsabs.harvard.edu/abs/1939PhRv...55..3740.

Orosz, J. A., McClintock, J. E., Aufdenberg, J. P., Remillard, R. A., Reid, M. J., Narayan,
R., and Gou, L. (2011). The Mass of the Black Hole in Cygnus X-1. *ApJ*, 742(2):84.
https://ui.adsabs.harvard.edu/abs/2011ApJ...742...840.

Palla, F., Salpeter, E. E., and Stahler, S. W. (1983). Primordial star formation - The role
of molecular hydrogen. *ApJ*, 271:632–641. https://ui.adsabs.harvard.edu/abs/
1983ApJ...271..632P.

Palla, F. and Stahler, S. W. (1991). The Evolution of Intermediate-Mass Protostars. I. Ba-
sic Results. *ApJ*, 375:288. https://ui.adsabs.harvard.edu/abs/1991ApJ...375.
.288P.

Partridge, R. B. and Peebles, P. J. E. (1967). Are Young Galaxies Visible? *ApJ*, 147:868.
https://ui.adsabs.harvard.edu/abs/1967ApJ...147..868P.

Patrick, S. J., Whalen, D. J., Latif, M. A., and Elford, J. S. (2023). The collapse of atomically
cooled primordial haloes - I. High Lyman-Werner backgrounds. *MNRAS*, 522(3):3795–
3808. https://ui.adsabs.harvard.edu/abs/2023MNRAS.522.3795P.

Pelupessy, F. (2005). *Numerical studies of the interstellar medium on galactic scales*. Phd
thesis, Leiden Observatory , Faculty of Science , Leiden University. Available at https:
//hdl.handle.net/1887/619.

Perlov, D. and Vilenkin, A. (2017). *Cosmology for the Curious*. https://ui.adsabs.
harvard.edu/abs/2017cocu.book.....P.

Peterson, B. M. and Wandel, A. (1999). Keplerian Motion of Broad-Line Region Gas as Evidence for Supermassive Black Holes in Active Galactic Nuclei. *ApJ*, 521(2):L95–L98. https://ui.adsabs.harvard.edu/abs/1999ApJ...521L..95P.

Planck Collaboration, Aghanim, N., Akrami, Y., Arroja, F., Ashdown, M., Aumont, J., Baccigalupi, C., Ballardini, M., Banday, A. J., Barreiro, R. B., Bartolo, N., Basak, S., Battye, R., Benabed, K., Bernard, J. P., Bersanelli, M., Bielewicz, P., Bock, J. J., Bond, J. R., Borrill, J., Bouchet, F. R., Boulanger, F., Bucher, M., Burigana, C., Butler, R. C., Calabrese, E., Cardoso, J. F., Carron, J., Casaponsa, B., Challinor, A., Chiang, H. C., Colombo, L. P. L., Combet, C., Contreras, D., Crill, B. P., Cuttaia, F., de Bernardis, P., de Zotti, G., Delabrouille, J., Delouis, J. M., Désert, F. X., Di Valentino, E., Dickinson, C., Diego, J. M., Donzelli, S., Doré, O., Douspis, M., Ducout, A., Dupac, X., Efstathiou, G., Elsner, F., Enßlin, T. A., Eriksen, H. K., Falgarone, E., Fantaye, Y., Fergusson, J., Fernandez-Cobos, R., Finelli, F., Forastieri, F., Frailis, M., Franceschi, E., Frolov, A., Galeotta, S., Galli, S., Ganga, K., Génova-Santos, R. T., Gerbino, M., Ghosh, T., González-Nuevo, J., Górski, K. M., Gratton, S., Gruppuso, A., Gudmundsson, J. E., Hamann, J., Handley, W., Hansen, F. K., Helou, G., Herranz, D., Hildebrandt, S. R., Hivon, E., Huang, Z., Jaffe, A. H., Jones, W. C., Karakci, A., Keihänen, E., Keskitalo, R., Kiiveri, K., Kim, J., Kisner, T. S., Knox, L., Krachmalnicoff, N., Kunz, M., Kurki-Suonio, H., Lagache, G., Lamarre, J. M., Langer, M., Lasenby, A., Lattanzi, M., Lawrence, C. R., Le Jeune, M., Leahy, J. P., Lesgourgues, J., Levrier, F., Lewis, A., Liguori, M., Lilje, P. B., Lilley, M., Lindholm, V., López-Caniego, M., Lubin, P. M., Ma, Y. Z., Macías-Pérez, J. F., Maggio, G., Maino, D., Mandolesi, N., Mangilli, A., Marcos-Caballero, A., Maris, M., Martin, P. G., Martinelli, M., Martínez-González, E., Matarrese, S., Mauri, N., McEwen, J. D., Meerburg, P. D., Meinhold, P. R., Melchiorri, A., Mennella, A., Migliaccio, M., Millea, M., Mitra, S., Miville-Deschênes, M. A., Molinari, D., Moneti, A., Montier, L., Morgante, G., Moss, A., Mottet, S., Münchmeyer, M., Natoli, P., Nørgaard-Nielsen, H. U., Oxborrow, C. A., Pagano, L., Paoletti, D., Partridge, B., Patanchon, G., Pearson, T. J., Peel, M., Peiris, H. V., Perrotta, F., Pettorino, V., Piacentini, F., Polastri, L., Polenta, G., Puget, J. L., Rachen, J. P., Reinecke, M., Remazeilles, M., Renault, C., Renzi, A., Rocha, G., Rosset, C., Roudier, G., Rubiño-Martín, J. A., Ruiz-Granados, B., Salvati, L., Sandri, M., Savelainen, M., Scott, D., Shellard, E. P. S., Shiraishi, M., Sirignano, C., Sirri, G., Spencer, L. D., Sunyaev, R., Suur-Uski, A. S., Tauber, J. A., Tavagnacco, D., Tenti, M., Terenzi, L., Toffolatti, L., Tomasi, M., Trombetti, T., Valiviita, J., Van Tent, B., Vibert, L., Vielva, P., Villa, F., Vittorio, N., Wandelt, B. D., Wehus, I. K., White, M., White, S. D. M., Zacchei, A., and Zonca, A. (2020). Planck 2018 results. I. Overview and the cosmological legacy of Planck. *A&A*, 641:A1. https://ui.adsabs.harvard.edu/abs/2020A&A...641A...1P.

Plummer, H. C. (1911). On the problem of distribution in globular star clusters. *MNRAS*, 71:460–470. https://ui.adsabs.harvard.edu/abs/1911MNRAS..71..460P.

Polak, B., Mac Low, M.-M., Klessen, R. S., Teh, J. W., Cournoyer-Cloutier, C., Andersson, E. P., Appel, S. M., Tran, A., Lewis, S. C., Wilhelm, M. J. C., Portegies Zwart, S., Glover, S. C. O., Wang, L., and McMillan, S. L. W. (2023). Massive Star Cluster Formation I. High Star Formation Efficiency While Resolving Feedback of Individual Stars. *arXiv e-prints*, page arXiv:2312.06509. https://ui.adsabs.harvard.edu/abs/2023arXiv231206509P.

Portegies Zwart, S. and McMillan, S. (2018). *Astrophysical Recipes; The art of AMUSE*. https://ui.adsabs.harvard.edu/abs/2018araa.book.....P.

Portegies Zwart, S. F., Baumgardt, H., Hut, P., Makino, J., and McMillan, S. L. W. (2004). Formation of massive black holes through runaway collisions in dense young star clusters. *Nature*, 428(6984):724–726. https://ui.adsabs.harvard.edu/abs/2004Natur.428..724P.

Portegies Zwart, S. F., Makino, J., McMillan, S. L. W., and Hut, P. (1999). Star cluster ecology. III. Runaway collisions in young compact star clusters. *A&A*, 348:117–126. https://ui.adsabs.harvard.edu/abs/1999A&A...348..117P.

Portegies Zwart, S. F. and McMillan, S. L. W. (2002). The Runaway Growth of Intermediate-Mass Black Holes in Dense Star Clusters. *ApJ*, 576(2):899–907. https://ui.adsabs.harvard.edu/abs/2002ApJ...576..899P.

Portegies Zwart, S. F. and van den Heuvel, E. P. J. (2007). A runaway collision in a young star cluster as the origin of the brightest supernova. *Nature*, 450(7168):388–389. https://ui.adsabs.harvard.edu/abs/2007Natur.450..388P.

Press, W. H. and Schechter, P. (1974). Formation of Galaxies and Clusters of Galaxies by Self-Similar Gravitational Condensation. *ApJ*, 187:425–438. https://ui.adsabs.harvard.edu/abs/1974ApJ...187..425P.

Price, D. J., Federrath, C., and Brunt, C. M. (2011). The Density Variance-Mach Number Relation in Supersonic, Isothermal Turbulence. *ApJ*, 727(1):L21. https://ui.adsabs.harvard.edu/abs/2011ApJ...727L..21P.

Price, D. J. and Monaghan, J. J. (2007). An energy-conserving formalism for adaptive gravitational force softening in smoothed particle hydrodynamics and N-body codes. *MNRAS*, 374(4):1347–1358. https://ui.adsabs.harvard.edu/abs/2007MNRAS.374.1347P.

Price, D. J., Wurster, J., Tricco, T. S., Nixon, C., Toupin, S., Pettitt, A., Chan, C., Mentiplay, D., Laibe, G., Glover, S., Dobbs, C., Nealon, R., Liptai, D., Worpel, H., Bonnerot, C., Dipierro, G., Ballabio, G., Ragusa, E., Federrath, C., Iaconi, R., Reichardt, T., Forgan, D., Hutchison, M., Constantino, T., Ayliffe, B., Hirsh, K., and Lodato, G. (2018). Phantom: A Smoothed Particle Hydrodynamics and Magnetohydrodynamics Code for Astrophysics. *Publ. Astron. Soc. Australia*, 35:e031. https://ui.adsabs.harvard.edu/abs/2018PASA...35...31P.

Prieto, J., Jimenez, R., and Haiman, Z. (2013). Gas infall into atomic cooling haloes: on the formation of protogalactic discs and supermassive black holes at $z > 10$. *Monthly Notices of the Royal Astronomical Society*, 436(3):2301–2325. https://doi.org/10.1093/mnras/stt1730.

Prieto, J., Padoan, P., Jimenez, R., and Infante, L. (2011). Population III Stars from Turbulent Fragmentation at Redshift ∼11. *ApJ*, 731(2):L38. https://ui.adsabs.harvard.edu/abs/2011ApJ...731L..38P.

Prole, L. R., Clark, P. C., Klessen, R. S., Glover, S. C. O., and Pakmor, R. (2022). Primordial magnetic fields in Population III star formation: a magnetized resolution study. *MNRAS*, 516(2):2223–2234. https://ui.adsabs.harvard.edu/abs/2022MNRAS.516.2223P.

Reber, G. (1944). Cosmic Static. *ApJ*, 100:279. https://ui.adsabs.harvard.edu/abs/1944ApJ...100..279R.

Reed, S. L., McMahon, R. G., Martini, P., Banerji, M., Auger, M., Hewett, P. C., Koposov, S. E., Gibbons, S. L. J., Gonzalez-Solares, E., Ostrovski, F., Tie, S. S., Abdalla, F. B., Allam, S., Benoit-Lévy, A., Bertin, E., Brooks, D., Buckley-Geer, E., Burke, D. L., Carnero Rosell, A., Carrasco Kind, M., Carretero, J., da Costa, L. N., DePoy, D. L., Desai, S., Diehl, H. T., Doel, P., Evrard, A. E., Finley, D. A., Flaugher, B., Fosalba, P., Frieman, J., García-Bellido, J., Gaztanaga, E., Goldstein, D. A., Gruen, D., Gruendl, R. A., Gutierrez, G., James, D. J., Kuehn, K., Kuropatkin, N., Lahav, O., Lima, M., Maia, M. A. G., Marshall, J. L., Melchior, P., Miller, C. J., Miquel, R., Nord, B., Ogando, R., Plazas, A. A., Romer, A. K., Sanchez, E., Scarpine, V., Schubnell, M., Sevilla-Noarbe, I., Smith, R. C., Sobreira, F., Suchyta, E., Swanson, M. E. C., Tarle, G., Tucker, D. L., Walker, A. R., and Wester, W. (2017). Eight new luminous $z \geq 6$ quasars discovered via SED model fitting of VISTA, WISE and Dark Energy Survey Year 1 observations. *MNRAS*, 468(4):4702–4718. https://ui.adsabs.harvard.edu/abs/2017MNRAS.468.4702R.

Rees, M. J. (1984). Black Hole Models for Active Galactic Nuclei. *ARA&A*, 22:471–506. https://ui.adsabs.harvard.edu/abs/1984ARA&A..22..471R.

Regan, J., Wise, J. H., O'Shea, B. W., and Norman, M. L. (2020). The emergence of the first star-free atomic cooling haloes in the universe. *Monthly Notices of the Royal Astronomical Society*, 492(2):3021–3031. https://mural.maynoothuniversity.ie/14852/.

Regan, J. A., Downes, T. P., Volonteri, M., Beckmann, R., Lupi, A., Trebitsch, M., and Dubois, Y. (2019). Super-Eddington accretion and feedback from the first massive seed black holes. *Monthly Notices of the Royal Astronomical Society*, 486(3):3892–3906. https://doi.org/10.1093/mnras/stz1045.

Regan, J. A. and Haehnelt, M. G. (2009a). Pathways to massive black holes and compact star clusters in pre-galactic dark matter haloes with virial temperatures $>_\sim$10000K. *MNRAS*, 396(1):343–353. https://ui.adsabs.harvard.edu/abs/2009MNRAS.396..343R.

Regan, J. A. and Haehnelt, M. G. (2009b). The formation of compact massive self-gravitating discs in metal-free haloes with virial temperatures of $\sim$13000-30000K. *MNRAS*, 393(3):858–871. https://ui.adsabs.harvard.edu/abs/2009MNRAS.393..858R.

Regan, J. A., Johansson, P. H., and Wise, J. H. (2014). The direct collapse of a massive black hole seed under the influence of an anisotropic lyman–werner source. *The Astrophysical Journal*, 795(2):137. https://dx.doi.org/10.1088/0004-637X/795/2/137.

Regan, J. A., Visbal, E., Wise, J. H., Haiman, Z., Johansson, P. H., and Bryan, G. L. (2017). Rapid formation of massive black holes in close proximity to embryonic protogalaxies. *Nature Astronomy*, 1:0075. https://ui.adsabs.harvard.edu/abs/2017NatAs...1E..75R.

Regan, J. A., Wise, J. H., O'Shea, B. W., and Norman, M. L. (2020). The emergence of the first star-free atomic cooling haloes in the Universe. *MNRAS*, 492(2):3021–3031. https://ui.adsabs.harvard.edu/abs/2020MNRAS.492.3021R.

Reid, M. J. (2002). Masers, from protostars to black holes: conference summary. In Migenes, V. and Reid, M. J., editors, *Cosmic Masers: From Proto-Stars to Black Holes*, volume 206, page 506. https://ui.adsabs.harvard.edu/abs/2002IAUS..206..506R.

Reid, M. J. and Moran, J. M. (1981). Masers. *ARA&A*, 19:231–276. https://ui.adsabs.harvard.edu/abs/1981ARA&A..19..231R.

Reinoso, B., Schleicher, D. R. G., Fellhauer, M., Klessen, R. S., and Boekholt, T. C. N. (2018). Collisions in primordial star clusters. Formation pathway for intermediate mass black holes. *A&A*, 614:A14. https://ui.adsabs.harvard.edu/abs/2018A&A... 614A..14R.

Rezzolla, L., Most, E. R., and Weih, L. R. (2018). Using Gravitational-wave Observations and Quasi-universal Relations to Constrain the Maximum Mass of Neutron Stars. *ApJ*, 852(2):L25. https://ui.adsabs.harvard.edu/abs/2018ApJ...852L..25R.

Riaz, R., Bovino, S., Vanaverbeke, S., and Schleicher, D. R. G. (2018). The formation of protostellar binaries in primordial minihaloes. *MNRAS*, 479(1):667–686. https://ui.adsabs.harvard.edu/abs/2018MNRAS.479..667R.

Riaz, R., Schleicher, D. R. G., Bovino, S., Vanaverbeke, S., and Klessen, R. S. (2023). Formation of metal-free binaries: Impact of H_2 line cooling and CIE cooling. *MNRAS*, 518(4):4895–4908. https://ui.adsabs.harvard.edu/abs/2023MNRAS.518. 4895R.

Riess, A. G., Anand, G. S., Yuan, W., Casertano, S., Dolphin, A., Macri, L. M., Breuval, L., Scolnic, D., Perrin, M., and Anderson, R. I. (2023). Crowded No More: The Accuracy of the Hubble Constant Tested with High-resolution Observations of Cepheids by JWST. *ApJ*, 956(1):L18. https://ui.adsabs.harvard.edu/abs/2023ApJ...956L..18R.

Riess, A. G., Casertano, S., Yuan, W., Macri, L. M., and Scolnic, D. (2019). Large Magellanic Cloud Cepheid Standards Provide a 1% Foundation for the Determination of the Hubble Constant and Stronger Evidence for Physics beyond ΛCDM. *ApJ*, 876(1):85. https://ui.adsabs.harvard.edu/abs/2019ApJ...876...85R.

Riess, A. G., Filippenko, A. V., Challis, P., Clocchiatti, A., Diercks, A., Garnavich, P. M., Gilliland, R. L., Hogan, C. J., Jha, S., Kirshner, R. P., Leibundgut, B., Phillips, M. M., Reiss, D., Schmidt, B. P., Schommer, R. A., Smith, R. C., Spyromilio, J., Stubbs, C., Suntzeff, N. B., and Tonry, J. (1998). Observational Evidence from Supernovae for an Accelerating Universe and a Cosmological Constant. *AJ*, 116(3):1009–1038. https://ui.adsabs.harvard.edu/abs/1998AJ....116.1009R.

Rothschild, R. E., Boldt, E. A., Holt, S. S., and Serlemitsos, P. J. (1974). Millisecond Temporal Structure in Cygnus X-1. *ApJ*, 189:L13. https://ui.adsabs.harvard. edu/abs/1974ApJ...189L..13R.

Safranek-Shrader, C., Agarwal, M., Federrath, C., Dubey, A., Milosavljević, M., and Bromm, V. (2012). Star formation in the first galaxies - I. Collapse delayed by Lyman-

Werner radiation. *MNRAS*, 426(2):1159–1177. https://ui.adsabs.harvard.edu/abs/2012MNRAS.426.1159S.

Sakurai, Y., Hosokawa, T., Yoshida, N., and Yorke, H. W. (2015). Formation of primordial supermassive stars by burst accretion. *MNRAS*, 452(1):755–764. https://ui.adsabs.harvard.edu/abs/2015MNRAS.452..755S.

Sakurai, Y., Yoshida, N., and Fujii, M. S. (2019). Growth of intermediate mass black holes by tidal disruption events in the first star clusters. *MNRAS*, 484(4):4665–4677. https://ui.adsabs.harvard.edu/abs/2019MNRAS.484.4665S.

Sakurai, Y., Yoshida, N., Fujii, M. S., and Hirano, S. (2017). Formation of intermediate-mass black holes through runaway collisions in the first star clusters. *MNRAS*, 472(2):1677–1684. https://ui.adsabs.harvard.edu/abs/2017MNRAS.472.1677S.

Sana, H., de Mink, S. E., de Koter, A., Langer, N., Evans, C. J., Gieles, M., Gosset, E., Izzard, R. G., Le Bouquin, J. B., and Schneider, F. R. N. (2012). Binary Interaction Dominates the Evolution of Massive Stars. *Science*, 337(6093):444. https://ui.adsabs.harvard.edu/abs/2012Sci...337..444S.

Sandage, A. (1965). The Existence of a Major New Constituent of the Universe: the Quasistellar Galaxies. *ApJ*, 141:1560. https://ui.adsabs.harvard.edu/abs/1965ApJ...141.1560S.

Sandage, A., Véron, P., and Wyndham, J. D. (1965). Optical Identification of New Quasi-Stellar Radio Sources. *ApJ*, 142:1307–1311. https://ui.adsabs.harvard.edu/abs/1965ApJ...142.1307S.

Santoliquido, F., Mapelli, M., Iorio, G., Costa, G., Glover, S. C. O., Hartwig, T., Klessen, R. S., and Merli, L. (2023). Binary black hole mergers from population III stars: uncertainties from star formation and binary star properties. *MNRAS*, 524(1):307–324. https://ui.adsabs.harvard.edu/abs/2023MNRAS.524..307S.

Schauer, A. T. P., Glover, S. C. O., Klessen, R. S., and Ceverino, D. (2019). The influence of streaming velocities on the formation of the first stars. *MNRAS*, 484(3):3510–3521. https://ui.adsabs.harvard.edu/abs/2019MNRAS.484.3510S.

Scheuer, P. A. G. (1965). A Sensitive Test for the Presence of Atomic Hydrogen in Intergalactic Space. *Nature*, 207(5000):963. https://ui.adsabs.harvard.edu/abs/1965Natur.207..963S.

Schlaufman, K. C., Thompson, I. B., and Casey, A. R. (2018). An Ultra Metal-poor Star Near the Hydrogen-burning Limit. *ApJ*, 867(2):98. https://ui.adsabs.harvard.edu/abs/2018ApJ...867...98S.

Schleicher, D. R. G., Palla, F., Ferrara, A., Galli, D., and Latif, M. (2013). Massive black hole factories: Supermassive and quasi-star formation in primordial halos. *A&A*, 558:A59. https://ui.adsabs.harvard.edu/abs/2013A&A...558A..59S.

Schleicher, D. R. G., Spaans, M., and Glover, S. C. O. (2010). Black Hole Formation in Primordial Galaxies: Chemical and Radiative Conditions. *ApJ*, 712(1):L69–L72. https://ui.adsabs.harvard.edu/abs/2010ApJ...712L..69S.

Schmidt, M. (1963). 3C 273 : A Star-Like Object with Large Red-Shift. *Nature*, 197(4872):1040. https://ui.adsabs.harvard.edu/abs/1963Natur.197.1040S.

Schmidt, M. and Matthews, T. A. (1964). Redshift of the Quasi-Stellar Radio Sources 3c 47 and 3c 147. *ApJ*, 139:781. https://ui.adsabs.harvard.edu/abs/1964ApJ...139..781S.

Schneider, F. R. N., Izzard, R. G., Langer, N., and de Mink, S. E. (2015). Evolution of Mass Functions of Coeval Stars through Wind Mass Loss and Binary Interactions. *ApJ*, 805(1):20. https://ui.adsabs.harvard.edu/abs/2015ApJ...805...20S.

Schneider, F. R. N., Podsiadlowski, P., Langer, N., Castro, N., and Fossati, L. (2016). Rejuvenation of stellar mergers and the origin of magnetic fields in massive stars. *MNRAS*, 457(3):2355–2365. https://ui.adsabs.harvard.edu/abs/2016MNRAS.457.2355S.

Schwarzschild, K. (1916). Über das Gravitationsfeld eines Massenpunktes nach der Einsteinschen Theorie. *Sitzungsberichte der Königlich Preussischen Akademie der Wissenschaften*, pages 189–196. https://ui.adsabs.harvard.edu/abs/1916SPAW.......189S.

Seyfert, C. K. (1943). Nuclear Emission in Spiral Nebulae. *ApJ*, 97:28. https://ui.adsabs.harvard.edu/abs/1943ApJ....97...28S.

Shakura, N. I. and Sunyaev, R. A. (1973). Reprint of 1973A&A....24..337S. Black holes in binary systems. Observational appearance. *A&A*, 500:33–51. https://ui.adsabs.harvard.edu/abs/1973A&A....24..337S.

Shang, C., Bryan, G. L., and Haiman, Z. (2010). Supermassive black hole formation by direct collapse: keeping protogalactic gas H_2 free in dark matter haloes with virial temper-

atures T$_{vir}$ > rsim 10^4 K. *MNRAS*, 402(2):1249–1262. https://ui.adsabs.harvard.edu/abs/2010MNRAS.402.1249S.

Shankar, F., Salucci, P., Granato, G. L., De Zotti, G., and Danese, L. (2004). Supermassive black hole demography: the match between the local and accreted mass functions. *MNRAS*, 354(4):1020–1030. https://ui.adsabs.harvard.edu/abs/2004MNRAS.354.1020S.

Sharda, P., Federrath, C., and Krumholz, M. R. (2020). The importance of magnetic fields for the initial mass function of the first stars. *MNRAS*, 497(1):336–351. https://ui.adsabs.harvard.edu/abs/2020MNRAS.497..336S.

Sharda, P., Federrath, C., Krumholz, M. R., and Schleicher, D. R. G. (2021). Magnetic field amplification in accretion discs around the first stars: implications for the primordial IMF. *MNRAS*, 503(2):2014–2032. https://ui.adsabs.harvard.edu/abs/2021MNRAS.503.2014S.

Shen, Y. and Liu, X. (2012). Comparing Single-epoch Virial Black Hole Mass Estimators for Luminous Quasars. *ApJ*, 753(2):125. https://ui.adsabs.harvard.edu/abs/2012ApJ...753..125S.

Shields, G. A. (1999). A Brief History of Active Galactic Nuclei. *PASP*, 111(760):661–678. https://ui.adsabs.harvard.edu/abs/1999PASP..111..661S.

Silk, J. and Rees, M. J. (1998). Quasars and galaxy formation. *A&A*, 331:L1–L4. https://ui.adsabs.harvard.edu/abs/1998A&A...331L...1S.

Skrutskie, M. F., Schneider, S. E., Stiening, R., Strom, S. E., Weinberg, M. D., Beichman, C., Chester, T., Cutri, R., Lonsdale, C., Elias, J., Elston, R., Capps, R., Carpenter, J., Huchra, J., Liebert, J., Monet, D., Price, S., and Seitzer, P. (1997). The Two Micron All Sky Survey (2MASS): Overview and Status. In Garzon, F., Epchtein, N., Omont, A., Burton, B., and Persi, P., editors, *The Impact of Large Scale Near-IR Sky Surveys*, volume 210 of *Astrophysics and Space Science Library*, page 25. https://ui.adsabs.harvard.edu/abs/1997ASSL..210...25S.

Slipher, V. M. (1917). The spectrum and velocity of the nebula N.G.C. 1068 (M 77). *Lowell Observatory Bulletin*, 3:59–62. https://ui.adsabs.harvard.edu/abs/1917LowOB...3...59S.

Smith, A., Bromm, V., and Loeb, A. (2017). The first supermassive black holes. *Astronomy and Geophysics*, 58(3):3.22–3.26. https://ui.adsabs.harvard.edu/abs/2017A&G...58c3.22S.

Smith, B. D., Regan, J. A., Downes, T. P., Norman, M. L., O'Shea, B. W., and Wise, J. H. (2018). The growth of black holes from Population III remnants in the Renaissance simulations. *MNRAS*, 480(3):3762–3773. https://ui.adsabs.harvard.edu/abs/ 2018MNRAS.480.3762S.

Smith, R. J., Glover, S. C. O., Clark, P. C., Greif, T., and Klessen, R. S. (2011). The effects of accretion luminosity upon fragmentation in the early universe. *MNRAS*, 414(4):3633– 3644. https://ui.adsabs.harvard.edu/abs/2011MNRAS.414.3633S.

Soltan, A. (1982). Masses of quasars. *MNRAS*, 200:115–122. https://ui.adsabs. harvard.edu/abs/1982MNRAS.200..115S.

Spera, M. and Mapelli, M. (2017). Very massive stars, pair-instability supernovae and intermediate-mass black holes with the sevn code. *MNRAS*, 470(4):4739–4749. https: //doi.org/10.1093/mnras/stx1576.

Spera, M., Mapelli, M., and Bressan, A. (2015). The mass spectrum of compact remnants from the PARSEC stellar evolution tracks. *MNRAS*, 451(4):4086–4103. https://ui. adsabs.harvard.edu/abs/2015MNRAS.451.4086S.

Spitzer, L. (1987). *Dynamical evolution of globular clusters*. https://ui.adsabs. harvard.edu/abs/1987degc.book.....S.

Springel, V. (2005a). The cosmological simulation code GADGET-2. *MN-RAS*, 364(4):1105–1134. https://ui.adsabs.harvard.edu/abs/2005MNRAS.364. 1105S.

Springel, V. (2005b). The cosmological simulation code GADGET-2. *MN-RAS*, 364(4):1105–1134. https://ui.adsabs.harvard.edu/abs/2005MNRAS.364. 1105S.

Springel, V., White, S. D. M., Jenkins, A., Frenk, C. S., Yoshida, N., Gao, L., Navarro, J., Thacker, R., Croton, D., Helly, J., Peacock, J. A., Cole, S., Thomas, P., Couchman, H., Evrard, A., Colberg, J., and Pearce, F. (2005). Simulations of the formation, evolution and clustering of galaxies and quasars. *Nature*, 435(7042):629–636. https://ui.adsabs. harvard.edu/abs/2005Natur.435..629S.

Spurzem, R. and Kamlah, A. (2023). Computational methods for collisional stellar systems. *Living Reviews in Computational Astrophysics*, 9(1):3. https://ui.adsabs.harvard. edu/abs/2023LRCA....9....3S.

Stacy, A. and Bromm, V. (2013). Constraining the statistics of Population III binaries. *MN-RAS*, 433(2):1094–1107. https://ui.adsabs.harvard.edu/abs/2013MNRAS.433.1094S.

Stacy, A., Bromm, V., and Lee, A. T. (2016). Building up the Population III initial mass function from cosmological initial conditions. *MNRAS*, 462(2):1307–1328. https://ui.adsabs.harvard.edu/abs/2016MNRAS.462.1307S.

Stahler, S. W., Palla, F., and Salpeter, E. E. (1986). Primordial Stellar Evolution: The Protostar Phase. *ApJ*, 302:590. https://ui.adsabs.harvard.edu/abs/1986ApJ...302..590S.

Stecher, T. P. and Williams, D. A. (1967). Photodestruction of Hydrogen Molecules in H I Regions. *ApJ*, 149:L29. https://ui.adsabs.harvard.edu/abs/1967ApJ...149L..29S.

Suazo, M., Prieto, J., Escala, A., and Schleicher, D. R. G. (2019). The Role of Gas Fragmentation During the Formation of Supermassive Black Holes. *ApJ*, 885(2):127. https://ui.adsabs.harvard.edu/abs/2019ApJ...885..127S.

Sugimura, K., Matsumoto, T., Hosokawa, T., Hirano, S., and Omukai, K. (2020). The Birth of a Massive First-star Binary. *ApJ*, 892(1):L14. https://ui.adsabs.harvard.edu/abs/2020ApJ...892L..14S.

Susa, H., Hasegawa, K., and Tominaga, N. (2014). The Mass Spectrum of the First Stars. *ApJ*, 792(1):32. https://ui.adsabs.harvard.edu/abs/2014ApJ...792...32S.

Tagawa, H., Haiman, Z., and Kocsis, B. (2020). Making a Supermassive Star by Stellar Bombardment. *ApJ*, 892(1):36. https://ui.adsabs.harvard.edu/abs/2020ApJ...892...36T.

Tanabashi, M., Hagiwara, K., Hikasa, K., Nakamura, K., Sumino, Y., Takahashi, F., Tanaka, J., Agashe, K., Aielli, G., Amsler, C., Antonelli, M., Asner, D. M., Baer, H., Banerjee, S., Barnett, R. M., Basaglia, T., Bauer, C. W., Beatty, J. J., Belousov, V. I., Beringer, J., Bethke, S., Bettini, A., Bichsel, H., Biebel, O., Black, K. M., Blucher, E., Buch-muller, O., Burkert, V., Bychkov, M. A., Cahn, R. N., Carena, M., Ceccucci, A., Cerri, A., Chakraborty, D., Chen, M.-C., Chivukula, R. S., Cowan, G., Dahl, O., D'Ambrosio, G., Damour, T., de Florian, D., de Gouvêa, A., DeGrand, T., de Jong, P., Dissertori, G., Dobrescu, B. A., D'Onofrio, M., Doser, M., Drees, M., Dreiner, H. K., Dwyer, D. A., Eerola, P., Eidelman, S., Ellis, J., Erler, J., Ezhela, V. V., Fetscher, W., Fields, B. D., Firestone, R., Foster, B., Freitas, A., Gallagher, H., Garren, L., Gerber, H.-J., Gerbier,

G., Gershon, T., Gershtein, Y., Gherghetta, T., Godizov, A. A., Goodman, M., Grab, C., Gritsan, A. V., Grojean, C., Groom, D. E., Grünewald, M., Gurtu, A., Gutsche, T., Haber, H. E., Hanhart, C., Hashimoto, S., Hayato, Y., Hayes, K. G., Hebecker, A., Heinemeyer, S., Heltsley, B., Hernández-Rey, J. J., Hisano, J., Höcker, A., Holder, J., Holtkamp, A., Hyodo, T., Irwin, K. D., Johnson, K. F., Kado, M., Karliner, M., Katz, U. F., Klein, S. R., Klempt, E., Kowalewski, R. V., Krauss, F., Kreps, M., Krusche, B., Kuyanov, Y. V., Kwon, Y., Lahav, O., Laiho, J., Lesgourgues, J., Liddle, A., Ligeti, Z., Lin, C.-J., Lippmann, C., Liss, T. M., Littenberg, L., Lugovsky, K. S., Lugovsky, S. B., Lusiani, A., Makida, Y., Maltoni, F., Mannel, T., Manohar, A. V., Marciano, W. J., Martin, A. D., Masoni, A., Matthews, J., Meißner, U.-G., Milstead, D., Mitchell, R. E., Mönig, K., Molaro, P., Moortgat, F., Moskovic, M., Murayama, H., Narain, M., Nason, P., Navas, S., Neubert, M., Nevski, P., Nir, Y., Olive, K. A., Pagan Griso, S., Parsons, J., Patrignani, C., Peacock, J. A., Pennington, M., Petcov, S. T., Petrov, V. A., Pianori, E., Piepke, A., Pomarol, A., Quadt, A., Rademacker, J., Raffelt, G., Ratcliff, B. N., Richardson, P., Ringwald, A., Roesler, S., Rolli, S., Romaniouk, A., Rosenberg, L. J., Rosner, J. L., Rybka, G., Ryutin, R. A., Sachrajda, C. T., Sakai, Y., Salam, G. P., Sarkar, S., Sauli, F., Schneider, O., Scholberg, K., Schwartz, A. J., Scott, D., Sharma, V., Sharpe, S. R., Shutt, T., Silari, M., Sjöstrand, T., Skands, P., Skwarnicki, T., Smith, J. G., Smoot, G. F., Spanier, S., Spieler, H., Spiering, C., Stahl, A., Stone, S. L., Sumiyoshi, T., Syphers, M. J., Terashi, K., Terning, J., Thoma, U., Thorne, R. S., Tiator, L., Titov, M., Tkachenko, N. P., Törnqvist, N. A., Tovey, D. R., Valencia, G., Van de Water, R., Varelas, N., Venanzoni, G., Verde, L., Vincter, M. G., Vogel, P., Vogt, A., Wakely, S. P., Walkowiak, W., Walter, C. W., Wands, D., Ward, D. R., Wascko, M. O., Weiglein, G., Weinberg, D. H., Weinberg, E. J., White, M., Wiencke, L. R., Willocq, S., Wohl, C. G., Womersley, J., Woody, C. L., Workman, R. L., Yao, W.-M., Zeller, G. P., Zenin, O. V., Zhu, R.-Y., Zhu, S.-L., Zimmermann, F., Zyla, P. A., Anderson, J., Fuller, L., Lugovsky, V. S., and Schaffner, P. (2018). Review of particle physics. *Phys. Rev. D*, 98:030001. https://link.aps.org/doi/10.1103/PhysRevD.98.030001.

Tanaka, T. L. (2014). Driving the growth of the earliest supermassive black holes with major mergers of host galaxies. *Classical and Quantum Gravity*, 31(24):244005. https://ui.adsabs.harvard.edu/abs/2014CQGra..31x4005T.

Tonry, J. L., Dressler, A., Blakeslee, J. P., Ajhar, E. A., Fletcher, A. B., Luppino, G. A., Metzger, M. R., and Moore, C. B. (2001). The SBF Survey of Galaxy Distances. IV. SBF Magnitudes, Colors, and Distances. *ApJ*, 546(2):681–693. https://ui.adsabs.harvard.edu/abs/2001ApJ...546..681T.

Tremaine, S., Gebhardt, K., Bender, R., Bower, G., Dressler, A., Faber, S. M., Filippenko,

A. V., Green, R., Grillmair, C., Ho, L. C., Kormendy, J., Lauer, T. R., Magorrian, J., Pinkney, J., and Richstone, D. (2002). The Slope of the Black Hole Mass versus Velocity Dispersion Correlation. *ApJ*, 574(2):740–753. https://ui.adsabs.harvard.edu/abs/2002ApJ...574..740T.

Tseliakhovich, D. and Hirata, C. (2010). Relative velocity of dark matter and baryonic fluids and the formation of the first structures. *Phys. Rev. D*, 82:083520. https://link.aps.org/doi/10.1103/PhysRevD.82.083520.

Turk, M. J., Abel, T., and O'Shea, B. (2009). The Formation of Population III Binaries from Cosmological Initial Conditions. *Science*, 325(5940):601. https://ui.adsabs.harvard.edu/abs/2009Sci...325..601T.

Umeda, H., Hosokawa, T., Omukai, K., and Yoshida, N. (2016). The final fates of accreting supermassive stars. *The Astrophysical Journal Letters*, 830(2):L34. https://dx.doi.org/10.3847/2041-8205/830/2/L34.

Verde, L., Treu, T., and Riess, A. G. (2019). Tensions between the early and late Universe. *Nature Astronomy*, 3:891–895. https://ui.adsabs.harvard.edu/abs/2019NatAs...3..891V.

Vergara, M. C., Escala, A., Schleicher, D. R. G., and Reinoso, B. (2023). Global instability by runaway collisions in nuclear stellar clusters: numerical tests of a route for massive black hole formation. *MNRAS*, 522(3):4224–4237. https://ui.adsabs.harvard.edu/abs/2023MNRAS.522.4224V.

Vergara, M. Z. C., Schleicher, D. R. G., Boekholt, T. C. N., Reinoso, B., Fellhauer, M., Klessen, R. S., and Leigh, N. W. C. (2021). Stellar collisions in flattened and rotating Population III star clusters. *A&A*, 649:A160. https://ui.adsabs.harvard.edu/abs/2021A&A...649A.160V.

Vestergaard, M. (2002). Determining Central Black Hole Masses in Distant Active Galaxies. *ApJ*, 571(2):733–752. https://ui.adsabs.harvard.edu/abs/2002ApJ...571..733V.

Vestergaard, M. and Osmer, P. S. (2009). Mass Functions of the Active Black Holes in Distant Quasars from the Large Bright Quasar Survey, the Bright Quasar Survey, and the Color-selected Sample of the SDSS Fall Equatorial Stripe. *ApJ*, 699(1):800–816. https://ui.adsabs.harvard.edu/abs/2009ApJ...699..800V.

Visbal, E., Haiman, Z., and Bryan, G. L. (2014). Direct collapse black hole formation from synchronized pairs of atomic cooling haloes. *MNRAS*, 445(1):1056–1063. https://ui.adsabs.harvard.edu/abs/2014MNRAS.445.1056V.

Vogelsberger, M., Genel, S., Springel, V., Torrey, P., Sijacki, D., Xu, D., Snyder, G., Nelson, D., and Hernquist, L. (2014). Introducing the Illustris Project: simulating the coevolution of dark and visible matter in the Universe. *Monthly Notices of the Royal Astronomical Society*, 444(2):1518–1547. https://doi.org/10.1093/mnras/stu1536.

Volonteri, M., Habouzit, M., and Colpi, M. (2021a). The origins of massive black holes. *Nature Reviews Physics*, 3(11):732–743. https://ui.adsabs.harvard.edu/abs/2021NatRP...3..732V.

Volonteri, M., Habouzit, M., and Colpi, M. (2021b). The origins of massive black holes. *Nature Reviews Physics*, 3(11):732–743. https://ui.adsabs.harvard.edu/abs/2021NatRP...3..732V.

Volonteri, M. and Rees, M. J. (2005). Rapid Growth of High-Redshift Black Holes. *ApJ*, 633(2):624–629. https://ui.adsabs.harvard.edu/abs/2005ApJ...633..624V.

Wang, F., Yang, J., Fan, X., Hennawi, J. F., Barth, A. J., Banados, E., Bian, F., Boutsia, K., Connor, T., Davies, F. B., Decarli, R., Eilers, A.-C., Farina, E. P., Green, R., Jiang, L., Li, J.-T., Mazzucchelli, C., Nanni, R., Schindler, J.-T., Venemans, B., Walter, F., Wu, X.-B., and Yue, M. (2021). A Luminous Quasar at Redshift 7.642. *ApJ*, 907(1):L1. https://ui.adsabs.harvard.edu/abs/2021ApJ...907L...1W.

Wang, F., Yang, J., Fan, X., Wu, X.-B., Yue, M., Li, J.-T., Bian, F., Jiang, L., Bañados, E., Schindler, J.-T., Findlay, J. R., Davies, F. B., Decarli, R., Farina, E. P., Green, R., Hennawi, J. F., Huang, Y.-H., Mazzuccheli, C., McGreer, I. D., Venemans, B., Walter, F., Dye, S., Lyke, B. W., Myers, A. D., and Nunez, E. H. (2019). Exploring Reionization-era Quasars. III. Discovery of 16 Quasars at $6.4 \lesssim z \lesssim 6.9$ with DESI Legacy Imaging Surveys and the UKIRT Hemisphere Survey and Quasar Luminosity Function at $z \sim 6.7$. *ApJ*, 884(1):30. https://ui.adsabs.harvard.edu/abs/2019ApJ...884...30W.

Wang, L., Iwasawa, M., Nitadori, K., and Makino, J. (2020). PETAR: a high-performance N-body code for modelling massive collisional stellar systems. *MNRAS*, 497(1):536–555. https://ui.adsabs.harvard.edu/abs/2020MNRAS.497..536W.

Warren, S. J., Hewett, P. C., Irwin, M. J., McMahon, R. G., and Bridgeland, M. T. (1987). First observation of a quasar with a redshift of 4. *Nature*, 325(6100):131–133. https://ui.adsabs.harvard.edu/abs/1987Natur.325..131W.

Weaver, T. A., Zimmerman, G. B., and Woosley, S. E. (1978). Presupernova evolution of massive stars. *ApJ*, 225:1021–1029. https://ui.adsabs.harvard.edu/abs/1978ApJ...225.1021W.

Webster, B. L. and Murdin, P. (1972). Cygnus X-1-a Spectroscopic Binary with a Heavy Companion ? *Nature*, 235(5332):37–38. https://ui.adsabs.harvard.edu/abs/1972Natur.235...37W.

Weinberger, R., Springel, V., and Pakmor, R. (2020). The AREPO Public Code Release. *ApJS*, 248(2):32. https://ui.adsabs.harvard.edu/abs/2020ApJS..248...32W.

Wise, J. H. (2023). The formation of the first black holes. *arXiv e-prints*, page arXiv:2304.09311. https://ui.adsabs.harvard.edu/abs/2023arXiv230409311W.

Wise, J. H., Regan, J. A., O'Shea, B. W., Norman, M. L., Downes, T. P., and Xu, H. (2019). Formation of massive black holes in rapidly growing pre-galactic gas clouds. *Nature*, 566(7742):85–88. https://ui.adsabs.harvard.edu/abs/2019Natur.566...85W.

Wollenberg, K. M. J., Glover, S. C. O., Clark, P. C., and Klessen, R. S. (2020). Formation sites of Population III star formation: The effects of different levels of rotation and turbulence on the fragmentation behaviour of primordial gas. *MNRAS*, 494(2):1871–1893. https://ui.adsabs.harvard.edu/abs/2020MNRAS.494.1871W.

Woods, T. E., Agarwal, B., Bromm, V., Bunker, A., Chen, K.-J., Chon, S., Ferrara, A., Glover, S. C. O., Haemmerlé, L., Haiman, Z., Hartwig, T., Heger, A., Hirano, S., Hosokawa, T., Inayoshi, K., Klessen, R. S., Kobayashi, C., Koliopanos, F., Latif, M. A., Li, Y., Mayer, L., Mezcua, M., Natarajan, P., Pacucci, F., Rees, M. J., Regan, J. A., Sakurai, Y., Salvadori, S., Schneider, R., Surace, M., Tanaka, T. L., Whalen, D. J., and Yoshida, N. (2019a). Titans of the early Universe: The Prato statement on the origin of the first supermassive black holes. *Publ. Astron. Soc. Australia*, 36:e027. https://ui.adsabs.harvard.edu/abs/2019PASA...36...27W.

Woods, T. E., Agarwal, B., Bromm, V., Bunker, A., Chen, K.-J., Chon, S., Ferrara, A., Glover, S. C. O., Haemmerlé, L., Haiman, Z., Hartwig, T., Heger, A., Hirano, S., Hosokawa, T., Inayoshi, K., Klessen, R. S., Kobayashi, C., Koliopanos, F., Latif, M. A., Li, Y., Mayer, L., Mezcua, M., Natarajan, P., Pacucci, F., Rees, M. J., Regan, J. A., Sakurai, Y., Salvadori, S., Schneider, R., Surace, M., Tanaka, T. L., Whalen, D. J., and Yoshida, N. (2019b). Titans of the early Universe: The Prato statement on the origin of the first supermassive black holes. *Publ. Astron. Soc. Australia*, 36:e027. https://ui.adsabs.harvard.edu/abs/2019PASA...36...27W.

Woods, T. E., Heger, A., and Haemmerlé, L. (2020). On monolithic supermassive stars. *MN-RAS*, 494(2):2236–2243. https://ui.adsabs.harvard.edu/abs/2020MNRAS.494.2236W.

Woosley, S. E., Heger, A., Cumming, A., Hoffman, R. D., Pruet, J., Rauscher, T., Fisker, J. L., Schatz, H., Brown, B. A., and Wiescher, M. (2004). Models for Type I X-Ray Bursts with Improved Nuclear Physics. *ApJS*, 151(1):75–102. https://ui.adsabs.harvard.edu/abs/2004ApJS..151...75W.

Woosley, S. E., Heger, A., and Weaver, T. A. (2002). The evolution and explosion of massive stars. *Reviews of Modern Physics*, 74(4):1015–1071. https://ui.adsabs.harvard.edu/abs/2002RvMP...74.1015W.

Wright, E. L., Eisenhardt, P. R. M., Mainzer, A. K., Ressler, M. E., Cutri, R. M., Jarrett, T., Kirkpatrick, J. D., Padgett, D., McMillan, R. S., Skrutskie, M., Stanford, S. A., Cohen, M., Walker, R. G., Mather, J. C., Leisawitz, D., Gautier, Thomas N., I., McLean, I., Benford, D., Lonsdale, C. J., Blain, A., Mendez, B., Irace, W. R., Duval, V., Liu, F., Royer, D., Heinrichsen, I., Howard, J., Shannon, M., Kendall, M., Walsh, A. L., Larsen, M., Cardon, J. G., Schick, S., Schwalm, M., Abid, M., Fabinsky, B., Naes, L., and Tsai, C.-W. (2010). The Wide-field Infrared Survey Explorer (WISE): Mission Description and Initial On-orbit Performance. *AJ*, 140(6):1868–1881. https://ui.adsabs.harvard.edu/abs/2010AJ....140.1868W.

Wurster, J., Price, D. J., and Bate, M. R. (2017). The impact of non-ideal magnetohydrodynamics on binary star formation. *MNRAS*, 466(2):1788–1804. https://ui.adsabs.harvard.edu/abs/2017MNRAS.466.1788W.

Yang, J., Wang, F., Fan, X., Hennawi, J. F., Davies, F. B., Yue, M., Banados, E., Wu, X.-B., Venemans, B., Barth, A. J., Bian, F., Boutsia, K., Decarli, R., Farina, E. P., Green, R., Jiang, L., Li, J.-T., Mazzucchelli, C., and Walter, F. (2020). Pōniuā'ena: A Luminous z = 7.5 Quasar Hosting a 1.5 Billion Solar Mass Black Hole. *ApJ*, 897(1):L14. https://ui.adsabs.harvard.edu/abs/2020ApJ...897L..14Y.

Yen, H.-W., Koch, P. M., Takakuwa, S., Krasnopolsky, R., Ohashi, N., and Aso, Y. (2017). Signs of Early-stage Disk Growth Revealed with ALMA. *ApJ*, 834(2):178. https://ui.adsabs.harvard.edu/abs/2017ApJ...834..178Y.

Yoshida, N., Omukai, K., and Hernquist, L. (2008). Protostar Formation in the Early Universe. *Science*, 321(5889):669. https://ui.adsabs.harvard.edu/abs/2008Sci...321..669Y.

Yoshida, N., Omukai, K., Hernquist, L., and Abel, T. (2006). Formation of Primordial Stars in a ΛCDM Universe. *ApJ*, 652(1):6–25. https://ui.adsabs.harvard.edu/abs/2006ApJ...652....6Y.

Yu, Q. and Tremaine, S. (2002). Observational constraints on growth of massive black holes. *MNRAS*, 335(4):965–976. https://ui.adsabs.harvard.edu/abs/2002MNRAS.335..965Y.

Yungelson, L. R., van den Heuvel, E. P. J., Vink, J. S., Portegies Zwart, S. F., and de Koter, A. (2008). On the evolution and fate of super-massive stars. *A&A*, 477(1):223–237. https://ui.adsabs.harvard.edu/abs/2008A&A...477..223Y.